Technische Universität München
TUM School of Natural Sciences

Internal Dynamics and Stability of Bulk Heterojunction Films for Application in Organic Photovoltaics

Dominik Mathias Schwaiger, M. Sc.

Vollständiger Abdruck der von der TUM School of Natural Sciences der Technischen Universität München zur Erlangung eines

Doktors der Naturwissenschaften (Dr. rer. nat.)

genehmigten Dissertation.

Vorsitz: Prof. Dr. Martin Zacharias

Prüfer*innen der Dissertation:

1. Prof. Dr. Peter Müller-Buschbaum
2. apl. Prof. Dr. Hristo Iglev

Die Dissertation wurde am 25.09.2023 bei der Technischen Universität München eingereicht und durch die TUM School of Natural Sciences am 30.10.2023 angenommen.

Abstract

In this thesis, PTB7:PCBM blend films, an important model system for active layers in organic solar cells, are investigated. Special focus is directed on the internal dynamics of the polymer side chains and the film stability in dependence of fabrication procedure and the use of solvent additives. The first quasielastic neutron scattering experiment for the material system is realized to examine dynamic processes on different timescales within the films. The influence of blending the polymer PTB7 with the fullerene derivate PCBM as well as different measures for the improvement of power conversion efficiencies of resulting devices is studied. Beyond this, the removal of residual solvent additive molecules from the dried films is tracked with time resolved QENS. On this basis, the stability of PTB7:PCBM films produced by different drying protocols with and without solvent additives is investigated at ambient atmosphere under illumination. The response of chemical and physical properties of the films is followed by XRD, UV-vis-, FTIR- and Raman spectroscopy. The results are set into context with literature and the performance of respective solar cells in order to extend the knowledge base of the present system and aid future developments in the field of organic photovoltaics.

Zusammenfassung

In dieser Arbeit wird die Untersuchung von PTB7:PCBM Filmen, einem wichtigen Modellsystem für aktive Schichten in organischen Solarzellen, präsentiert. Besonderer Fokus liegt dabei auf der internen Dynamik der Polymer Seitenketten sowie der Stabilität der Filme in Abhängigkeit von Herstellungsparametern und der Nutzung von Lösungsmittelzusätzen. Für dieses System wurde das erste Experiment mit quasielastischer Neutronenstreuung durchgeführt um dynamische Prozesse in den Filmen auf verschiedenen Zeitskalen zu beobachten. Es wird der Einfluss der Mischung des Polymers PTB7 mit dem Fulleren PCBM und verschiedenen Methoden, die der Erhöhung des Wirkungsgrads von entsprechenden Modulen dienen, untersucht. Darüber hinaus wird mit zeitaufgelöstem QENS verfolgt wie verbliebene Moleküle des Lösungsmittelzusatzes den getrockneten Film verlassen. Darauf aufbauend wird die Stabilität der PTB7:PCBM Filme unter regulären atmosphärischen

Bedingungen bei Beleuchtung untersucht. Das Hauptaugenmerk liegt dabei auf dem Einfluss von verschiedenen Trocknungsbedingungen sowie der Nutzung von Lösungsmittelzusätzen. Die Reaktion von chemischen und physikalischen Parametern der Filme wird mit XRD, UV-vis-, FTIR- und Raman Spektroskopie verfolgt. Die Ergebnisse werden in Kontext mit vorhandener Literatur und der Funktion von entsprechenden Solarzellen gesetzt, um die Wissensbasis dieses Modellsystems zu erweitern und zu zukünftigen Entwicklungen im Bereich der organischen Solarzellen beizutragen.

Table of contents

Abbreviations

A	acceptor
B^+	positive bipolaron
B^-	negative bipolaron
BDT	benzodithiophene (-unit in PTB7)
BHJ	bulk heterojunction
BR	bacteriorhodopsin
BS	backscattering
BTP-2F2Cl	2,2'-((2Z,2'Z)-((12,13-bis(2-ethylhexyl)-3,9-diundecyl-12,13-dihydro-[1,2,5] thiadiazolo[3,4-e]thieno[2",3'':4',5']thieno[2',3':4,5]pyrrolo[3,2-g]thieno[2',3':4,5] thieno[3,2-b]indole-2,10-diyl)bis(methanylylidene))bis(5,6-dichloro-3-oxo-2,3-dihydro-1H-indene-2,1-diylidene))dimalononitrile
CB	chlorobenzene
CCD	charge coupled device
CFRP	carbon fiber reinforced plastic
D	diffusion coefficient
D18	Poly[(2,6-(4,8-bis(5-(2-ethylhexyl-3-fluoro)thiophen-2-yl)-benzo[1,2-b:4,5-b']dithiophene))-alt-5,5'-(5,8-bis(4-(2-butyloctyl)thiophen-2-yl)dithieno [3',2':3,4;2",3":5,6]benzo[1,2-c][1,2,5]thiadiazole)]
DERHD7T	5Z,5′Z)-5,5′-((3,3‴′,3⁗,3⁗′,4′,4″-hexaoctyl-[2,2′:5′,2″:5″,2‴:5‴,2⁗:5⁗,2⁗′:5⁗′, 2⁗′-sepithiophene]-5,5⁗′-diyl)bis(methanylylidene))bis(3-ethyl-2-thioxothiazolidin-4-one)
DIO	1,8-diiodooctane
DOS	density of states
DPE	diphenyl ether
DPPEZnP-TEH	5,15-Bis(2,5-bis-(2-ethyl-hexyl)-3,6-di-thienyl-2-yl-2,5-dihydro-pyrrolo[3,4-c] pyrrole-1,4-dione-5'-yl-ethynyl)-10,20-bis(5-(2-ethylhexyl)-thienyl)-porphyrin-zinc
EBL	electron blocking layer
E_F	Fermi energy
E_g	band gap
EISF	elastic incoherent structure factor
ETL	electron transport layer
FOC	frame overlap chopper
FRET	fluorescent/Förster resonant energy transfer
FRM II	Forschungsreaktor München 2

FTIR	Fourier-transform-infrared (spectroscopy)
HBL	hole blocking layer
HOMO	highest occupied molecular orbital
HORC	higher order removal chopper
HTL	hole transport layer
HWHM	half width at half maximum
I(Q, t)	intermediate scattering function
$IC_{60}BA$	1′,1″,4′,4″-Tetrahydro-di[1,4]methanonaphthaleno[1,2:2′,3′,56,60:2″,3″]-[5,6]fullerene-C_{60}
$IC_{70}BA$	1′,1″,4′,4″-Tetrahydro-di[1,4]methanonaphthaleno[1,2:2′,3′,56,60:2″,3″]-[5,6]fullerene-C_{70}
IDIC	2,2'-((2Z,2'Z)-((4,4,9,9-tetrahexyl-4,9-dihydro-s-indaceno[1,2-b:5,6-b']dithiophene-2,7-diyl)bis(methanylylidene))bis(3-oxo-2,3-dihydro-1H-indene-2,1-diylidene))dimalononitrile
IT-4F	3,9-bis(2-methylene-((3-(1,1-dicyanomethylene)-6,7-difluoro)-indanone))-5,5,11,11-tetrakis(4-hexylphenyl)-dithieno[2,3-d:2’,3’-d’]-s-indaceno[1,2-b:5,6-b’]dithiophene
ITIC	3,9-bis(2-methylene-(3-(1,1-dicyanomethylene)-indanone))-5,5,11,11-tetrakis (4-hexylphenyl)-dithieno[2,3-d:2’,3’-d’]-s-indaceno[1,2-b:5,6-b’]dithiophene
ITO	indium tin oxide
KWW	Kohlrausch-Williams-Watt
L8-BO	2,2'-((2Z,2'Z)-((12,13-bis(2-ethylhexyl)-3,9-(2-butyloctyl)-12,13-dihydro-[1,2,5]thiadiazolo[3,4-e]thieno[2",3’’:4’,5']thieno[2',3':4,5]pyrrolo[3,2-g]thieno[2',3':4,5]thieno[3,2-b]indole-2,10-diyl)bis(methanylylidene))bis(5,6-difluoro-3-oxo-2,3-dihydro-1H-indene-2,1-diylidene))dimalononitrile
LCAO	linear combination of atomic orbitals
LiF	lithium flouride
LUMO	lowest unoccupied molecular orbital
MCRC	monochromating counter-rotating chopper
MEH-PPV	Poly-[2-methoxy-5-(2-ethylhexyloxy)-1,4-phenylenvinylen]
MLZ	Heinz Meier-Leibnitz Zentrum
MoO_3	molybdenum oxide
MoS_2	molybdenum sulfide
NSE	neutron spin-echo
OPV	organic photovoltaic
OSC	organic solar cell
P^+	positive polaron
P^-	negative polaron
P3HT	Poly-(3-hexylthiophen-2,5-diyl)
PA	polyacetylene

$PC_{61}BM$	[6,6]-Phenyl-C_{61}-buttersäure-methylester
$PC_{71}BM$	[6,6]-Phenyl-C_{71}-buttersäure-methylester
PCE	power conversion efficiency
PCE12	Poly[(5,6-difluoro-2,1,3-benzothiadiazol-4,7-diyl)-alt-(3,3'''-di(2-nonyltridecyl)-2,2';5',2'';5'',2'''-quaterthiophen-5,5'''-diyl)]
PCRC	pulsing counter-rotating chopper
PEO	polyethylene oxide
PEDOT	Poly-3,4-ethylendioxythiophen
PM6	Poly[(2,6-(4,8-bis(5-(2-ethylhexyl-3-fluoro)thiophen-2-yl)-benzo[1,2-b:4,5-b'] dithiophene))-alt-(5,5-(1',3'-di-2-thienyl-5',7'-bis(2-ethylhexyl)benzo[1',2'-c:4',5'-c']dithiophene-4,8-dione)]
PSS	polystyrene sulfonate
PTB7	Poly [[4,8-bis[(2-ethylhexyl)oxy]benzo[1,2-b:4,5-b']dithiophene-2,6-diyl][3-fluoro-2-[(2-ethylhexyl)carbonyl]thieno[3,4-b]thiophenediyl]]
PTB7-Th	Poly[4,8-bis(5-(2-ethylhexyl)thiophen-2-yl)benzo[1,2-b;4,5-b']dithiophene-2,6-diyl-alt-(4-(2-ethylhexyl)-3-fluorothieno[3,4-b]thiophene-)-2-carboxylate-2-6-diyl)]
PT	polythiophene
PTQ10	Poly [[6,7-difluoro[(2-hexyldecyl)oxy]-5,8-quinoxalinediyl]-2,5-thiophenediyl]]
PV	photovoltaic
QENS	quasielastic neutron scattering
S^+	positive soliton
S^-	negative soliton
S^0	neutral soliton
S(Q, ω)	scattering function
SERS	surface enhanced Raman spectroscopy
TiO_x	titanium oxide
TOF	time-of-flight
TOFTOF	name of the cold-neutron TOF spectrometer at MLZ
TPTI	thieno[20,30:5,6]pyrido[3,4-g]thieno[3,2-c]-isoquinoline-5,11(4H,10H)-dione
TT	thienothiophene (-unit in PTB7)
UV-vis	ultraviolet-visible (spectroscopy)
V_2O_5	vanadium oxide
Wp	Watt peak
XRD	X-ray diffraction
Y6	2,2'-((2Z,2'Z)-((12,13-bis(2-ethylhexyl)-3,9-diundecyl-12,13-dihydro-[1,2,5] thiadiazolo[3,4-e]thieno[2'',3'':4',5']thieno[2',3':4,5]pyrrolo[3,2-g]thieno[2',3':4,5] thieno[3,2-b]indole-2,10-diyl)bis(methanylylidene))bis(5,6-difluoro-3-oxo-2,3-dihydro-1H-indene-2,1-diylidene))dimalononitrile
ZnO	zinc oxide

1 Introduction

With the increasing world population and the legitimate striving for prosperity and well-being of all nations, the global demand for energy is constantly increasing. This increase exceeded 60 % within the past 20 years.[1] Fossil sources such as oil, gas and coal are very convenient primary energy sources due to their high energy density and good transportability. Thus, large scale infrastructure for their production, transport and processing has developed. This infrastructure is the economic basis for large parts of world industry and even whole countries. Nonetheless, fossil fuels bring a major drawback, the release of greenhouse gases, mainly CO_2, upon their combustion. This CO_2 dramatically drives the well-known change of the composition of our earth´s atmosphere and the concomitant climate change.[2] Since the combustion of oil, gas and coal follows stoichiometric equations and the reaction products are generally not stored but escape into the atmosphere, the amount of emitted climate gases is proportional to the amount of energy that is produced from fossil sources.[3] To avoid a further uncontrolled and irreversible carbonization of the atmosphere and the oceans, the choice of primary energy sources is a critical factor. The substitution of fossil sources by renewables like solar, wind and water power reduces the emission of greenhouse gases and offers a sustainable way of energy provision without consuming limited resources.

The example of Germany shows that a significant shift in the primary energy sources is possible within reasonable time. In 2012, around 23 % of the electrical power originated from renewable sources. Only ten years later the fraction has doubled to 46 % in 2022.[4], [5] Photovoltaic power generation showed an overproportionally large increase within this time interval of approximately 160 %, showing the great potential of this technology to lead the transition to green energy production. Thus, solar energy plays an important role in the German federal energy strategy, which plans to extend the present (2022) installed photovoltaic (PV) power of 66.5 GWp

(peak power) to about 400 GWp until 2040.[4], [5] This could be sufficient to reach the goals of climate neutrality, if other sectors reach their goals as well.

In order to accomplish such ambitious goals, much effort is put into research in the field of photovoltaic technology to improve the performance and availability of solar cells, not only in Germany, but all over the world. The rise of thin film technology in the field of photovoltaics in the 1990´s provided comparably low-cost solar cells. Even though at the cost of tendentially lower efficiencies this second generation of solar cells shows high economic potential and increase their market share constantly.[6] The latest step in the development of photovoltaics is the introduction of the third generation of solar cells, which aims to further increase cost efficiency by the use of simple manufacturing processes and abundant materials.[7], [8] This third generation includes approaches of e.g. fully organic, perovskite, dye sensitized, quantum dot or multi junction solar cells. These emerging PV technologies are based on a stack of thin layers that brings several advantages compared to conventional bulk crystalline silicon solar cells, which have dominated the market for 3 decades. The solution based fabrication of the thin layers consumes far less energy than the melting of silicon to produce monocrystalline (also polycrystalline Si solar cells are used) doped silicon wafers and thus reduces the energy payback times significantly.[9] Beyond this, the thin film approach offers the possibility for the production of light weight, flexible devices, if flexible substrates like plastic foil are used.[10], [11] Flexible, lightweight solar cells reduce transportation costs of the modules and offer new fields of applications, for example as part of architecture in facades of buildings, artificial trees, etc.[12], [13], [14] Perhaps the most important advantage of the novel PV technologies, especially organic solar cells, is the fact that they can be produced from abundant materials and do not rely on pure silicon or other inorganic material as base material. Roll to roll processing with e.g. spray coating or printing fosters the transition from lab scale to the economically relevant large scale production.[15], [16] Being based on polymers or/and organic molecules, they further offer the possibility of molecular engineering in the organic photovoltaic (OPV) stack. Optical and electrical properties can be fine-tuned according to the desired application and the potential to increase the solar cell performance by the modification/choice of the used organic materials is immense.[17], [18]

Besides the very promising advantages of organic solar cells, also this technology brings some challenges for its profitable large-scale application and the big economic breakthrough. Degradation of OPV modules has been found to be a major challenge

in the field.[19] It results in decreased device performance and solar cells that are practically unusable after a very short time. This prevents both, an economically profitable and ecologically sustainable way for providing electrical energy. The origins of the degradation of OPVs are diverse. Examples are the loss of contact between individual layers due to delamination [20] or the alteration of the chemical structure of organic materials due to e.g. photo-oxidation.[21], [22] Also the physical microstructure, which is critical for the function of organic solar cells, can be affected by e.g. temperature induced aging. For example, bulk heterojunctions are generally achieved by frustrating the demixing process of different materials when the desired morphology is reached. This thermodynamically metastable state may undergo changes if respective external stimuli are present.[23], [24] A successful way of preventing or delaying degradation, especially caused by the presence of oxygen, has been found in the encapsulation of OPV devices.[25] Nonetheless, a more elegant and desirable way to achieve stable organic solar cells is to develop material systems with sufficient intrinsic stability at ambient conditions.

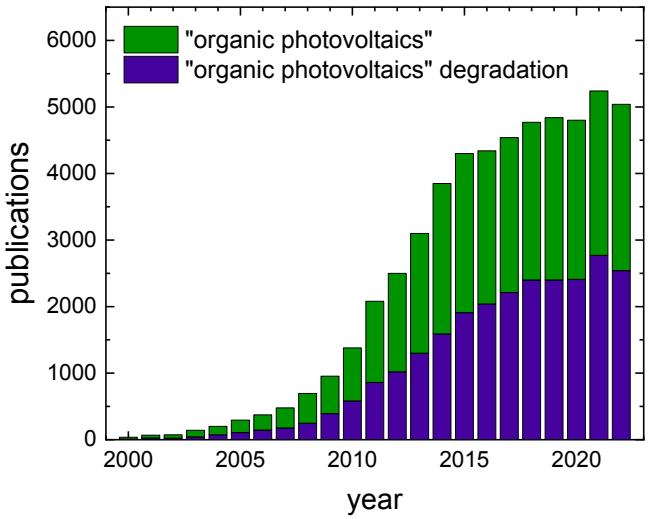

Figure 1: Number of published articles in the field of organic photovoltaics as function of publication year from 2000 until 2022. The height of the green columns indicates the number of publications that mention "organic photovoltaics" and the violet part of the columns represents the fraction of the published articles, that also mention the word "degradation". Data are obtained by the number of results provided by a Google Scholar search for the respective keywords, anywhere within the publication.

Due to these wide-spread possibilities for the variation and improvement of the used materials and the design of devices, much scientific effort has been put into this field, recently.

Figure 1 shows the development of the number of published research articles related to organic photovoltaics since the beginning of the century. Alongside the absolute number of publications in the field (green bars), the fraction of studies with reference to OPV degradation is indicated (violet area).

Figure 1 shows constantly increasing numbers for both, studies in the general field of OPV and related to the degradation of organic solar cell in particular. After a slow initial increase from 2000 until 2006, a rapid increase in the number of OPV related publications is observed until 2015. From 2016 on the increase slows down, but is generally still continuing until 2021. The slight dips for the years 2020 and 2022 might be explained by the forced reduction of research activity due to the Covid19 pandemic and yet incomplete recent statistics. This underlines the great scientific relevance of the field of OPV and shows that the need for further research is not decreasing, yet. The awareness of OPV degradation and the importance of research in this field is shown by the increase of the fraction of the violet bars from around 30 % in the early years up to around 50 % recently.

The main goal of the present thesis is the fundamental investigation of the degradation behavior of PTB7:PCBM bulk heterojunction films that can be used as active layers in organic solar cells. This system was chosen because it is a basic model system in the development of organic solar cells, introducing PTB7 as low band gap electron donor polymer. Thus, new insights are of great relevance and fit into a fundamental knowledge context. In chapters 5 and 6 the PTB7 polymer dynamics on molecular level are studied in detail with quasielastic neutron scattering (QENS). These QENS experiments represent the first ever reported studies in the system PTB7:PCBM. Chapter 7 focuses on the chemical and physical degradation processes that occur in the PTB7:PCBM bulk heterojunction when exposed to light irradiation and ambient atmosphere. Therefore, X-ray diffraction (XRD) as well as time resolved UV-visible (UV-vis), Fourier-transform-infrared (FTIR) and Raman spectroscopy were used. The investigations are not limited to simple PTB7:PCBM blend films, but also include the influence of the addition of the solvent additives 1,8-diiodooctane and diphenyl ether (DIO and DPE) in the production process and the effect of different drying procedures on the physicochemical stability of the resulting films.

After the introduction of the fundamental aspects of the layout and working principle of organic solar cells, including the materials used in this study, and a description of the used characterization techniques in chapter 2, chapter 3 describes the practical aspects of sample preparation for the different experiments. In chapter 4, the actual

setups for the applied characterization techniques are presented, including the *in situ* illumination realization, if applied. The following three chapters provide the obtained results, ordered by the respective article in which they were published. Chapter 5 summarizes the publication “Investigation of Molecular Dynamics of a PTB7:PCBM Polymer Blend with Quasi-Elastic Neutron Scattering”[26] that comprises the QENS study of PTB7 and its blend with PCBM. Chapter 6 further deepens the QENS study of molecular dynamics in the system PTB7:PCBM by the extension of the sample range with additional blend ratios and the application of the solvent additive DIO. The content of this section was published in “The Influence of the Blend Ratio, Solvent Additive, and Post-Production Treatment on the Polymer Dynamics in PTB7:PCBM Blend Films”.[27] In Chapter 7, the influence of solvent additive and drying procedure on the light and oxygen mediated degradation of PTB7:PCBM bulk heterojunction films are studied with UV-vis, FTIR and Raman spectroscopy. These findings were published in “*In Situ* Study of Degradation in PTB7 : PCBM Films Prepared with the Binary Solvent Additive DPE : DIO”.[28] A summary of the key findings and a short outlook to future perspectives in the field is given in chapter 8.

2 Background

2.1 Organic Photovoltaics

The focus of this thesis is the investigation of PTB7:PCBM blend films, as used in photovoltaic applications. This section will briefly set the theoretical background of organic photovoltaics and the working principle of organic solar cells. From organic semiconductors over the working principle of solar cells, typically used materials for the individual functional layers to the construction of actual OPV devices and performance limiting factor in their application, basic principles are explained to set the investigated material system into a wider context.

2.1.1 Organic semiconductors

The scope of the present thesis is the investigation of active layers for organic solar cells. The name already implies that for the construction of such devices, predominantly organic materials are used as active materials, which have to fulfill certain requirements.

The concepts, presented in the following section describe organic semiconductors and are theoretically valid for both categories, polymers and small organic molecules. In the following, explanations are given for polymers since they offer the required features in a more descriptive way.

Since their discovery and first use in the early 20th century, polymers have attracted significant attention from science and industry due to their very versatile and tunable properties. This is mainly based on the large variety of organic building blocks, or monomers, and practically infinite possibilities for their combination. Many of the advantages of conventional polymers can also be utilized for conductive polymers, which were first described in 1977 with the example of polyacetylene (PA) that increased its electric conductivity significantly upon exposure to iodine vapor.[29], [30] Thus, the first organic semiconductor including a suitable doping procedure was

discovered. First reports of electrical conductivity in organic systems have been published already in the 1950´s, though.[31] Since that time, significant progress in terms of development and discovery of novel organic semiconductor materials has been made, but the simple structure of PA can be used as a model to describe the theory of organic semiconductors.[32]

Conjugated backbone, band structure and charge carriers in organic molecules

The basic requirement for a polymer to be electrically conductive is the presence of an extended system of alternating C-C single and double bonds along its backbone, as schematically shown in Figure 2 for the polyacetylene polymeric backbone. The two depicted mesomers are chemically identical and represent edge structures of the respective molecules. The actual bond structure of the molecule can transform from mesomer 1 to mesomere 2 and backwards. For elongated polymer chains the actual structure is most likely somewhere in between the two extreme structures, which are depicted in Figure 2.

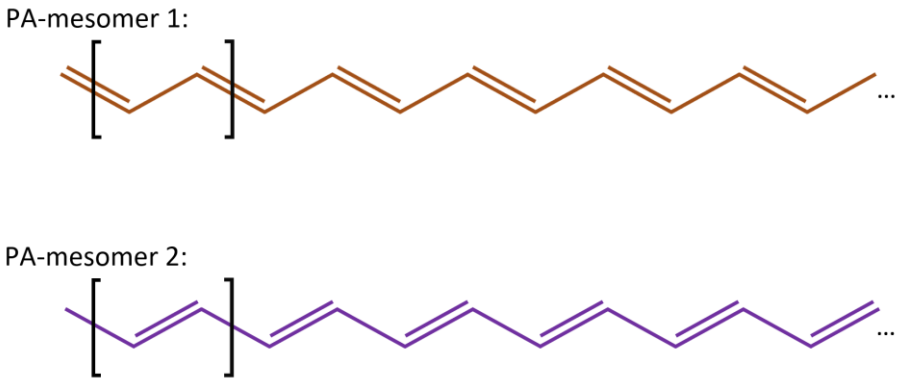

Figure 2: Two mesomeric ground states of polyacetylene, caused by the delocalization of C=C double bonds.

The actual band structure of polymeric semiconductors can be described by the theory of linear combination of atomic orbitals (LCAO). Therefore, it is important to understand the bonding situation of the carbon atoms in the conjugated backbone. Two of the valence electrons are taken by the 2s orbital, the other two are statistically equally distributed into the tree $p_{x,y,z}$ orbitals. Due to energetic reasons the s orbital hybridizes with two of the p orbitals, leaving the p_z orbital unhybridized. The overlap of

different types of orbitals leads to the formation of different types of bonds: σ-bonds (overlapping hybrid orbitals), which are characterized by a high degree of electron localization, and π-bonds (overlapping p_z orbitals) that are less localized and thus are the mobile constituents of the π-conjugated network, as discussed before.

The electrons forming the π-bond, thus called π-electrons, are delocalized within this so-called conjugated network. They are represented as the additional lines of the double bonds or black dots in Figure 2 and Figure 5.

Since only “opposite” orbitals can overlap to form π bonds, in the sp^2-hybridized system, LCAO theory assumes that every π-bond contains one binding π-orbital (π) and one antibinding π-orbital (π*).[33] In its ground state, the π orbital is energetically lower and thus occupied, whereas the π* orbital remains unoccupied, denoted as the highest occupied atomic orbital(s) and lowest unoccupied atomic orbital(s) in Figure 3. As depicted in Figure 3, one single π-bond yields discrete energy levels of π and π* orbitals. The number of available states increases with increasing polymer chain length (and size of the conjugated system). For a large number of monomers, the discrete levels become indistinct and fuse into energy bands, commonly referred to as highest occupied molecular orbitals (HOMO), representing the π-states, and lowest unoccupied molecular orbital (LUMO), representing the π*-states. HOMO and LUMO levels are not overlapping and separated by the band gap E_g. In analogy to classical inorganic semiconductors, the statistical electron occupation probability follows the Fermi-Dirac distribution which leads to an incomplete occupation of both, highest occupied and lowest unoccupied molecular orbitals.

An overlap of the π-orbitals of neighboring conjugated chains enables a charge transport between the different chains and is called π-π-stacking. Therefore, the structure and in particular the interchain distance of the π-π-stacking is an important characteristic for the electrical conductivity of organic semiconductors.

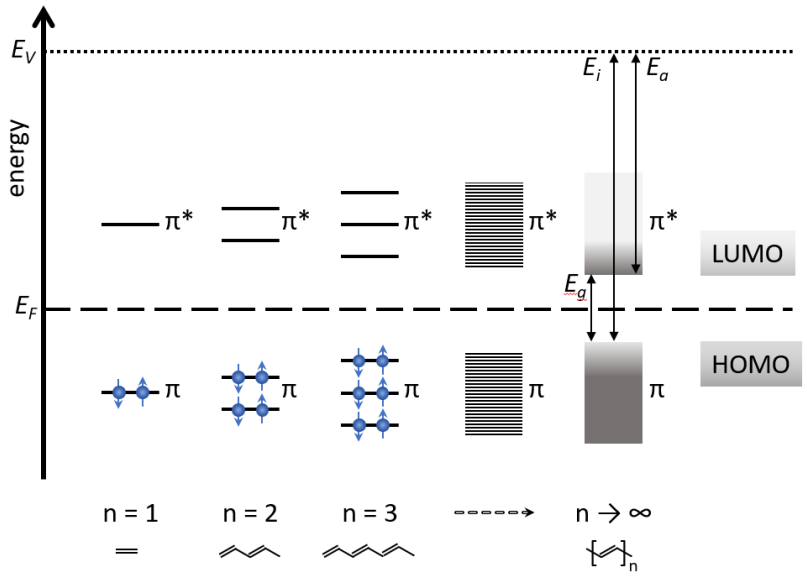

Figure 3: Formation of HOMO and LUMO energy bands according to the LCAO theory. According band gap E_g, ionization energy E_i and electron affinity E_a as well es Fermi level E_F and vacuum energy E_v are indicated.

Figure 4a depicts the dispersion of allowed energy states of a regular 1-dimensional chain with constant spacing *a* between the individual sites. This would be the case for a chain of carbon atoms where one freely moving electron is positioned at each of them. The availability of one free electron per site is caused by the sp_2 hybridization. Because it is energetically more favorable to build pairs instead of occurring solitary, a super lattice with exactly the double spacing *2a* is formed (still each C atom contributes one electron to the delocalized system). The C=C double bonds statistically also appear in regular distances. According to the Peierl´s instability theorem, this regular 1-dimensional lattice is unstable and subject to distortions.[34] The Peirl´s theorem describes the deformation of a lattice, caused by electron waves, characterized by the electron vector $\vec{k}$. The lattice distortion and the effective doubling of the unit cell a yields to the opening of a band gap at $\vec{k} = \frac{\pi}{2a}$. This detachment of the wave functions around the Fermi energy, which leads to the formation of the band gap, is depicted in Figure 4b. The Fermi level can not be accessed by the electron distribution function in this case. The size of the band gap is determined by the degree of instability that can be induced by the mobile electron charge density waves against the lattice energy.

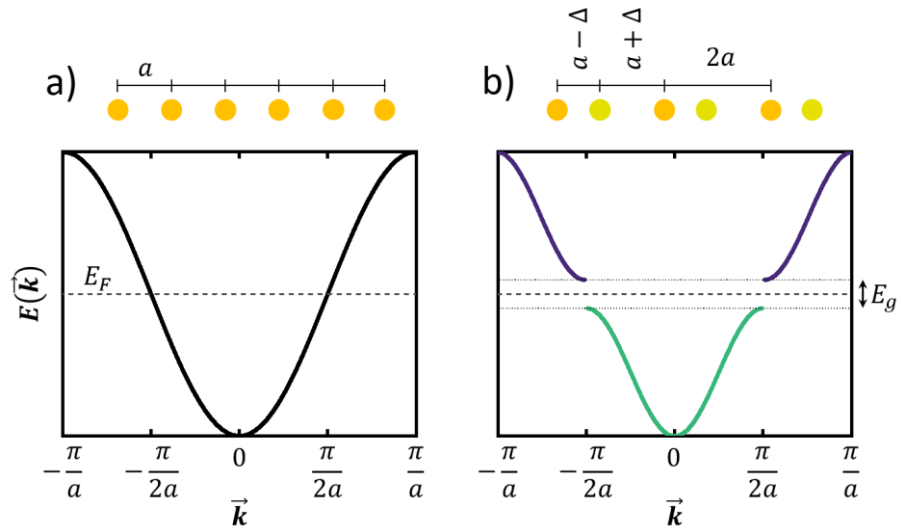

Figure 4: Schematic drawing of lattice and polymeric bands according to Peierl´s instability theorem: a) Case for a simple 1-dimensional lattice, b) band structure in the case with a superstructure introducing a second lattice constant. This leads to the detachment of wave functions at $\vec{k}$ and $-\vec{k}$, respectively and the creation of a band gap E_g.

The Su-Schriefer-Heeger theory describes the charge carrier transport in polymers in the form of quasiparticles, namely solitons, polarons and bipolarons, rather than the more simple concept of the transport of free electrons or holes, respectively.[35], [36] In the picture of the electron distribution along the polymer chain as depicted in Figure 2, solitons, polarons and bipolarons are schematically drawn in Figure 5. Due to the delocalization of electrons, not only one mesomeric state exists within a polymer chain, but different states are in contact with each other, which leads to lattice distortions. This can be enforced by doping of the polymer chain, i.e. the introduction of additional positive (p-type) or negative (n-type) charges. At the interface between two opposite mesomeric states, a defect, called soliton is formed.

Three kinds of solitons can be differentiated according to their charge, positively charged (S^+), neutral (S^0) and negatively charged (S^-). The soliton charge is determined by the number of π-electrons bound to the C-atom at the mesomeric interface. An uneven number of π-electons (1 in the case of a S^0 soliton) leads to a spin of the soliton of 0.5. The different types of solitons are depicted for the example of the linear PA chain in Figure 5.

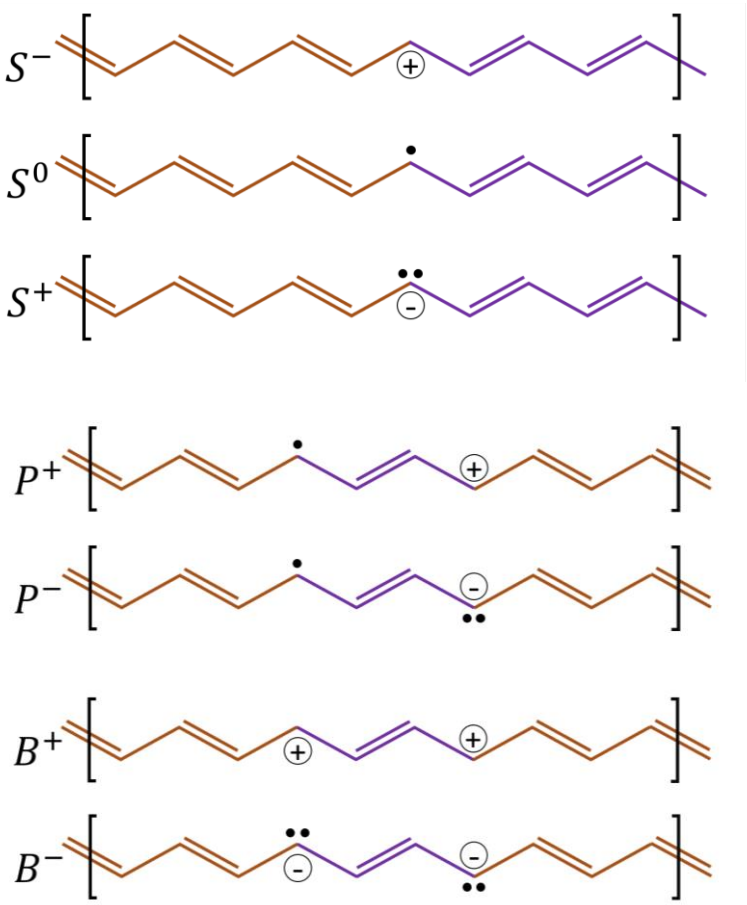

Figure 5: Schematic representation of the tree different kinds of solitons S^-, S^0 and S^+, polarons P^+ and P^- as well as bipolarons B^+ and B^- on the example of a polyacetylene polymer chain. Black points represent π-electrons at the respective C-atoms.

In the case of multiple solitons within a single polymer chain, they can interact with each other. If a charged soliton meets a neutral one, the result is a polaron. A polaron represents a charged state, either +1 for P^+ or -1 for P^- polarons, in combination with an effective spin (0.5 for both kinds of polarons). Polarons as well as bipolarons (described in the following) are lattice distortions since the lattice (in this case the polymer chain) is matching before and after the (bi-)polaron (compare Figure 5).

If two identically charged solitons or polarons are combined, the result is called bipolaron. Thus, bipolarons yield no spin but double elemental charge, either +2 for B^+ bipolarons or -2 for B^- bipolarons, respectively. Solitons and especially polarons are considered to be the dominant mechanisms for charge transport in π-conjugated organic systems. The occurrence of Solitons can also be favored by appropriate doping. The possibility for these quasiparticles to occur and their energy distribution

depend on the chemical structure, the resulting electronic band structure of the material and the presence and sort of dopants.

Band-like conduction within a single conjugated chain/network is very efficient and yields low resistance. For charge transport on a macroscopic level, which is required for the use of polymers in e.g. organic photovoltaics, though, charge carriers must be able to transfer from one molecule to another. This transition is realized by the process of tunneling of charge carriers through the barrier, that is caused by the interruption of the conjugated network and dependent on the π-π stacking structure described before. This process is also called hopping transport, since the charge carrier must hop from molecule to molecule in order to reach the destination (e.g. an electrode in an actual device). Each molecule can be simplified as one energetic and spatial state. The probability for charge carrier tunneling from molecule *i* to molecule *j* can be described by a hopping rate $r_{h,ij}$ estimated according to Equation (1):[37], [38]

$$r_{h,ij} = r_0 \, exp\left(-2\gamma R_{ij}\right) \begin{cases} exp\left(-\dfrac{\Delta E_{ji}}{k_B T}\right) & for: E_j > E_i \\ 1 & for: E_j \leq E_j \end{cases} \tag{1}$$

With a prefactor r_0, the inverse localization radius γ, the tunneling distance R and the respective energy levels $E_{i,j}$. The first exponential expression in Equation (1) describes the probability for tunneling between sites, based on the charge carrier mobility and the distance between the sites. In the case of (energetically) downward or lateral jumps, this term is not further modified, whereas for upward jumps an additional Boltzmann term has to be considered, taking into account the energy barrier and the available thermal energy. To translate these quantum mechanical probabilities into a useful description of the macroscopic charge transport in unordered polymer systems, the Monte-Carlo based Bässler model is used frequently.[39], [40] It assumes a Gaussian energy distribution (with width σ) of the available states and yield the phenomenological field dependent charge carrier mobility μ according to Equation (2):

$$\mu = \mu_\infty exp\left\{-\left(\frac{2\sigma}{3kT}\right)^2 + C\left[\left(\frac{\sigma}{kT}\right)^2 - \Sigma\right]F^{0.5}\right\} \quad (2)$$

Here μ_∞ and C are model dependent parameters, Σ a spatial disorder parameter and F a measure for the present electric field. Thus, the charge carrier mobility is dependent on both, $F^{0.5}$ and $1/T^2$. A graphical illustration of this principle can be found in Figure 9 in Chapter 2.1.2.

In the case of organic active layers for solar cell applications, as studied in the present thesis, the key property of an eligible material is its ability of conducting charge carriers and their semiconductor behavior as described above. The system PTB7:PCBM, which is studied here, consists of two different kinds of organic semiconductors:

- **PTB7** is a (homo-)polymer, consisting of elongated chains, built from identical monomer units. It shows p-type semiconductor properties.
- **PCBM** is a fullerene molecule, consisting of a cage of carbon atoms, arranged in pentagons and hexagons, respectively. It shows n-type semiconductor properties.

More detailed information about all used materials can be found in Chapter 3.1.

After the introduction of the basic properties of organic semiconductors, in the following section specific processes therein will be explained. The focus will be specifically on those processes, which are essential for the function of solar cells.

2.1.2 Working principle of organic solar cells

In the past years significant research effort has been put into the development and improvement of organic photovoltaic devices. This family of photovoltaic devices is based on the functionality of organic materials, mainly polymers with semiconductor properties. The use of such materials brings several advantages compared to the traditional inorganic solar cell technology where mainly silicon is used as the active material. Most prominently organic solar cells can be designed as thin film devices and

processed from solutions. This offers new areas of application due to e.g. flexibility and semitransparency of solar cell devices and an energy and resource efficient production process.

For any solar cell, the photoelectric effect in semiconductors is the basic underlying physical principle. It was discovered already in the 19th century and thereafter investigated by many well-known scientists. Not least Heinrich Hertz, Wilhelm Hallwachs, Albert Einstein, who received the Nobel prize for this work in 1922 and Robert A. Millikan dedicated their research to this very important physical phenomenon.[41], [42], [43], [44], [45] The photoelectric effect describes the mechanism that certain materials emit charged particles if they are exposed to electromagnetic radiation.

From a quantum mechanical point of view in a solid, electrons are bound in certain energy levels, so called bands. It is differentiated between allowed bands where electrons can be located and forbidden bands (band gaps) where electrons cannot reside. That describes the allowed states in the solid. Schematically spoken, these bands are filled from the lowest to the higher electronic states, as depicted in Figure 6.

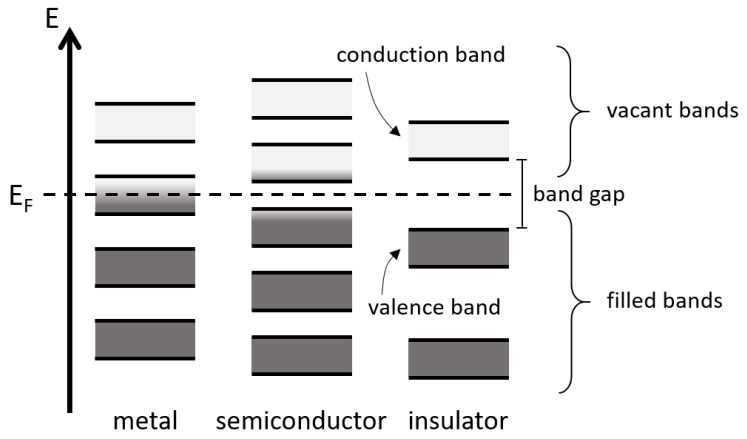

Figure 6: Schematic representation of the electronic band structure in relation to the Fermi level E_F. The greyscale indicates the occupation probability according to the Fermi-Dirac distribution.

In the case of electric conductors such as metals, there exists at least one band that is only partially filled with electrons. These electrons are mobile inside the respective band due to their ability to move to vacant positions. In this case, the Fermi level E_F is located within this electronic band. The Fermi level describes the energy

that is needed to add an electron to the system and is thus located at a position where the theoretical occupation probability is 50 %. This occupation probability is given by the Fermi-Dirac distribution.

Insulators are characterized by one completely filled band, which is called valence band, whereas the next higher band, the conduction band is completely empty. Thus, E_F is located in between two different bands. The band gap E_g around E_F is so large that thermal energies are insufficient to facilitate electron jumps between the bands, thus no mobility of electrons is given. In semiconductors the band gap between valence and conduction band is smaller and the Fermi level lies in the vicinity of a band edge. This allows for partially filled bands because the temperature dependent broadening of the Fermi-Dirac distribution around the Fermi level predicts the presence of holes in the valence band or the presence of electrons in the conduction band, respectively.

Equation (3) describes the electron occupation probability *f(E)* in dependence of temperature *T* and the Fermi energy *μ* according the Fermi-Dirac statistics:

$$f(E) = \frac{1}{e^{(E-\mu)/k_B T} + 1} \tag{3}$$

Doping of semiconductors can shift its band structure relative to the Fermi level. This leads to the introduction of electrons into the conduction band (n-type) or of holes into the valence band (p-type).

In solar cells, generally the absorption of photons by semiconducting materials is a key mechanism and the first step in the process of the generation of free charges. If the energy of an incoming photon is now sufficient to move electrons from the valence into the conduction band of a semiconductor, the generated excitations are relatively mobile and the conductivity of the material can be significantly increased. This effect is also referred to as photoconductivity. As explained in Chapter 2.1.1, in the case of organic semiconductors, the concept of fixed bands is not applicable. Because the material is not an infinitely (on molecular scale) periodic solid, instead of valence band and conduction band, the terms highest occupied molecular orbital (HOMO) and the lowest unoccupied molecular orbital (LUMO) of the molecular chain are introduced.

In solar cells the so-called photovoltaic effect is used, which is based on the photoelectric effect. In short, the photovoltaic effect describes the ability of a material (-system) to generate a voltage by the absorption of light. Thus, the goal of a solar cell is to separate the generated charges, produced by the absorption of the photons. This is realized by a so-called p-n junction, which is the combination of different semiconducting materials, one of them is rather p-type, the other rather n-type doped. Upon the light-induced generation of mobile electrons and holes in the two different materials, a voltage arises across the junction. Organic photovoltaic devices utilizing the conjunction of two (or more) materials are called heterojunction solar cells.[46] This is the technically and economically most relevant and promising species since the power conversion efficiency (PCE) of single material OSCs, which do not have a p-n junction, in the range 0.01 % cannot compete with heterojunction devices, which reached PCE values of around 1 % already in the earliest stages of their development.[47]

To create free charges at the p-n junction, several steps are needed. Figure 7 illustrates the processes that occur at the n-p junction upon absorption of a photon. The initial step is the absorption of a photon in the so-called electron donor material, which is generally the p-type doped semiconductor and provides the transport for positive charge carriers. By the absorption of a photon, an electron reaches an excited state to create an exciton, which is a bound pair of negative and positive charge carriers, as depicted in steps (1) and (2).

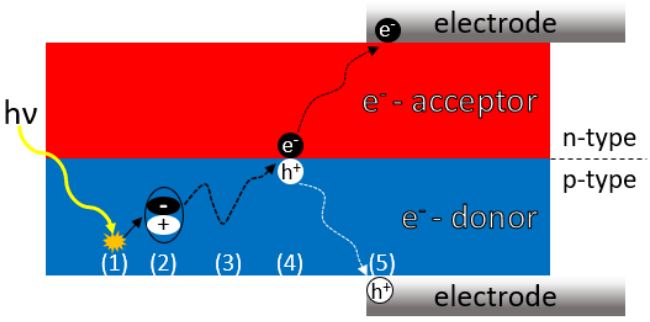

Figure 7: Steps from absorption of a photon to the extraction of free charges. (1): a photon is absorbed and an exciton (2) created; this can also happen in the e-acceptor material. (3): the exciton diffuses to the interface. (4): the negative and positive charge carriers are separated from each other at the interface via a charge transfer state and subsequently conducted to the respective electrodes where they can be extracted (5). Steps (1) to (5) happen consecutively and in in the respective sequence.

Subsequently, the exciton has to reach the interface with the acceptor material, which is n-type doped and conducts electrons, via diffusion within its lifetime (step (3)). In organic photovoltaics, Frenkel excitons are the dominant species due to the material´s relatively low dielectric constant and weak Van-der-Waals forces that facilitate the formation of this spatially restricted excited state.[48], [49] Frenkel excitons have binding energies of 0.1 eV – 1 eV, a lifetime of below 1 ps and diffusion lengths on the order of 20 nm.[50] This already shows the importance of thin films or small interconnected structures. If the exciton reaches the donor-acceptor interface within its lifetime, it can be split into free charges, as indicated in step (4). Finally, in step (5) the free negative charge carriers and holes are conducted in the respectively doped materials to the electrodes, through which they are fed into the external circuit. In the following the individual steps that are visualized in *Figure 7* are described in more detail.

Absorption of light and exciton generation

In order to be absorbed in the photoactive layer of a solar cell, the energy of a photon has to be equal or higher than the band gap energy E_g according to Equation (4):

$$E_{photon} = hv = \frac{hc}{\lambda} \geq E_g = E_{LUMO} - E_{HOMO} \quad (4)$$

The energy provided by the photon has to be sufficient to lift one electron from the highest occupied molecular orbital (HOMO) to the lowest unoccupied molecular orbital (LUMO) (similarly from valence to conduction band in the case of inorganic semiconductors). This indicates the advantageousness of low band gap polymers in OSCs as their band gap matches the solar spectrum better than polymers with a large band gap and thus allow for a larger number of photons to be absorbed. Upon the absorption of a photon, an electron is excited from its ground state in the HOMO into the LUMO level. The created hole, that is the vacancy in the HOMO, is subsequently bound to the electron that is now in the LUMO via coulombic attraction. Since the spin of the photon is zero, the created exciton must be a singlet due to spin conservation. In contrast to Wannier-Mott excitons, found in inorganic semiconductors, the Frenkel

excitons present in organic semiconductors are characterized by much a smaller distance between electron and hole and higher resulting Coulombic binding energies that cannot be overcome by thermal energies at ambient conditions of around 25 meV.[33], [51] Thus, the exciton is stable against dissociation and at room temperature and its separation requires an additional driving force. The process of exciton generation can occur in both, donor and acceptor material. In polymer:fullerene blend systems (like e.g. PTB7:PCBM) the specific absorbance in the relevant spectral range is typically much higher for the polymer compared to the fullerene due to the better matching of the polymer band gap. Thus, the polymer contributes significantly more to the exciton generation than the fullerene. The absorption of photons and the transition of electrons between coupled electronic and vibrational states can be described according to the Franck-Condon principle, which is explained in Chapter 2.2.2.[52], [53], [54], [55], [56]

Diffusion of the exciton

After its generation, the exciton has to diffuse through the respective material to the interface between donor and acceptor in order to be split into free charges.[57], [58] This is a statistical process and the probability to reach this interface is mainly determined by the exciton lifetime (τ_E) and the exciton diffusion length l_E, which is given in Equation (5):

$$l_E = \sqrt{d D_E \tau_E} \tag{5}$$

Here, d is the dimensionality of the diffusion medium taking values of 1, 2 or 3 (for 1-, 2- or 3-dimensional systems) and D_E the effective exciton diffusion coefficient, also dependent on the diffusion medium (and on the nature of the exciton). Improving this exciton diffusion length is one critical approach to improve the performance of organic photovoltaics.[59] The effective exciton diffusion length l_E is generally shorter than the total travelled distance because the diffusion path is not a straight line but can be described by a random walk approximation. This yields a Gaussian distribution for the effectively travelled distance within a given time. In addition, the distribution of exciton lifetimes τ_E is also Gaussian. As a consequence, l_E yields a Gaussian distribution,

actually the convolution of the two Gaussian distributions of specific effective travel velocity and exciton lifetime. This diffusion process must not be misunderstood as the movement of a particle (in this case an exciton) through a matrix, but rather as a radiation mediated propagation of the charge separation potential. In addition to this diffusion-like process, the exciton can reach the donor-acceptor interface also by fluorescent resonance energy transfer (FRET) that is one form of Förster resonance energy transfer (also often referred to as FRET).[60] This nonradiative transmission of energy is based on dipole-dipole coupling of a fluorescent donor-acceptor pair that show sufficient fluorescence properties. Further prerequisite for this kind of energy transfer are overlapping emission- and absorption spectra of donor and acceptor as well as similar vibrational excitation levels. The spatial range of FRET interaction reaches up to approximately 10 nm. If the use of this effect is desired, the choice of matching donor and acceptor materials is essential.[61], [62], [63]

Dissociation of the exciton

The binding energies of excitons in organic semiconductors, in the range of 0.1 eV to 1 eV, are far beyond thermal energies at operating conditions of solar cells. Thus, the driving force that is required for exciton splitting is provided by the electric field that is present at the electron-donor:electron-acceptor interface in the active layer.[64] The exciton reaches the material interface where it can be seen as a coulombically bound stationary charge transfer complex. The negative charge carrier is located in the acceptor material and the positive charge carrier in a neighboring molecule of the donor material (see *Figure 7*). The binding energy E_b is described by Equation (6):

$$E_b = \frac{e^2}{4\pi\varepsilon_0\varepsilon_p r} \tag{6}$$

with e being the charge of the respective charge carrier, ε_0 the permittivity of vacuum and ε_p the materials dielectric constant ($\varepsilon_p \sim 2$-4 for organic semiconductors). [65], [66] The difference in energy levels between HOMO and LUMO between donor and acceptor materials enables the separation of the charge carriers that are not further than ~1 nm apart in their bound state. If the electron reaches the LUMO of the acceptor material and the hole the HOMO of the donor material, respectively, in the

electronic state, their distance increases also in space. Thus, the probability for the distance between negative and positive charge to exceed the capture radius for the Coulombic force, r_C, increases. r_C describes the minimum distance between two oppositely charged particles where complete charge separation is possible and the charge carriers can be considered to be “free”, given by Equation (7).

$$r_C = \frac{e^2}{4\pi\varepsilon_0\varepsilon_p k_B T_{eq}} \tag{7}$$

where T_{eq} is the temperature where thermal energy is equal to the Coulombic binding energy between negative and positive charge. The splitting process of the exciton due to energetically favorable arrangement of HOMO and LUMO levels of donor and acceptor is illustrated in *Figure 8*.

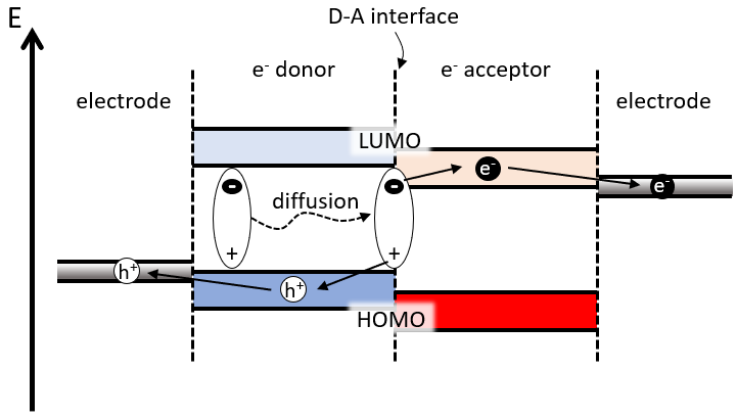

Figure 8: Schematic energy diagram of the donor-acceptor interface. An exciton diffuses to the interface and is split into a free negative and positive charges. The negative charge carrier is transferred into the LUMO of the acceptor and the positive charge carrier into the HOMO of the donor material. The generated free charges can be extracted by electrodes.

The process of exciton splitting at the D-A interface can occur irrespective if the exciton was created in the donor or the acceptor domain.

Extraction of free charges

In order to use the generated charges, they have to be transported from the donor-acceptor interface through the active layer material to the respective electrodes. This can be supported by an applied electric field to guide the charges, a so-called bias voltage. The process is rather simple and efficient in inorganic conductors due to the presence and arrangement of their valence and conduction bands where charge carrier transport is hindered only by e.g. phonons, crystalline defects or impurities.[67] These causes for increasing resistance get more probable with increasing temperature and thus conductivity generally decreases in inorganic systems at higher temperatures. Organic semiconductors are more disordered and charge transport follows different processes. Depending on the degree of crystallinity and thus disorder, the orbitals of neighboring molecules may overlap only weakly. This degree of overlap determines the probability of charge carrier tunneling from one state to another. The distribution of these available electronic states can be described by the so-called Gaussian disorder model and it is characteristic for any organic semiconductor material.[68], [69], [51] The effective transport energy E_t is given by Equation (8):

$$E_t = E_{0,\,max\,DOS} - \frac{\sigma^2}{k_B T} \tag{8}$$

The disorder parameter σ describes the width of the Gaussian energy distribution of the density of states (DOS). The level of E_t is dependent on the temperature as higher thermal energies increase the probability of upward jumps, consequently increasing the energy level of the effective charge transport. Charge carriers that are generated above E_t relax over several steps towards E_t where they are conducted along this quasi-equilibrium between gradient of density of states and thermal activation. This mechanism has been theoretically introduced in Chapter 2.1.1 and is sketched in *Figure 9*.

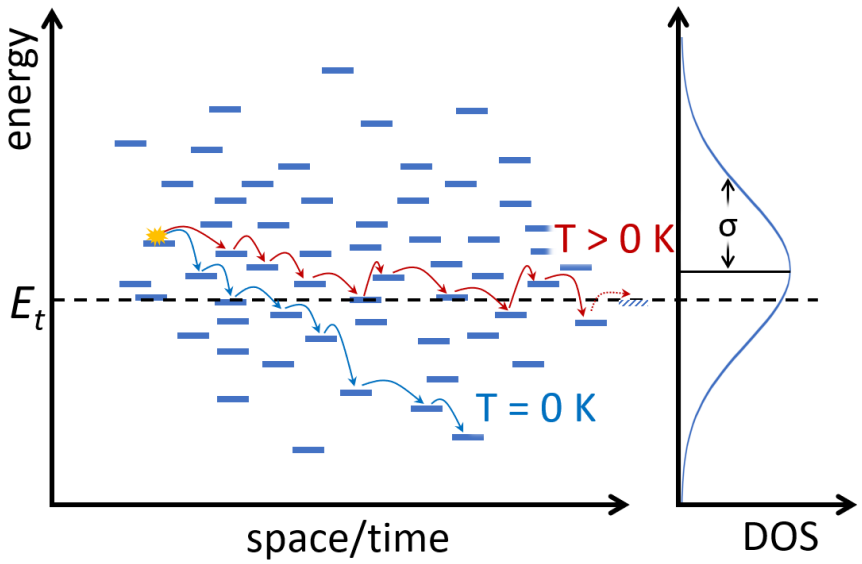

Figure 9: Schematic energy diagram describing charge carrier transport by hopping. As described by the graph on the right, the localized energy states have a Gaussian distribution with HWHM σ. At T = 0 K, charge carriers can only perform downward jumps in terms of energy and relax until they get trapped when no lower energy state is within hopping range, as indicated by blue arrows. For T > 0 K, thermal energy is available to perform upward jumps, as indicated by red arrows. After an initial relaxation from a possibly higher level of creation of the free charge carrier, the transport takes place around the transport energy E_t. Graphics reproduced from [69].

In the case of T = 0 K no thermally activated upwards hopping is possible and the charges relax until they reach the lowest energy state. From there, no further hopping is possible and charge carriers are trapped. The hopping process in organic semiconductors such as polymers is favored by higher temperatures because the thermal energy facilitates also upward jumps, which increases the number of available travel paths for the charge carriers. As the structure of a polymer can theoretically range from purely amorphous to fully crystalline, the shape of the Gaussian disorder of available states can vary strongly and thus the material´s conduction properties. Generally, it can be stated that the narrower distribution and higher density of states in more ordered or even crystalline domains favor the hopping transport, which has to be considered in the production of active layers. After transport, the charge carriers are fed into the external circuit via anode (positive charge carriers) and cathode (negative charge carriers).

2.1.3 Materials

Organic solar cells consist of various materials in order to fulfill different functions and requirements. As established before, scope of this thesis is the investigation of active layer materials by spectroscopic methods with regard to degradation processes, however it is important to present all components of OSCs. Therefore, a complete overview of the used materials is essential as they must match in many characteristics and obviously exhibit functional internal interfaces.

In the following, materials are differentiated according to their function in the organic solar cell: active layer, blocking layers and electrodes. This section is a general overview of the development and state of science for each category. The specific materials that were used in the research for this thesis can be found in Chapter 3.1. For better readability, all materials that are mentioned in this section are given in their abbreviated form, e.g. P3HT for poly-(3-hexylthiophen-2,5-diyl). A full list of the abbreviations is given in the beginning of this thesis.

Active layer

In the active layer, photons are absorbed leading to the creation of excitons, which are transported and split. Finally, the free charges are drained to the electrodes, as described in the previous chapter.

Active layers of pure single organic semiconductor materials were used in the beginning of the development of organic photovoltaics.[47] Due to their comparably bad photovoltaic performances, especially in terms of exciton splitting and conductivity, multi-component systems have become prevalent and large efforts have been made to discover and develop novel materials to improve solar cell performances.[70] The first organic active layer in bilayer geometry was reported in 1986 using a p-n-junction, with the p-type material acting as electron donor and the n-type material as electron acceptor. In the early 2000s polymers like P3HT ($E_g \approx 2$ eV) and MEH-PPV were used as electron donor materials and blended with fullerene derivates such as $PC_{61}BM$ in first bulk heterojunction devices. P3HT:$PC_{61}BM$ became a famous model system for organic photovoltaics made from homopolymers and fullerene acceptors with efficiencies reaching up to 4 %.[71], [72], [73], [74]

The next step was made with the introduction of low band gap donor-acceptor polymers or even acceptor-donor-acceptor molecules, which yield properties of both, electron donor and electron acceptor at the same time. Different engineerable parts of these molecules show either electron donating or accepting properties. These kinds of polymers/molecules offer an improved intramolecular charge transfer and a higher light-harvesting potential due to the possibility achieve smaller band gaps by molecular engineering.

The variety of applied low band gap donor polymers is very large and contains further candidates like PTB7-Th, PThTPTI, PCE12, DERHD7T, DPPEZnP-TEH and corresponding acceptors $IC_{60}BA$, $IC_{70}BA$ and e-PPMF. The important model system from this era is PTB7 blended with the larger fullerene derivate $PC_{71}BM$.[75], [76] Due to improved internal charge transport properties and optimized light harvesting spectra, this generation of organic solar cells reached PCE values of up to 9 – 12 %.[77], [78], [79]

In the following step of the development, the fullerene molecules were exchanged by small molecule (non-fullerene) acceptors like ITIC, IDIC, IT-4F or Y6.[80], [81], [82], [83] This addresses the problem that the fullerene domains in the active layer are hardly contributing to the light absorption and the provision of excitons. These non-fullerene acceptors can be molecularly engineered and helped to improve the PCEs for organic photovoltaic up to over 13 %.[84]

By the introduction of a third component or the combination of several material systems in tandem-cells, PCEs of over 17 % were reached.[85]

The intrinsic absorption of novel non-fullerene acceptors offers new possibilities for donor materials. In order to achieve complementary absorption spectra of acceptor and donor, wide band gap donor materials became attractive again. With the use of wide band gap polymer donors like PM6, PTQ10, D16 or D18 in combination with nonfullerene acceptors, PCEs of over 18 % were reached.[85], [86], [87], [88] The current cutting edge single junction OSCs use the system PM1:L8-BO:BTP-2F2Cl and are reported with a PCE of 19.17 %.[89], [90]

Blocking layers

Blocking layers are located between the active layer and the electrodes. They are used to avoid recombination of negative and positive charges in the conducting electrodes.[91] While an electron blocking layer (EBL) is introduced between active layer and anode and does not allow electrons to pass, a hole blocking layer (HBL) between the active layer and the cathode is impermeable to holes. By instance, also the terms hole transporting layer (HTL) and electron transporting layer (ETL) are used in some literature. Besides the already discussed blocking function, such interlayers can significantly improve the performance of organic solar cells also by increasing the photocurrent through the reduction of the potential steps between the active layer material and the electrodes. In principle it would be sufficient to add a continuous layer of the donor material at the anode and an equivalent layer of the acceptor material at the cathode, but research has given rise to further improved systems. This would address the problem that due to the generally statistical material distribution in a bulk heterojunction as explained in Chapter 2.1.4 both, donor and acceptor material are in contact with the electrode, leading to tremendous recombination of charge carriers in the electrodes. An ideal hole/electron transport layers material is characterized by a high hole/electron mobility, chemical inertness, the ability to form good contacts with the neighboring layers and stability in ambient conditions, especially temperature, humidity and light. Concerning the use in commercial products additional factors like costs and processability play an important role. Many materials, organic as well as inorganic, have been used as blocking layers, Table 1 gives an overview.[92], [93], [94], [95]

electron blocking layer	**hole blocking layer**
p-type semiconductors	*n-type semiconductors*
PEDOT:PSS [96], [97], [98], [99]	ZnO [98]
Graphene oxide [100]	TiO_x [100]
V_2O_5 [96]	PEO[101]
MoO_3 [96]	LiF [102]
MoS_2 [103]	Ca [99]

Table 1: Examples of common materials for electron blocking layers (left column) and hole blocking layers (right column) as used in organic solar cells. Literature references are only examples for successful application of the respective material and not a full bibliography.

In early stages of organic photovoltaic research mainly p-type inorganic semiconductors like transition metal sulfides and oxides were used as anode coating due to their very good hole mobility, optical transparency and stability. In following years, organic EBLs were discovered and especially PDOT:PSS emerged as promising candidate, but many other conjugated polymer have been used.[94] A similar development of the transition from the use of inorganic materials towards the development of innovative organic compounds can be seen for the development of cathode coatings.

Electrodes

Electrodes are the contact point between the solar cell device and the external circuit. They should have high electric conductivity to not compromise the solar cell efficiency by limiting the generated photocurrent. Additionally, electrodes should exhibit a good stability as they are often the outmost layer and therefore have a large interface area with ambient conditions. Regarding the cathode material´s work function, it is important to match the acceptor´s LUMO, while the anode´s work function should match the donor HOMO level.[64], [95], [104], [105] In addition at least one of the electrodes has to be transparent to not shield the solar cell from the incident light. There is a large variety of used materials used as contact materials. Thin transparent layers of e.g. indium tin oxide (ITO), zinc oxide (ZNO) or nanostructured carbon, like carbon nanotubes,[106], [107], [108] or metals, such as silver nanoparticles,[109] are often used at the cathode side. Depending on the architecture of the cell, anode materials often consist of opaque metals like gold, silver, aluminum or copper.[110], [111], [112]

2.1.4 Bulk heterojunction

As already described in Chapter 2.1.3, the active layer in organic solar cells is generally composed of different materials. The splitting of exciton requires the potential of a donor-acceptor interface and as the effective exciton diffusion length is limited to approximately 20 nm in organic materials, a high interface area / volume ratio is desirable. Regarding the transport of the free charges through the active layer towards the electrodes, a well interconnected network of the respective domains is needed.

Thus, the arrangement of these materials is a critical point to fully use the materials´ potential.

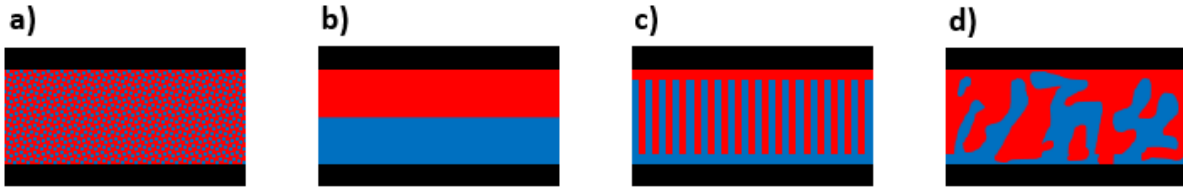

Figure 10: Different structures of OSC active layers composed of two materials, electron donor (blue) and electron acceptor (red), including the electrodes (black). The four presented structures are: a) solid solution, b) layered system, c) ideal bulk heterojunction and d) realistic bulk heterojunction from solution processing.

Figure 10 shows possible structures that can be formed by a blend of different materials. A homogeneous blend, or solid solution (Figure 10a) of donor and acceptor molecules are not desired since both, sharp material interfaces and pure domains, are needed for exciton splitting and charge carrier transport.

A simple layered structure as depicted in Figure 10b) fulfills all requirements to be used in a working solar cell. In fact, early organic photovoltaic research used such bilayer structures reaching power conversion efficiencies of ~1 %.[46] Nevertheless, the performance of layered devices is strongly limited by the low exciton splitting rate due to the relatively small interfacial area between donor and acceptor material and the large average distances from the bulk to the donor-acceptor (D-A) interface. Since the lifetime and diffusion length of excitons are limited, this simple layered structure does not allow most excitons to efficiently reach the interface.

This limitation is addressed by the introduction of so-called bulk heterojunction (BHJ) structures for active layers in organic solar cells. Due to their higher specific D-A interface area they offer more efficient exciton splitting leading to a higher photovoltaic performance. BJH structures are achieved by solation of donor and acceptor precursor materials in one solution simultaneously and coated together. First successful BHJ solar cells have been reported already in 1995.[71], [113], [114] The ideal configuration of a BHJ is shown in Figure 10c) where the lamella distance is in the range of the effective exciton diffusion length of around 10 nm and percolating pathways from every D-A interface towards both electrodes are available.[115] Such close to ideal structures as shown in Figure 10c can be realized with expensive and

time-consuming lithography techniques.[116], [117] In reality, solution processed bulk heterojunctions are less regular and can be imagined as depicted in Figure 10d).

Efforts have been made to improve the blend microstructure in bulk heterojunctions in order to achieve more efficient organic solar cells. Due to the complex requirements of the active layers, numerous factors such as degree of phase separation, domain sizes, domain interconnectivity, degree of crystallization and orientation of crystalline structures, especially the important π-π stacking of the conjugated system have to be considered. One way to tailor the blend microstructure is the control over thermodynamic processes during sample fabrication. This involves material miscibility according to Flory Higgins theory [118] and crystallization properties. Both can be influenced by adjusting the chemical structure of the materials and with post-production treatments of active layers by e.g. thermal or vapor treatments. Another approach is to control the dynamics of the solvent evaporation and film formation. One critical point in this approach is the choice of solvent(s) and solvent additives. By varying the solvents boiling point or/and the selective solubility of solvent components/additives, one can influence the state and sequence at which the structures inside the thin film solidify and thus realize thermodynamically metastable states to a certain degree.[90]

2.1.5 OSC devices

In order to exhaust their full ecologic and economic potential, organic photovoltaics must be produced in high quantity at a price as low as possible. Since the previous chapters are restricted to theoretical aspects, this section introduces the actual layout of OPV modules followed by a discussion of challenges that still retard the large-scale break-through of this emerging technology.

Architecture & layout

While Chapter 2.1.2 describes all processes that are necessary to convert electromagnetic radiation into usable electric energy in more detail, *Figure 11* presents the full energetic diagram of the involved materials and an exemplary stack of the respective layers.

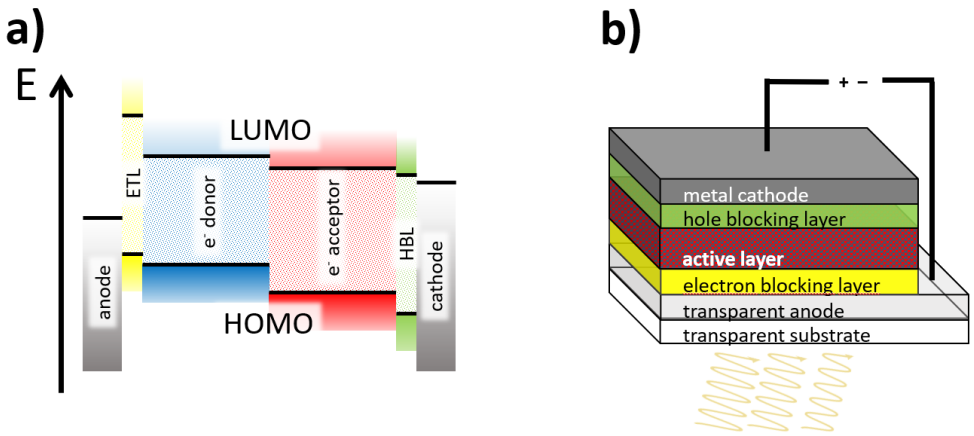

Figure 11: a) schematic energy diagram of an exemplary organic solar cell with anode, electron blocking layer (EBL), electron donor, electron acceptor, hole blocking layer (HBL) and cathode (from left to right). The shaded area between the black lines (upper line: LUMO, lower line: HOMO) indicate the band gaps of semiconducting materials. b) Exemplary material stack of an organic solar cell. Illumination comes from below (yellow arrows) and the external circuit is indicated by thick black lines.

According to the stack sequence of the layers with special focus on the electrodes, organic solar cell geometries can be divided into conventional and inverted geometries. In the conventional architecture, as presented in *Figure 11b)*, a high work function transparent electrode, often a thin e.g. indium tin oxide (ITO) coated on a glass substrate, is utilized as anode, whereas the low work function metal electrode (e.g. aluminum) acts as cathode. In order to improve primarily different stability issues that come with the use of the conventional geometry the so-called inverted geometry was introduced.[119] In this alternative approach, the role of the electrodes is switched by tuning the work functions by the use of suitable electrode coating materials (commonly metal- and transition metal oxides). In this way the ITO layer acts as cathode in the present example and the opposite metal layer as the anode. Besides a more beneficial material layout of the inverted geometry in terms of stability, it has also been shown that the power conversion efficiency of OSC devices can be improved by the use of this configuration. [78], [120], [121] For the construction of larger OPV modules, several cells have to be connected since the size of single cells that can be produced at good quality with reasonable cost is limited and the voltage that can be generated by single cells is not sufficient for usual applications. Therefore, the cathode of one cell has to be connected in series to the anode of the next one. The series can be extended over multiple cells, as shown in Figure 12.

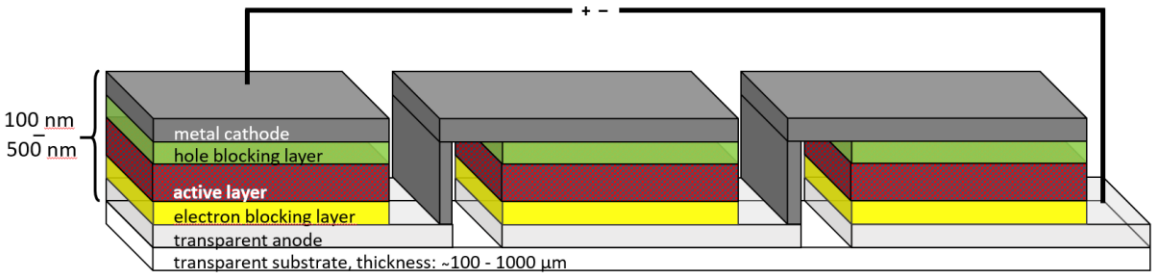

Figure 12: Exemplary connection of single organic solar cells to build up a functioning module. Typical thicknesses of the substrate and the OSC stack are indicated.

In this way the generated photovoltage adds up and as the desired voltage is reached, several cell sequences with the respective number of cells can be connected in parallel to increase the current.[122], [123]

Please note that *Figure 11*, like most typical schematic sketches of organic solar cells, features distorted length scales since the substrate is thicker by two to three orders of magnitude compared to the functional OSC stack. If e.g. ITO coated glass is used, the substrate thickness ranges around 100 µm to 1 mm. In contrast typical layer thicknesses within the OSC functional stack are 50 nm to 200 nm and thus very small compared to the substrate thickness. For the lateral dimensions, common sizes for individual cells are in the range of some cm^2, separated by some tens to hundreds µm.[20]

Usual challenges for the use of OPVs are the loss of energy between the available solar irradiation and the final extracted electrical power, which is the power conversion efficiency, and degradation of the used materials, which leads to impaired performance. Mechanisms and approaches to meet them are discussed in the following sections.

Loss mechanisms

Organic solar cells are designed to convert the energy of electromagnetic radiation into free charges, which can be used to power devices or charge e.g. batteries. Not all of the generated charges can reach the electrodes to be used, but are lost on the way, though. These losses can occur during every step that is described in Chapter 2.1.2.

In order to achieve the highest possible photocurrent and thus good solar cell efficiencies, loss mechanisms have to be understood and inhibited as much as possible.[69], [91], [124]

In the process of light absorption itself, the largest portion of theoretically available energy is lost already. Photons with energies lower than the band gap(s) of the material(s) used in the active layer cannot cause an electronic transition and are thus not absorbed. Photons, whose energies exceed the respective band gap energy do also contribute only partially to the charge generation because the excess energy is lost in non-radiative thermalization processes. More precisely, the difference between band gap and photon energy, is lost and not usable. Thus, the selection of materials with band gaps matching the incident solar spectrum (*Figure 13*) is a key factor in the design process of organic solar cells. The theoretical upper limit of a single junction solar cell, dependent on its band gap, is described by the Shockley-Queisser limit, which considers not only the spectral losses, but also recombination losses.[125], [126]

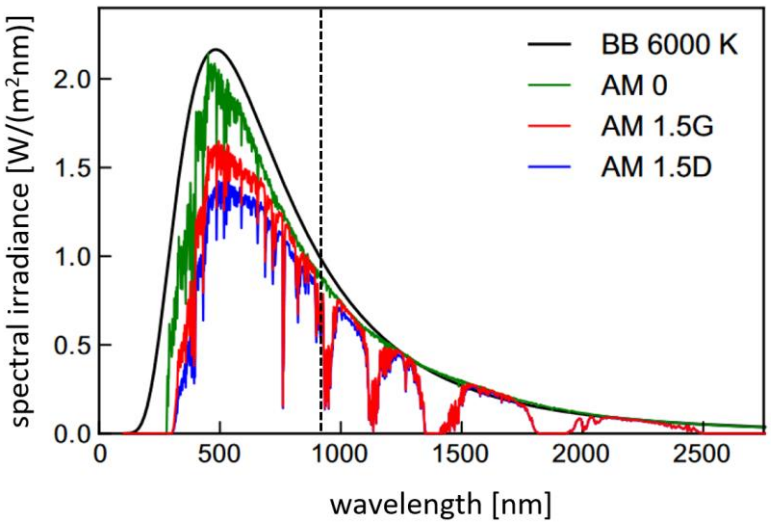

Figure 13: Solar irradiation spectra (according to ASTM G173-03) outside the earth's atmosphere (green), direct normal irradiation on the earth surface (blue) and direct plus scattered irradiation (red). In black the radiation of an ideal black body with surface temperature of 6000 K is indicated. The dashed line indicates the theoretically ideal band gap energy of 1.34 eV (925 nm). Adapted from [126].

In the concept of Shockley and Queisser, an incident spectrum is assumed and the theoretical maximum PCE for a homojunction (i.e. one material provides photon absorption) solar cell with specific band gap is calculated, considering only thermodynamic factors and the principles of the so-called detailed balance, which

includes processes like radiative recombination as a function of charge carrier concentration. As an example, for the theoretically ideal band gap of around 1.34 eV indicated in Figure 13, a maximum PCE of 33.16 % is predicted. This band gap energy is ideal as it offers the best compromise between absorbing as many photons from the available solar spectrum (see Figure 13) and not cutting off too much energy from the higher energy photons.

After the absorption of photons and the creation of excitons, recombinational loss is another efficiency limiting factor in organic solar cells. It occurs inside the functional materials and can be divided into geminate and nongeminate recombination mechanisms.[124], [127], [128]

Geminate recombination describes a process in which the positive and the negative charge that originate from the same photon-absorption process, are annihilated by each other. Thus, predominantly excitons and charge transfer complexes are subject to geminate recombination. The probability for geminate recombination thus increases with increasing distance between the point of exciton generation and the location where dissociation is possible.

Solitary charge carriers, not stemming from the same exciton, are subject to so-called nongeminate recombination. Consequently, this type of charge carrier loss can happen from the moment of charge carrier separation at the donor-acceptor interface until the extraction at the electrodes (and theoretically also during further conduction). Not only photogenerated charges can contribute to nongeminate recombination but also externally injected charges, e.g. in the form of a cell bias. There are three main non-geminate recombination mechanisms that play a role in organic semiconductors. Nongeminate recombination between bound charge carriers is unlikely under regular conditions and thus not considered here.

Band-to-band recombination of free negative and positive charge carriers is called bimolecular recombination.[129] The recombination rate is limited by charge carrier diffusion and the probability for such a meeting event and thus proportional to the modified Langevin recombination strength k_L given by Equation (9):[130], [131]

$$k_L = \frac{16\pi}{9} \frac{J_p J_n}{(J_D)^2 - \left(J_p + J_n\right)^2} \frac{e}{\varepsilon} \left(\mu_p + \mu_n\right) \tag{9}$$

with $J_{p,n,D}$ being *p* and negative and double carrier current, $\mu_{p,n}$ the respective charge carrier mobilities, *e* the elementary charge and ε the material´s permittivity.

In trap-assisted recombination, one charge carrier is trapped and localized within an energetic minimum. If the opposite charge carrier diffuses into close enough vicinity to the filled localized trap, the recombination process can take place. A frequently applied model in organic photovoltaics is the Shockley Read-Hall recombination, which predicts the rate of trap-mediated nongeminate recombination r_{RSH} according to Equation (10).[128], [132], [133]

$$r_{RSH} = r_{ec} - r_{ee} - r_{pc} + r_{pe} \tag{10}$$

where $r_{ec,\ pc}$ are trapping rates for free charge carriers and $r_{ee,\ pe}$ are the rates at which positive or negative charge carriers escape their traps and transition back to the respective free population. All components of Equation (10) and thus the recombination rate itself strongly depend on the average depth of the traps.

The third pathway for nongeminate recombination is Auger recombination, which involves three entities.[134] While an electron from the LUMO is recombined with a hole in the HOMO, the released energy is transferred to another electron that is excited to a higher state by this process. Since this process requires a strong driving force in the form of high charge carrier density, it is not as prominent in organic systems as the two mechanisms discussed before.

In order to avoid such losses of charge carriers, the full-scale structure, including crystallinity, microstructure, morphology and quality of the applied layers, is critical. Especially the presence of defects and impurities in the structure as well as isolated domains without connection to the respective electrode have to be avoided as far as possible, since they can hinder the diffusion of excitons, charge carriers, build spatial traps and thus increase the probability for charge recombination.

Degradation mechanisms

While the improvement of power conversion efficiencies develops towards marketable values of around 20 %, another critical factor in the development of organic solar cells is the long-term stability. Practically all layers of the typical OSC stack are subject to different mechanisms of degradation.[20], [69], [119], [128] Their relatively small thickness of several tens to hundreds of nm induces additional susceptibility to degradation. Electrodes can suffer from oxidation as well as chemical reactions with e.g. polymers from neighboring layers.[135] Electron and hole blocking layers undergo slow degradation pathways, depending on the respective materials, e.g. PDOT:PSS appears to be sensitive to high temperature, moisture and oxygen.[136], [137] One topic of this thesis, tough, is connected to the degradation of the active layer at the example of PTB7:PCBM BHJs, that can be divided into chemical and physical degradation.

Chemical degradation describes the process of reactions of the active layer materials with the result of an altered chemical structure that can lead to a decrease of solar cell performance.

For chemical degradation the major concern is the photooxidation of the active materials under illumination that can be induced by the infiltration of reactive species such as H_2O or O_2 into the layer.[138], [139] The introduction of radicals can detrimentally influence parameters such as interface potential, electrical conductivity and optical absorption capability.[139], [140] These processes are mediated and accelerated by light irradiation, thus photooxidation. Further possible pathways for chemical degradation are e.g. temporary p-doping with O_2, a shift of the material´s HOMO and LUMO levels and thus a change of the band gap, formation of secondary reaction products that hinder the transport of charge carriers [141] or the fragmentation of donor and acceptor materials.[21] A more direct way for light induced degradation is the breakup of organic bonds by ultraviolet light with photon energies exceeding 3.5 eV. Beyond these extrinsic causes for chemical degradation, which can be partly reduced by e.g. cell encapsulation, there are also intrinsic reactions like oligomerization of fullerene molecules.[142]

Also, physical degradation mainly concerning the microstructure can be caused by both, intrinsic material properties and external causes. Physical degradation of an OSC device is generally accompanied by the modification of the blend microstructure of the active layer. A coarsening of donor and acceptor domains leads to an increased

recombination rate due to higher statistical mean interface distances, whereas a stronger intermixing of the components can negatively influence the generated photocurrent by the formation of unconnected domains, so-called trap islands, and a general reduction of conductivity by a reduction of the effective degree of percolation. Due to the fact that metastable structures yield the best performance and are thus desired, the degradation mechanisms in organic solar cells are thermodynamically controlled and promoted by increasing temperature. As for the initial formation of the blend microstructure, the structural impact of physical degradation in organic systems can be described by the general model of Ostwald ripening, which assumes a reaction nucleus and an incorporation or attachment of neighboring domains. The coarsening alteration then propagates outwards from the starting nucleus as long as it is kinetically favored.[143], [144], [145] The respective degradation rate that describes the propagation rate of the reaction front shows Arrhenius behavior and is thus higher at increased temperatures.

Additionally to microstructural alteration, also macroscopic physical degradation can reduce OSC lifetime or performance. For example mechanical and thermal stress can induce delamination or breaking of parts of the OSC stack resulting in a reduction of conductivity right up to complete device failure.[146]

In order to improve the resistance of OSC devices to physical and chemical degradation, material engineering is the central approach. For example, non-fullerene acceptor systems,[147], [148] cross linkable [149] polymers and more stable block-copolymer structures [150] have shown their potential for this purpose.

Since most of the discussed degradation mechanisms depend strongly on chemical and physical properties of the used materials, their understanding is of particular interest for the development of commercially usable organic photovoltaics. In Chapters 6 & 7 of this thesis, the degradation mechanisms in the system PTB7:PCBM are studied in particular. Therefore, spectroscopic methods like quasielastic neutron scattering, optical, FTIR and Raman spectroscopy are used, supplemented by structural investigation methods. With these methods, internal molecular dynamics as well as physical and chemical structures are investigated in PTB7:PCBM films. Further variations, induced by the use of solvent additives and different drying protocols, are studied.

2.2 Fundamentals of characterization techniques

In the present thesis polymer:fullerene blend films for the application as active layer in organic photovoltaics are studied. Therefore, different characterization techniques were used. For the determination of basic film properties like thickness and roughness, profilometry was used. In the context of the application as active layer in solar cells, optical absorption properties are of particular interest. They were investigated with UV-visible (UV-vis) absorption spectroscopy. Microstructural aspects were studied with X-ray diffraction (XRD). To follow the degradation and possible changes in the chemical structure of the samples, Raman and Fourier-transform-infrared (FTIR) spectroscopy were used. The major focus of this work is the investigation of dynamics on a molecular level. Time-of-flight (TOF) quasielastic neutron spectroscopy (QENS), using the TOFTOF spectrometer (FRM II, Garching, Germany) was used to study the diffusive motions of hydrogen atoms in the polymer side chains. For the analysis that is presented in Chapter 7, some techniques were used under illumination of the sample *in situ*. The practical implementation of the illumination for *in situ* experiments is described in Chapter 4.

The following part briefly introduces the background and technical aspects of the applied characterization methods.

2.2.1 Profilometry

For the determination of film thicknesses and profiles of the samples surface, profilometry was used.[151], [152] With thicknesses in the range of micrometers to tens of micrometers, the samples studied in this thesis are relatively thick (compared to the classical meaning of “thin films” with thicknesses of up to ~500 nm), thus profilometry is a fast and simple method to sufficiently measure the film dimensions. More sophisticated, but also more expensive methods like atomic force microscopy or X-ray/neutron reflectometry were not applied. A Dektak XT stylus profilometer (Bruker, USA) was used. Its working principle is described in the following. The sample is placed on an X-Y stage, which is moved by software controllable motors and an additional actuator that ensures smooth and precise lateral motion during measurements. To determine the sample profile a reference is needed, usually in the form of the substrate

surface. Therefore, the scan length is chosen in a way that the bare substrate on both sides of the film area is covered. If this is not practical, there is also the possibility to scratch away parts of the sample and uncover the underlying substrate at any position of interest. The normal force which presses the tip (radius: 2 µm) onto the surface is kept constant at around 10^{-5} N and controlled by an actuator, so the measured vertical dilatation is directly proportional to the sample height at the respective position. By moving the sample stage laterally underneath the sample at a certain speed, a one-dimensional profile is recorded. This principle is depicted in Figure 14.

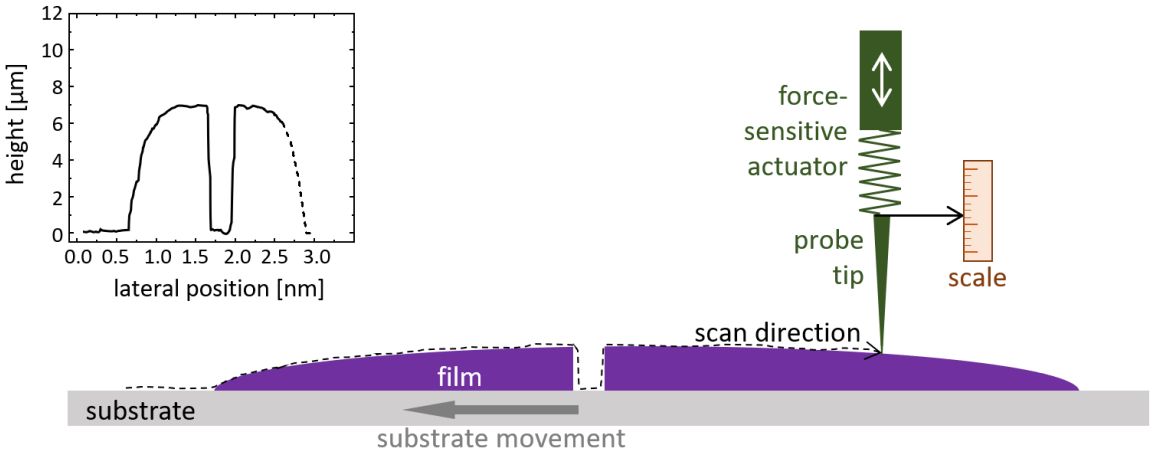

Figure 14: Schematic drawing of the profilometry measurement. The substrate (grey) with the sample film (violet) is moved laterally while the tip (green) is kept in contact with the surface with constant normal force, controlled by a force-sensitive actuator (green). The inset shows the resulting profile.

System control, data acquisition and primary treatment is performed with the software Vision 64 (Bruker), which also offers possibilities for calculation of e.g. average step heights, surface roughness, or the acquisition of topographic maps by joining several parallel profiles together.

The technique can be destructive to the sample due to the possible need to scratch away sample material in order to measure the substrate surface reference. The applied vertical force might also be sufficient to push the sharp tip of the probe into soft sample materials such as polymers or leave scratches on more brittle materials. In addition, the tip could be contaminated from earlier measurements or pick up debris particles from the sample or the substrate that can fall off and be deposited at other locations on the sample. Thus, profilometry measurements were only performed on especially

produced reference samples or on actual samples after all other techniques have been completed.

2.2.2 UV-visible absorption spectroscopy

UV-vis absorption spectroscopy is used to determine the light absorption of a sample in the wavelength range between 350 nm and 1000 nm. The measurements were performed with a Lambda 35 UV-vis spectrometer (Perkin Elmer, USA). For the studied wavelength range, the installed halogen lamp (wavelength range 330 – 1100 nm) was sufficient and a switch to the deuterium lamp (wavelength range 190 – 330 nm), also available in the instrument, was not necessary. From the optical properties, one can draw conclusions about the electronic structure of the sample. The technique is well suited for both, liquid samples, usually prepared as solutions in cuvettes and solid samples, prepared as thin films on transparent substrates such as (coated) glass, crystals or plastics. A polychromatic light source with sufficient intensity in the desired wavelength range is used. The light is focused on an adjustable monochromator that unfolds the spectrum and only allows a narrow band to pass through a slit towards the sample.

The linewidth of the monochromator determines the spectral resolution of the UV-vis measurement. A higher resolution is typically accompanied with lower usable intensity and increased measurement time. Acquiring a UV-vis absorption spectrum requires a stepwise readjustment of the monochromator in order to scan the chosen wavelength range.

In a regular transmission geometry, the beam passes through the sample and the light intensity is measured after the sample. This principle is illustrated in Figure 15.

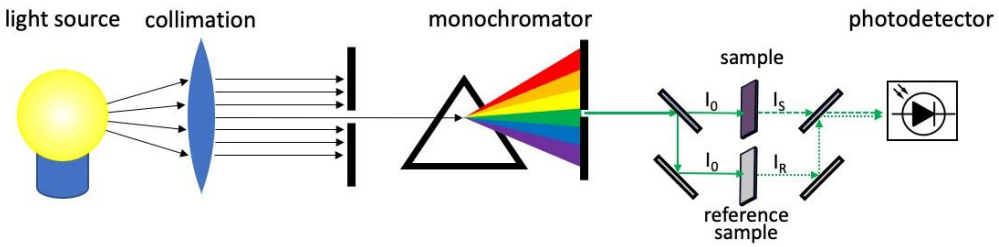

Figure 15: Schematic layout of a double beam UV-vis spectrometer. The unattenuated beam intensity is termed I_0, the sample attenuated beam I_S and the beam, attenuated by the reference sample I_R

The depicted spectrometer uses a second beam path to determine the substrate/cuvette and sample absorption simultaneously. The absorbance is calculated according to Equation (11) on basis of the Lambert-Beer law describing the attenuation of radiation traveling through a medium of thickness *l* with wavelength dependent extinction coefficient ε_λ and concentration *c*.[153], [154]

$$A_\lambda = \left[-log_{10}\left(\frac{I_S}{I_0}\right)\right] - \left[-log_{10}\left(\frac{I_R}{I_0}\right)\right] = log_{10}\left(\frac{I_R}{I_S}\right) = \varepsilon_\lambda cl \qquad (11)$$

According to Figure 15, I_0 is the unattenuated light intensity, which is measured without sample or reference inside the beam, while I_R and I_S are the reference and actual sample absorption, respectively. The inverse quantity “transmittance” *T* can be calculated from the absorbance with Equation (12).

$$A_\lambda = \log_{10}\frac{1}{T_\lambda} \quad \rightarrow \quad T_\lambda = 10^{-A_\lambda} \qquad (12)$$

Deviations from the Lambert-Beer Law, which describes a linear relation between concentration and absorbance, can be both, negative as well as positive, but such deviations are not expected for the thin film samples of the present study. Thus, for this thesis, a transmission geometry is used for the thin film samples of polymer blends, coated on flat and cleaned glass substrates.

For semiconductors, the UV-vis absorption spectrum can be used to determine the band gap via the Tauc plot, where the specific absorbance is plotted against the photon energy. A straight line is fitted to the inflection point of the initial absorbance rise and the intersect of this line with the x-axis gives the value for the optical band gap energy (E_g), as described by the Tauc equation (Equation (13)):[155]

$$(\alpha h\nu)^{\frac{1}{n}} = A\left(h\nu - E_g\right) \qquad (13)$$

with *A* being a proportional constant and α the absorption coefficient:

$$\alpha = -\frac{\ln T}{l} \tag{14}$$

The relation between wavelength *λ*, frequency *v* and energy *E* for electromagnetic radiation is given by the Planck-Einstein relation, which is described in Equation (22).

The exponent *n* in Equation (13) describes the nature of the observed band gap. A value of 0.5 represents an allowed transition in a direct band gap, whereas a value of 2 is used for indirect band gaps. The application of this method in the Tauc plot is illustrated in Figure 16, where the inflection point of the slope of the absorption edge of the 0-0 transition (see Franck-Condon Principle, explained in the following), is a fit with a straight line for a PTB7:PCBM blend film.

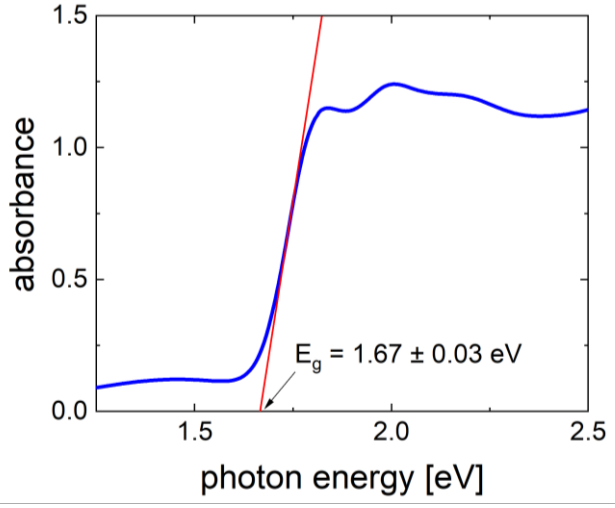

Figure 16: Exemplary UV-vis absorbance spectrum of a PTB7:PCBM blend thin film. The red line is a fit according to a Tauc plot and the optical band gap is determined to be 1.67 ± 0.03 eV.

Originally, this method was developed for the interpretation of the optical absorption spectrum of amorphous germanium, but is well established for the determination of optical band gaps in disordered and amorphous semiconductors.

For the interpretation of UV-vis absorbance spectra, the Franck-Condon Principle is essential.[52], [156], [157] It describes the transition probability of molecules from

certain electronic and vibrational states to others, which is principally determined by the overlap of the wave functions that represent the electrons´ probability of presence. The energy landscape of the sample consists of different electronic states, each of which containing multiple vibrational substates, as sketched in Figure 17. The position of the respective atom can be changed by absorption of a photon, which is indicated as lateral shift of the electronic states in Figure 17.

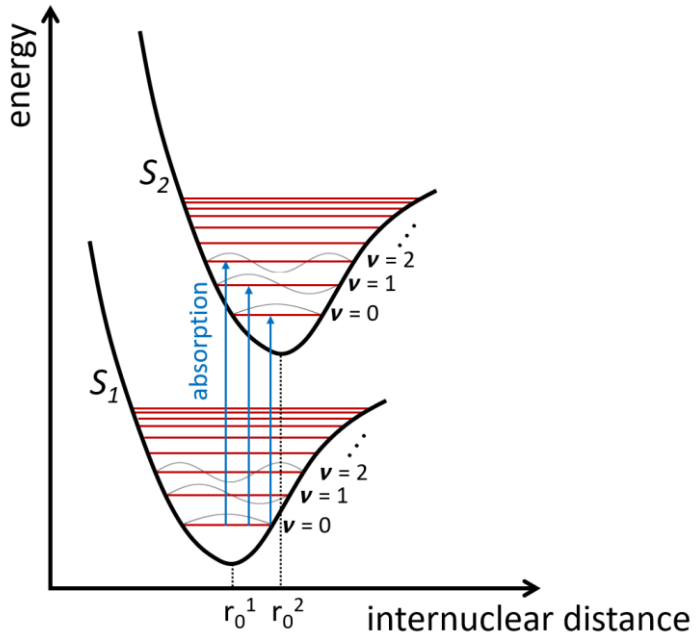

Figure 17: Schematic energy diagram, visualizing the Franck-Condon principle. A molecule in its ground state (S_1, $\nu = 0$) is excited by the absorption of a photon into a higher electronic state (S_2, $\nu = 0$) and possibly also higher vibronic states ($\nu = 1, 2, \ldots$).

The energy landscape for each state at internuclear distance (r_0), and thus a certain displacement of the atoms from their equilibrium distance, in this simplification is described with unharmonic oscillators (black lines in Figure 17). The individual vibronic levels ($\nu = 0, 1, 2, \ldots$) at characteristic energies are occupied by wave functions, which describe the probability to find an electron at the respective position. Upon absorption of a photon, sufficient energy presumed, the molecule transitions into an electronically (S_2) and possibly vibrationally ($v \geq 0$) excited state. The blue absorption arrows in Figure 17 thus represent transitions from the electronic ground state S_1 to an electronically excited state S_2. From left to right, the 0-2, 0-1 and 0-0 transitions are shown which represent different vibronic end states that are reached by the absorption of the photon. The probability of a certain transition is determined by the overlap of the

individual wave functions.[158] Since absorption happens practically instantaneously, occurring on a femtosecond time scale, no lateral shift during the absorption process is expected. This can be different for slower emission processes like fluorescence or phosphorescence.

In the analysis of an absorption spectrum plotted against photon energy. The characteristic transitions appear as multiple peaks starting at the low energy absorption edge and continuing towards higher energies.[159], [160] The 0-0 transition at the lowest specific energy, followed by 0-1, 0-2 and so forth. This is indicated in Figure 18. Assuming harmonically oscillating systems, which is in approximation feasible for the first few transitions, the peaks yield the same width and distance to their respective neighbor peaks. Thus, they are fitted with Gaussian peaks with equal width and constant distance to their neighbors. If the sample shows inhomogeneity, e.g. by the combination of multiple compounds or in their intrinsic electronic structure, additional sets of equally wide equidistant Gaussian peaks are introduced and a precise allocation can be difficult.

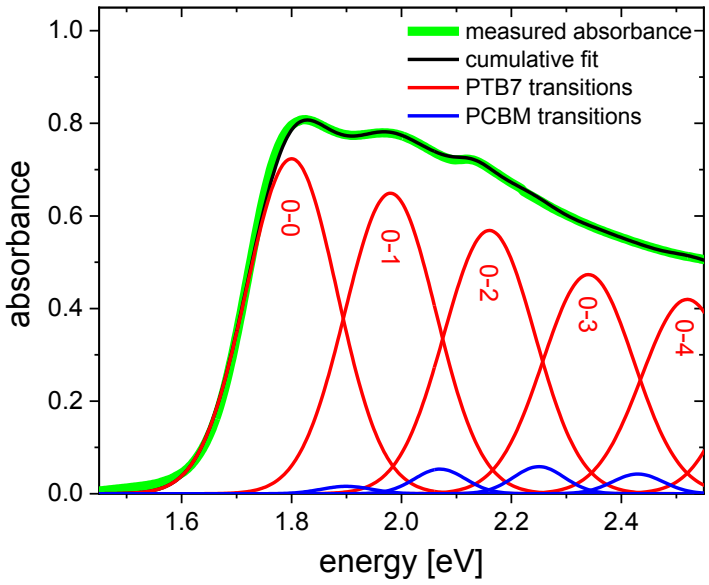

Figure 18: Determination of electronic transitions of PTB7 in a PTB7:PCBM blend film. Gaussian functions for PTB7 are indicated in red (PCBM in blue). The sum of all peaks (black curve) gives the overall absorbance of the sample (thick green curve).

2.2.3 X-ray diffraction

For crystalline and partly crystalline samples, X-ray diffraction (XRD) can be used to study properties such as crystal structure, crystallinity, and crystallite sizes. In the present work XRD was primarily used to determine stacking parameters of the π-π-conjugated network in the PTB7:PCBM blend films under investigation.

Constructive interference of X-ray radiation, scattered from the probed material, is analyzed in reciprocal space to determine structural properties as stated above. For this purpose, a X-ray beam is generated and hits the crystal, which is characterized by lattice planes with their distance d_{hkl}. Most laboratory instruments use characteristic X-rays that are emitted from a metal anode upon the impact of electrons. A commonly used electron transition is the dropping of L-shell (2s & 2p) electrons into vacant K-shell positions in copper which generates characteristic lines at 1.5406 Å (8047.8 eV) and 1.5444 Å (8027.9 eV). Compared to single emission lines, this double peak naturally leads to a peak broadening in the measurement, but considering the vicinity of the two lines this is acceptable for most purposes and definitely for the investigation of the polymer samples for this thesis. For the present study, an Advance D8 diffractometer (Bruker, USA) is used with a copper X-ray tube yielding an effective X-ray wavelength of 1.5418 Å. The applied Bragg-Brentano geometry with symmetrically moving source- and detector arms is schematically depicted in Figure 19.[161]

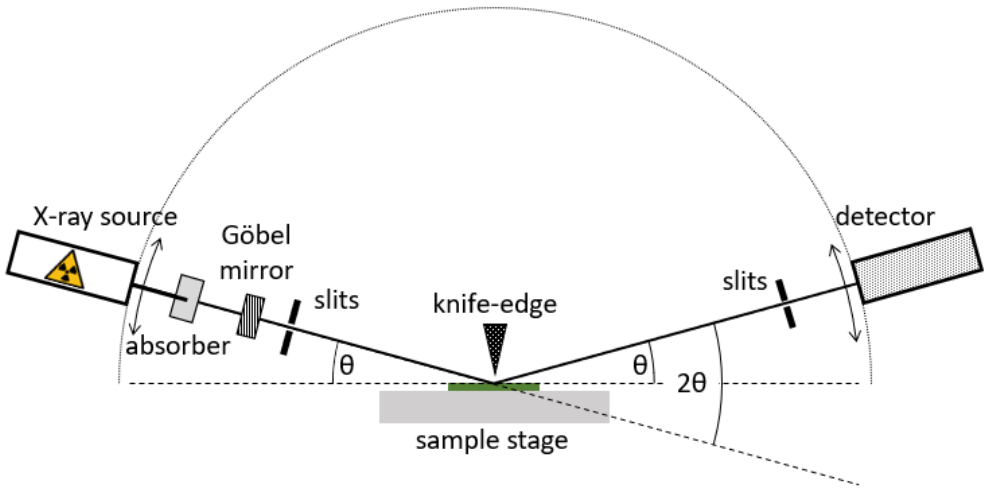

Figure 19: Schematic drawing of the used setup for X-ray diffraction measurements. X-rays are generated in a X-ray tube, the beam is shaped by a set of absorbers and slits and hits the sample at an angle of θ. In the coupled θ - 2θ geometry, the detector simultaneously measures the scattered intensity, also at an angle of θ. The sample stage is stationary during the measurement.

In a θ - 2θ setup, the X-ray source and the detector are mobile and move symmetrically on a vertically oriented semicircle around the sample in the center and always stay directed towards it. The initial X-ray beam can be shaped by slits and attenuated by absorber plates, which both can be inserted at various positions along the beam path, also on the detector arm, e.g. to improve signal quality by the use of detector slits. Göbel mirror and Soller slits are used to ensure a parallel (non-divergent) X-ray beam. A knife edge can be lowered towards the sample in order to reduce the sampling footprint, especially at shallow incidence. The desired 2θ range is scanned in a selectable number of steps and the intensity at each 2θ configuration is measured for a certain time. In the resulting X-ray diffractogram the background can be subtracted and peaks are fitted with Voigt-like functions. The use of a Voigt function, i.e. the convolution of a Gaussian and a Lorentzian peak, to fit XRD peaks has the advantage to account for both, sample related broadening of the peak and the finite instrumental resolution at the same time.[162]

Elastically scattered beams interfere constructively at certain scattering angles θ, dependent on the lattice plane distances d_{hkl} of the sample that are given by Bragg´s law:

$$\sin\theta = \frac{n\lambda}{2d_{hkl}} \tag{15}$$

where n is an integer (order of reflex) and λ the X-ray wavelength. In the case of amorphous polymeric samples, no distinct reflexes are present in the diffractogram since the long-range order is very limited compared to fully crystalline samples. Nevertheless, the frequently observed broad peaks of partly amorphous or semicrystalline samples yield information about average crystallinity, stacking structures and distances of polymer chains.[68], [163], [164]

Detectors can only measure the intensity from which one can infer the conditions of constructive or destructive interference, but any phase information that would yield information about the distribution of electron density in the structure is lost. The measured intensity of any reflex is proportional to the square of the structure factor F_{hkl}, which is the sum of all waves that are scattered by the electrons and thus depends on the atomic form factor f_j (see Equation (18)). The atomic form factor describes the angular scattering power of the electron cloud around the respective atom as described

by Equation (17). It is thus a Fourier transform that translates the electron density distribution in real space into a scattering intensity in reciprocal space.

$$I_{hkl} \propto |F_{hkl}|^2 \tag{16}$$

$$f_j(\vec{q}) = \int_0^V \rho(\vec{r}) exp[2\pi i(\vec{q} \cdot \vec{r})]\, dV \tag{17}$$

$$F_{hkl} = \sum_j^n f_j exp\left[2\pi i\left(hx_j + ky_j + lz_j\right)\right] \tag{18}$$

x, y, z are coordinates of the unit cell and *h, k, l* the Laue-indices of the lattice planes, which are also used to describe the respective set of parallel lattice planes in the Bragg equation (Equation (15)). The structure factor F_{hkl} is the sum over all n atoms in the sample. The condition for constructive interference according to Bragg´s law and thus a reflex of certain intensity is fulfilled (Laue condition) at the scattering vector $\vec{q}$ for the reciprocal lattice vectors *a*, b** and *c**:

$$\vec{q} \equiv ha^* + kb^* + lc^* \tag{19}$$

Since the phase information is lost by measuring the reflex intensity only, the direct determination of the real crystalline structure is not possible, but different methods for structure refinement exist. Since the samples in this thesis are not crystalline and only π-π stacking distances are determined, these refinements were not applied.

2.2.4 Fourier-transform-infrared spectroscopy

Fourier-transform-infrared (FTIR) spectroscopy is a technique for the investigation of the chemical structure and the presence of certain functional groups in a sample. In infrared spectroscopy a sample is exposed to IR radiation and the transmitted, scattered or reflected light is analyzed. The comparison of incident and measured light reveals the material´s absorption features that are characteristic for certain bonds or functional groups. These absorption bands in the infrared region originate from transitions of the respective molecule between discrete vibrational excitation levels within the eigenstates. The number of such normal vibrational eigenstates n_v is defined by the number of atoms n in the molecule, which can move in 3 dimensions, and can be calculated with Equation (20).

$$n_v = 3n - 6 \tag{20}$$

3 purely translational and 3 purely rotational modes are subtracted as they exclude changes of bond vibrations per definition. The potential energy of the vibrational states in dependence of the displacement from the equilibrium positions is given by an inharmonic Morse oscillator, as sketched in Figure 20. While for a symmetric harmonic oscillator, the vibronic energy levels occur at regular distances, their density increases towards the dissociation energy in the Morse oscillator.

The characteristic vibration frequency of a bond depends on the bond strength and the connected masses. The IR absorbance spectrum of a compound, a molecule or a functional group is characteristic for all IR-active vibrational transitions of the bonds therein. Only bond vibrations, that involve a change in dipole moment are IR active. This significantly reduces the number of IR absorption features compared to the total number of normal modes (Equation (20)).

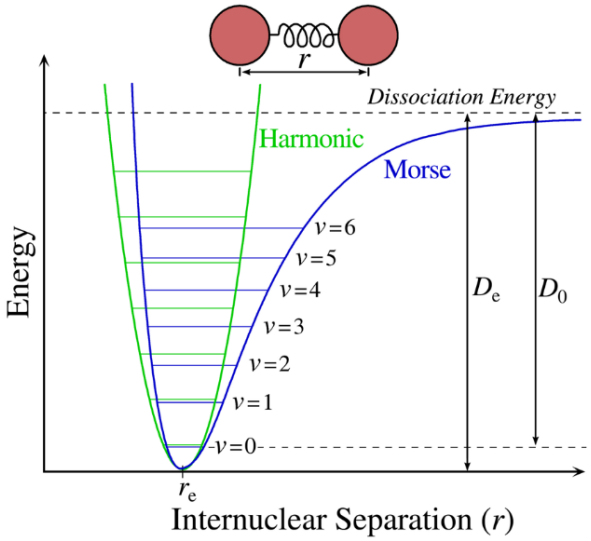

Figure 20: Graphical representation of the Morse potential (blue) and comparison with a symmetric (harmonic) oscillator model (green). Energy levels (v = 0, v = 1, ...) and the dissociation energy are indicated. Graphics created by Mark Somoza.[165]

In traditional dispersive instruments the geometry is arranged similar to the one shown for UV-vis spectroscopy (Chapter 2.2.2). A dispersive element spreads the light of the polychromatic IR source and the absorbance of the sample is measured for every wavelength individually one after another. This brings the disadvantage of a comparably slow measurement process, low intensity and inaccuracies due to the need for multiple moving mechanical parts along the beam path. In comparison, FTIR uses the entire source spectrum at once and reduces the number of moving components. The typical setup of a FTIR spectrometer is sketched in Figure 21.

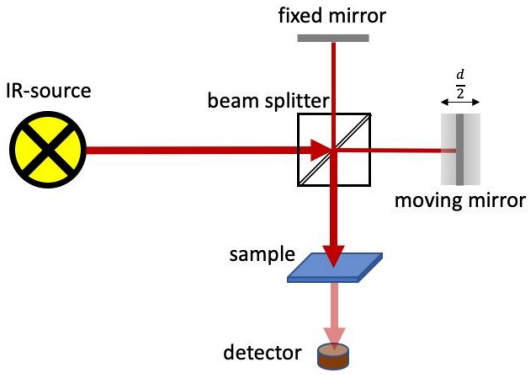

Figure 21: Schematic representation of the working principle of a FTIR spectrometer. Indicated are the components IR source, Michelson interferometer which consists of a beamsplitter, a fixed and a moving mirror, sample position and the light detector.

A Michelson interferometer is used to encode the light spectrum with one stationary and one moving mirror. The initial IR beam is split into two parts in a beam splitter, reflected at the two mirrors and recombined in the beam splitter again. From there, the recombined light beams continue to the sample position and the transmitted part further to the detector. Depending on the position of the moving mirror, a certain wavelength fulfills constructive interference in the recombined beam. This wavelength is tuned by changing the position of the moving mirror and thus the path difference. The transmitted intensity $I_{trans}(d)$ is measured as a function of the path difference. The measurement, which contains information of all wavelength, is called interferogram and is described by Equation (21):

$$I_{trans}(d) = \int I_{trans}(\nu) \cos(\pi f d)\, d\nu \tag{21}$$

with d being the path difference between the two light paths that is determined by the mirror position and ν the frequency of the IR radiation, which is the inverse of the wavelength and proportional to the energy E and the respective wave number $\tilde{\nu}$ of a photon:

$$E = h\nu = h\frac{c}{\lambda} = hc\tilde{\nu} \tag{22}$$

To get from the measured distance domain into frequency a fast Fourier back-transformation is performed as shown in Equation (21). The IR transmission is calculated with the measured reference (I_0) and sample intensity (I_S) (Equation (23)) and can be transformed into the absorbance (Equation (24)).

$$T(\nu) = \frac{I_S(\nu)}{I_0(\nu)} \tag{23}$$

$$A(\nu) = log_{10} \frac{1}{T(\nu)} \tag{24}$$

In case IR active materials like H_2O, CO_2 from ambient atmosphere or the substrate itself are in the beam path, a reference measurement can be performed and the sample results are corrected for the respective bands.

In summary, the technique of FTIR spectroscopy brings several advantages such as increased speed, higher sensitivity and signal to noise ratio, mechanical simplicity due to only one moving part (the interferometer mirror) and the automatic self-calibration of the instruments using a reference laser with known wavelength.

For this thesis, a Bruker Equinox 55 laboratory FTIR spectrometer was used to acquire IR absorbance spectra in the frequency range from 4000 cm^{-1} to 400 cm^{-1} with a spectral resolution of 2 cm^{-1}. Baseline correction and atmospheric compensation was performed with the software OPUS (Bruker).

2.2.5 Raman spectroscopy

Raman spectroscopy is the spectroscopic investigation of light that was scattered at solids or molecules.[166], [167], [168] The underlying principle of characteristic inelastic scattering of light was discovered by the Indian physicist C.V. Raman in 1928. He was awarded with the Nobel prize for this discovery in 1930. The principle of Raman scattering is the inelastic scattering of photons upon interaction with molecules or parts of molecules. More precisely, individual bond and small atom assembly (e.g. functional groups) vibrations have the ability to interact with photons. A requirement for Raman scattering is the ability of the respective vibration to change the polarizability of the molecule via the induction of a dipole moment. The molecular polarizability α of a bond is defined as the ratio of the dipole moment p_d to the electric field E that induces p_d (Equation (25)). The variation of the polarizability by the displacement of an atom along the vibronic normal coordinate $\vec{r}$ over time t is given by Equation (26). The time dependence of the dipole moment $p_d(t)$ induced by a photon is then given by Equation (27).

$$\alpha = \frac{p_d}{E} \tag{25}$$

$$\alpha(q) = \alpha_0 + \left(\frac{\partial \alpha}{\partial q}\right)_0 \vec{r}, \quad \alpha(t) = \alpha_0 + \alpha_1 \cos(2\pi \nu_m t) \tag{26}$$

$$\begin{aligned} p_d(t) = \alpha_0 E_0 \cos(\nu_0 t) + \frac{1}{2}\alpha_1 E_0 \cos[(\nu_0 - \nu_m)t] \\ + \frac{1}{2}\alpha_1 E_0 \cos[(\nu_0 + \nu_m)t] \end{aligned} \tag{27}$$

ν_0 represents the frequency of the incident photon and ν_m the frequency of the molecular vibration. Detailed derivation of the equations can be found in literature.[167], [168]

Equation (27) consists of three terms, each describing light scattering phenomena with different energy transfer processes. In the first term the photon frequency remains unchanged, thus the photon scattering process is elastic. This interaction is referred to as Rayleigh scattering. In the second and third term the frequency changes due to atomic interactions and the photon is thus scattered inelastically. If the scattering process involves a decrease of the photon frequency and thus an increase of λ, it is called Stokes Raman scattering. A scattering process with an increase of the photon frequency and a decrease of λ, is called anti-Stokes Raman scattering. The difference in terms of energy between the Rayleigh line and the two Stokes lines (that belong to the same virbonic transition) is identical. Due to the fact that α_0, responsible for Rayleigh scattering, is far larger than α_1, responsible for Raman scattering, the usable Raman intensity is very low compared to the overall scattering intensity. The ratio between Stokes ($\nu_{photon,\ final} < \nu_{photon,\ initial}$) and anti-Stokes ($\nu_{photon,\ final} > \nu_{photon,\ initial}$) is proportional to the occupation probability of vibronic states given by the Boltzmann factor and thus are temperature dependent:

$$\frac{I_{Stokes}}{I_{anti-Stokes}} \propto exp\left(\frac{-h\nu}{k_B T}\right) \tag{28}$$

At room temperature, the Stokes-lines are usually significantly more intense and thus commonly considered in Raman spectroscopy.

The energy scheme for Raman scattering is shown in the Jablonski diagram in Figure 22. If an interaction between the incident light and the molecules in the sample occurs, the induced dipole moment of the vibrations of the chemical bonds is visualized by the occupation of a virtual state. Subsequently the molecule relaxes back to its initial state. Since the initial and final state can differ in terms of their vibrational energy, the energy of the "emitted" or scattered photon is also not necessarily identical with the energy of the incident photon. This was introduced before as Stokes and anti-Stokes scattering. This energy difference is the Raman shift and can be both, an energy gain or energy loss. The case of an interaction, where no energy shift is involved, i.e., the molecule relaxes back into the ground state, is called Rayleigh scattering, as described before. It should be noted that this short-lived occupation of virtual states is not dependent on resonance matching between photon and actual energy states of the system like e.g. fluorescence. The fraction of Raman scattering compared with Rayleigh scattering is very low (in the range of 10^{-4}) and even lower compared to the total incident intensity (down to 10^{-9} – 10^{-10}). For meaningful use in scientific instruments, thus both is required, a high intensity laser source and sophisticated optics to analyze the low intensity Raman scattering in the presence of a very bright laser beam.

Raman shifts are characteristic for each bond type and vibration mode, thus any Raman active compound, functional group or individual bond has its specific Raman fingerprint and can be detected with the technique. Since the process of Raman scattering requires a molecule deformation which changes the polarizability of the system, not all types of vibrations are detectable with Raman spectroscopy. Here the rule of mutual exclusion with FTIR spectroscopy, explained in the previous chapter, applies. It states, that if a molecule possesses a center of symmetry, there is no normal mode that is both, Raman and IR active. In molecules without center of symmetry, modes can be Raman active as well as IR active.

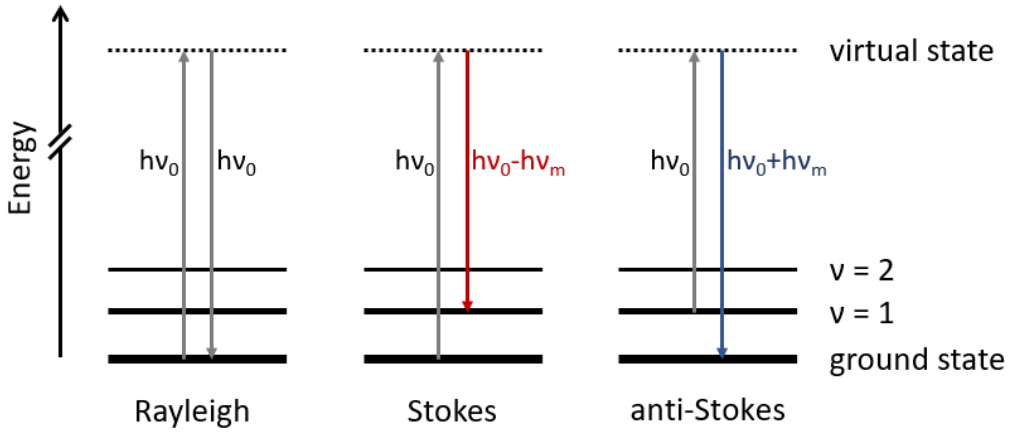

Figure 22: Schematic representation of the origin of Raman scattering on basis of a Jablonski energy diagram. The vibrational ground state is indicated as thick solid line and excited vibrational states as thinner lines. The characteristic molecular vibration frequency ν_m is the vertical distance between ground state and v = 1. Upon absorption of a photon, the system can be excited to a virtual state, that subsequently relaxes with the emission of another photon. If the two photons have the same energy (elastic scattering) the process is called Rayleigh scattering. If the scattered photon has less or more energy than the incident (inelastic scattering) the process is called Stokes or anti-Stokes scattering, respectively. The respective Raman shift for Stokes and anti-Stokes scattering is indicated as $h\nu_m$.

Further developments to increase the Raman signal like surface enhanced Raman (SERS), resonance Raman or stimulated Raman are applied frequently. It is also possible to perform a polarization analysis of the Raman signal, which allows to study aspects such as crystallinity, crystal orientation and strain.

For this thesis, Raman spectroscopy was used to investigate the change of the chemical bond structure in PTB7:PCBM thin films during illumination. For this purpose, a modular Raman system from Horiba-Yobin (Japan) was used that was designed for the use in the TOFTOF spectrometer at FRM II (MLZ, Garching) to enable simultaneous QENS and Raman measurements. A sketch of the optical path system of the setup is shown in Figure 23.

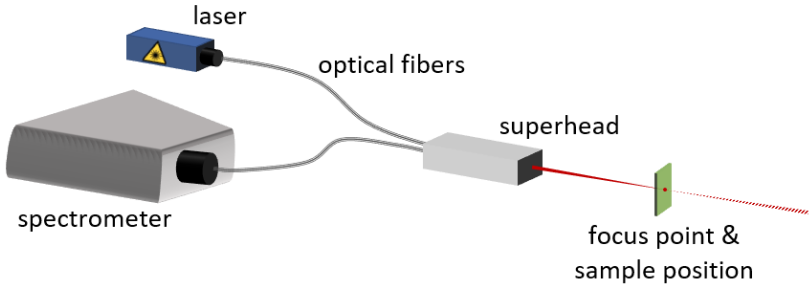

Figure 23: Schematic drawing of the optical system of the Raman system as used in the TOFTOF neutron spectrometer.

The superhead defines the heart of the system, since it merges the different light paths. The pump laser has a wavelength of 785 nm and a power of 100 mW. It can be attenuated by the use of optical grey filters. The laser light is guided through fibers into the superhead which is then guided towards the sample position. Adjustable optics after the superhead focus the laser beam onto the sample position. The superhead also collects the scattered light and removes the Rayleigh line with an interference filter. Here the light paths are divided and the (back)scattered light is guided into another fiber which leads to the spectrometer where it is analyzed. The spectrometer shapes the beam with an entrance slit and unfolds the spectrum of the scattered light with an optical grid (600, 1200 and 1800 lines per mm are available). The unfolded spectrum is measured with a charge-coupled device (CCD) camera (1025 x 256 pixels á 26 µm x 26 µm). The use of flexible fibers instead of a rigid geometry makes the setup extremely versatile and adaptable to many spatial conditions.

2.2.6 Neutron scattering

Quasielastic neutron scattering is one major technique, used in this thesis. There is a large variety of possibilities to use neutrons for the investigation of materials. The asset of the use of neutrons as a probe is their sensitivity also for light elements and different isotopes of the same element due to their interaction with the atomic nuclei. The use of respective materials as e.g. solvents or matrices yields the possibility for masking or highlighting certain parts of the sample. This is not given for e.g. X-ray scattering, which probes the electron clouds around the nuclei. Additionally, it is possible to use polarized neutrons for the investigation of various material properties.

In contrast to electromagnetic radiation, neutrons are particles, that can be described by classical Newtonian physics in extreme cases, but in general they obey both, properties of particles and waves. Key parameters like De Broglie wavelength (λ_{DB}), mass and velocity (m_n, v_n) are connected by the De Broglie relation:[169]

$$\lambda_{DB} = \frac{h}{p_n} = \frac{h}{m_n v_n} \tag{29}$$

For the kinetic energy of a neutron (E_n) follows:

$$E_n[meV] = \frac{{p_n}^2}{2m_n} = \frac{h^2}{2m_n{\lambda_n}^2} = \frac{81.82}{{\lambda_n}^2[\text{Å}^2]} \tag{30}$$

where the energy is given in meV and the wavelength in Ångstrom.

With the Planck-Einstein relation, the kinetic energy of e.g. a neutron can be translated into a wave frequency ω:

$$\frac{E}{\hbar} = \omega \tag{31}$$

The intrinsic properties of a neutron are listed in Table 2:

Mass	1.675 x 10^{-27} kg
Charge	0
Spin	½
Magnetic moment	-1.913 μ_n
Lifetime	$T_{1/2}$ = 820 s
Gyromagnetic ratio	-2.92 x 10^7 Hz T^{-1}

Table 2: Properties of the neutron

Neutrons have a magnetic moment, $^1/_2$ spin but zero charge, which offers a big range of opportunities such as the use of polarized neutron beams and the investigation of magnetic structures.

The use of neutrons as a probe is always based on some kind of interaction between the neutrons and the studied sample. Different kinds of scattering events can be distinguished:

- Absorption is used in neutron imaging and tomography.
- Coherent neutron scattering is frequently applied to study structure, whereas incoherent scattering yield information about individual scatterers.
- The ratio between elastic and inelastic neutron scattering and the possible energy shift is used for the investigation of different kinds of dynamics.

The detailed definitions for these kinds of scattering is given later in this chapter.

Principles of neutron scattering

In a neutron scattering experiment, the sample is hit by neutrons of certain velocity and direction, defined by $\bar{k}_i$, as depicted in Figure 24:

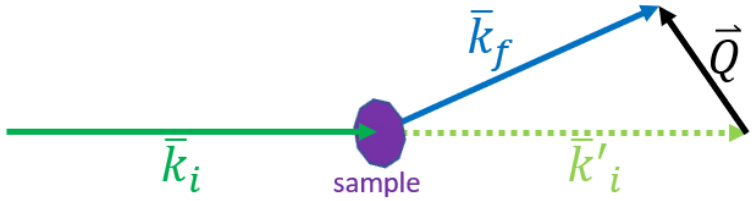

Figure 24: Schematic representation of a scattering event expressed by initial and final wave vectors $\bar{k}_i$ & $\bar{k}_f$ and the scattering vector $\vec{Q}$.

An incident neutron with defined momentum and direction $\bar{k}_i$ is scattered at the sample. The momentum (velocity and direction) of the neutron after the scattering event is described by the vector $\bar{k}_f$. The scattering vector $\vec{Q}$ is the difference between the initial and the final neutron momentum vectors as given in Equation (32):

$$\vec{Q} = \overline{k}_f - \overline{k}_i \tag{32}$$

This scattering event can be of varying nature. It is differentiated between coherent and incoherent as well as between elastic and inelastic scattering events. It is worth to note that any scattering event is always a combination of both factors, incoherent/coherent and inelastic/elastic. In the following sections the basic principles of scattering cross section, coherent/incoherent and elastic/inelastic neutron scattering are introduced.

Neutron scattering cross section

As depicted in Figure 24, in a neutron scattering event incident neutrons are scattered into various directions in space. In addition, the energy of the neutron is subject to a possible change, which induces a change of momentum. The double differential cross section describes the number of neutrons that are scattered into a given solid angle and energy interval. The double differential cross section for a system with sufficient distance between the point of the scattering event and the detector is given by Equation (33).[170] Here, sufficient distance means that it significantly exceeds the dimensions of the detector and the scattering system, respectively.

$$\frac{d^2\sigma}{d\Omega dE} = \frac{n}{\Phi_i d\Omega dE} \tag{33}$$

dΩ and *dE* are the considered solid angle, defined by the angles *θ* and *φ* as shown in Figure 25, and the energy interval around E_0 ($E = E_0 + dE$), respectively and Φ_i is the incident neutron flux. *n* in Equation (33) denotes the number of neutrons that are scattered into *dΩ* with *dE*. The visualization of the solid angle element *dΩ* and the angles *θ* and *Φ* is given in Figure 25.

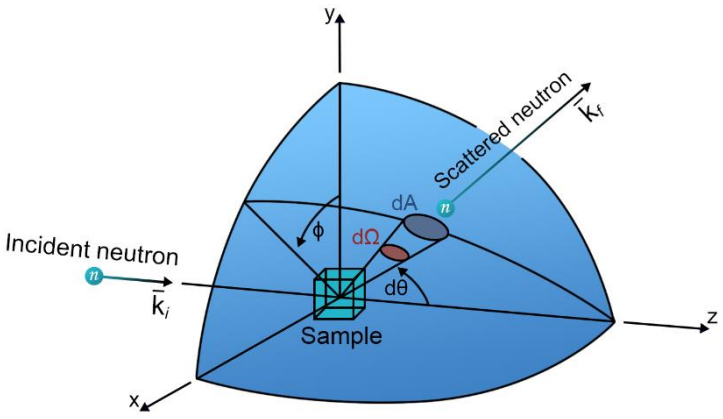

Figure 25: Geometry of a neutron scattering experiment with incident beam $\bar{k}_i$ and scattered beam $\bar{k}_f$. The solid angle element dΩ, defined by the non-parallel angles θ and Φ, is indicated on the imagined circle, centered at the position of the scattered event. Image adapted from [171].

The total scattering cross section σ can be calculated by integration over all energies and directions:

$$\sigma = \int_0^{4\pi} \int_0^{\infty} \frac{d^2\sigma}{d\Omega dE} dE d\Omega \tag{34}$$

In order to connect the isotope specific, direction-independent scattering length *b* to the total cross section σ that was described before, a wave-like probability approach can be used. As the scattering length *b* describes the radius of an interaction circle around the center of the nucleus, the respective cross section σ represents the probability that this interaction takes place. Thus, for a plane wave impinging on an unit area, the cross section tells the likelihood of an interaction. The scattered and the incident wave functions ψ_{sc} & ψ_i are differing in the amplitude modulating parameter b and a geometric expansion, as described by Equations (35) & (36):

$$\psi_i = exp\left(i\bar{k}z\right) \tag{35}$$

$$\psi_{sc} = \frac{-b}{r} exp\left(i\overline{k}\overline{r}\right) \tag{36}$$

The total scattering cross section σ (in barn, 1 barn ≙ 100 fm^2 ≙ 10^{-28} m^2) is related to the scattering length *b* (in fm) as given in Equation (37):

$$\sigma = 4\pi b^2 \tag{37}$$

All considerations presented to this point are for single scatterers. For an ensemble of scatterers, which represents the reality in scattering experiments, the interference between the outgoing spherical waves needs to be considered.

In the presence of multiple scatterers, Equation (37) can be extended and adapted to yield the coherent double differential cross section:[172]

$$\left(\frac{d^2\sigma}{d\Omega dE}\right)_{coh} = \frac{k_f}{k_i}\frac{\sigma_{coh}}{4\pi}\frac{1}{2\pi\hbar}\sum_{jj'}\int_{-\infty}^{\infty}\left[exp\left(-i\vec{Q}\vec{R}_{j'}(0)\right)exp\left(-i\vec{Q}\vec{R}_j(t)\right)\right]exp(-i\omega t)dt \tag{38}$$

as well as the incoherent double differential cross section:

$$\left(\frac{d^2\sigma}{d\Omega dE}\right)_{inc} = \frac{k_f}{k_i}\frac{\sigma_{inc}}{4\pi}\frac{1}{2\pi\hbar}\sum_{j}\int_{-\infty}^{\infty}\left[exp\left(-i\vec{Q}\vec{R}_j(0)\right)exp\left(-i\vec{Q}\vec{R}_j(t)\right)\right]exp(-i\omega t)dt \tag{39}$$

where $\vec{R}_j$ denotes the position of the j_{th} scatterer (*j* = 1, 2, …, n) and the sum goes over all atoms *j* in the sample.

Coherent/incoherent neutron scattering

The total scattering cross section can be divided into a coherent and an incoherent scattering cross section. Physical reasons for that and experimental consequences will be discussed in the following section.

Different instruments use different kinds of scattered neutrons and are technically optimized for their specific purpose. While incoherent scattering contains information about individual scatterers only and is uniform in all directions, coherent scattering is an interference effect between the scattering of different objects, dependent on the scattering vector Q, thus enables the investigation of the relative positions of the scatterers to each other. In other words, in coherent scattering, the scattered neutrons are phase correlated due to well aligned scattering lengths of the different nuclei in the system. This order can be impaired by e.g. nuclear spin disorder or the presence of isotopes of varying b. Thus, most systems show very different amplitudes and ratios of coherent and incoherent scattering. The total cross section σ_{tot} is composed not only from the coherent and incoherent scattering cross sections, but also includes an absorption contribution, arising from nuclear reactions of the incident neutron with the nucleus that lead to the absorption of the neutron, according to Equation (40):

$$\sigma_{tot} = \sigma_{abs} + \sigma_{coh} + \sigma_{inc} \tag{40}$$

Values for the respective cross sections can be determined experimentally and examples for elements that are relevant for this thesis are given in *Table 3*, presented later in this chapter.[173]

For an ensemble of scatterers, the coherent cross section is determined by the square of the average scattering length $\langle b \rangle$ over all participating scatterers:

$$\sigma_{coh} = 4\pi\langle b \rangle^2 \tag{41}$$

whereas the incoherent cross section arises from a disorder of the respective scattering lengths:

$$\sigma_{inc} = 4\pi(\langle b^2 \rangle - \langle b \rangle^2) \tag{42}$$

The small (but important) differences in Equations (38) & (39), indicate that coherent scattering yields information about the relations of different scatterers and incoherent scattering statistical representation of individual nuclei´s properties, this will be further discussed with the correlation functions at a later point.

Elastic and inelastic neutron scattering

As already mentioned before, a scattering event of a neutron at a nucleus might not only change the direction of the neutron´s motion but potentially also its kinetic energy, as described by the double differential cross section, shown in Equation (34). In an elastic scattering event, the scattered neutron possesses the same kinetic energy, thus, the respective wave vectors have the same length:

$$\left|\overline{k}_i\right| = \left|\overline{k}_f\right| \tag{43}$$

Considering the scattering triangle, as shown in Figure 24, the momentum transfer for elastically scattered neutrons is given by:

$$\left|\vec{Q}_{el}\right| = \frac{4\pi}{\lambda_n} sin(\theta) \tag{44}$$

with θ being the angle between $\overline{k}_i$ and $\overline{k}_f$.

An inelastic scattering event on the other side is accompanied by an energy transfer between the nucleus and the neutron, thus the length of the scattering vector is changed:

$$\left|\overline{k}_i\right| \neq \left|\overline{k}_f\right| \tag{45}$$

The resulting momentum transfer of inelastically scattered neutrons, thus also includes this energy transfer, which can be positive as well as negative:

$$\left|\vec{Q}_{inel}\right| = \overline{k}_f - \overline{k}_i = \left(\frac{1}{2m\hbar^2}\{2E_i + \hbar\omega - 2[E_i(E_i + \hbar\omega)]^{0.5}cos(\theta)\}\right)^{0.5} \tag{46}$$

The energy transfer between neutron and nucleus generally originates from collisions of the two, thus the energy change of the neutron is representative for the motion of the nuclei in the sample. This effect is used by the technique of quasielastic neutron scattering (QENS) in this thesis. Inelastic scattering can also be coherent and have large energy transfers (e.g. scattering at phonons, magnons, lattice vibrations, etc. as indicated in Figure 26). The quasielastic regime generally covers energy transfers of up to ±1 meV.

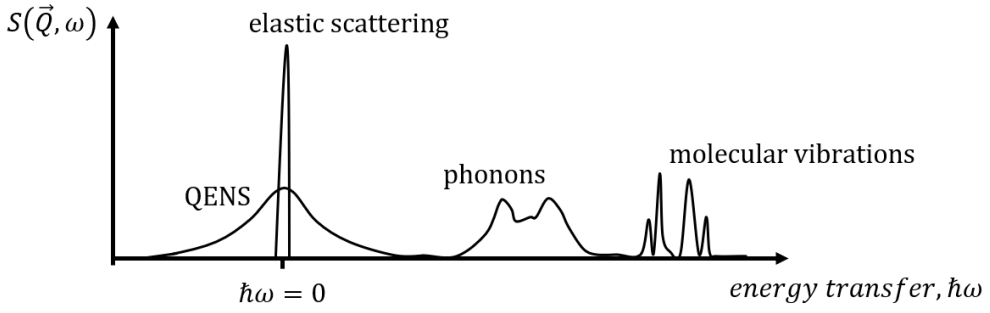

Figure 26: Schematic representation of dynamic structure factor $S(\vec{Q}, \omega)$ over the energy (transfer) range that can be probed by inelastic neutron scattering. The quasielastic regime is found at low energies around the elastic peak. Adapted from [174].

Correlation functions for neutron scattering

The use of correlation functions allows the determination of the movement and structure of scatterers. Therefore, the relevant parts of the respective cross sections are related to time dependent positions and distances. The measured quantity, the total double differential cross section, is composed of the respective coherent and incoherent part, as explained by Equations (38) & (39), and with the introduction of the scattering functions $S(\vec{Q},\omega)$ can be written as:

$$\frac{d^2\sigma}{d\Omega dE} = \frac{k_f}{k_i}\frac{n}{4\pi}\left(\sigma_{coh}S_{coh}(\vec{Q},\omega) + \sigma_{inc}S_{inc}(\vec{Q},\omega)\right) \tag{47}$$

According to Equations (38) & (39), the respective scattering functions (or dynamic structure factors can be expressed in the following way:

$$S_{coh}(\vec{Q},\omega) = \frac{1}{2\pi\hbar n}\sum_{jj'}\int_{-\infty}^{\infty}\left[exp\left(-i\vec{Q}\vec{R}_{j'}(0)\right)exp\left(-i\vec{Q}\vec{R}_j(t)\right)\right]exp(-i\omega t)dt \tag{48}$$

$$S_{inc}(\vec{Q},\omega) = \frac{1}{2\pi\hbar n}\sum_{j}\int_{-\infty}^{\infty}\left[exp\left(-i\vec{Q}\vec{R}_j(0)\right)exp\left(-i\vec{Q}\vec{R}_j(t)\right)\right]exp(-i\omega t)dt \tag{49}$$

with $_j$ and $_{j'}$ being the sites where the respective nuclei reside. $S(\vec{Q},\omega)$ represents the Fourier transform of the intermediate scattering function $I(\vec{Q},t)$ in time, as described by Equation (50):

$$S(\vec{Q},\omega) = \frac{1}{2\pi\hbar}\int I(\vec{Q},t)\,\exp(-\mathrm{i}\omega\mathrm{t})\,dt \tag{50}$$

A further Fourier transform of $I(\vec{Q},t)$ in space brings the problem from reciprocal into real space and yields the so-called Van Hove correlation functions:[175], [176]

$$G_{pair}(\vec{r},t) = \frac{\hbar}{(2\pi)^3}\iint S_{coh}(\vec{Q},\omega)exp\left(-i\left(\vec{Q}\vec{r}-\omega t\right)\right)d\vec{Q}d\omega \qquad (51)$$

$$G_{self}(\vec{r},t) = \frac{\hbar}{(2\pi)^3}\iint S_{inc}(\vec{Q},\omega)exp\left(-i\left(\vec{Q}\vec{r}-\omega t\right)\right)d\vec{Q}d\omega \qquad (52)$$

Equations (51) & (52) demonstrate that with coherent scattering, e.g. structure or correlated motion can be determined and with incoherent scattering, single nucleus properties such as statistical diffusive and localized motions can be probed.

According to the Fourier inversion theorem, all of these transformations can be performed in either direction without the loss of information.[177]

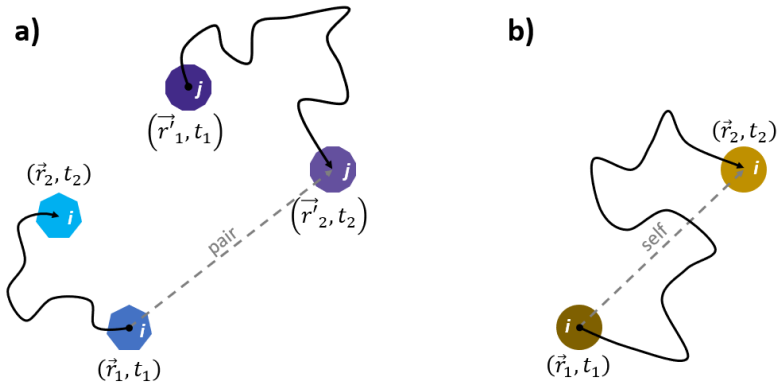

Figure 27: Reproduction of the commonly used sketch to describe pair- and self-correlation. a) the pair correlation function describes the probability that a scatterer j is found at position r'₂ at time t₂ when scatterer i was at position r₁ at time t₁. b) The self-correlation function describes the probability that a scatterer i is found at position r₂ at time t₂ when it was at position r₁ at time t₁. Solid black arrows indicate possible diffusion paths of the particles and dashed grey arrows the observation of the respective correlation functions.

As shown in Equation (51), the coherent structure factor $S_{coh}(\vec{Q},\omega)$ is related to the space and time Fourier transformation of the pair-correlation function$G_{pair}(\vec{r},t)$ which describes the probability to find a particle *j* at time *t* at position *r* if another particle *i* was at *r* = *0* at *t* = *0*.

According to Equation (52), the incoherent structure factor $S_{inc}(\vec{Q},\omega)$ is related to the space and time Fourier transformation of the self-correlation function $G_{self}(\vec{r},t)$ which describes the probability to find the same particle at time *t* at position *r* if this exact particle was at *r = 0* at *t = 0*.

Implications for the practical application of these correlation functions are illustrated in Figure 27. In order to extract the information about position as well as motion of the scatterers, encoded in $S(\vec{Q},\omega)$, the double Fourier transform in both, space and time domain, has to be applied, leading to the respective Van Hove correlation functions.

Quasielastic neutron scattering

The term quasielastic neutron scattering (QENS) describes a broadened intensity distribution of $S(\vec{Q},\omega)$ around zero energy transfer ($\hbar\omega$ = 0) as depicted in Figure 26 (shown earlier in this chapter). The energy transfer scale of Figure 26 spans from 0 at the elastic line to several tens and hundreds of meV for phonon and molecular vibration scattering, respectively, and could be extended into the eV range for e.g. electronic scattering.[174]

While QENS is defined by energetic aspects, typically in the range of $|\Delta E| \leq 1\ meV$, it consists of a coherent and an incoherent part. The coherent part contains information about collective dynamics. The incoherent part on the other hand yields information about the motion of individual scatterers, which is not quantized and thus shows a broad peak around zero energy transfer. At $|\Delta E| = 0$, a sharp peak, the elastic line is located, which represents elastically scattered neutrons. Diffusive motions are manifested by a Lorentzian broadening of the elastic line. Its width is related to the characteristic time scale of the probed motion.[174] Generally, several Lorentzians can be present in a QENS spectrum and each one represents a characteristic timescale of the observed motion(s). While a pure Lorentzian shape indicates either discrete localized rotations or simple Fick diffusion, other shapes are possible for $S(\vec{Q},\omega)$, especially in the case of partially obstructed diffusive motions.

The elastic incoherent structure factor

For the evaluation of QENS data, the so-called elastic incoherent structure factor (EISF) is an important parameter, which can yield information about the nature and geometry of the probed motions. Figure 28 shows exemplary spectra for freely diffusional (dashed lines) and localized (solid lines) processes. The self-part of the van Hove correlation function forms the connection between scattering intensity and the respective self-correlation function as mentioned before. Thus, the intermediate scattering function I($\vec{Q}$, t) decays to zero for classical free diffusion, it approaches a finite value for the case of localized motions (Figure 28a). The respective time-Fourier transformed curves of $S(\vec{Q},\omega)$ are shown in Figure 28b, yielding a purely Lorentzian shape for long range diffusion. For localized motions, an additional delta peak is present. The shape of this elastic peak is determined by the instrumental's resolution function. It is surrounded by a Lorentzian distribution for the localized process, whereas the elastic peak is absent for long range diffusion.[178] This is valid for a single exponential decay of I($\vec{Q}$,t), only.

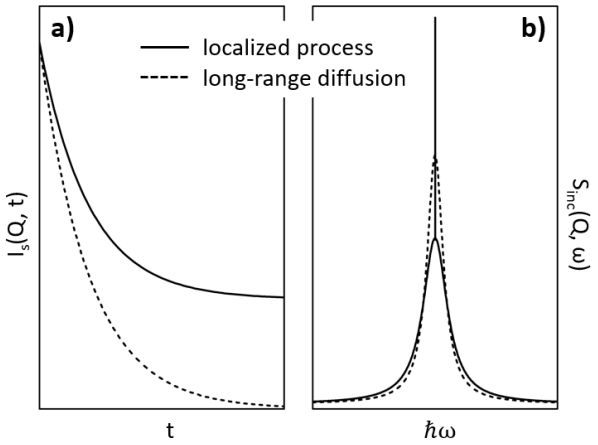

Figure 28: a) Self-part of the intermediate scattering functions and b) corresponding incoherent structure factors for localized (solid line) and long-range (dashed line) movements of the scatterers. Adapted from[178]

The EISF is defined simply as the fraction of the elastic intensity of the total scattering intensity in the quasielastic region, as given by Equation (53).

$$EISF(\vec{Q}) = \frac{I(\vec{Q},\omega = 0)}{I(\vec{Q},\omega = 0) + I(\vec{Q},\omega \neq 0)} \tag{53}$$

where I denotes the intensity of the scattering function $S(\vec{Q},\omega)$.

The EISF contains information about all motions of individual scatterers and has established as one of the most frequently applied methods to determine the type of motion probed with QENS since it can be evaluated without model assumptions.[179], [180], [181], [182], [183]

In the following section, the background for the evaluation of QENS data in respect to different kinds of dynamics is explained briefly and some exemplary models for the description of molecular motions are presented.

Localized vibrations

The simplest case of localized motion can be considered to be a random vibration of an atom within a restricted volume around its equilibrium position. These, usually thermally activated fluctuations, can be described with the so-called Debye-Waller factor (DWF). It can be found in the general representation of the incoherent scattering cross section:

$$\left(\frac{d\sigma}{d\Omega dE}\right)_{inc} = \frac{k_f}{k_i}\frac{n\sigma}{m8\pi}\vec{Q}^2\exp\left(-2W(\vec{Q})\right)\frac{Z(\omega)}{\omega}\left(\frac{1}{exp\left(\frac{\hbar\omega}{k_BT}\right)-1}+1\right) \quad (54)$$

where Z is the normalized density of states and $W(\vec{Q})$ the actual DWF. The value in the exponent describes the expected fraction of the mean square displacement u along $\vec{Q}$:

$$exp\left(-2W(\vec{Q})\right) = \langle\left[\vec{Q}\vec{u}(l)\right]^2\rangle \quad (55)$$

Averaging over all available directions of the vibration sphere gives the following expression for the DWF:

$$W(\vec{Q}) = \frac{1}{6}\vec{Q}^2\langle u^2\rangle \tag{56}$$

Translational diffusive motions

While quantized inelastic scattering from e.g. Phonons or molecular vibrations happen on characteristic timescales of 10^{-12} s to 10^{-15} s (compare Figure 26 & Figure 30), diffusive motions as studied in this thesis usually happen on longer timescale in the ps- to ns-range. In the case of free unobstructed diffusion (comparable to Brownian motion of suspended particles) Fick's second law is applicable for the self-correlation function $G_{self}(r,t)$, which yields a partial differential equation:

$$\frac{\partial}{\partial t}G_{self}(r,t) = D\Delta G_{self}(r,t) \tag{57}$$

with the starting condition:

$$G_{self}(r,0) = \delta(r) \tag{58}$$

and *D* being the effective diffusion coefficient. It can be solved to get:

$$G_{self}(r,t) = [4\pi D|t|]^{-\frac{3}{2}}\, exp\left(-\frac{r^2}{4Dt}\right) \tag{59}$$

A Fourier transform from real to reciprocal space yields the corresponding self-part of the intermediate scattering function:

$$I_{self}(\vec{Q},t) = \exp(-\vec{Q}^2 Dt) \tag{60}$$

and a further Fourier transform from time to frequency the incoherent part of the scattering function:

$$S_{inc}(\vec{Q},\omega) = \frac{1}{\pi}\frac{D\vec{Q}}{\left(D\vec{Q}^2\right)^2 + \omega^2} \tag{61}$$

which represents a Lorentzian function with the half width at half maximum (HWHM) Γ. For ideal free diffusion, Γ increases quadratically with increasing momentum transfer. Thus, the general model for Fickian diffusion is described by:

$$\Gamma(\vec{Q}) = \hbar D\vec{Q}^2 \tag{62}$$

This relation allows a direct determination of the self-diffusion coefficient by analyzing the slope of Γ, plotted against Q^2.

Since atoms and molecules move in an energy landscape and are more or less restricted to energetically favorable discrete positions, jump diffusion models have been developed to describe jump-like motions. These models assume the introduction of a specific residence time τ and a mean jump length r. Models presented exemplarily in the following section are all for isotropic diffusion. The common model for jump diffusion with fixed jump lengths, i.e. distances between residence positions was proposed by Chudley and Elliott and yields the $\vec{Q}$-dependence of the HWHM (Γ_{CE}) of:[184]

$$\Gamma_{CE}(\vec{Q}) = \frac{\hbar}{\tau}\left(1 - \frac{\sin(\vec{Q}r)}{\vec{Q}r}\right) \tag{63}$$

The model, developed by Hall and Ross assumes a Gaussian distribution of jump length, following:[185]

$$\rho_{HR}(r) = \frac{2r^2}{r_0^3\sqrt{2\pi}}\ exp\left(\frac{-r^2}{2r_0^2}\right) \tag{64}$$

Which leads to the following $\vec{Q}$-dependent behavior of the corresponding Lorentzian half width Γ_{HR}:

$$\Gamma_{HR}(\vec{Q}) = \frac{\hbar}{\tau}\left[1 - exp\left(\frac{-\vec{Q}^2 r_0^2}{6}\right)\right] \tag{65}$$

The third jump diffusion model which is presented at this point was proposed by Singwi and Sjölander and is based on an exponential distribution of jump lengths, described by:[186]

$$\rho_{SS}(r) = \frac{r}{r_0^2} exp\left(\frac{-r}{r_0}\right) \tag{66}$$

This leads to a $\vec{Q}$-dependence of Γ_{SS} of:

$$\Gamma_{SS}(\vec{Q}) = \frac{\hbar}{\tau}\ \frac{\vec{Q}^2 r_0^2}{1 + \vec{Q}^2 r_0^2} \tag{67}$$

A graphical impression about the distribution of jump lengths and the corresponding $\vec{Q}$-dependence of the Lorentzian HWHM according to Equations (63) - (67) is given in Figure 29:

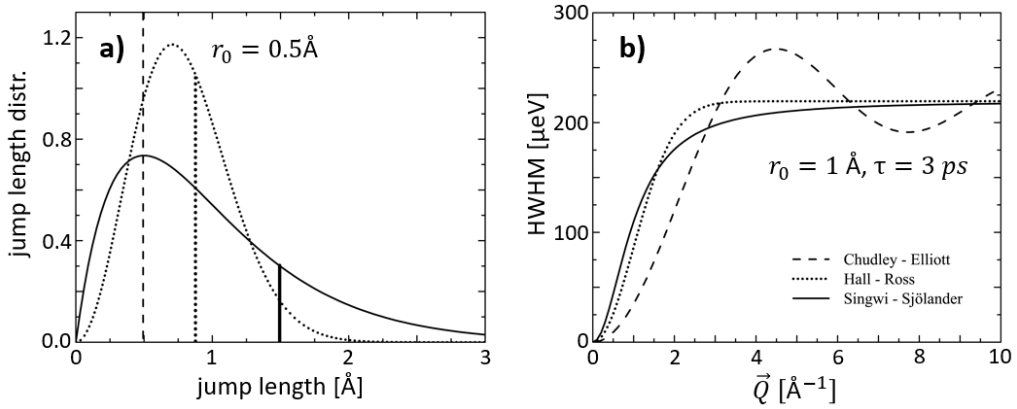

Figure 29: a) Jump lengt distributions for the diffusion modesl of Chudley-Elliott (dashed, discrete), Hall-Ross (dotted, Gaussian) and Singwi-Sjölander (solid, exponential) for r_0 = 0.5 Å. The vertical lines indicate the mean jump length for the respective distribution. b) Corresponding behavior of Γ_{CE}, Γ_{HR} and Γ_{SS} for r_0 = 1 Å, τ = 3 ps. Adapted from [178]

The general $\vec{Q}^2$-like dependence of the models depicted in Figure 29b at small $\vec{Q}$ indicates almost free motion of the scatterers in the on the respective length scale. The leveling off at large $\vec{Q}$ shows the influence of neighbors on the diffusive mobility.

Localized diffusional motions

Between vibrations of atoms around an equilibrium, described by the Debye-Waller factor, and translational diffusion, there exist many kinds of localized motions that are of diffusive nature. Examples are e.g. rotational dynamics or reorientations of certain parts of the molecules, such as alkyl side chains. Such motions can be also described by QENS data models if correct and sufficient assumptions are taken as a basis. The EISF can be helpful in this context to determine the kind of motion and the geometry. Since e.g. rotations of atoms on a sphere or reorientational jumps between alternating sites are not the scope of this thesis, description of the underlying models are not discussed in detail here, but can be found elsewhere.[183], [187], [188]

Stretched exponential approach

For some sample systems, a consistent fit of $S(\vec{Q},\omega)$ with discrete Lorentzians is not possible due to a statistical distribution of diffusive modes. Examples for such systems are glass forming liquids, condensed polymers or highly concentrated proteins since the motion of single atoms/parts of the molecules can be spatially more or less obstructed by neighboring structures, which leads to a distribution of local environments. Expressed in a more simple way, this means that different scatterers, sitting on different positions with different environments in the system, yield different diffusive properties. This behavior can be described by modelling the intermediate scattering function $I(\vec{Q},t)$ with a phenomenological stretched exponential decay function, well known as the Kohlrausch-Williams-Watts function:[189], [190], [191], [192]

$$I(\vec{Q},t) = A\ exp\left[-\left(\frac{t}{\tau}\right)^{\beta}\right] \tag{68}$$

with *A* being a ($\vec{Q}$-dependent) amplitude scaling factor and β the so-called stretching exponent, a measure for the dynamic disorder in the system. The relaxation time τ that is determined by Equation (68) is indirectly proportional to the HWHM of a Lorentzian in $S(\vec{Q},\omega)$:

$$\Gamma \propto \frac{1}{\tau} \tag{69}$$

In the physical sense, the decay of $I(\vec{Q},t)$ represents a distribution of structural relaxation of the system, according to its timescale, thus τ in Equation (68) stands for a characteristic relaxation time. An average relaxation time $\langle\tau\rangle$ can be derived according to:

$$\langle \tau \rangle = \frac{\tau\, \Gamma(\beta)}{\beta^2} \tag{70}$$

With *Γ* being the actual gamma function of the object within the brackets and must not be confused with the HWHM of Lorentzian fits, also abbreviated with *Γ* before. Same as *τ*, this average relaxation time is inversely proportional to the Lorentzian HWHM in $S(\vec{Q}, \omega)$ and can thus be described with the diffusion models, as discussed before. For the research in this thesis, a spatially obstructed jump diffusion model, based on the one from Chudley and Elliott was used to describe the diffusional motions of polymer side chains in a solid PTB7:PCBM blend. For the determination of diffusion coefficients, Equation (71) was used:

$$\langle \tau \rangle^{-1}(\vec{Q}) = \frac{D_{eff} \vec{Q}^2}{1 + D_{eff}\, \vec{Q}^2\, \tau_0} \tag{71}$$

Since, due to the dynamic disorder, the derived diffusion coefficient can not be seen as such in the classical sense, Equation (71) derives an effective diffusion coefficient that is representative for all hydrogen motions in the sample.

Practical aspects for QENS measurements

Each isotope has an individual coherent scattering, incoherent scattering and absorption length specific for neutrons of certain energy, which is, in contrast to X-ray scattering lengths, not directly correlated with the atomic number, i.e. the number of electrons, but rather a function of nuclear strong force and magnetic interaction. *Table 3* lists some scattering/absorption cross sections σ of relevant isotopes, which can be derived from the scattering/absorption length b according to Equation (37).

isotope	σ_{coh}	σ_{inc}	σ_{abs}
^{1}H	1.76	80.27	0.33
^{2}H	5.59	2.05	0.00
^{10}B	0.14	3.00	3835
^{12}C	5.56	0	0.00
^{13}Al	1.50	0.01	0.23
^{16}O	4.23	0.00	0.00
^{51}V	0.02	5.07	4.90
^{113}Cd	12.10	0.30	20600

Table 3: Neutron scattering and absorption cross sections of isotopes relevant for neutron instrumentation and the topic of the present thesis. Values are taken from [193], [194]. Cross sections are given in barn. 1 barn ≙ 100 fm^2 = 10^{-24} cm^2

Values for b can be positive as well as negative. The respective algebraic sign describes if a phase shift of the neutron wave function is involved in the scattering process with a neutron or not. A negative scattering length indicates an attractive interaction potential between nucleus and neutron, whereas a positive sign means repulsive interaction. *Table 3* shows neutron scattering and absorption cross sections which are relevant in the neutron scattering part of this thesis. Of particular interest is the difference between ^{1}H and ^{2}H, the extremely high incoherent scattering cross section of ^{1}H, the very high absorption of ^{10}B and ^{113}Cd, the overall low cross sections of aluminum and the purely incoherent scattering of vanadium.

The high incoherent scattering cross section of ^{1}H which exceeds all the other incoherent cross sections by at least one order of magnitude and the fact that hydrogen is extremely abundant in organic or soft matter makes it the very prominent isotope in quasielastic neutron scattering. Taking into account the correlation between scattering cross section and scattering function, in many cases it is fair to say that QENS probes hydrogen motions and neglect contributions from other components.

The difference to the chemically similar isotope ^{2}H enables highlighting or masking parts of the sample system, alternatively.

Boron and cadmium are frequently used as shielding, former mainly as additive in glass, concrete, ceramics, etc. and the latter also as pure metal foil.

Aluminum is almost transparent to neutrons and structurally rather solid which makes it suitable for e.g. sample containers and windows for neutron experiments.

In the typical quasielastic region, Vanadium is a purely elastic, incoherent scatterer, i.e. neutrons are isotropically scattered in all directions without change in energy. Thus, it is extremely useful as material for detector calibration, time-of-flight normalization and the determination of the spectrometer's energy resolution function.

While inelastic neutron scattering ranges up to several eV covering many vibrational modes and transitions, QENS instruments are sensitive to energy transfer ranging from neV up to the meV range, as shown in Figure 30. Large quasielastic scattering intensity around the elastic line are an indication for highly diffusive samples such as solutions or classical melts, whereas low energy transfer in the order of neV are measured for very slow dynamics like the motion of macromolecules or domain walls. This indicates the broad applicability of QENS for the investigation of dynamics on molecular scale. It is frequently applied in scientific fields like material science, soft matter, metallurgy, biology, etc.

In short, QENS uses neutrons of a known energy which interact with the sample of interest. If the sample shows dynamics on an energy range that is compatible to the neutron energy, the neutrons interact with the atoms in the sample. During this scattering process, the neutrons can either gain or lose energy. If the used instrument is characterized by a sufficient energy resolution (ΔE), this change in neutron energy is represented in a broadening on both, positive and negative side of the elastic line, which usually still contains most of the intensity.

A better energy resolution is in general compromised by the narrowing of the dynamic range, which describes the range of measurable energy transfer. Neutrons yielding an energy transfer smaller than the instrumental resolution function (slow processes) fall into the elastic line and are conceived as elastically scattered. On the other side, a small dynamic range that cuts of QENS features may exclude faster processes (broader Lorentzians in $S(\vec{Q}, \omega)$) from the analysis. Thus, the choice of a QENS instrument with characteristics, matching to the sample of interest is essential and the use of multiple instruments or settings may be necessary to study the complete range of dynamics in the sample.

Three big families of QENS instruments can be distinguished:

- time-of-flight (TOF) spectrometers
- backscattering (BS) crystal analyzers
- neutron spin-echo (NSE) instruments

They are ordered from low (large ΔE) to high (low ΔE) energy resolution. As mentioned before, a better energy resolution has generally the consequence of a restricted dynamic range, i.e. the energy transfer range that can be observed with the respective instrument. For completeness, in the following the working principle of the three kinds of spectrometers are briefly explained.

TOF spectrometers use short pulses of monochromatic neutrons and measure the time that the scattered neutrons need from the sample position to the time sensitive detectors. This distance and the respective pulse length has to be precisely defined and well known to ensure a good spectrometer resolution. As QENS experiments for this thesis have been performed at the time-of-flight spectrometer TOFTOF (MLZ, Garching, Germany), this technique is explained in more detail in the following section.

Backscattering spectrometers use specific crystal reflections for monochromating the incoming neutrons as well as for the determination of the energy of scattered neutrons.

The potential energy resolution from a crystal analyzer is mainly determined by the length of the neutron flight path and crystal quality and can be estimated from the differentiated Bragg equation:

$$\frac{\Delta\lambda}{\lambda} = \frac{\Delta d}{d}\,\frac{\Delta\theta}{tan(\theta)} \tag{72}$$

Equation (72) shows that low angular beam divergence (low $\Delta\theta$) and a high quality crystal (low Δd) is critical for good energy resolution. The challenge of providing variable neutrons energies, still in backscattering geometry, can be met by a translational movement of the crystal using a doppler drive or in some cases a thermal variation of the crystal´s lattice plane distances by either cooling or heating.[195], [196], [197], [198]

Neutron spin-echo spectroscopy offers the best energy resolution and thus allows to study comparably slow motions. The technique was discovered in 1972 by the Hungarian physicist Ferenc Mezei.[199], [200] Spin-polarized neutrons are guided through precession coils where the magnetic field induces Larmor precession, which encodes the neutron velocity as coil length and magnetic field properties are known, or to be precise attuned to the second magnetic field after the sample position that decodes the neutron velocity by a reverse precession process. A change in neutron energy due to an inelastic scattering event results in a change of precession angle and thus a decrease of the final neutron beam polarization after passing the decoder coil(s). The change (and backchange) of neutron beam polarization Φ due to Larmor precession in a perpendicular (to the neutron´s magnetic moment) magnetic field of strength B is described by:

$$\phi = \gamma B \frac{l}{v} \tag{73}$$

with the Larmor frequency

$$\omega_L = \gamma B \tag{74}$$

γ is the gyromagnetic ratio of the neutron, v the velocity and l the path length inside the field. Beyond the classical NSE setup there exist modifications, such as the resonant NSE, which employs resonant spin flippers.[201], [202]

It has to be noted that in contrast to TOF and BS, NSE is operating in time space and thus directly determines the intermediate scattering function $I(\vec{Q}, t)$. Since NSE is still a rather young technique and offers powerful possibilities in various aspects of QENS, the development of new concepts and instruments is advancing particularly rapid.[198], [203], [204]

Characteristic energy transfer and dynamic working ranges for the three kinds of QENS spectrometer and the comparison to complementary/alternative techniques as well as corresponding probed time- and length scales are indicated in Figure 30.

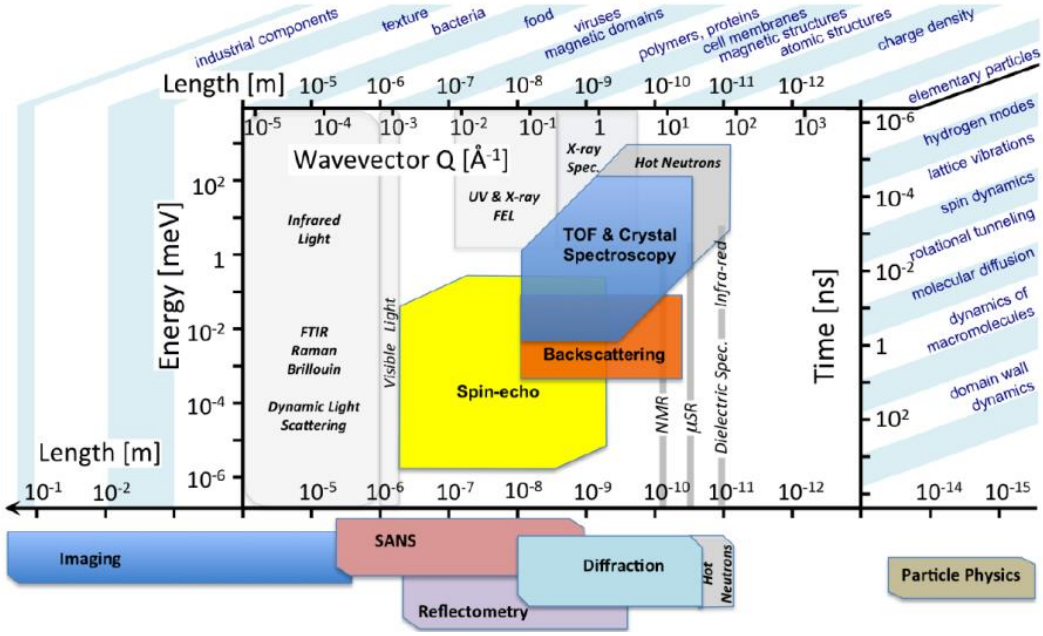

Figure 30: Characteristic time- and length scales studied with TOF and crystal spectrometers, backscattering and neutron spin-echo spectrometers including fields of application (top row) and examples of investigable processes (right column). Alternative and complementary techniques are indicated at the respective position in the size – time landscape. The figure is taken from [174].

In the present thesis the time-of-flight spectrometer TOFTOF, which is situated at the FRM II (Heinz Meier-Leibnitz Zentrum, Garching), is used for the QENS experiments. The *in situ* Raman and light excitation setup, which were newly developed within the framework of this thesis, are also specifically designed for this instrument. TOFTOF is a disc chopper spectrometer employed in direct geometry. In the following part the time-of-flight technique for quasielastic neutron scattering is discussed in more detail, followed by the presentation of the TOFTOF instrument.

Time-of-flight neutron scattering

TOF spectroscopy requires a monochromatic neutron pulse. The technical realization in the chopper spectrometer TOFTOF and possible sources of uncertainties, which define the instrumental resolution function, are discussed in the following sections.

TOFTOF instrument

TOFTOF is a cold neutron direct geometry time-of-flight chopper spectrometer at FRM II (Forschungs-Neutronenquelle Heinz Meier-Leibnitz, Garching, Germany). [205], [206] Neutrons are provided by the cold source of FRM II. They pass through a s-shaped double bended (radius = 2000 m) neutron guide to remove residual thermal neutrons as well as γ-radiation. The neutron beam is shaped to the desired dimensions of approximately 23 mm x 47 mm (width x height) by a focusing guide section in the chopper cascade. The spectral flux that reaches the sample position of TOFTOF is given by Figure 31.

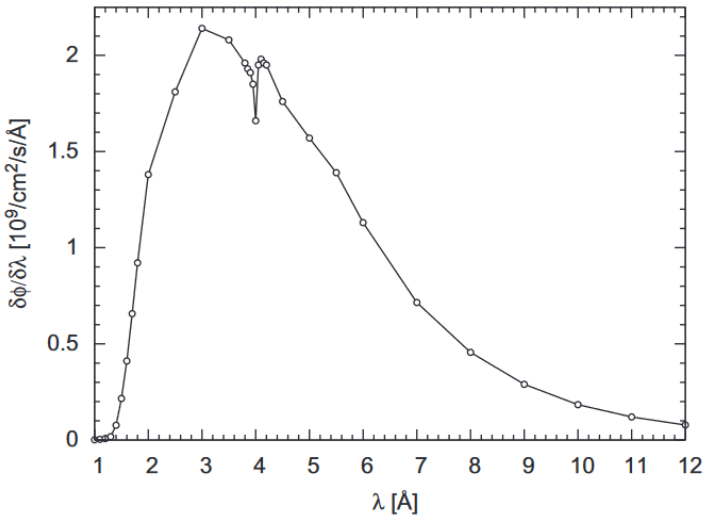

Figure 31: Differential neutron flux that is available at the sample position during regular reactor operation of FRM II at 20 MW. Graphics adapted from [205].

The general instrument layout is sketched in Figure 32. Pulsing counter rotating choppers (PCRC) and monochromating counter rotating choppers (MCRC) consist of two oppositely rotating chopper disks.

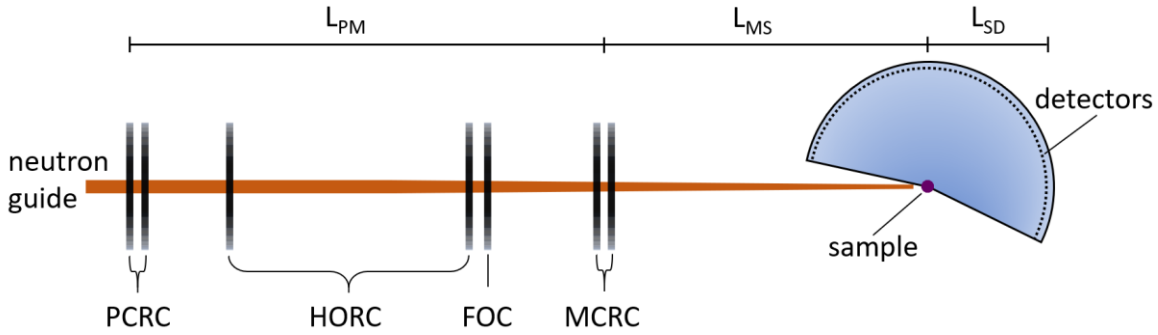

Figure 32: Schematic representation of the TOFTOF instrument. Indicated are the neutron guide, which narrows towards the sample, 7 chopper discs, separated in 2 pulsing counter rotating choppers (PCRC), 2 higher order removal choppers, 1 frame overlap chopper (FOC) and 2 monochromating counter rotating choppers (MCRC), sample position and the position of the ~1000 detector tubes. [206] The top row defines the distances from pulsing to monochromator choppers (L_{PM}), monochromator choppers to sample position (L_{MS}) and sample position to the detectors (L_{SD}).

The chopper system is used to transform the continuous white neutron beam that is delivered by the neutron guide into monochromatic short pulses. This is achieved with the two chopper pairs PRCR and MCRC. Higher order neutron wavelengths, which also fulfill transmission criteria for the PCRC and MCRC pairs, are removed by additional chopper discs, the higher order removal choppers (HORC). An overlap of the data of two consecutive pulses, i.e. the slowest neutrons of one pulse are overtaken by the fastest neutrons of the consecutive pulse, may occur due to the inelastic scattering events. Since the detectors are not energy sensitive, the individual pulses can not be distinguished in this case. In order to avoid this, a frame overlap chopper (FOC) is used to block a certain fraction of the neutron pulses.

To avoid multiple scattering a neutron transmission rate of the sample of 90-95 % is desired. These unscattered neutrons as well as neutrons that are nonetheless multiply scattered in extended samples or parts of the instrumentation and thus have an undesired angle that impairs their correct time-of-flight measurement are caught in a beam stop or the radial collimator, respectively. All other scattered neutrons travel through the argon-filled flight tank to the ~1000 ^{3}He filled detector tubes which are located in a distance of 4 meters from the sample position. The exact time from the

scattering event until the neutron reaches the detector is measured for all detected neutrons. This is the data basis for all QENS studies. In the following the instrument characteristics of TOFTOF are explained in short:

The chopper system of TOFTOF, also called the primary spectrometer ensures the correct conditioning of the neutrons before interacting with the sample. It comprises seven chopper discs with a diameter of 60 cm and a mass of 5.9 kg each. They consist of carbon fiber reinforced plastic (CFRP) and rotate with frequencies of up to 22,000 rpm, mounted in and controlled by a magnetic bearing system. All choppers rotate at the same speed ν_{ch}, except the frame overlap chopper (#5 in Figure 32), whose rotation frequency ν_{FOC} yields the following relation to ν_{ch} for the respective chopper ratio n under the condition that an overlap of neutron pulses occurs only for neutrons with final wavelength 1.5 times larger than the initial neutron wavelength λ_i:[205]

$$\nu_{FOC} = f_{ch}\frac{n-1}{n} \tag{75}$$

$$\nu_{ch}[rpm] = 1.978 * 10^4 \frac{n}{\lambda_i[\text{Å}]} \tag{76}$$

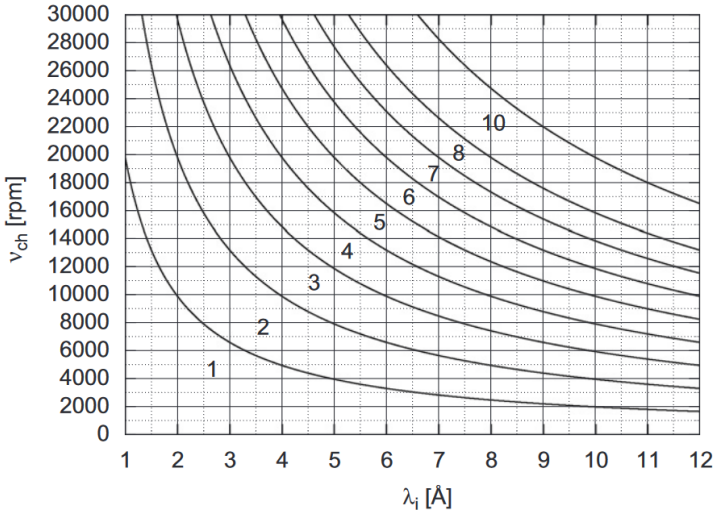

Figure 33: Determination of the frame overlap ratio n for the TOFTOF instrument (FRM II, Garching, Germany). Recommended values for n are located in the respective field, determined by chopper speed ν_{ch} and incident neutron wavelength λ_i. Taken from [205]

With Equation (76), the lines in Figure 33 are calculated, which give a practical suggestion for the correct frame overlap ratio, located the respective field according to the instrumental settings.

A frame overlap ratio of n means, that only every n^{th} pulse is allowed to pass the frame overlap chopper. For $n = 1$, the FOC rotates with the same frequency as the other choppers, whereas for higher frame overlap ratios, the frequency deviates and it has to be considered that FOC and PCRC have two openings, each. The values for the incident neutron wavelength and the frequency of the other choppers, that determine n according to Figure 33, have to be chosen appropriately to the respective experimental requirements in terms of energy resolution and dynamic measurement range. Therefore, the graphs in Figure 34, as available on the Instrument homepage, can be very helpful for the determination of suitable instrument settings:

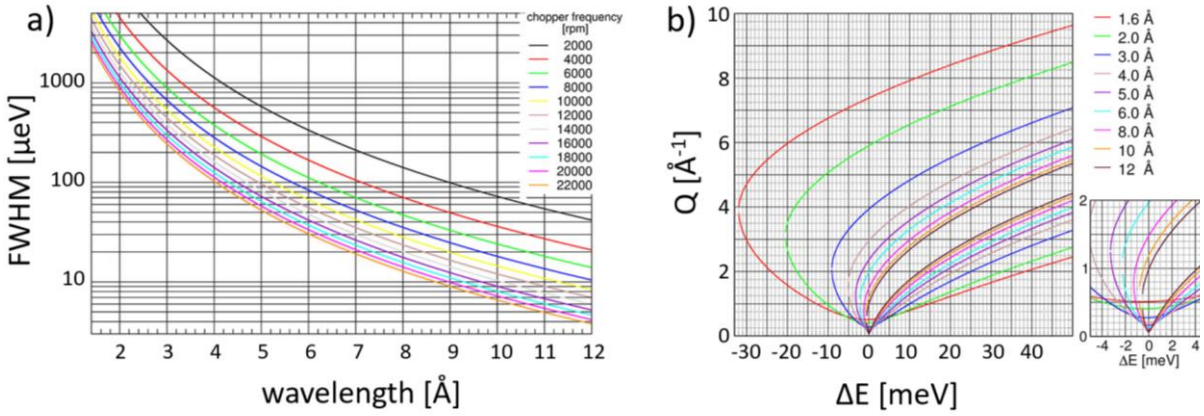

Figure 34: a) TOFTOF resolution of the elastic line for selected chopper rotation frequencies. b) available dynamic range of TOFTOF for selected incident neutron wavelengths. The insert in b) shows a zoom-in into the low Q, low ΔE range with the detachment of the measurement range from the x-axis ($\vec{Q}$ = 0) for lower wavelengths. Adapted from [207]

In general, Figure 34 yields following consequences for the practical operation of TOFTOF:

- increasing the chopper speed increases the elastic energy resolution
- higher wavelength neutrons increase the elastic energy resolution
- higher wavelength neutrons narrow the dynamic range in $\vec{Q}$-*ΔE*-space but allow resolving very small $\vec{Q}$-values

Between chopper system and sample position the beam intensity is controlled and compared to the detector signal by a ^{235}U monitor. Neutrons trigger detectible fission processes with a specific efficiency of around 10^{-5}.

The sample environment of TOFTOF offers a large range of possible experimental conditions. Temperatures from 0.5 K up to 2100 K and magnetic fields can be realized. Also electromagnetic/-static sample levitation and pressure cells (GPa) can be applied. *In situ* Raman and optical excitation parallel to neutron experiments have been developed in the framework of this thesis and are presented in the thesis annex.

After scattering at the sample and passing the radial collimator, which is built from absorbing Gd_2O_3 sheets, the neutrons enter the argon filled flight chamber. The argon gas reduces air scattering due to its relatively low scattering cross sections, compared to the components of the ambient atmosphere, especially ^{1}H from e.g. humidity.

The ~1000 ^{3}He detectors are located in a distance of 4 m from the sample center. They are arranged vertically in 4 banks, stacked on top of each other, tangentially to intersection lines of sample-centered Debye-Scherer-cones. Every detector consists of a squashed 1-inch Aluminum tube with elongated shape. The active area is 40 cm x 3 cm and the average thickness is 1.45 cm. The detector tube is filled with a gas mixture of ^{3}He and a stopping gas (CF_4) at a pressure of 10 bar. Incoming neutrons trigger the following reaction:

$$n + {}^{3}He \rightarrow {}^{3}H + {}^{1}H + 0.764\ MeV \tag{77}$$

Between an anode, which is a wire along the long axis, in the center of the detector and the outer cylinder, a voltage of 1,500 V is applied that accelerates and ionizes the reaction products. This ionization can then transfer to the anode where it is measured in the form of an electric signal.

The exact geometry of the entire TOFTOF system from cold source to the detector bank can be found in [205]. The most important instrument characteristics of TOFTOF are summarized in Table 4.

time resolution (detector)	50 ns (typically, time bins are larger)
detector area	12 m^2 (0.75 sr) vertical: -7 ° to 15 ° horizontal: -7 to 140 °
chopper frequency	400 rpm – 22,000 rpm
dimension of neutron beam	10 x 10 mm^2 up to 23 x 47 mm^2
wavelength range	1.4 Å – 12 Å
energy resolution	10 µeV – 3 meV
dynamic range	-30 meV – 50 meV

Table 4: Characteristics of the TOFTOF neutron spectrometer during regular operation of FRM II.[207]

Sources of uncertainties in TOF spectroscopy

The general working principle TOF spectrometers and the TOFTOF at FRM II (Garching, Germany) in particular has been introduced in the previous sections. In this technique, there are several possible sources for uncertainties that influence the energy resolution, which are discussed in the following section:

- the energy distribution of the neutrons that hit the sample
- a finite pulse length that is larger than 0 (in both, time and space)
- an uncertain flight path through the extended sample, due to multiple scattering and the extended detector before the detection reaction

Figure 35 explains the working principle of a direct geometry time-of-flight spectrometer graphically:

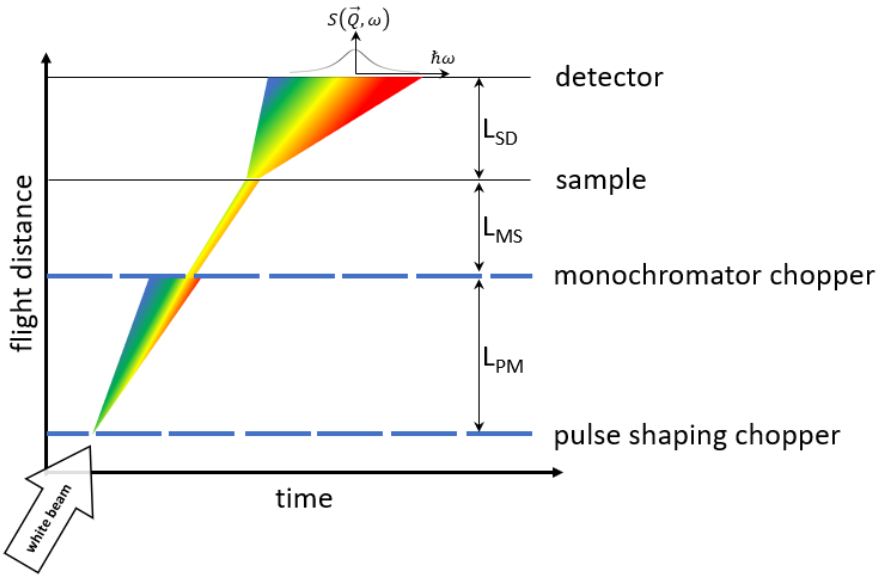

Figure 35: Schematic time-distance-diagram visualizing the working principle of a TOF chopper-spectrometer. The dashed horizontal lines (blue) represent the chopper positions. Following the x-axis, breaks in the lines represent the opening condition of the respective chopper, i.e. neutrons are able to pass. A schematic $S(\vec{Q},\omega)$ spectrum (with fixed $\vec{Q}$) on top of the detector line indicates the measured QENS spectrum. The width and different colors of the spectra indicate time and energy uncertainty.

While the vertical axis represents the neutron`s travel distance and the horizontal axis the time, faster neutrons are described by a larger slope and slower neutrons by a shallower slope. As the white spectrum, provided by the neutron source (yielding a Maxwellian distribution), hits the transmission window of the first chopper, the pulse shaping chopper, a polychromatic pulse is proceeding to the next chopper (monochromator chopper). Over the flight path between the choppers, the pulse spreads due to the wavelength distribution of the white beam. Assuming an infinitely short opening of the PCRC (which is not the case in reality), the time spread Δt_{TOF} can be calculated using the time that a neutron of wavelength λ needs to travel the distance l:

$$t_{TOF} = l\,\lambda * 252.77 * 10^{-10}\,\frac{\mu s}{m^2} \tag{78}$$

like:

$$\Delta t_{TOF}[\mu s] = l[m]\,\Delta\lambda[m] * 252.77 * 10^{-10}\,\frac{\mu s}{m^2} \tag{79}$$

The transmission window of the MCR-chopper now cuts out a “monochromatic” piece of the pulse. The wavelength spread of the final pulse is determined by the opening time of MCRC t_2 given by the rearrangement of Equation (79) under the assumption of an infinitely short opening time of the PCRC:

$$\Delta\lambda = \frac{t_2}{l * 252.77 * 10^{-10}\,\frac{\mu s}{m^2}} \tag{80}$$

This pulse hits the sample and is inelastically scattered, indicated by the further wavelength spread between sample and detector position in Figure 35. Figure 35 underlines the importance of the geometric accuracy and the beneficial influence of increased instrument dimensions on energy resolution. The different contributions to the inaccuracy in the measurement of the time-of-flight and Δt_{TOF}, respectively, indicated in Figure 35 can be seen as independent and the total inaccuracy can thus be determined as the root of the square´s sum. Also taking into account the possible path length difference Δl, this yields Equation (81) for the overall time uncertainty Δt_{TOF} at the detector, which determines the energy resolution of the instrument ΔE:[208]

$$\begin{aligned}\Delta t &= \frac{1}{L_{PM}}\sqrt{\left(\frac{m_n}{h}L_{PM}\lambda_f\Delta l\right)^2 + t_P^2\left(L_{MS}+\frac{\lambda_f^3}{\lambda_i^3}L_{SD}\right)^2 + t_M^2\left(L_{PM}+L_{MS}+\frac{\lambda_f^3}{\lambda_i^3}L_{SD}\right)^2} \\ &= \frac{1}{L_{PM}}\sqrt{A^2+B^2+C^2}\end{aligned} \tag{81}$$

$$\Delta E = \frac{\mathrm{h}^3}{e\,m_n^2\,\lambda_f^3 L_{PM} L_{SD}} * \sqrt{A^2+B^2+C^2} \tag{82}$$

with $L_{PM,\ MS,\ SD}$ standing for the distance from pulse to monochromator chopper, monochromator chopper to sample position and sample position to detector, respectively (like indicated in Figure 32 for the example of TOFTOF), *A, B, C* for the quadratic terms from Equation (81), the subscript $_i$ for neutrons of the incoming central wavelength and $_f$ for neutrons of the final wavelength after the scattering event. This shows that following characteristics are in general beneficial for a high resolution (low ΔE) spectrometer:

- high distance between pulse and monochromator choppers L_{PM} to improve the spectral accuracy of the primary spectrometer
- small distance between monochromator chopper and sample position L_{MS} to reduce the time spread at the sample position
- the use of higher incident neutron wavelength due to the λ^{-3}- dependence of ΔE
- short opening periods of the choppers to reduce both, time and energy spread
- high L_{SD} distance → smaller λ uncertainty of the respective time-channel

While the first two points may be conflicted by available space or sample environment requirements, the latter two are accompanied with a loss in neutron flux (depending on available neutron spectrum) and thus statistics.

In order to avoid undesired temporal interference of neutrons from different pulses at the detector or the passing of higher order neutron wavelengths of $\lambda_i/2$, $\lambda_i/3$,… so-called frame overlap and higher order removal coppers are usually installed between the pulse and the monochromator choppers, as indicated in Figure 36:

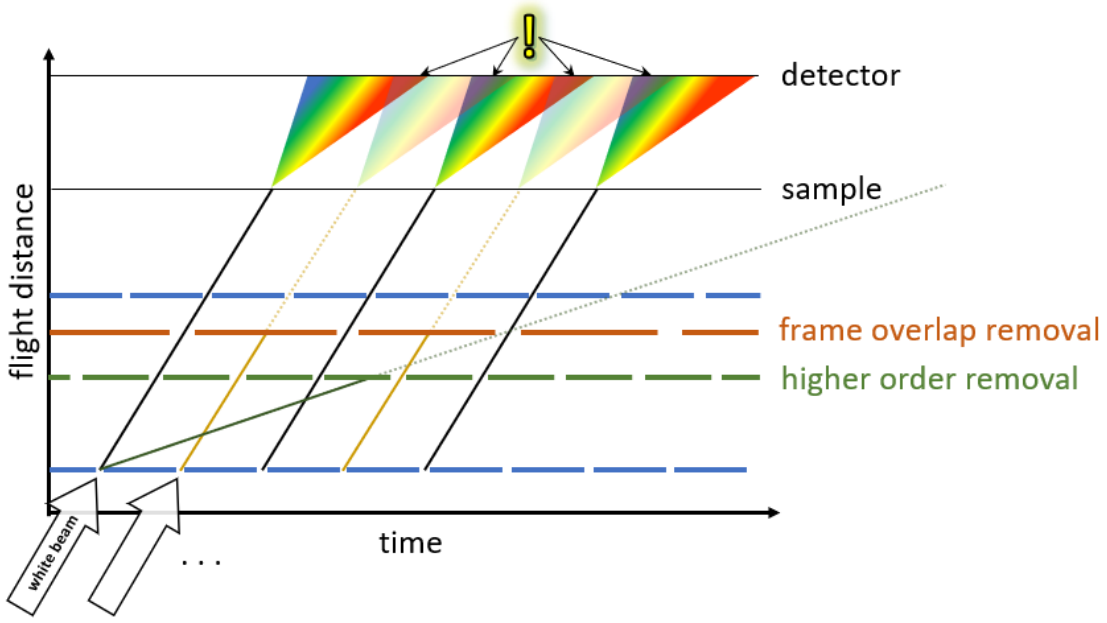

Figure 36: Visualization of the working principle of frame overlap (brown) and higher order (green) removal choppers. Flight paths in time and space are simplified compared to Figure 35 with simple black lines and only the scattering from the sample is indicated. Areas of frame overlap at the detectors are indicated by the !. Theoretical time-distance curves of frame overlapping pulses and higher harmonic wavelength neutrons are indicated as dashed lines and more transparent spectra.

As mentioned before, for the arrival of pulses at the sample with high frequency, a frame overlap at the detector (as depicted in Figure 36) can occur. This can be prevented by a frame overlap chopper (orange), which ensures sufficient distance between the individual pulses by allowing only every n^{th} pulse to pass. Neutrons with higher order wavelength may also fulfil the condition to pass all choppers, discussed so far, and disturb the measurement. Thus, the higher order removal chopper (green) is introduced to remove higher harmonic neutrons.

3 Sample preparation

In this chapter the used materials and preparation methods are described. First, polymer and fullerene derivates as well as all used solvents and solvent additives which are used for the production of the bulk-heterojunction active layer samples. Since every employed characterization technique imposes unique requirements on the sample, different preparation techniques are applied. They are presented in the second part of this chapter.

3.1 Used materials

The focus of this thesis is the investigation of PTB7:PCBM bulk-heterojunction materials as used in organic solar cells. Thus, no complete solar cells are built and the used materials are restricted to the polymer PTB7, the fullerene PCBM, the used solvents and solvent additives as well as cleaning agents.

Polymer PTB7

As already presented in Chapter 2.1, the conducting polymer poly({4,8-bis[(2-ethylhexyl)oxy]benzo[1,2-*b*:4,5-b′]dithiophene-2,6-diyl}{3-fluoro-2-[(2-ethylhexyl)carbonyl] thieno[3,4-*b*]thiophenediyl}), commonly abbreviated with PTB7 in this thesis, is one of the key model conductive polymers responsible for the progress in the development of organic solar cells. Due to its weak polarity, PTB7 is well soluble in organic solvents like chlorobenzene, dichlorobenzene or chloroform. Figure 37 depicts the chemical structure of PTB7, also revealing the presence of the two building units, namely the thienothiophene (TT) and the benzodithiophene (BDT) entities.

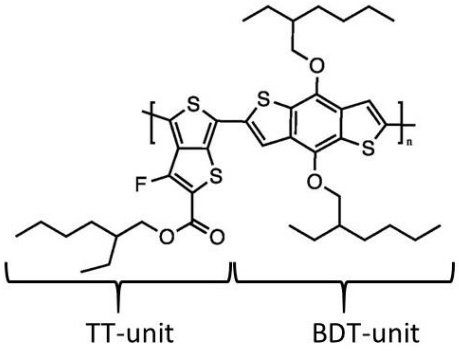

Figure 37: Chemical structure of PTB7. Thienothiophene (TT) and benzodithiophene (BDT) units are indicated.

PTB7 yields good properties for the use in organic solar cells due to its extended conjugated π-π system along the backbone and the ability to act as electron donor in combination with e.g. fullerene derivates.

PTB7 was received from 1-Material (Canada) and used for sample preparation as received without further treatment. Fabrication key figures as well as important material characteristics are presented in Table 5.

molecular weight	80,000 – 120,000 Da
polydispersity index	2.6
purity	> 99.9 %
HOMO energy	-5.15 eV
LUMO energy	-3.31 eV
band gap	1.84 eV

Table 5: Key figures of PTB7. Lines 1-3 contain data, provided by the manufacturer 1-Material (Canada) for the respective batch. Lines 4-6 are literature values taken from [84].

Fullerene derivate PCBM

PCBM is a hypernym for a family of fullerene derivates which differ in the size of their bucky ball (from Buckminster-fullerene) conjugated carbon cage and an attached tail/functional group. In the early stages of organic photovoltaic research, mainly [6,6]-phenyl C_{61} butyric acid methyl ester ($PC_{60}BM$) was used in combination with homopolymers. In a further step in the development of OPVs, the larger fullerene [6,6]-phenyl C_{71} butyric acid methyl ester ($PC_{70}BM$) is used, blended with low band gap polymers, where it acts as electron acceptor. This derivate is used for the preparation of the active layer samples for this thesis, and thus generally abbreviated with the simple term “PCBM”. The full chemical formula is given by 3′*H*-cyclopropa[8,25] [5,6]fullerene-C_{70}-D_5h(6)-3′butanoic acid, 3′Phenyl-3′*H*-cyclopropa[8,25] [5,6]fullerene-C_{70}-D_5h(6)-3′butanoic acid, methyl ester and is visualized in Figure 38.

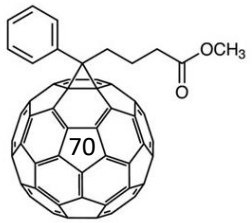

Figure 38: Chemical structure of $PC_{70}BM$. The number of carbon atoms within the cage is indicated by the number in the central pentagon.

Analogously to PTB7, PCBM shows good solubility in most organic solvents, which makes this material combination suitable for easy single solution processing. PCBM was purchased from Solenne BV (Netherlands) in a purity of >99 % and also used without further treatment. In the application in active layers of organic solar cells the n-type semiconductor properties of PCBM are utilized. In literature energy values for the HOMO level of 6.0 eV and 3.9 eV for the LUMO level can be found in [76], which gives rise to a band gap of around 2.1 eV.

Chlorobenzene

Chlorobenzene (CB) is a common organic solvent, frequently used for solution processing of organic semiconductors. It offers good solubility for both, PTB7 and PCBM and is thus chosen as the bulk solvent for the production of polymer:fullerene blend samples. CB yields a boiling point of 132 °C and a gravimetric density of 1.11 g/cm^3. The chemical structure consisting of a benzene ring chlorinated with one chlorine atom is shown in Figure 39a. The used chlorobenzene was purchased from Sigma Aldrich (Merck, Germany) in anhydrous form and a purity of >99.8 %.

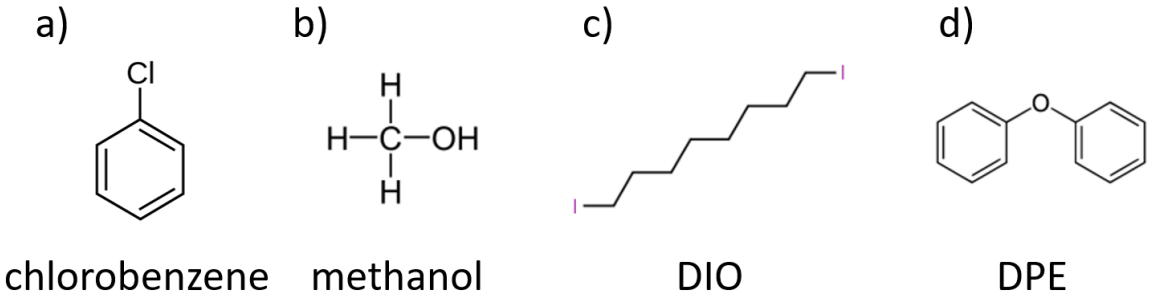

Figure 39: Chemical structures of a) chlorobenzene, b) methanol, c) 1,8-diiodooctane (DIO) and d) diphenyl ether (DPE).

Methanol

In Chapter 6.4, the influence of a methanol (CH_3OH) post-treatment on the molecular dynamics of the PTB7:PCBM blend is investigated. Therefore, methanol is used as a washing solvent to remove residual primary solvent and solvent additive molecules more effectively. The used anhydrous methanol was purchased from Sigma Aldrich (Merck, Germany) in a purity of >99.8 %. The chemical structure of methanol is depicted in Figure 39b. Methanol yields a boiling point of 98 °C and a gravimetric density of 0.79 g/cm^3.

DIO

1,8-diiodooctane (DIO, $I(CH_2)_8I$) is used as solvent additive in the solution-based production of PTB7:PCBM layers. Its function in the blend solution is that of a selective solvent for the fullerene molecules. The use of DIO can improve the blend microstructure and thus resulting solar cell performance parameters. The chemical structure of DIO can be found in Figure 39c. DIO was purchased from Sigma Aldrich (Merck, Germany) with a purity of 98 %, where the remaining 2 vol % are taken by metallic copper as stabilizer (Cu grains are leftover in the vial upon removal of DIO). Besides, the used DIO features a high boiling point (BP ≈ 168 °C) and high density (ρ_{DIO} ≈ 1.85 g/cm^3).

DPE

Diphenyl ether (DPE, $(C_6H_5)_2O$) is also used as solvent additive for the production of PTB7:PCBM blend films. Due to its selective solubility to the polymer PTB7, it can be used in combination with DIO as so-called binary solvent additive, which can further improve microstructural aspects of the blend. The chemical structure of DPE consists of two aromatic rings, connected by one oxygen atom as shown in Figure 39d. DPE (BP_{DPE} ≈ 256 °C, ρ_{DPE} ≈ 1.07 g/cm^3) was purchased in Selectophore® quality from Sigma Aldrich (Merck, Germany) with a purity of ≥99.9 %.

Substrates

Samples were prepared on different kinds of substrates, namely glass slides, pieces of silicon wafers and aluminum foil. Glass microscopy slides were purchased from Carl Roth (Germany) and were used in the supplied dimensions of 25 mm x 75 mm and a thickness of 1 mm.

To ensure sufficient transmittance for infrared radiation (FTIR spectroscopy was performed in transmission mode) boron doped silicon wafers (resistivity: 20 – 50 Ω/cm)

from Silicon Materials (USA) were used. The thickness was given by the company with 525 ± 25 µm and the wafers (diameter: 100 mm) were cut down to approximately 25 mm x 25 mm pieces for the individual samples.

Due to the good neutron transparency of aluminum, QENS samples were drop cast on pieces of aluminum foil. Unstructured aluminum foil was purchased from Carl Roth (Germany) in laboratory quality (purity ≥ 99 %) with a thickness of 30 µm.

Cleaning agents

In order to remove any kind of stain from the surfaces of the substrates, both, an acid and an ultrasonic cleaning in organic solvents was performed for glass and silicon. The used acid bath consisted of deionized water, sulfuric acid (H_2SO_4) and hydrogen peroxide (H_2O_2). The ultrasonic cleaning was performed sequentially with the solvents Alconox®, deionized water, acetone and isopropanol. The more fragile aluminum foils that were used as substrates for QENS experiments were cleaned with isopropanol and deionized water to remove any traces of fat and dust particles. All of these chemicals were purchased from Carl Roth (Germany) in regular laboratory quality, with the exception of Alconox® that was supplied by Sigma Aldrich (Merck, Germany) and dissolved in deionized water with 16 g/l. Deionized water was produced with a PURELAB® Chorus 1 water purifying system from Veolia (France) with a final resistance of < 10 MΩ cm.

3.2 Preparation of samples for QENS experiments

The conduction of quasielastic neutron scattering (QENS) experiments imposes special requirements to the sample. First of all, QENS is measured at large scale neutron sources, where beamtime is scarce and precious. Since generally, counting statistics is the limiting factor for the quality of the resulting data, the sample has to be designed in way that uses the available neutrons in the most efficient way possible, i.e. ensure sufficient scattering. In the case of TOFTOF, this statistics issue is getting even

more severe if better elastic resolution is needed due to the non-constant neutron flux over the wavelength spectrum (see Figure 31 in chapter 2.2.6). For optimal results, the maximum scattering power is desired as long as multiple scattering inside the sample can still be assumed to be neglectable. A transmittance of 90 % to 95 % has proven to be viable in this respect. Usually, this requires much more sample material in the beam compared to other thin film characterization techniques like (grazing incidence) small angle neutron scattering ((GI)SANS), neutron reflectometry (NR), X-ray and real space techniques and thus thicker sample films.

Further, the substrate or sample holder material, which is neither contributing to the scattering pattern, nor is activated by the neutron irradiation, is preferred. Aluminum offers very good neutron transmission (compare Table 3 in Chapter 2.2.6) and is thus well suitable as substrate, sample holder or for any construction that has to reside in the vicinity of the neutron beam.

Obviously, the sample has to be uniform in thickness and composition and cover the whole area of the neutron beam, which is approximately 20 mm x 50 mm in the present study.

Calculation of sample mass

As described in the previous section, the QENS sample should yield a neutron transmittance of 90 % - 95 %. As the chemical composition of the sample is known, the needed amount of material to achieve the desired transmittance value can be calculated. Table 6 shows the calculation steps that were applied to obtain the needed amount of material for the pure PTB7 and PCBM samples, as well as the 1:1 and 1:1.5 wt. blends. For the calculation a natural isotope distribution is assumed and absorbance is not taken into account since it doesn’t contribute to multiple scattering. Values for neutron scattering cross sections can be found in respective publications and online data bases.[193], [194]

	mol. Weight [g/mol]	scattering cross section per molecule [barn/unit]	scattering cross section per gram [barn/g]	scattering cross section per gram [cm^2/g]	sample mass [g]	Total film thickness [µm]
PTB7						
$C_{41}H_{53}FO_4S_4$	757.121	4599.701	3.66E+24	3.659	**0.109**	**100**
PCBM						
$C_{81}H_{14}O_2$	1018.999	1606.375	9.49E+23	0.949	**0.421**	**330**
blend 1:1 wt.	1776.120	6206.076	2.10E+24	2.104	**0.190**	**180**
blend 1:1.5 wt.	2285.619	7009.264	1.85E+24	1.847	**0.217**	**200**

Table 6: Calculation of sample masses for QENS experiments in order to fulfill a transmittance of 95 %. The calculation is performed for the individual samples from left to right, using the conditions and constants that are given below. Final results for the required sample masses and thicknesses are marked in green and orange, respectively. Following constants/conditions were used: Avogadro number: $6.022*10^{23}$ molecules/mol, 1 cm^2 = 10^{24} barn, desired film area: 8 cm^2, desired transmittance: 95 % → scattering cross section per sample: 0.4 cm^2

All used conditions and constants are given in the caption of Table 6, while the actual calculation is performed from left to right parallel for all samples in the upper part:

The molecular weight of the respective compounds is calculated from the chemical formulae. For the blend samples the molecular weights of the pure materials are simply added in the respective ratio.

In the next column the scattering cross section of one molecule/monomer/blend unit is calculated in barn. Barn is a commonly used unit for scattering cross section and 1 barn equals an area of 10^{-24} cm^2.

In the fourth column the gravimetric scattering cross section is calculated by multiplying the previous column with the Avogadro number and dividing by the respective weight. The following column shows the normalized scattering cross section per gram that is obtained by diving by the barn to cm^2 conversion factor.

The final sample mass can then be calculated by dividing the weight-normalized scattering cross section by the desired total scattering cross section, which itself is obtained by multiplying the covered sample area with the desired scattering percentage. The calculated optimal sample masses are displayed in the last column in Table 6 and highlighted in green.

From these sample masses, the approximate average film thicknesses with the gravimetric densities of around 1.2 g cm^{-3} for PTB7, 1.6 g cm^{-3} for PCBM and 1.3 g cm^{-3} for the blends,[209], [210] respectively, are calculated. For the pure PTB7 films, this yields a total sample thickness of 100 µm, for pure PCBM 330 µm, for the 1:1 blend 180 µm and for the 1:1.5 blend 200 µm. These values refer to the total sample thickness and have to be divided by 8 for information about individual films. The use of 8 stacked films is needed due to the required high amount of sample material in the beam and as explained in more detail at a later point. When using 8 films, the total film area of the samples ranges around 80 cm^2 (8 aluminum foils x ~10 cm^2 film per foil).

Drop casting of QENS samples

Due to the instability of PTB7 and its blend with PCBM at ambient conditions, the production of the samples was performed in the inert N_2 atmosphere of a glovebox. When the samples were ready to be measured in TOFTOF, they were packed in boxes, sealed with Parafilm® and directly transferred to FRM II (< 5 min foot walk from the glovebox lab of *"TUM School of Natural Sciences, Chair for Functional Materials"* to the TOFTOF end station).

Two main solutions were prepared:

- PTB7 in chlorobenzene, 20 mg/ml
- PCBM in chlorobenzene, 20 mg/ml

The solutions were magnetically stirred in closed brown vials at 70 °C for at least 12 hours to ensure complete solvation.

Subsequently, solutions were mixed in the respective ratio (here, volumetric ratio of the solutions equals gravimetric ratio of the resulting films) and stirred again at 70° C for at least 12 hours.

If solvent additives were used, they were added to the freshly mixed solutions in the respective volumetric fraction:

- 3 vol % for DIO as single solvent additive
- 3 vol % DIO plus 2 vol % DPE for binary solvent additive samples

The value for the desired film thickness that was derived in the previous section of tens of µm is a very large number in the context of thin film research.[211] Due to this, in combination with the fact that a possibly thin aluminum substrate is preferable, the choice for drop casting of the sample films was made. Other classical lab casting methods like spin or spray coating have been tested extensively but did not provide sufficient results. Even for drop casting, the upper thickness limit for solid film has been determined to be around some tens of µm in preliminary experiments. In order to maintain a reasonable counting time for the QENS experiment, 8 pieces of aluminum foil were drop cast, each with the respective volume (0.68 ml up to 2.63 ml) solution (to reach the calculated sample masses as shown in Table 6), resulting in film thicknesses of 12 µm up to 40 µm, depending on the respective sample.

The drop casting process was performed on a heating plate at 100 °C and left to dry for 20 minutes (unless stated differently in the sample description). The aluminum foil was attached to a clean, flat glass substrate by the attractive capillary force of a thin chlorobenzene film to ensure a flat and level surface of the aluminum foil for drop casting. After the liquid was apparently evaporated, the samples were transferred to another hot plate without the potentially insulating glass slide to complete the 20 minutes drying process.

If a methanol post-treatment was performed, the final dried films were rinsed with methanol for around 20 seconds, comparable to procedures applied previously.[212] An example of an aluminum slide with the used sample container is sown in Figure 40.

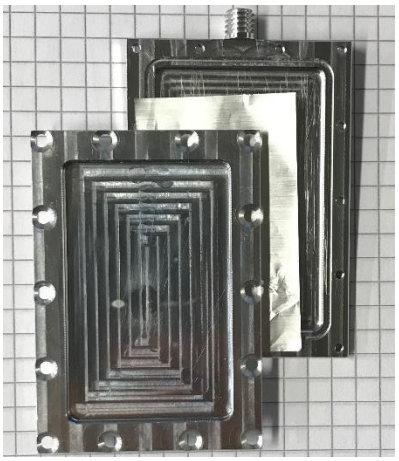

Figure 40: Flat aluminum cell and aluminum substrate as used for the QENS experiments at TOFTOF. Background: regular square paper (1 square ≙ 5 mm x 5 mm)

Subsequently, 8 coated aluminum slides were carefully stacked on top of each other and places into the aluminum sample holder, which is shown in Figure 40. The sample holder consists out of a bottom plate with a cavity where the samples are placed and a lid, which is fixed with 14 screws to close the sample holder. Between the two aluminum elements an indium or aluminum thread is fitted into a groove around the cavity and is compressed by tightening the screws to seal the cell.

Calculation of scattering contributions

For the analysis of QENS data, it is essential to know the fraction of incoherent scattering intensity. For the present samples the chemical composition varies according to the respective blend ratio between PTB7 and PCBM. Table 7 shows scattering and absorption cross sections, normalized to sample mass and the corresponding fraction of incoherent scattering. All samples are dominated by incoherent scattering cross section, mainly arising from the high hydrogen content of the organic compounds (compare Table 8).

	coherent scattering cross section [cm^2/g]	incoherent scattering cross section [cm^2/g]	absorption cross section [cm^2/g]	contribution of incoherent scattering
PTB7	0.00275	0.03384	0.00016	92.1 %
PCBM	0.00286	0.00743	0.00003	72.0 %
blend 1:1 (wt.)	0.00281	0.02063	0.00010	87.7 %
blend 1:1.5 (wt.)	0.00282	0.01799	0.00008	86.1 %

Table 7: Coherent, incoherent and absorption neutron cross sections of the four different QENS samples, normalized to weight. The last column shows the share of incoherent scattering from the total scattering.

The highest share of incoherent scattering is calculated for the pure PTB7 sample with about 92 %, whereas the pure PCBM sample´s incoherent scattering ranges around 72 %. Naturally, the blends are found at intermediate values. Comparing the gravimetric incoherent scattering cross sections (third column in Table 7) of PTB7 and PCBM reveals that PTB7 contributes much stronger to the incoherent scattering of the blend samples. For example, the 1:1 blend sample´s incoherent scattering is composed out of 82 % scattering from PTB7 and only 18 % from PCBM. This indicates that in the QENS experiment predominantly polymer dynamics are probed, also in the blend samples.

To get an impression about the origin of incoherent scattering within the polymer molecules, the calculation was further refined to calculate the contributions of individual elements.

	PCBM			PTB7			blend		
	Coh.	Inc.	Abs.	Coh.	Inc.	Abs.	Coh.	Inc.	Abs.
H	5.7 %	100.0%	94.9%	26.9%	100.0%	88.6%	16.1%	100.0%	89.6%
C	92.3 %	0.0 %	5.1%	65.8%	0.0 %	0.7%	79.4%	0.0 %	1.5%
O	2.0 %	0.0 %	0.0 %	4.9%	0.0 %	0.0 %	3.4%	0.0 %	0.0 %
F	0.0 %	0.0 %	0.0 %	1.2%	0.0 %	0.0 %	0.6%	0.0 %	0.0 %
S	0.0 %	0.0 %	0.0 %	1.2%	0.0 %	10.7%	0.6%	0.0 %	8.8%

Table 8: Contributions of individual elements to the total coherent (Coh.), incoherent (Inc.) and absorption (Abs.) cross sections. All calculations are based on the abundant isotopes ^{1}H, ^{12}C, ^{16}O, ^{18}F and ^{32}S.[193], [194] Taken from [26] (supporting information) with permission from ACS publishing.[26]

For all samples, the coherent signal is dominated by scattering from carbon atoms which are mainly found in the fullerene cage or the polymer backbone, respectively (compare the structure formula of PCBM and PTB7 in Figure 37 and Figure 38). This means that the structural information, provided by the coherent part of the scattering refers to the stacking of PCBM cages and PTB7 backbones. Incoherent scattering, on the other hand, is almost exclusively provided by hydrogen atoms. These are predominantly found in the polymer side chains. To be more precise, 51 of the total 53 hydrogen atoms in each TB7-monomer are located in its side chains. This suggests that the present QENS study is sensitive to diffusive dynamics of the polymer side chains rather than polymer backbone reorientation or displacements of fullerene molecules.

3.3 Preparation of samples for X-ray diffraction

Since the purpose of the X-ray diffraction (XRD) experiments was to confirm that the films, obtained by drop casting, which was chosen to be the technique to fulfill the QENS sample requirements best, show similar structural features like films that are used in OPV devices, samples for XRD have been prepared in a similar way as described in Chapter 3.2 with silicon wafers as substrates.

Due to the atmospheric instability of the samples, the film production was performed in the inert nitrogen atmosphere of a glovebox. Silicon wafers were cut in ca. 2 cm x 2 cm squares that were cleaned and transferred into the glovebox. A volume of 50 µl of the respective solution (20 mg/ml, for solution preparation see Chapter 3.2) were dropped onto the polished side of the level silicon substrate at 100 °C under the avoidance of the introduction of e.g. bubbles or solid contaminants. The liquid film spread to a circular shape of around 1.5 cm diameter with smooth and even surface. The sample was left to dry at 100 °C for 20 minutes to form a solid, dry film.

The final samples were stored inside the glovebox and were taken out only directly prior to the XRD measurements, which were performed in the same building.

3.4 Preparation of samples for UV-vis spectroscopy

Since the purpose of the UV-vis measurements was to confirm that the films, obtained by drop casting, which was chosen to be the technique to fulfill the QENS sample requirements best, show similar optical properties like films that are used in OPV devices, samples for UV-vis have been prepared in a similar way as described in Chapter 3.2 with glass slides as substrates.

Samples for UV-vis spectroscopy were drop cast on cleaned glass slides with dimensions of 76 mm x 26 mm x 1 mm in the nitrogen atmosphere of a glovebox. The substrates were inclined by approximately 20 ° against horizontal in their longest direction. 30 µl of the respective solution (20 mg/ml, for solution preparation see Chapter 3.2) were dispensed on the top part of the substrate equally across the whole width and let run down the glass slide. The substrate was heated to 100 °C before to ensure fast evaporation of the solvent and rapid film formation without macroscopic phase segregation. The sample was left to dry at 100 °C for 10 minutes to ensure complete solvent evaporation. This technique and the mentioned parameters have proven to yield films of a suitable thickness and optical absorbance to be measured by the used spectrometer. For the samples, used for Chapter 7, drying parameters were varied according to the description in the respective sections.

The final samples were stored inside the glovebox and were taken out only directly prior to the UV-vis experiments, which took place in the same building.

3.5 Preparation of samples for Raman & FTIR spectroscopy

Fourier-transform-infrared (FTIR) and Raman spectroscopy were performed to track changes in the chemical bond structure of the samples. Films for these characterization techniques were produced in the same way like the XRD samples, as described in Chapter 3.3, also on silicon substrates inside a glovebox. The only difference to the XRD sample preparation is the use of a larger amount of the respective solution of 100 µl per substrate. The resulting larger sample thickness is

beneficial to increase especially Raman scattering intensity, but also infrared absorbance. For the samples, used for Chapter 7, drying parameters were varied according to the description in the respective sections.

The final samples were stored inside the glovebox and were taken out only directly prior to their investigation with Raman or FTIR spectroscopy, respectively. FTIR experiments were performed in the same building, whereas the Raman spectrometer was located at the TOFTOF instrument in the Neutron guide hall west of the FRM II, a 5-minute foot walk away from the glovebox. Before taken out of the glovebox, the samples were stored in a Parafilm®-sealed box until their actual measurement.

4 Sample characterization & measurement setup

For the characterization of the samples studied in this thesis, different methods are used. This includes profilometry, quasielastic neutron scattering (QENS), X-ray diffraction (XRD), ultraviolet visible (UV-vis), Fourier-transform-infrared (FTIR) and Raman spectroscopy. In this section, details about the experimental setups and procedures are presented. The application mode of the respective instruments and the implementation of the samples is explained and pictures of the setups are shown. In Chapter 7, FTIR and Raman spectroscopy are performed *in situ* under illumination. The changes that are applied for these measurement modes are shown in the respective sections.

4.1 Profilometry measurements

For the determination of sample thickness and surface topography a Dektak XT stylus profilometer (Bruker, USA) is used. The scanning length and the topography range (resolution, max. amplitude) is set according to the expected sample properties. If possible, the scan line (indicated as white dashed line in Figure 41b) is chosen to cover bare substrate on both sides of the sample (Figure 41c, top image) to obtain a solid baseline. If this is not possible, the sample is scratched at certain spots along the scan line to serve the purpose of baseline determination (Figure 41c, bottom image).

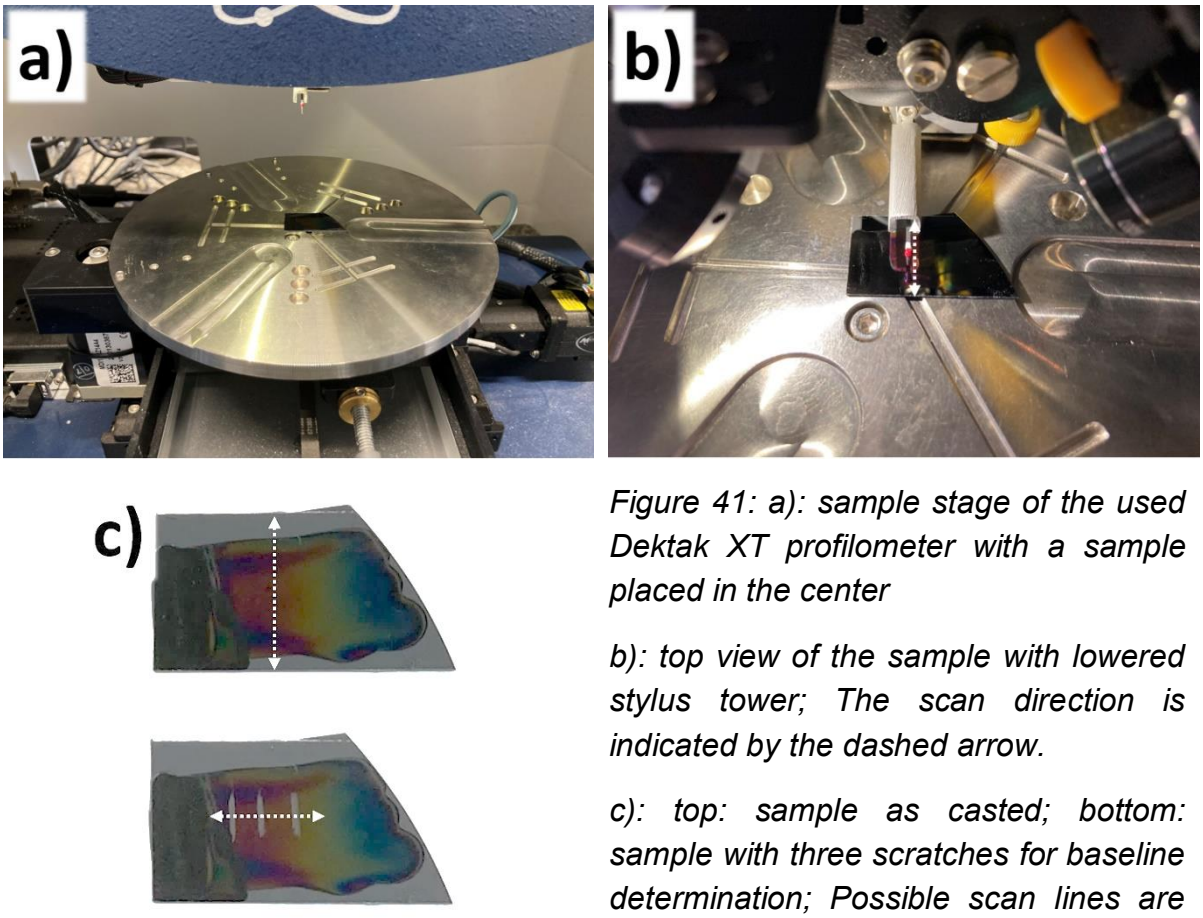

Figure 41: a): sample stage of the used Dektak XT profilometer with a sample placed in the center

b): top view of the sample with lowered stylus tower; The scan direction is indicated by the dashed arrow.

c): top: sample as casted; bottom: sample with three scratches for baseline determination; Possible scan lines are indicated with dashed arrows.

For a measurement, a sample is placed on the sample stage of the instrument according to the desired scan line (see Figure 41b).

4.2 Setup for QENS experiments

QENS is performed at the cold neutron time-of-flight chopper spectrometer TOFTOF (MLZ) to investigate molecular dynamics of the samples on molecular level. Drop casted PTB7 or PTB7:PCBM films on aluminum foil turned out to be a feasible method to get enough material into the neutron beam if eight coated foils are stacked on top of each other. Thus, a flat sample cell is used. This is attached to a stick equipped with a heating element and a temperature sensor to monitor the actual temperature at the sample position (Figure 42a). This stick is inserted into the cryostat installed in the TOFTOF sample chamber and its length is adjusted to position the sample on the exact height of the neutron beam. The use of both, heating element at

the sample stick and a cryostat, enables measurements in a large temperature range without the need to change the sample environment.

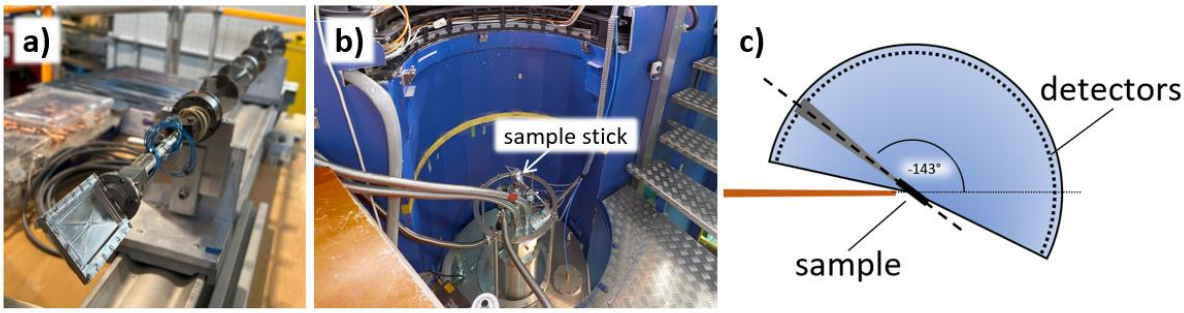

Figure 42: a) Sample stick with temperature sensor, heating element and sample cell installed at its bottom end (bottom left), b) image of the cryostat installed in the TOFTOF sample chamber with the sample stick inserted into the central channel; c) top-view sketch to illustrate the used orientation of the flat sample cell and the resulting absorption-shadow on the detectors. Images taken by Marcell Wolf.

The sample is oriented to yield an angle of ~37 ° between the neutron beam and the sample surface by tilting the stick (see Figure 42c). This orientation is chosen to prevent multiple scattering and self-absorption of neutrons by the extended sample and the container towards the very efficient low-scattering-angle range of the TOFTOF detectors, since most neutrons are scattered with small angles. The position of the sample mounted at the bottom of the sample stick, inserted into the cryostat is shown in Figure 42b.

4.3 Setup for XRD

The microstructure, especially the stacking properties of the conjugated system of PTB7, is investigated with XRD. A D8 Advance lab diffractometer (Bruker, USA) was used. The placement of the sample in the center of the Θ-2Θ geometry, characterized by the symmetrically moving arms of X-ray source and detector, is shown in Figure 43a.

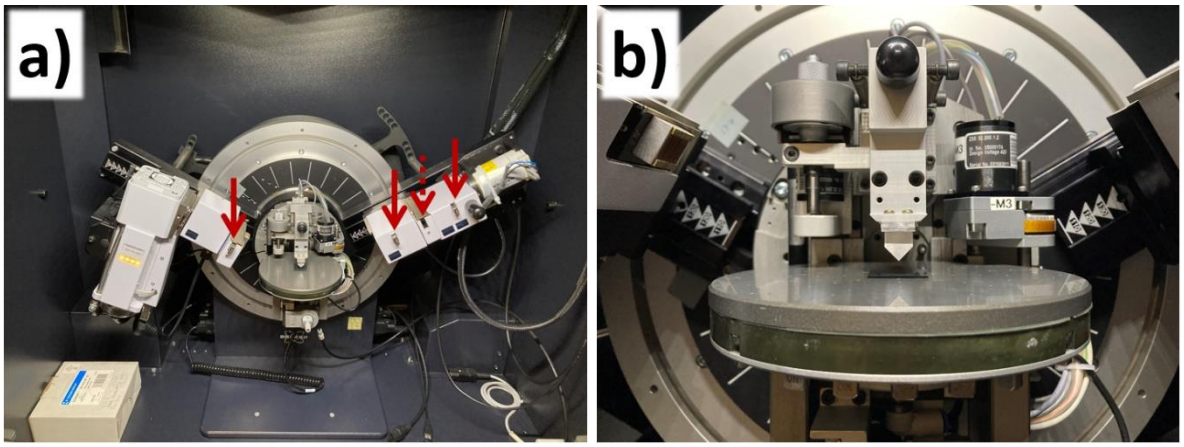

Figure 43: a) Overview image of the used D8 Advance diffractometer X-ray source arm on the left and detector arm on the right; Slots for absorber/slit modules are indicated with red arrows (dashed ≙ unoccupied). b) Close view of the sample position under the knife edge. On the top left, the exit of the Soller slit is visible.

The slots in the X-ray beam path, visible in Figure 43a can be used for absorbers and slits to attenuate or shape the beam. At the end of the X-ray source arm, a Soller slit is installed to reduce beam divergence and improve data quality (Figure 43b). Figure 43b shows the knife edge of the instrument above the center of the sample. It can be lowered in order to reduce the X-ray footprint on the sample, especially at small angles.

4.4 Setup for UV-vis

For the determination of the specific spectral absorbance of a sample, UV-vis spectroscopy is used. In the used Lambda 35 (Perkin Elmer, USA) spectrometer, the spectrum of a white light source is spread out and the wavelength is selected by a slit. Wavelength range and scan speed can be set to the desired values. The sample and the reference sample are illuminated and the transmission is measured. Subsequently sample transmission and absorbance data are calculated. The placement of the actual and the reference sample is shown in Figure 44a.

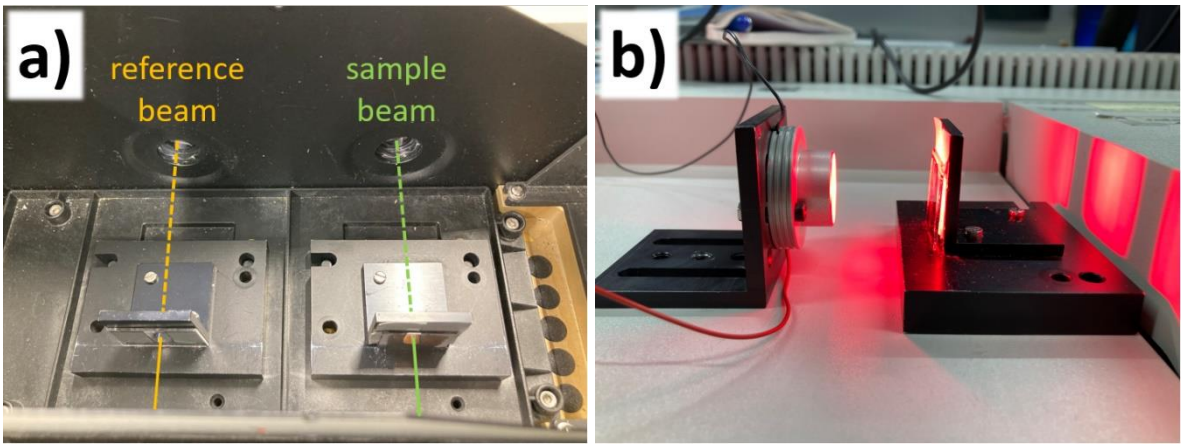

Figure 44: a) Sample chamber of the used Lambda 35 UV-vis spectrometer with reference (left) and actual (right) sample. The light paths are indicated accordingly. b) Setup for illuminating the samples between UV-vis measurements; For better visibility of the setup, the image is taken with ambient light on, the actual illumination experiments were performed without external light sources.

Since the method of UV-vis does not allow for additional light inside the sample chamber, the illumination for the experiments, presented in Chapter 7 are performed *ex situ*. Therefore, the sample is taken out of the instrument and placed in front of the LED light source for the respective time. This is performed in a light shielded cage in close vicinity to the UV-vis spectrometer to avoid further influences as far as possible. After the illumination, the sample is installed back into the spectrometer in the identical (as good as possible) position and measured again. The illumination setup and position on top of the closed UV-vis spectrometer is shown in Figure 44b.

4.6 Setup for FTIR & *in situ* FTIR spectroscopy

Fourier-transform-infrared (FTIR) measurements are performed on an Equinox 55 lab spectrometer (Bruker, USA). Different than for UV-vis, the reference sample (bare substrate) is measured before the actual sample. A triglycerine sulfate detector is used and the spectra are collected at room temperature by summing up 125 scans with a resolution of 2 cm^{-1}. For static FTIR measurements, the sample is attached to the circular frame of the sample holder with sticky tape and aligned perpendicular to the instrument reference laser and the probe light path in the respective height. This regular configuration is shown in Figure 45a.

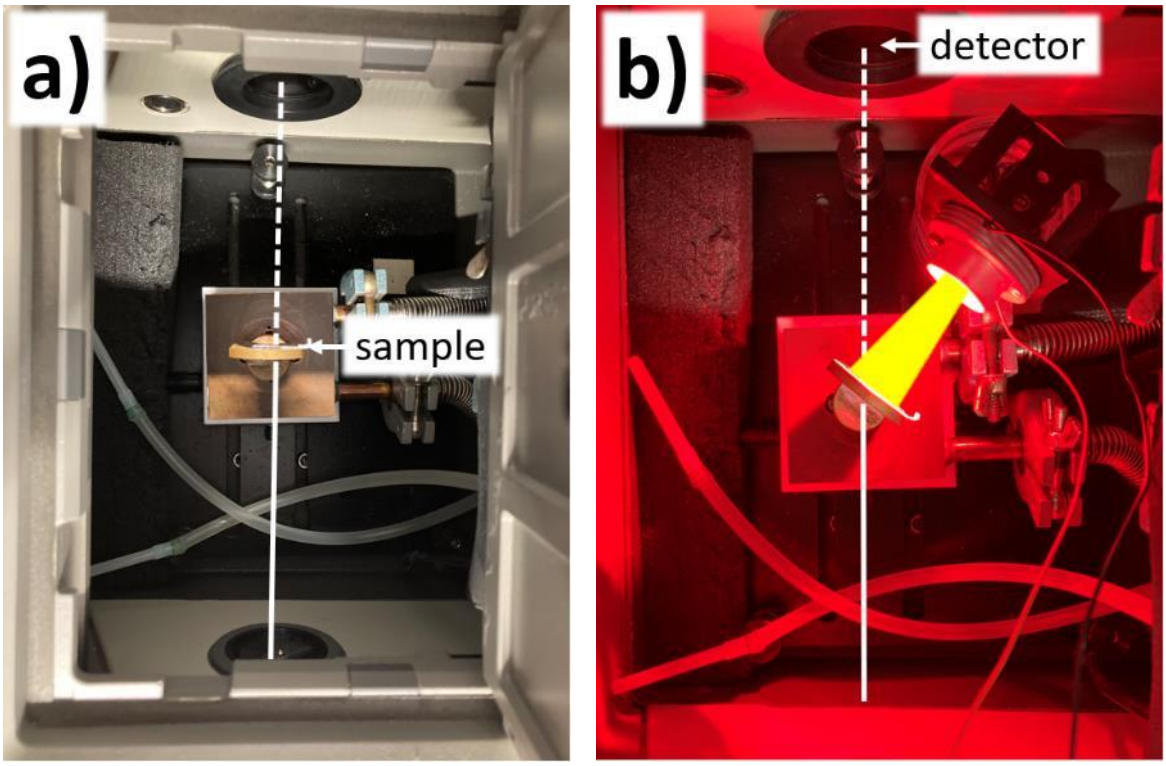

Figure 45: Top view of the open sample chamber of the used Equinox 55 FTIR spectrometer with the IR probe beam path indicated in white; a) Regular configuration with the sample surface perpendicular to the IR beam; b) In situ FTIR configuration under illumination with a LED light source inside the sample chamber and the sample tilted to yield an angle of 90 ° against the LED light

For *in situ* FTIR measurement during LED illumination, the setup is slightly modified as visible in Figure 45b. The LED module is mounted on a holder that can be placed inside the instrument on the same central height as the sample in the distance that is calculated to give the correct light intensity (see Chapter 7.2). The sample is tilted towards the light source (substrate perpendicular to incident light) to keep the irradiation intensity comparable to *ex situ* illumination experiments. The reference sample is measured in the same orientation as the loaded sample. Figure 45b shows that the light of the LED is directed away from the detector of the FTIR spectrometer, thus the measurement is expected not to be influenced.

4.5 Setup for Raman & *in situ* Raman spectroscopy

The Raman measurements for this thesis are performed with a modular, fiber-based system, particularly designed for the application at the TOFTOF neutron spectrometer to allow for the unique possibility of simultaneous QENS and Raman measurement. The system consists of several individual components like laser control, laser module, spectrometer, CCD detector, optical fibers and a superhead. The superhead combines, respectively deconvolves the light paths of incoming laser beam and scattered Raman light and is shown in Figure 46.

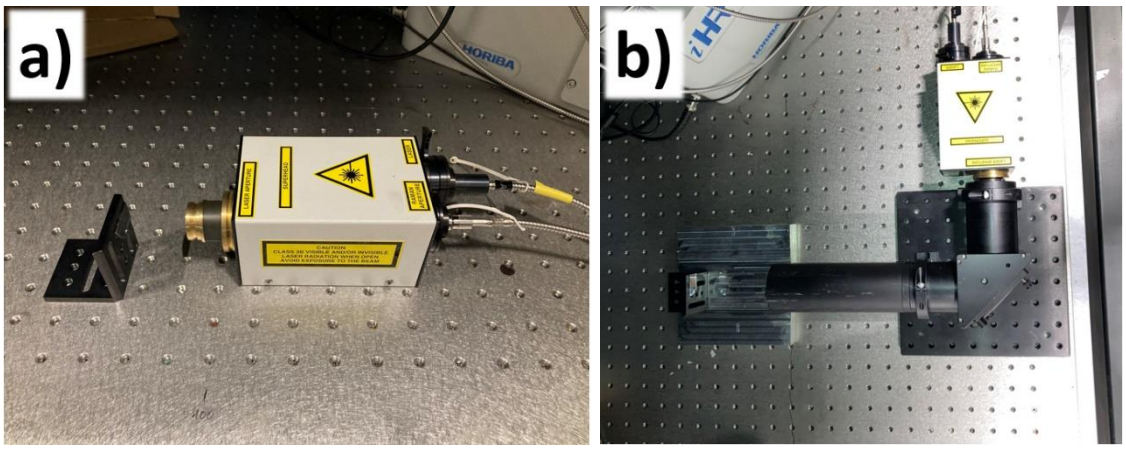

Figure 46: Laboratory setup of the used modular Raman system a) without and b) with the optical system that is needed for the application at the TOFTOF instrument.

For measurements outside the TOFTOF instrument, the sample is placed at a distance of ~4 cm from the front lens of the superhead, in the focus point of the convergent laser beam (Figure 46a). The scattered light is caught by the front lens of the superhead and transferred to the spectrometer by an optical fiber.

The black mounting plate, as shown in Figure 46b facilitates the use of the Raman spectrometer inside the sample chamber of TOFTOF. Instead of a simple convex lens, a custom-made optical system is installed in front of the superhead (see Figure 46b). This system is specifically designed for the application at the TOFTOF instrument. It can be mounted at the top of the sample chamber to direct the focus of the superhead

exit lens to the sample position (for QENS measurements). The working distance (from the last lens) of the optical system is ~11 cm. The application of the Raman system in the TOFTOF sample chamber offers the possibility to use the TOFTOF sample environment like the chi-phi-xyz sample stage and temperature control. For the *in situ* measurements described in Chapter 7, the Raman laser is continuously running while directed on the same spot and the scattered light is detected right after the respective illumination times.

5 Molecular dynamics of PTB7:PCBM blend films

This chapter presents the investigation of molecular dynamics of PTB7 and a PTB7:PCBM (1:1 wt.) blend by means of quasielsatic neutron scattering (QENS). For the sake comparability of the studied films, also structural and optical properties are studied by X-ray diffraction and UV-vis spectroscopy, respectively.

The results shown in the this chapter are published in the article “Investigation of Molecular Dynamics of a PTB7:PCBM Polymer Blend with Quasielastic Neutron Scattering” (Schwaiger et al. ACS Applied Polymer Materials, 2020, DOI: 10.1021/acsapm.0c00455).[26] Reproduced with permission of ACS publishing, copyright 2023.

5.1 Introduction

As explained in Chapter 1, the field of organic photovoltaics has shown great potential to contribute to the satisfaction of the world´s increasing energy demand. The consecutively increasing scientific effort generated a large number of available material systems. In the field, the two model systems for OSC active layers are the combination of P3HT and $PC_{60}BM$, succeeded by PTB7 and $PC_{70}BM$, both arranged in bulk heterojunction structures. The latter replaced the former due to the fact that a low band gap polymer is used, which fits the available solar spectrum better and thus facilitates higher power conversion efficiencies. While a large number of reports on electrical and structural properties in these systems are available, the quantity is very limited when it comes to the investigation of dynamics. For P3HT some QENS data was published,[213], [214], [215] whereas in the system PTB7:PCBM, the study presented here,[26] marks the first application of QENS. This work, i.e. the application of time-of-flight QENS on PTB7:PCBM blend films and the consecutive data analysis, is summarized in the following section.

The combination of the electron donor polymer PTB7 and the electron acceptor fullerene molecule PCBM has evolved to the big model system in the field of low band gap polymer:fullerene organic solar cells. The maximum power conversion efficiency is reported with almost 10 %[216] and the system is extensively described in terms of structure, morphology, electrical and photovoltaic aspects.[75], [76], [217], [218], [219], [220], [221] Nonetheless, polymer side chain dynamics do critically influence important properties for the application in organic solar cells. This has been shown for the system P3HT:PCBM, e.g. in terms of crystallization properties, AC switching behavior and electrical conductivity.[222], [223] Beyond this, also degradation susceptibility, drying kinetics and the resulting film formation is influenced by the material´s internal dynamics. Mayor loss mechanisms like recombination and charge trapping happen on a femtosecond to nanosecond timescale, which coincides with the timescale that is studied in this thesis.[218], [224], [225]

Regarding the high number of studies that have been published for PTB7 and PTB7-Th based organic solar cells with fullerenes such as PCBM as electron acceptor, this is the established model system for low band gap polymer photovoltaics. The big majority of studies are directed towards structural aspects and the characterization of solar cell performance.[75], [76], [217], [218], [219], [220], [221] On the other hand, internal dynamics on the molecular level have not been considered before, even though they play an important role for electrical properties, film formation and stability. No sophisticated data about molecular dynamics of PTB7 and the effect of the addition of PCBM in the blend system were available. This knowledge gap is targeted by the investigations presented in this and the following chapters. Both, diffusion coefficients and values for mean square displacements are calculated and activation energies for the respective processes are compared. The focus is on the realization of the QENS experiment and data analysis, which is performed in a similar way for this and the following chapter.

5.2 Data analysis & transformation of S($\vec{Q}$, ω) to I($\vec{Q}$, t)

Three samples were prepared in a QENS suitable film format: pure PCBM, pure PTB7 and a PTB7:PCBM blend with a weight ratio of 1:1. As described in Chapter 3.1, these samples were drop cast on aluminum substrates and stacked to reach total film thicknesses of around 100 µm (PTB7), 180 µm (blend) and 330 µm (PCBM). Because the obtained films are around one order of magnitude thicker than films that are commonly used in functioning organic solar cells and drop casting is not a very common production method, the fundamental structural and optical properties were investigated prior to the QENS experiments.

For this preliminary characterization of drop cast films with X-ray diffraction and UV-visible absorption spectroscopy, reference samples were prepared by the same method on silicon and glass substrates, respectively (see Chapter 3).

Structural aspects studied with X-ray diffraction

To study the stacking structure of the investigated samples, X-ray diffraction (XRD) experiments were performed. Primary aim of this investigation was the comparison of PTB7 and PTB7:PCBM blend films produced with drop casting with results from literature for thinner films, which were actually used in working solar cells. The corresponding X-ray diffractograms for PCBM, PTB7 and the PTB7:PCBM (1:1 wt.) blend are shown in Figure 47.

The pure PTB7 film (Figure 47b) shows only one prominent feature. The broad peak with center at 22.8 ° originates from the π-π stacking of the polymer backbone and corresponds to a stacking distance of 3.9 Å. For the blend sample, this peak shifts to a lower 2 θ value of 19.6 °. This indicates an expansion of the PTB7 stacking distance to 4.5 Å upon 1:1 blending with PCBM. As the structure of the conjugated π-π system is essential for the semiconducting properties of the polymer, several reports on its structures are available, generally agreeing with the present findings.[229]

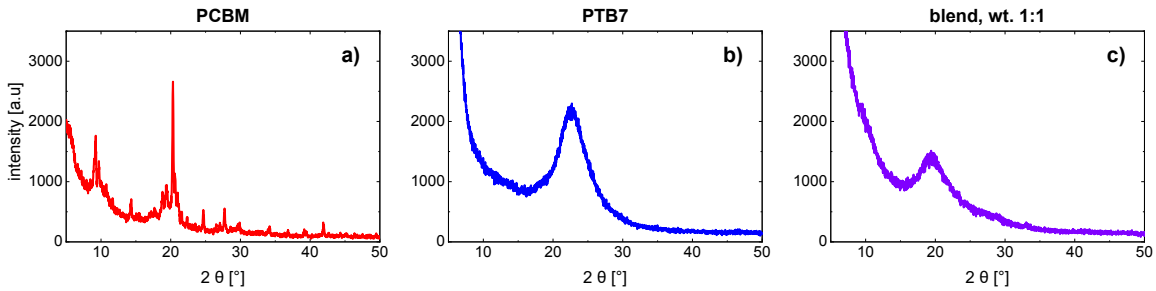

Figure 47: X-ray diffractograms of a) PCBM, b) PTB7 and c) the PTB7:PCBM (1:1 wt.) thin films in a 2 θ range from 5 ° to 50 °.

Figure 47a shows multiple sharp Bragg peaks for the PCBM sample. This indicates a well ordered lattice that is formed by the fullerene molecules, which is well known in literature.[226], [227], [228] The corresponding reflexes are found at 2 θ values of 9.2 °, 14.4 °, 18.8 °, 19.4 °, 20.3 °, 24.7 ° and 27.7 °.

The XRD investigation of the present films shows that the thicker drop cast films have similar structural features as the thinner counterparts, which are used in working solar cells produced with e.g. spin coating.

Optical properties

For comparison of the optical properties of the films that are produced by drop casting with thinner films, as typically used in working solar cells, UV-vis absorption spectroscopy was performed. The obtained UV-vis absorbance spectra are shown in Figure 48.

PCBM (red curve in Figure 48) does not show any prominent absorbance features in the covered wavelength range. Only a slight increase of the absorbance towards smaller wavelengths can be observed. The pure PTB7 (blue curve) and the blend sample (violet curve), in contrast, show distinct absorption maxima between 550 nm and 750 nm. This indicates the existence of electronic transitions in the polymer, that can be activated by light of the respective energies. It is evident that the two characteristic absorption peaks of PTB7 at 622 nm and 670 nm, respectively, are shifted by approximately 10 nm towards larger wavelengths if it is blended with PCBM.

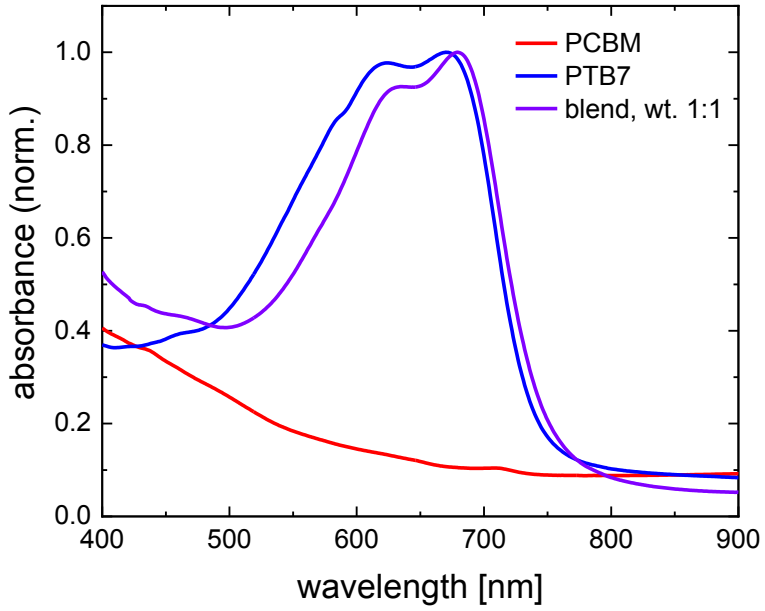

Figure 48: Optical absorbance spectra of the three samples PCBM (red), PTB7 (blue) and the 1:1 wt. blend (violet) in the wavelength range between 400 nm and 900 nm. Data was normalized to the highest-wavelength peak (if present).

These findings are in line with previously published results.[227], [229], [230] Optical band gaps of the sample films have been determined with the Tauc plot method, as described in Chapter 2.2.2. The results of around 2.0 eV for PCBM and 1.7 eV for PTB7 are also in good agreement with literature values.[84], [231] This enhances the validity of the QENS results, as films, prepared with the present casting method can reproduce literature findings for organic solar cell layers.

Neutron scattering at TOFTOF

The investigation of molecular dynamics in this thesis was performed with the use of quasielastic neutron scattering (QENS). Experiments were conducted at the direct geometry, cold neutron time-of-flight (TOF) chopper spectrometer TOFTOF (FRM II, Garching, Germany), which is described in Chapter 2.2.6. An energy resolution of the elastic line of approximately 20 μeV was achieved by the use of neutrons with a wavelength of 8 Å and a chopper rotation frequency of 14,000 rpm. According to the instrument characteristics a chopper ratio of 6 was applied in order to avoid frame overlap of consecutive pulses. The accessible $\vec{Q}$-range was 0.05 $Å^{-1}$ – 1.35 $Å^{-1}$. Measurable energy transfers ranged from -5 meV (energy gain of the neutron) to 0.75 meV (energy loss of the neutron). More detailed information about the setup and the

conduction of the experiments can be found in Chapters 3.2 and 4.2. QENS experiments were conducted at different temperatures (10 K, 240 K, 280 K, 200 K, 320 K and 400 K for the pure PCBM sample; 3 K, 150 K, 200 K, 250 K, 300 K, 350 K and 400 K for PTB7 and blend samples) and the obtained data was treated and analyzed with the Mantid software package.[232], [233] The following section describes the data handling and the evaluation to calculate values for diffusion coefficients and mean square displacements, respectively.

Because it is not possible to directly measure the scattering function S($\vec{Q}$, ω) with a neutron time-of-flight spectrometer for samples that need to be contained during the experiment, several corrections and data treatment steps are needed.

First of all, the total scattering intensity (as measured by the detectors) is generally normalized by the incident neutron flux, which is measured with a uranium fission neutron monitor in front of the sample position.

Every detected neutron at the spectrometer TOFTOF gets allocated a certain time-of-flight (TOF) from the sample to the detector and a scattering angle. To obtain the scattering function S($\vec{Q}$, ω), several steps of data treatment, i.e. background correction, are needed.

First of all, a reference measurement of the used sample container without the actual sample is performed in order to subtract the scattering contribution of the materials that are in the beam but not of interest. Thus, for the present study a flat aluminum cell including 8 empty pieces of aluminum foil and all sealing material and bolts was measured before the “filled” systems. In addition, also self-absorption of both, the sample and the container can be taken into account to yield the corrected intensity, scattered by the sample itself:[183], [234], [235]

$$I_s = \frac{1}{f_{s;c+s}}\left[I_{c+s,meas} - I_{c,meas}\frac{f_{c;c+s}}{f_{c;c}}\right] \tag{83}$$

With the measured intensities $I_{c+s,meas}$ (for sample inside the container) and $I_{c,meas}$ (for the empty cell reference) and the self-absorption coefficients $f_{s;c+s}$ (self-absorption of the sample when measured in the container), $f_{c;c+s}$ (self-absorption of the container

in the measurement with sample) and $f_{c;c}$ (self-absorption of the container in the empty cell reference measurement).

For the conversion of the time-of-flight into energy transfer $\hbar\omega$, a measurement of a vanadium sample of the same size and orientation as the sample is used. Vanadium is a purely elastic, incoherent scatterer and thus the arrival time of elastically scattered neutrons and their respective time-of-flight can be measured for each detector. If a neutron from a certain pulse is detected within an earlier or later time channel than found by the vanadium measurement, its energy transfer due to the scattering process is calculated on basis of the measured time difference, the travel pathlength and the incident neutron velocity.

The same measurement is used for the calibration of the detector efficiency due to the purely incoherent scattering properties of vanadium (neutron scattering cross sections of V can be found in Table 3 in Chapter 2.2.6). Purely incoherent scattering implies that the scattering is isotropic in all direction. The sample signal is thus normalized to the measured vanadium intensity. At the same time, detectors whose vanadium intensity deviates significantly from the average, e.g. due to defective detector electronics, can be identified and subsequently excluded from the analysis.

The inelastic momentum transfer vector $\vec{Q}$ (see Chapter 2.2.6) for each detected neutron is calculated from the energy transfer and the scattering angle, which is assigned to the detector where the respective neutron was detected.

For the graphical presentation and further analysis of S($\vec{Q}$, ω), the obtained data set that is defined by energy transfer $\hbar\omega$ on one and momentum transfer $\vec{Q}$ on the other axis has to be binned into regular fields of $\Delta\hbar\omega$ and ΔQ. The binning intervals can be chosen freely and are typically influenced by several factors like counting statistics, computing/data handling power or desired energy and momentum transfer resolution.

Neutron diffractogram

In the case of highly ordered crystalline or semicrystalline systems, the neutron scattering pattern of the sample may show Bragg peaks, which are formed by coherent scattering. Since the evaluation of QENS data in view of diffusive dynamics of the scatterers is based on incoherent scattering, $\vec{Q}$-regions with a high fraction of coherent scattering intensity can impair the validity of the result. Thus, it may be necessary to to identify the incoherent part of the scattering intensity in these areas or entirely exclude them from the analysis. Figure 49 shows the neutron diffractograms for the three samples. The shown data is restricted to scattered neutron intensity which falls into a window from -30 µeV to 30 µeV around the elastic line in order to be able to identify Bragg peaks. A wider integration window would lead to a strong broadening of the peaks due to the additional momentum transfer caused by the exchange of energy. In contrast to Figure 47 the intensity is plotted against momentum transfer and not against the scattering angle directly.

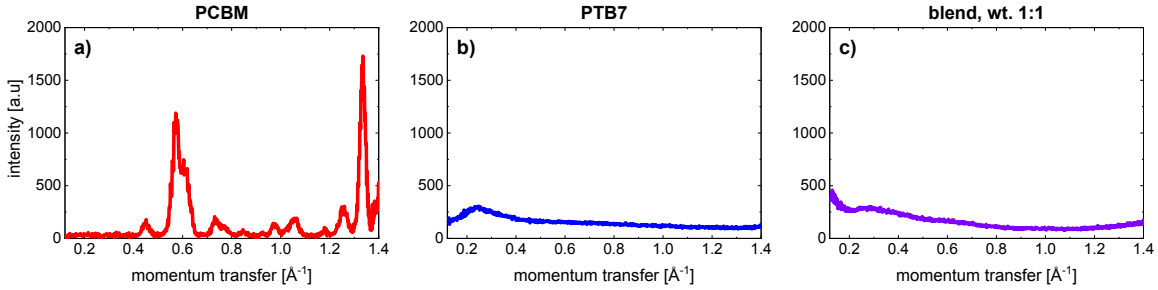

Figure 49: Neutron diffractograms in a momentum transfer range between 0.12 Å^{-1} and 1.4 Å^{-1} for a) pure PCBM, b) pure PTB7 and c) the 1:1 (wt.) blend of the two. The data is acquired at 300 K and integrated around the elastic line from -30 µeV to 30 µeV.

Figure 49a shows several rather sharp peaks for the pure PCBM sample, indicating a high degree of crystallinity in the structure. The intensity is concentrated in these Bragg peaks, which have their origin in coherent scattering. This coherent intensity comes on the cost of a low fraction of incoherent scattering for the PCBM sample, which is also calculated from the respective cross section in Chapter 3.2. This may be problematic for the evaluation of QENS data in respect of individual atom dynamics. Figure 49b and c yield a very different distribution of the measured intensity. Except one broad peak in the low $\vec{Q}$ region, which is discussed in the next chapter in more

detail, the intensity is more evenly distributed over the entire momentum transfer range. This can be caused by a high fraction of incoherent intensity, which would be very much desired for the evaluation of QENS data or by a general structural disorder. Some of the very intense Bragg peaks of pure PCBM, i. e. at around 0.6 $Å^{-1}$ and 1.35 $Å^{-1}$ can be found in the blend diffractogram as slight intensity increases compared to the pure PTB7 sample. This observation and the indication of a small angle tail below 0.2 $Å^{-1}$ reveal the presence of small pure PCBM domains within the PTB7 matrix, which has a characteristic stacking structure itself, described by the broad peak at approximately 0.25 $Å^{-1}$. Because TOFTOF is not a neutron diffractometer and the shown data is biased with different kinds of instrumental influence, also X-ray diffraction (XRD) experiments were performed in order to investigate the structure of the treated samples, as presented in the previous section.

QENS: S($\vec{Q}$, ω) spectra

In this section, the results from QENS measurements at the TOFTOF spectrometer of the three samples pure PCBM, pure PTB7 and the 1:1 wt. blend of the former are presented in the form of the dynamic structure factor S($\vec{Q}$, ω).

In order to determine the temperature where the structures become flexible and diffusive dynamics set in, a fast “pseudo”-fixed ΔE scan was performed from the deepest accessible temperature (3 K) up to 400 K. S($\vec{Q}$, ω) was integrated over the large momentum transfer range between 0.3 $Å^{-1}$ to 1.3 $Å^{-1}$ and the elastic ($|\Delta E| < 20$ μeV) and quasielastic (20 μeV < $|\Delta E|$ < 100 μeV) intensity was calculated. The respective areas are illustrated in Figure 50. The green area stands for the quasielastic intensity, whereas blue indicates the intensity that is considered elastic in this analysis.

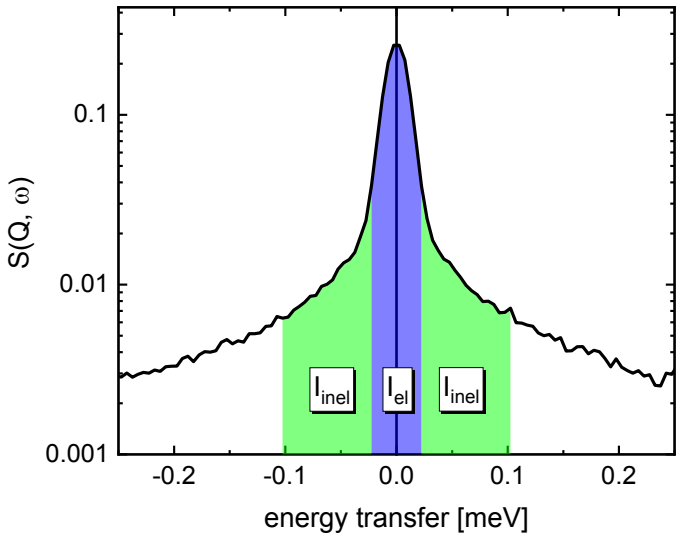

Figure 50: Generic $S(\vec{Q}, \omega)$ spectrum for the explanation of the intensities used for the "pseudo"-fixed ΔE scan. Elastic intensity (|ΔE|< 20 μeV) is indicated by the blue and quasielastic intensity (20 μeV <|ΔE|< 100 μeV) by the green area.

Results from this scan are presented in Figure 51 for pure PTB7 (red) and the PTB7:PCBM (1:1 wt.) blend sample (blue).

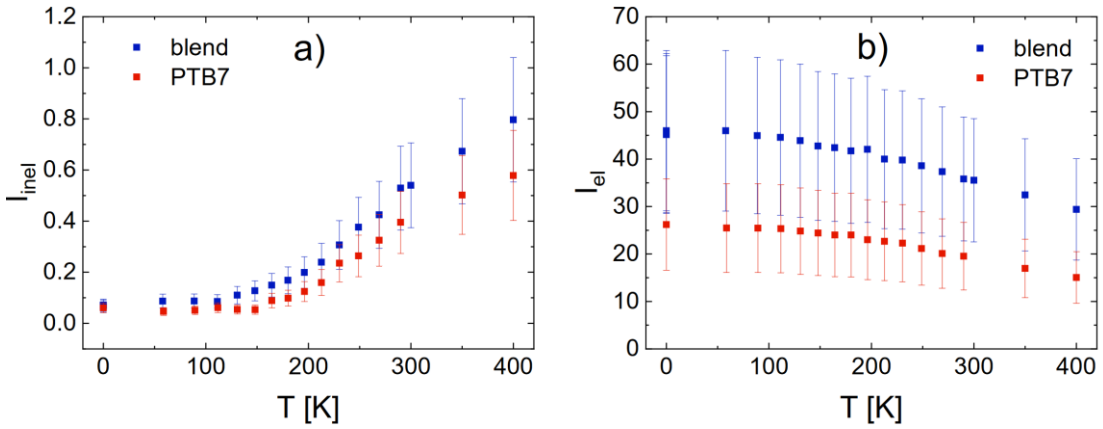

Figure 51: Fast fixed ΔE scan with the pure PTB7 sample (red) and the blend sample (blue). The quasielastic intensity plotted in a) covers an energy transfer range from ±20 μeV up to ±100 μeV, whereas the elastic intensity plotted in b) is defined by |ΔE| < 20 μeV. Each measurement took 10 minutes while constantly heating with a rate of 2 K/min. Datapoints are plotted at the average temperature of the respective time interval. Scales are given in arbitrary units. Figure reproduced from [26] (supporting information) with permission from ACS Publications.

The quasielastic intensity, which is shown in Figure 51a, is very low for both samples at temperatures below 150 K and then increases gradually towards higher temperatures. The elastic intensity, on the other hand, significantly decreases towards higher temperatures, also showing a change of the slope between 150 K and 200 K. Based on this finding the measurement temperatures were determined to be 3 K, 150 K, 200 K, 250 K, 300 K, 350 K and 400 K. This includes a reference measurement at low temperature (3 K) where all motions are considered to be entirely frozen, which is used as resolution function to correct for instrumental parameters. With this protocol, one can follow the temperature dependence of the hydrogen motions in the polymer side chains. It is interesting to see that the blend sample shows the onset of quasielastic intensity at slightly lower temperatures, compared to the pure PTB7 sample. The absolute measured intensity of both, elastic and quasielastic scattering is generally higher for the blend sample. Since data have not been normalized to sample mass, this indicates that the blend sample might have been slightly thicker or at least had more material within the neutron beam.

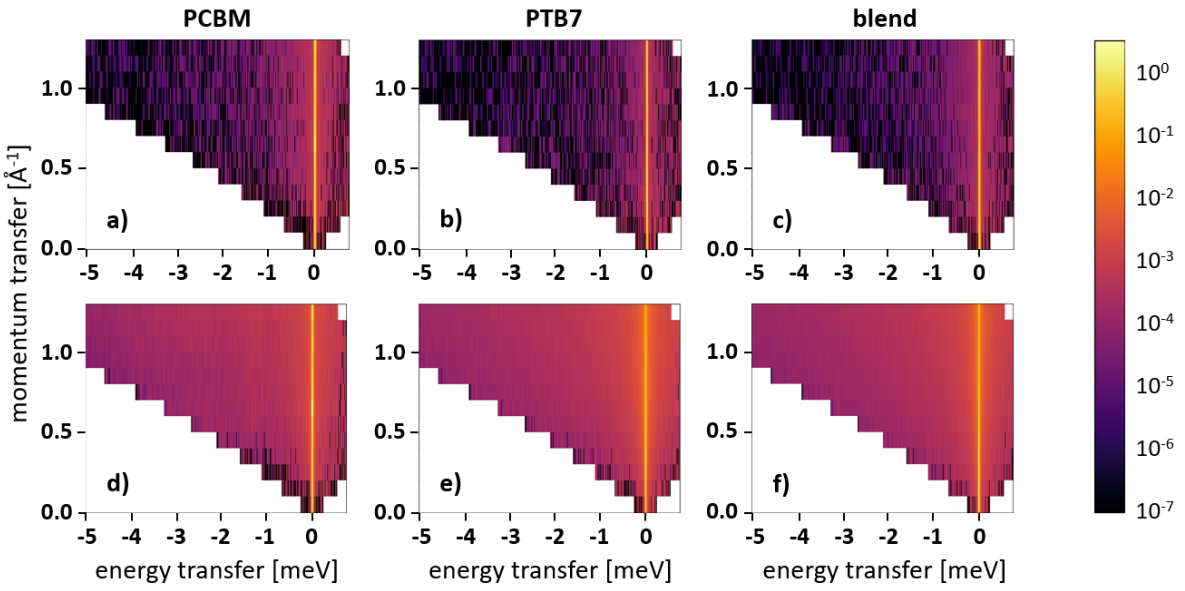

Figure 52: Dynamic range plot of the TOFTOF QENS measurement of the three samples PCBM (a & d), PTB7 (b & e) and the 1:1 wt. blend of the two (c & d). The top row (a – c) shows QENS data, acquired at low temperature (<10 K), whereas the bottom row (d – f) represents high temperature measurements (400 K). The binning intervals are 0.1 Å^{-1} for the momentum transfer and 0.005 meV for the energy transfer. Colors indicate the scattering intensity according to the scale on the right.

Figure 52 shows the full dynamic range plot S($\vec{Q}$, ω). On the y-axis the $\vec{Q}$-value and on the x-axis the measured energy transfer is plotted. While the scattering intensity is indicated by a color code (black stands for low intensity, bright yellow for high intensity), the energy transfer increases laterally towards both sides, starting from the elastic line, which is characterized by the highest intensity. All data are binned in boxes of certain *ΔE* and $\vec{Q}$ sizes. Due to the present experimental count rates, a window of 0.1 Å^{-1} and 0.005 meV width is chosen for the initial data binning. From bottom to top increasing $\vec{Q}$-values are shown with the visible step height corresponding to the binning interval in $\vec{Q}$-space. In Figure 52, the low temperature measurements in the top row show significantly lower total scattering intensity outside the elastic line than the corresponding high temperature measurements in the bottom row. Nonetheless, the different samples do not show large visible qualitative differences among each other. Between the pure PCBM and the other two samples, a slight difference is evident, namely a lower quasielastic intensity for the PCBM sample compared to the other two. Between the different temperatures, though, clear differences are visible. While at 400 K (bottom row) a smooth intensity distribution in the quasielastic region is present for all samples, the intensity in this region is much lower at temperatures <10 K (top row).

For an evaluation of the dynamic structure factor S($\vec{Q}$, ω), cuts are made along specific $\vec{Q}$-values of the dynamic range plots as depicted in Figure 52. The resulting S($\vec{Q}$, ω) spectra are displayed in Figure 53 and show the intensity distribution with respect to energy transfer along certain $\vec{Q}$-values. All datasets shown in Figure 53 represent measurements at a temperature of 400 K. Figure 53a shows data for the pure PCBM, Figure 53b for the pure PTB7 and Figure 53c for the 1:1 blend sample. The individual curves represent different $\vec{Q}$-values of the scattered neutrons. Low $\vec{Q}$-values are shown in bright yellow and darker colors (up to dark blue) indicate increasing momentum transfer. Figure 53 b and Figure 53c look qualitatively rather similar and show a clear increase in quasielastic broadening with increasing $\vec{Q}$-value, on the cost of the intensity of the elastic line. This indicates the presence of diffusive hydrogen dynamics that occur within the observable time/energy window of the applied instrument setup. In contrast, Figure 53a shows practically no broadening around the elastic line for the pure PCBM sample at any momentum transfer. This indicates that there are no diffusive hydrogen motions on the observable timescale.

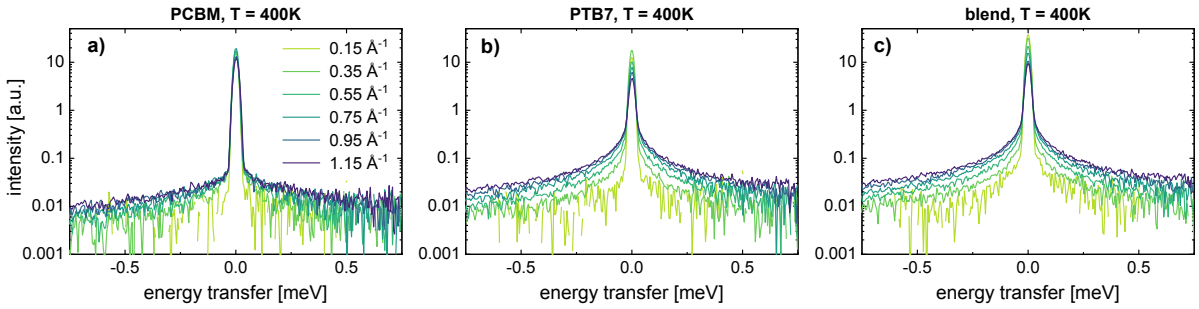

Figure 53: Dynamic structure factor S($\vec{Q}$, ω) in dependence of $\vec{Q}$-value for a) pure PCBM, b) pure PTB7 and c) the 1:1 wt. blend of the two. For all spectra the temperature is 400 K. The binning in momentum space includes 0.1 Å^{-1} around (0.05 Å^{-1} below and 0.05 Å^{-1} above) the central value that is given in the legend. Figure adapted from [26].

Figure 54 compares S($\vec{Q}$, ω) spectra at a constant $\vec{Q}$-value for different temperatures. All shown data is binned between 1.0 Å^{-1} and 1.1 Å^{-1}, which results in an average momentum transfer of 1.05 Å^{-1}. This $\vec{Q}$-value is chosen due to two reasons:

- The relatively large momentum transfer allows to observe distinct quasielastic broadening of S($\vec{Q}$, ω).
- Increased coherent scattering, which may impair the picture, due to PCBM crystal reflections is found at values around 0.65 Å^{-1} as well as 1.35 Å^{-1} and is thus avoided by the present choice.

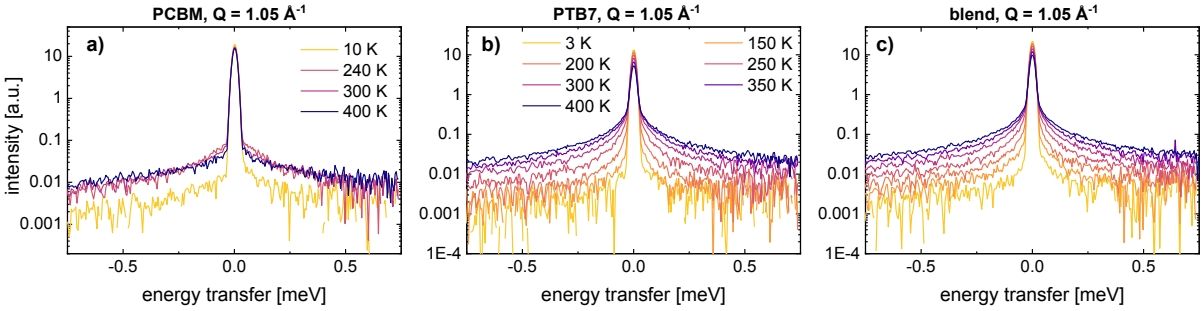

Figure 54: Dynamic structure factor S($\vec{Q}$, ω) in dependence of temperature for a) pure PCBM, b) pure PTB7 and c) the 1:1 wt. blend of the two. All spectra are taken at the momentum transfer range between 1.0 Å^{-1} and 1.1 Å^{-1}. Figure adapted from [26].

Also in Figure 54, PTB7 and the blend (b and c) show similar behavior, whereas the data for PCBM (a) looks clearly differently. With increasing temperature at fixed momentum transfer, no quasielastic increasing broadening is visible for PCBM, while PTB7 and the blend sample again show a distinct broadening. This behavior can be expected for diffusive motions because increasing temperature provides additional thermal energy to the system, which accelerates the diffusion. This, in turn, leads to the observed broadening of the measured QENS spectra with increasing temperature.

Even though Figure 53 and Figure 54 show distinct quasielastic broadening with both, increasing momentum transfer and temperature, for the pure PTB7 as well as the PTB7:PCBM blend sample, a consistent fit of all S($\vec{Q}$, ω) spectra with a reasonable number of Lorentzian functions was not possible. Single spectra could be fitted well, but it was not possible to apply the same fit to all spectra. Thus, the results of the Lorentzian fits to S($\vec{Q}$, ω) were not directly comparable among each other due to unequal fitting parameter that had to be used. A reason for this can be a great inhomogeneity of the diffusive motions. Due to the very different positions that the hydrogen atoms occupy on the polymer side chains, this might be the case for the present study. This effect has been observed frequently in polymers and many approaches exist to meet this problem.[236], [237], [238]

As described in Chapter 2.2.6, a transformation of S($\vec{Q}$, ω) spectra into the intermediate scattering function I($\vec{Q}$, t) is possible by a Fourier transform from frequency to time. The intermediate scattering function can be fitted with a stretched exponential approach to account for inhomogeneity of the observed motions according to a Kohlrausch-Williams-Watts (KWW) model.[189], [190], [191]

QENS: I($\vec{Q}$, t) spectra

Since a consistent fit of S($\vec{Q}$, ω) with discrete Lorentzian functions was not possible for the present data, the measured scattering function was transformed into the intermediate scattering function I($\vec{Q}$, t). This is done by a Fourier transform from frequency to time domain as explained in Chapter 2.2.6. The used energy transfer range for the transformation was from -100 µeV to 100 µeV. During the transformation procedure, which is done with the Mantid software, all spectra are normalized by the

corresponding low temperature measurement, thus theoretically all start with a value of 1 at t = 0.

Selected examples for the resulting I($\vec{Q}$, t) spectra are plotted in Figure 55 and Figure 56. All graphs therein show decaying functions, which describes the distribution of the density of diffusive states over the covered timescales. Stretched exponential fits according to the KWW model (Equation (68)) are shown as solid lines. Analogously to S($\vec{Q}$, ω) as shown in Figure 53, Figure 55 shows the intermediate scattering function for the three samples at different $\vec{Q}$-values at a fixed temperature of 400 K.

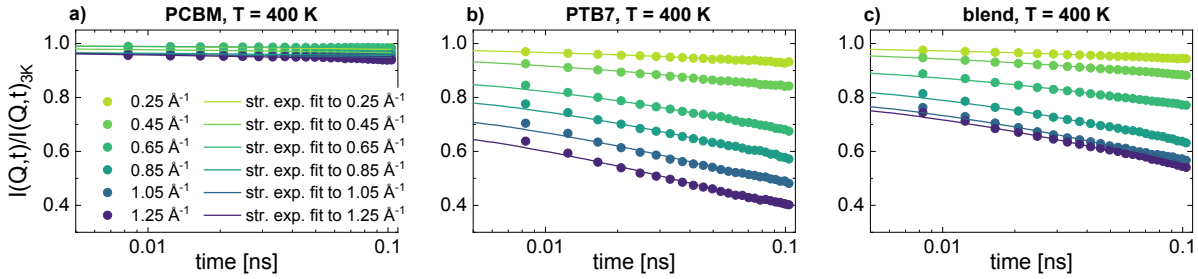

Figure 55: Symbols represent the intermediate scattering function I($\vec{Q}$, t) in dependence of $\vec{Q}$-value for a) pure PCBM, b) pure PTB7 and c) the 1:1 wt. blend of the two. All spectra were measured at 400 K. The binning in momentum space includes 0.1 Å^{-1} around (0.05 Å^{-1} below and 0.05 Å^{-1} above) the central value that is given in the legend. Solid lines are stretched exponential fits to the respective data. Figure adapted from [26].

Figure 55a shows the pure PCBM sample where generally no significant decay of I($\vec{Q}$, t) is evident. Nonetheless, measurements at higher momentum transfer yield slightly lower values of the intermediate scattering function. The decay of I($\vec{Q}$, t) for PTB7 is clearly visible in Figure 55b and becomes more distinct at increasing momentum transfer. This observation is equivalent to the quasielastic broadening of S($\vec{Q}$, ω) discussed before. Figure 55c shows the intermediate scattering function of the PTB7:PCBM blend sample which also yields a decay with increasing time. This decay is not as strong as for pure PTB7, though. This difference, which is much more evident than in the dynamic structure factor, indicates that the motion of the PTB7 side chains is partly obstructed when it is blended with PCBM. Especially the spectra taken at momentum transfers above 1.0 Å^{-1} show a significantly lower drop of I($\vec{Q}$, t) compared to lower momentum transfers. This indicates some sort of limitation of the observed motions on the corresponding length scale.

Figure 56 shows the intermediate scattering function at a fixed $\vec{Q}$-value of 1.05 Å^{-1} (binned from 1.0 Å^{-1} until 1.1 Å^{-1}) in dependence of temperature.

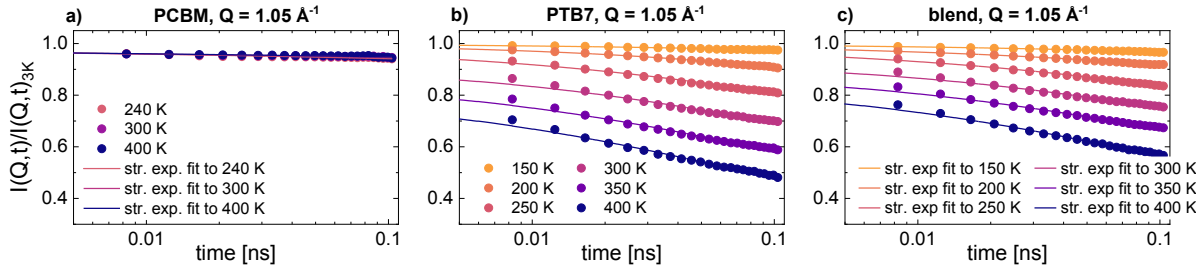

Figure 56: Symbols represent the intermediate scattering function I($\vec{Q}$, t) in dependence of temperature for a) pure PCBM, b) pure PTB7 and c) the 1:1 wt. blend of the two. All spectra are taken at the momentum transfer range between 1.0 Å^{-1} and 1.1 Å^{-1}. Solid lines are stretched exponential fits to the respective data. Due to different experimental protocols a) has its own legend and the legend of b) and c) is split and placed in both windows. Figure adapted from [26].

For pure PCBM (Figure 56a) no decay of the intermediate scattering function in the accessible timescale range is observed and temperature seems to have no influence on the signal. PTB7 (Figure 56b) shows an almost flat curve at 150 K followed by an increasingly pronounced decay of I($\vec{Q}$, t) at higher temperatures. Figure 56c shows a weak decay of I($\vec{Q}$, t) at 150 K for the blend sample, which confirms the slightly earlier onset of observable dynamics compared to pure PTB7 that was already suggested by the fixed *ΔE* scan. For increasing temperatures the decrease of I($\vec{Q}$, t) of the blend becomes more pronounced, which indicates faster polymer side chain dynamics, but is not as strong as for the pure PTB7 sample for all investigated temperatures exceeding 150 K.

Given the weak quasielastic broadening of S($\vec{Q}$, ω) (see Figure 53a & Figure 54a) and the low decay of I($\vec{Q}$, t) over the observable timescale (see Figure 55a & Figure 56a) for pure PCBM, the further evaluation of molecular dynamics is performed only for the PTB7 and the blend, but not for the pure PCBM sample.

Due to the energy resolution of TOFTOF with the applied settings of 20 μeV the trustworthy timescales of I($\vec{Q}$, t) range up to approximately 33 ps. Only data up to this value was used for the stretched exponential fits that are shown in Figure 55 and Figure

56 and used for the calculation of diffusion coefficients as presented in the following section.

5.3 Calculation of diffusion coefficients

For the pure PCBM sample the QENS data did not suggest any diffusive dynamics due to the lack of quasielastic broadening. The fits in Figure 56a give no rise to a relaxation process that occurs on the observable timescale. Hence, this section focusses on the comparison of the pure PTB7 and the PTB7:PCBM (1:1 wt.) blend film in terms of a calculated apparent diffusion coefficient for the polymer side chain motions.

For the determination of relaxation times, a stretched exponential fit according to a KWW model (see Chapter 2.2.6) was performed on the individual spectra of the intermediate scattering function at all measured temperatures (150 K, 200 K, 250 K, 300 K, 350 K and 400 K). For the fitting of I($\vec{Q}$, t), Equation (68) was used. It gives an effective relaxation time τ of the process and a stretching exponent β. β can take values between 0 and 1, depending on the heterogeneity of the observed motion. Starting from unity, which represents one discrete motion, a decreasing value of β indicates an increasing degree of dynamic disorder in the system. A free fit showed that a value of 0.66 describes the data best, independent of $\vec{Q}$-value and temperature, which is a common finding for QENS investigations of polymer samples.[239], [240] Thus, this value was used for all fits consistently. The fitted functions are plotted in Figure 55 and Figure 56 as solid lines.

Due to the inhomogeneity of the observed motions, the average relaxation time is given by Equation (70) with $\langle\tau\rangle$ the average relaxation time of the observed process. Results for $\langle\tau\rangle$ are shown in Figure 57 for both samples, PTB7 and the blend for three different exemplary temperatures, 200 K, 300 K and 400 K.

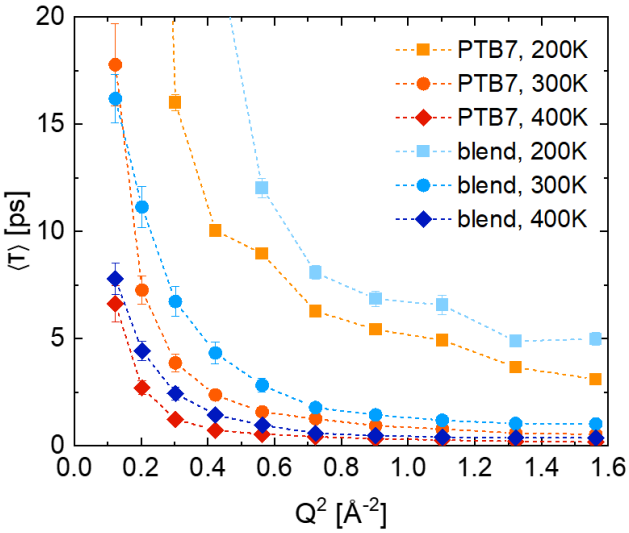

Figure 57: Calculated average relaxation times for PTB7 (red/orange) and the PTB7:PCBM (1:1 wt.) blend (blue)at three different temperatures: 200 K (squares), 300 K (circles) and 400 K (diamonds). Dashed lines are guides for the eye, only.

It is expected that the average relaxation times are higher for samples with slower dynamics. For both samples, this trend is found with decreasing temperatures. This indicates the thermal motion of the polymer side chains are the predominant mode within the experimental energy window. When comparing pure PTB7 and the blend sample, PTB7 shows significantly lower average relaxation times at all temperatures and all relevant $\vec{Q}$-values. The relevant $\vec{Q}$-range, which was used for the further analysis was defined from 0.3 Å^{-1} to 1.3 Å^{-1} because the instrumental resolution could not resolve the low-Q part and the counting statistics in the high-Q region were not sufficient for a reasonable evaluation.

$\langle\tau\rangle$ for the blend is higher by a factor of around 1.5 compared to pure PTB7 uniformly at 400 K and 300 K. Data measured at 200 K appears more noisy and does not follow the relatively smooth decay functions that are found at higher temperatures. Thus, the dynamics at 200 K seem to be very slow and on the edge if the resolution of the present experiment.

As mentioned in Chapter 2.2.6, the relaxation times, derived from I($\vec{Q}$, t), can be inverted in order to yield an analogous quantity as the HWHM of a Lorentzian in S($\vec{Q}$, ω), which can be evaluated by the chosen spatially restricted jump diffusion model, described by Equation (71).

The respective inverse average relaxation times at the three exemplary temperatures are plotted in Figure 58a for pure PTB7 and Figure 58b for the blend sample. The resulting fits of the diffusion model are indicated as solid lines.

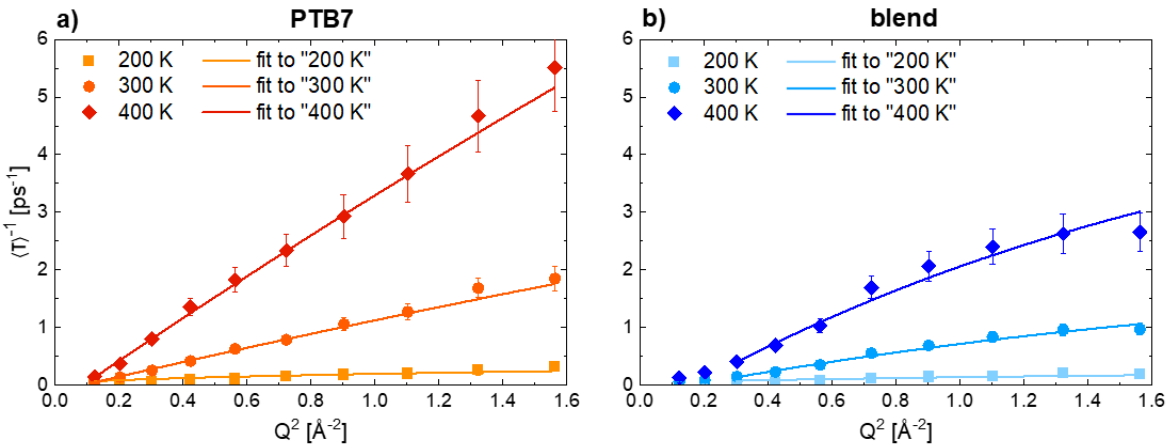

Figure 58: Inverse average relaxation times for PTB7 (a) and the PTB7:PCBM (1:1 wt.) blend (b) at three different temperatures: 200 K (squares), 300 K (circles) and 400 K (diamonds). The solid lines indicate according fits with the applied diffusion model.

The comparison between PTB7 and the blend shows higher absolute values of $\langle\tau\rangle^{-1}$ for pure PTB7 as already seen in the lower values of $\langle\tau\rangle$ in Figure 57. Beyond this, PTB7 shows a rather straight increase of $\langle\tau\rangle^{-1}$with Q^2, which is associated with free diffusion, but it flattens out towards high $\vec{Q}$-values for the blend especially at 400 K a plateau seems to form at $Q^2 > 1.3$ Å^{-2}. This is an indication for a spatial obstruction of the observed motion, which is the limiting factor especially in the case of high mobility, introduced by thermal energy. From the jump diffusion model that is shown in Figure 58 and defined by Equation (71), effective diffusion coefficients D_{eff} are calculated. They are shown in Figure 59. For both samples, the exact same diffusion model was used to determine D_{eff}.

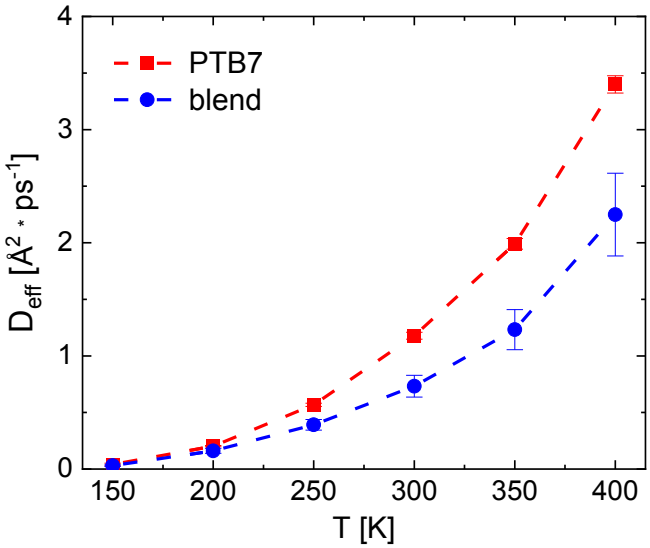

Figure 59: Effective diffusion coefficients for PTB7 (red squares) and the PTB7:PCBM (1:1 wt.) blend (blue circles) in the temperature range between 150 K and 400 K. Dashed lies are a guide to the eye, only. Figure reproduced from [26] with permission from ACS Publications.

The calculated effective diffusion coefficients at 150 K are very low for both samples and indistinguishable within the error margin due to the present resolution. At higher temperatures, the diffusion coefficients increase for both samples following an apparently exponential temperature dependence. The absolute values of D_{eff} are uniformly higher for PTB7 compared to the blend sample by a factor of approximately 1.5. All values that are plotted in Figure 59 are also given in Table 9. Their order of magnitute is comparable with values, which were measured by QENS in the similar system of P3HT:PCBM.[213], [214]

	D_{eff} (PTB7) [Å^{2}ps^{-1}]	D_{eff} (PTB7:PCBM) [Å^{2}ps^{-1}]
150 K	0.04 ± 0.01	0.03 ± 0.01
200 K	0.20 ± 0.01	0.16 ± 0.02
250 K	0.57 ± 0.01	0.39 ± 0.05
300 K	1.18 ± 0.03	0.73 ± 0.10
350 K	2.00 ± 0.05	1.23 ± 0.18
400 K	3.40 ± 0.08	2.25 ± 0.37

Table 9: Calculated effective diffusion coefficients for pure PTB7 ant the PTB7:PCBM (1:1 wt.) blend.

It is remarkable that the error for the fit of the diffusion model to the blend is significantly larger than for pure PTB7. This could be due to the presence of PCBM domains that do not contribute to the quasi-elastic incoherent scattering that is described by the model in the same way like pure PTB7.

5.4 Evaluation of the mean square displacement

For the studied structure of polymer and polymer:fullerene blend films not only jump diffusion of the polymer side chains, but also faster vibrational motions of the entire molecules, are expected. Thus, in the following part a mean square displacement $\langle u^2 \rangle$ is calculated by analyzing the elastic fraction of the QENS results.

To quantify the elastic contribution, S($\vec{Q}$, ω) spectra were fitted with two Lorentzians to roughly account for any quasi-elastic intensity and a delta function, which represents elastic scattering and scattering that falls inside the resolution function (*Res*) of the instrument. For the background correction, a linear function has been applied. The fitting function is given by Equation (84) and a graphical example for a respective fit is shown in Figure 60.

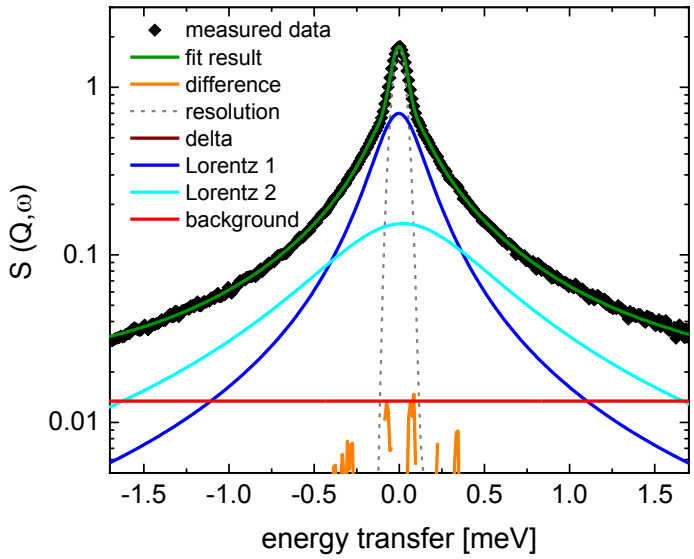

Figure 60: Schematic representation of the single components of the fit function (green curve). The data, shown as black symbols, is taken at another experiment. The components of the fit function (delta, Lorentz function, background) are shown as solid lines.

$$S(\vec{Q},\omega) = Res \otimes [D + L_1 + L_2] + bg \tag{84}$$

As mentioned above, the information provided by the Lorentzian functions as shown in Figure 60 was not used for the evaluation of diffusive dynamics because the use of $I(\vec{Q}, t)$ provided more stable fit results. The dependence of the extracted height of the delta function (I_{el}) from $\vec{Q}$ was fitted according to:

$$I_{el}(\vec{Q}) = I_0\, exp(-u^2\vec{Q}^2) \tag{85}$$

From this fit to the decay of the elastic scattering fraction with increasing $\vec{Q}$-value, the mean square displacement (MSD) $\langle u^2 \rangle$ is determined. Resulting MSDs for both, pure PTB7 and the PTB7:PCBM blend are displayed in Figure 61.

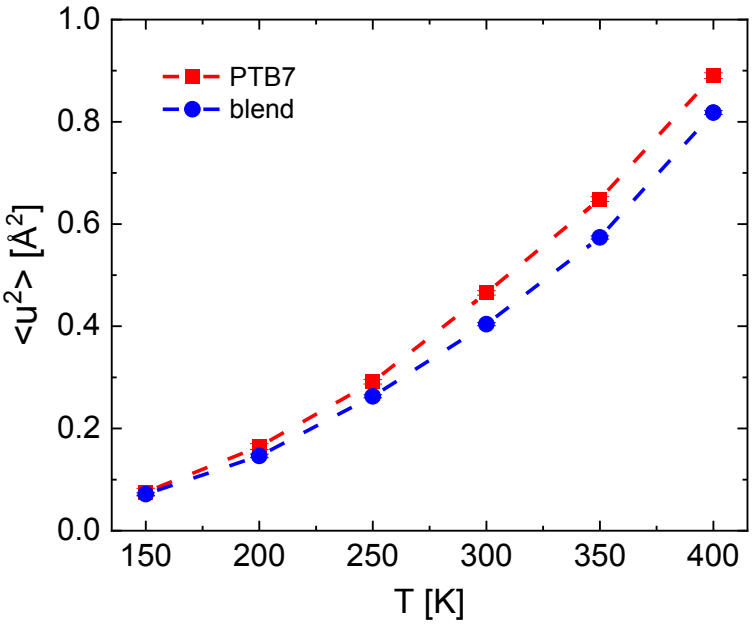

Figure 61: Effective mean square displacement $\langle u^2 \rangle$ for PTB7 (red squares) and the PTB7:PCBM (1:1 wt.) blend (blue circles) in the temperature range between 150 K and 400 K. Dashed lies are a guide to the eye, only. Figure reproduced from [26] with permission from ACS Publications.

Similar to the observations for the effective diffusion coefficient before, the values for the MSD increase apparently exponentially with increasing temperature and the absolute values are consistently higher for pure PTB7 compared to the blend sample. While there was a factor of around 1.5 for diffusive motions, this value is significantly reduced for the vibrational motions, represented in the MSD. Here the relative difference between the samples is only in the range of 4 % to 7 % and also rather decreases for higher temperature as the absolute difference stays constant at increasing temperature. This suggests that the spatial obstruction that is found upon the introduction of PCBM in the blend sample becomes more relevant for long ranged motions than for localized vibrations. Another feature that is found in Figure 61 is the earlier onset of vibrational compared to diffusional motions as the samples show already around 10% of their 400 K $\langle u^2 \rangle$-value at the lowest probed temperature (150 K). This could be investigated in more detail with a better energy resolution. Since only elastic intensity is regarded for the calculation of $\langle u^2 \rangle$ the error bars of the two samples are comparable.

Summarizing, $\langle u^2 \rangle$ seems to follow the same trend with temperature as D_{eff}, i.e. both processes seem to be thermally activated. Thus, the respective activation energies are calculated in the subsequent section.

5.5 Determination of activation energies for the probed dynamic processes

As shown in Figure 59, the calculated effective diffusion coefficients for both, pure PTB7 and the PTB7:PCBM (1:1 wt.) blend start to increase significantly between 150 K and 200 K. Towards higher temperatures a fast increase of the diffusion coefficient is observed for both samples. A similar trend is described by the MSD, shown in Figure 61, except the fact that the onset of mobility in the vibrational regime occurs at lower temperatures and the differences between pure polymer and the blend are significantly smaller.

Activation energies E_A for the respective processes are calculated with the Arrhenius equation in the form of:

$$D(T) = D_0 \, exp\left(\frac{-E_{A,diff}}{RT}\right) \tag{86}$$

and

$$\langle u^2 \rangle(T) = \langle u^2 \rangle_0 \, exp\left(\frac{-E_{A,vib}}{RT}\right) \tag{87}$$

Here, *R* stands for the universal gas constant (8.314 J mol^{-1} K^{-1}) ant *T* for the temperature in Kelvin.

Arrhenius plots of the calculated effective diffusion coefficients and mean square displacements are shown in Figure 62, including fits according to Equations (86) and (87).

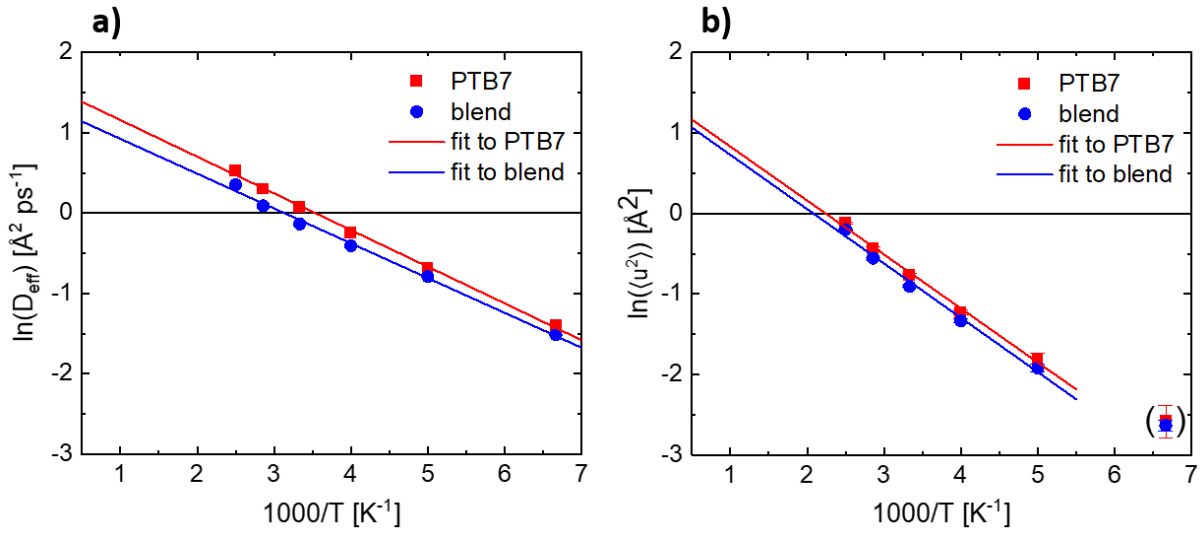

Figure 62: Arrhenius plots for the temperature dependence of a) the effective diffusion coefficient and b) mean square displacement of pure PTB7 (red) and the PTB7:PCBM (1:1 wt.) blend. Solid lines are linear fits according to the Arrhenius model.

All data presented in Figure 62 follow the Arrhenius law for their temperature dependence and thus confirm the assumption of thermally activated processes that do not change their characteristics throughout the entire temperature range. One

exception are the $\langle u^2 \rangle$ values at 150 K (shown in Figure 62b) which deviate from the linear relation that is observed at higher temperatures.

The resulting apparent activation energies are given in Table 10:

	$E_{A,diff}$ [kJ mol^{-1}]	$E_{A,vib}$ [kJ mol^{-1}]
PTB7	8.7 ± 0.1	5.6 ± 0.2
blend	8.3 ± 0.7	5.6 ± 0.2

Table 10: Calculated apparent activation energies for the diffusional and the vibrational dynamics in pure PTB7 ant PTB7:PCBM (1:1 wt.) blend films.

E_A is significantly higher for the diffusive process compared to the vibrations, which is expected from the higher amount of energy that is required for the diffusive delocalization. Activation energies for the mean square displacements are, within the error margin, identical for the pure polymer and the polymer:fullerene blend. This is indicated by the almost perfectly parallel linear fits plotted in Figure 62b. In Figure 62a, these Arrhenius fits show a difference in gradient, which already reveals a difference in the respective activation energies. 8.7±0.1 kJ mol^{-1} for pure PTB7 stand in contrast to 8.3 ±0.7 kJ mol^{-1} for the PTB7:PCBM blend. This indicates a difference in the characteristics of the studied motions between the two samples.

5.6 Summary

In the present chapter, the first ever reported investigation of molecular dynamics of films of the polymer PTB7 and its blend with the fullerene PCBM (1:1 wt.) with QENS is presented. For pure PCBM, no relaxational process was found within the observable time/energy window, which made a meaningful evaluation of the QENS data impossible for this sample.

The studied temperature range was chosen to include the dynamic transition of the systems but to also cover the relevant regions for the application in organic solar cell devices.

Relaxation times, effective diffusion coefficients and mean square displacements for the hydrogen-rich PTB7 side-chains are calculated and compared amongst the

samples. As expected, the PTB7 side-chain mobility is very sensitive to temperature. Below 150 K diffusive motions within the chosen timescale for observation are inactive and their intensity increases gradually with increasing temperature from 200 K on.

When PTB7 is blended with PCBM the polymer dynamics are clearly affected. The effective diffusion coefficients are reduced by approximately 1/3. The relative difference between PTB7 and blend is increasing at higher temperatures. The atomic displacement due to vibrational motions are also reduced upon blending, even though only around 4 % to 7 %, without showing a distinct trend within the covered temperature range.

In accordance, the analysis of the apparent activation energies shows a difference in the temperature dependence for the diffusional, but not for the vibrational process on the observable timescale.

The two dynamic modes that were found, namely a diffusional and a vibrational process show similar temperature response as they both follow Arrhenius behavior, even though the vibrational process is measurable already at lower temperature than the diffusional mode. Their behavior upon blending, on the other hand, is different. While long ranged diffusion is strongly obstructed by the presence of PCBM domains, local reorientations of the polymer side-chain can take place almost unhindered.

Since the amorphous parts of the polymer are in closer contact to the fullerene, the assumption seems reasonable that particularly their dynamics are affected by the confining effect of PCBM in the blend.

6 Influence of blend ratio, alcohol treatment and additives on dynamics in PTB7:PCBM films

In the previous chapter, the investigation of molecular dynamics in the system PTB7:PCBM with quasielastic neutron scattering (QENS) was presented. The performance of OSCs depends on blend ratio and preparation method that results in different microstructure. Therefore, this chapter extends the range of studied samples to make the results more relevant and applicable for the actual state of science in the OPV model system PTB7:PCBM. Additional blend ratios as well as the use of a solvent additive in the production process and the application of an alcohol treatment of the casted film are investigated in respect of their influence on polymer side chain dynamics. The basic principles and data treatment steps were explained in the previous chapter. This chapter relies on the same concepts and a similar analysis procedure. Thus, some steps of data handling and the evaluation are held shorter with a reference to the respective section in Chapter 5.

The key findings from the results presented in this chapter were published in the article “The Influence of the Blend Ratio, Solvent Additive, and Post-production Treatment on the Polymer Dynamics in PTB7:PCBM Blend Films” (Schwaiger et al. Macromolecules, 2021, DOI: 10.1021/acs.macromol.1c00313).[27] The content of this article is partly reproduced for the use in this thesis with permission from ACS publishing.

6.1 Introduction

Chapter 5 presents a proof of concept for the application of time-of-flight QENS in the system PTB7:PCBM. In addition to the 1:1 (wt.) blend studied so far, in this chapter, the influence of the blend ratios on molecular dynamics is investigated. It is known that the performance of PTB7:PCBM solar cells depends on blend ratio with 1:1.5 (PTB7:PCBM wt.) giving the best results.[78], [241], [242] Thus, this ratio is chosen as additional blend ratio for this study.

The state of science for organic photovoltaics is not limited to the choice of materials used as electron donor and acceptor, but several methods were applied successfully in order to increase power conversion efficiencies of the resulting devices. This chapter focuses on the investigation of the influence of two fundamentally different methods that were found to significantly increase the PCE of PTB7:PCBM solar cells. Generally, an improvement of the bulk heterojunction microstructure is their common goal.

One of them is the treatment of the casted blend film with alcohol to remove residual solvent and stabilize the desired microstructure, which is characterized by a decreased domain size that facilitates a more efficient splitting of excitons.[212], [243]

The other investigated performance enhancing method is the use of a solvent additive in the solution based fabrication process. For this study 1,8-diiodooctane (DIO) is chosen. DIO is a selective solvent for the fullerene derivate PCBM and due to its higher boiling point compared to the used bulk solvent chlorobenzene it fosters the formation of purer domains that lead to a higher conductivity and thus also potentially increased PCE.[217], [244], [245], [246], [247], [248], [249], [250], [251]

6.2 Samples and precharacterization

For good comparability of the results, all data presented in this section was acquired from samples that were freshly produced with the same fabrication procedure (as far as possible) and not recycled from any earlier measurement. From the results of Chapter 5 it can be learned that PCBM does not show any diffusive dynamics on the instrumental time scale and thus, it is excluded from this QENS study from the beginning in order to use the beamtime at TOFTOF more efficiently. In total, 6 different

samples were prepared on aluminum foils, as described in Chapter 3.2, for the QENS analysis and 8 different samples on glass and silicon for UV-vis and XRD, respectively:

- PTB7
- blend 1.5:1 (PTB7:PCBM wt.) (only UV-vis and XRD)
- blend 1:1 (PTB7:PCBM wt.)
- blend 1:1.5 (PTB7:PCBM wt.)
- blend 1:2 (PTB7:PCBM wt.) (only UV-vis and XRD)
- PCBM
- methanol (applied on 1:1.5 PTB7:PCBM wt. blend)
- DIO removed, intense drying at 400 K & vacuum (applied on 1:1.5 PTB7:PCBM wt. blend)
- DIO fresh (applied on 1:1.5 PTB7:PCBM wt. blend)

The difference between the samples “DIO removed” and “DIO fresh” is an additional drying step for the former, which intends to remove all DIO molecules that are apparently leftover in the film after the regular drying procedure. A detailed analysis about the difference between the two DIO samples and the reasons for this difference is given at a later point (Chapter 6.4). QENS measurements were performed at 300 K, 350 K and 400 K to cover the operation temperature of solar cells and to be able to follow the thermally activated diffusive processes of the polymer side chains. In addition, a measurement at 10 K was performed for each sample to obtain the respective resolution function.

X-ray diffraction and UV-visible spectroscopy were used for a preliminary structural and optical characterization. Therefore, samples were prepared on silicon and glass substrates, respectively, by drop casting analogously to the QENS samples.

Structural aspects studied with X-ray diffraction

To investigate the microstructure of the samples, X-ray diffraction (XRD) was performed on all samples. The used X-ray wavelength was 1.5419 Å and the diffractograms were obtained in a *2θ* range between 5 ° and 80 °. Figure 63 shows the measured diffractograms until 2θ = 32 ° because no features were found at higher scattering angles. The positions of Bragg peaks were determined by Voigt-peak fits to account for both, the instrumental and the intrinsic sample peak broadening. In contrast to QENS, XRD was performed at a regular lab instrument, which offered the possibility to measure a higher number of samples, including further blend ratios to gain a more complete picture of the series.

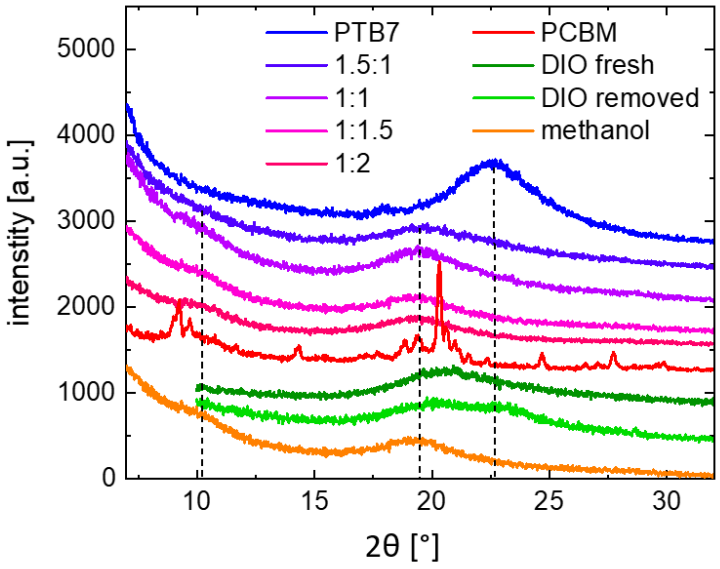

Figure 63: X-ray (λ = 1.5418 Å) diffractograms in the 2 θ range between 7 ° and 32 °. The curves are shifted along the y axis for better visibility. Characteristic positions of Bragg peaks at 10.3 °, 19.6 ° and 22.6 ° are marked with dashed lines. Blend ratios are given as PTB7:PCBM wt. Figure adapted from [27].

In Figure 63, PTB7 is displayed in blue at the top and the blends are arranged underneath until pure PCBM in red. In green, the fresh DIO (dark green) and the heat treated DIO (light green) sample are plotted. The diffractogram of a methanol treated 1:1.5 (PTB7:PCBM wt.) blend sample is shown in orange. As described before, PCBM shows distinct reflexes at 2 θ values of 9.2 °, 14.4 °, 18.8 °, 19.4 °, 20.3 °, 24.7 ° and 27.7 °. They arise from the crystalline lattice that is formed by pure PCBM.[226], [227], [228]

The PTP7 diffractogram yields one broad Bragg peak with its center at around 22.6 °, which is marked by a dashed black line in Figure 63. This peak corresponds to the π-π stacking of the homopolymer and indicates a stacking distance of 3.9 Å, which has also been measured and reported elsewhere for the (100) crystal planes.[220]

If PTB7 is blended with PCBM, the major peak shifts towards a *2θ* value of approximately 19.6 °. This indicates a general expansion of the π-π stacking distance to 4.5 Å. Within the studied range, the blend ratio seems to have no significant influence on the position of this peak. All blend samples, displayed in different shades of violet, show this peak at the same position, but also a second peak at a lower angle of 10.3 °, which is not found for pure PTB7. This low angle peak represents an interplanar spacing of around 8.6 Å, probably corresponding to PCBM domains. The XRD features of the two discussed samples, pure PTB7 and the PTB7:PCBM blend are consistent with those, found in the previous chapter.

The application of a methanol treatment on the casted film did not show any influence on the π-π stacking, as the positions of both fitted peaks are matching the ones of the untreated 1:1.5 (PTB7:PCBM wt.) sample very well.

The sample produced with DIO as solvent additive shows a slight backshift of the main peak to a *2θ* value of 20.5 °. A heat treatment for the removal of any possibly remaining DIO molecules leads to a splitting of this peak into two, one at 20.0 ° and one at 22.8 °.

sample	as cast	heat treated
PTB7	22.8° ± 0.1°	22.6° ± 0.1°
1.5:1	19.6° ± 0.1°	19.9° ± 0.1°
1:1	19.7° ± 0.1°	19.7° ± 0.1°
1:1.5	19.6° ± 0.1°	19.5° ± 0.1°
1:2	19.4° ± 0.1°	19.4° ± 0.1°
DIO	20.5° ± 0.1°	20.0° ± 0.1° & 22.8° ± 0.1°
methanol	19.6° ± 0.1°	19.6° ± 0.1°

Table 11: Bragg peaks of the PTB7 (100) plane determined by XRD. The diffractograms were baseline corrected and fitted with Voigt peaks.

To confirm that the splitting of the peak into two is not caused by the response of the PTB7:PCBM blend structure to the heat treatment, but is an effect of the use of DIO, also the other film samples were heat treated in the same way and the XRD measurements were repeated.

Table 11 shows the resulting positions of the peak centers and confirms no systematic peak shift of the major peak upon heat treatment, except for the DIO sample. The regular drying procedure as described in Chapter 3.2, referred to as “as cast” in

Table 11, was 20 minutes at 100 °C. During the heat treatment the samples were kept at around 100 °C for additional 4 hours. Since the sample produced with DIO is the only that shows a significant change upon heat treatment, the diffractogram of the heat treated DIO sample is also shown in Figure 63 (as “DIO removed”), whereas all other heat treated samples are not shown.

Optical properties

For the evaluation of optical properties and a fundamental comparison of the present samples with literature, UV-visible (UV-vis) absorption spectroscopy was performed with samples that were equivalent to the QENS samples plus further PTB7:PCBM blend ratios as described in the previous section.

Resulting absorbance curves are shown in Figure 64a. All spectra are normalized to the first distinct peak after the absorption edge (coming from high wavelengths) at around 680 nm. The PCBM data was scaled according to its IR absorbance because the scaling peak is caused by the polymer PTB7 and is thus not present in the PCBM absorbance spectrum.

Two distinct peaks are visible for all samples containing PTB7. They mark the well-known absorption maxima of the polymer at around 620 nm and 670 nm.[230] Upon blending with PCBM the absorption peaks shift to higher wavelengths by about 10 nm and their relative ratio changes. The one at lower wavelength loses intensity compared to the other one. For the sample produced with DIO, this trend is even more pronounced. A methanol post-treatment of the 1:1.5 blend does not show any influence on the optical absorbance as the two spectra are almost identical after normalization. It should be noted that from the normalized spectra it is not evident if one peak

decreases or the other one increases. For a more detailed investigation of the UV-vis spectra, see Chapter 7.3.

The absorption tail towards the UV region (starting at ~500 nm) seems to be caused by the PCBM content exclusively. It is not visible for the PTB7 homopolymer, whereas it is the only feature of the pure PCBM spectrum. With increasing PCBM content, the blend samples show a gradual increase of this low wavelength absorption.

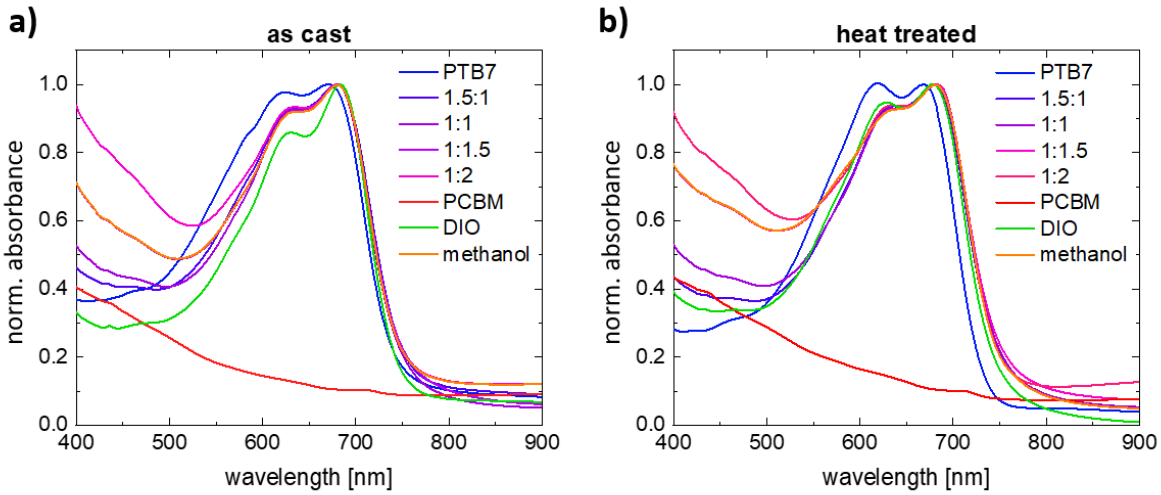

Figure 64: a) Optical absorbance spectra of all samples measured directly after production. b) Optical absorbance spectra of all samples measured after a 20 minutes heat treatment at 130 °C. Spectra are normalized to the peak at ~680 nm. The scaling factor for PCBM was extrapolated from the high wavelength regime since the normalization-peak is not existing for this sample. Figures adapted from [27].

Since during the QENS experiments the samples are heated up to 400 K and the polymers gain mobility, as demonstrated in the previous chapter already, a similar heat treatment was performed with the samples for UV-vis measurement. Figure 64b shows the absorbance spectra for the respective samples after a thermal annealing at 130 °C for 20 minutes.

The two prominent absorption peaks as well as the absorption edge towards high wavelength of pure PTB7 are blueshifted by about 5 nm by the heat treatment and the weak shoulder at ~585 nm is lost almost completely. Further, the relative intensity of the absorption peak at lower wavelength increases in comparison to the peak at higher wavelength. The spectra of all blend samples are very much unchanged in their shape, peak positions and relative peak intensities. This also holds for the methanol treated

sample. The sample produced with DIO shows an intermediate behavior. Same as for the blends, the peaks do not show a wavelength shift, but the relative intensity of the low wavelength absorption peak increases against the intensity of the higher wavelength peak, like for the PTB7 homopolymer.

6.3 Neutron scattering at TOFTOF

In comparison to XRD and UV-vis, the number of samples that could be measured with QENS had to be reduced due to the limitation of neutron beamtime and a certain required counting time. Therefore, only pure PTB7, the 1:1 and 1:1.5 (PTB7:PCBM wt.) blends, the methanol and the two DIO ("fresh" and "removed") samples were studied.

The treatment of the data, as provided by the cold neutron time-of-flight (TOF) chopper spectrometer TOFTOF was performed in a similar way as described in Chapter 5. From the measured time-of-flight and the scattering angle, both, momentum transfer $\vec{Q}$ and energy transfer *ΔE* were calculated for each neutron. With measurements of an empty sample cell, the vanadium standard and the respective sample at low temperature (10 K) the scattering functions S($\vec{Q}$, ω) and the intermediate scattering functions I($\vec{Q}$, t) were determined and all required corrections applied. Large parts of the data reduction and handling were done with the software Mantid.[233], [232]

The chopper system of the neutron spectrometer TOFTOF was set to achieve a neutron wavelength of 8 Å, therefore a rotation speed of 14,000 rpm and a chopper ratio of 6 were used. These settings provided a resolution at the elastic line of approximately 20 µeV, an energy transfer range from 0.75 meV neutron energy loss to 3 meV neutron energy gain ($\vec{Q}$-dependent) and an effectively accessible momentum transfer window from 0.15 $Å^{-1}$ to 1.25 $Å^{-1}$. The obtained QENS data was binned in steps of 0.1 $Å^{-1}$ for momentum transfer and 10 µeV for energy transfer, respectively. All samples were measured for 6 hours at each temperature.

To determine the temperature, where the thermally activated mobility starts to increase, a fast temperature scan was performed on the 1:1.5 (wt. PTB7:PCBM) blend sample prior to the actual experiments. Details about the procedure can be found in

Chapter 5. During constant cooling from 400 K down to 10 K, data was binned within 10-minute time intervals. The average temperature that was measured at the sample cell was determined for the respective 10 min interval. The measured neutron scattering intensity as function of energy transfer is divided into three fractions: elastic scattering ($|\Delta E| < 20$ µeV), quasielastic scattering (20 µeV < $|\Delta E| < 100$ µeV) and inelastic scattering ($|\Delta E| > 100$ µeV, not used here). The normalized elastic and quasielastic scattering intensities for each time interval are plotted according to the respective average temperature of the time interval in Figure 65.

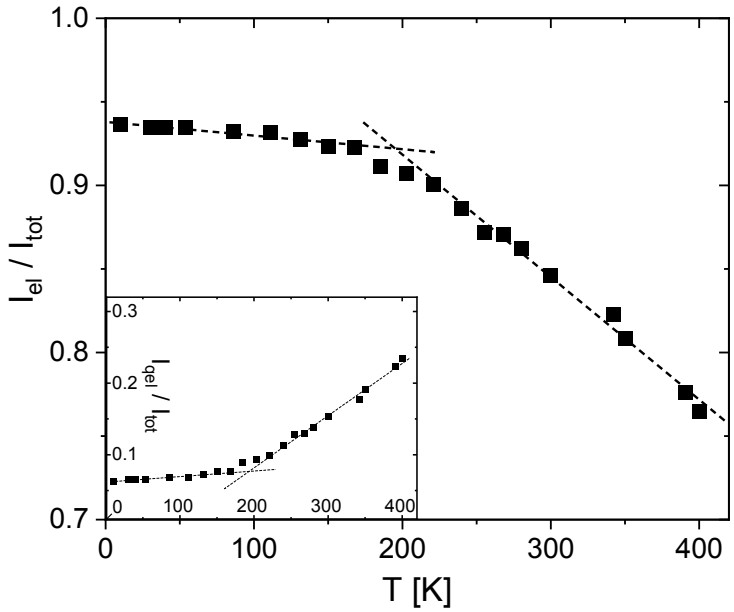

Figure 65: Relative scattering intensities from the QENS measurement during a fast temperature scan with a 1:1.5 (wt. PTB7:PCBM) sample. The main graph shows the elastic and the inset the quasielastic scattering intensity, both normalized to the total scattering intensity. The cut between elastic and inelastic scattering was made at the instrumental energy resolution of ΔE = 20 µeV. The dashed lines are a guide to the eye only and intend to mark the dynamic crossover in the system. Graphics reproduced from [27] (supporting information) with permission from ACS publishing.

The data suggests a dynamical crossover at approximately 200 K, where the intersect of the dashed lines is located. Here, the fraction of quasielastic scattering (inset in Figure 65) increases significantly on the cost of the elastic intensity (main graph in Figure 65). This distinct increase of quasielastic intensity indicates that molecular motions are entering the experimental time/energy window and are thus detectable with TOFTOF and the chosen settings. Thus, the measurement temperatures were chosen well above this crossover temperature. Although this temperature scan was only evaluated for the 1:1.5 (PTB7:PCBM wt.) blend, the

polymer side chain motions in the other samples are assumed to occur on similar temperature scales. For better comparability, the measurement temperatures that were determined on the basis of the 1:1.5 blend sample were used for all samples uniformly.

Since the goal of the present study is to probe the diffusional regime, temperatures for the actual measurement were chosen well above this transition temperature. Because the availability of neutron beamtime is limited, six different samples had to be studied and 6 hours were needed to reach sufficient counting statistics, time allowed for 3 different temperatures to be measured. Based on the findings from the temperature scan, these temperatures were fixed to be 300 K, 350 K and 400 K.

QENS: S($\vec{Q}$, ω) spectra

As described in the previous section, data in $\vec{Q}$-*ΔE* space are binned in order to perform a meaningful analysis of the QENS measurements. Resulting spectra of the scattering function S($\vec{Q}$, ω) for all studied samples are displayed in Figure 66. Spectra for certain momentum transfer bins from $\vec{Q}$ = 0.2 Å^{-1} up to $\vec{Q}$ = 1.2 Å^{-1} are shown. The temperature is fixed to 400 K where the maximum diffusional mobility is expected.

The diffusive dynamics in all samples is confirmed by the distinct increase of quasielastic broadening on the cost of the intensity of the elastic line with increasing momentum transfer in all diagrams of Figure 66. A clear difference can be seen between Figure 66 a & b (pure PTB7 and the 1:1 wt. PTB7:PCBM blend) and the 1:1.5 blend (Figure 66c) and the latter treated with methanol (Figure 66d) as the 1:1.5 blends show a significantly lower quasielastic intensity. This quasielastic intensity seems to be strongly increased in the fresh DIO sample (Figure 66e) but also for the DIO removed sample (Figure 66f).

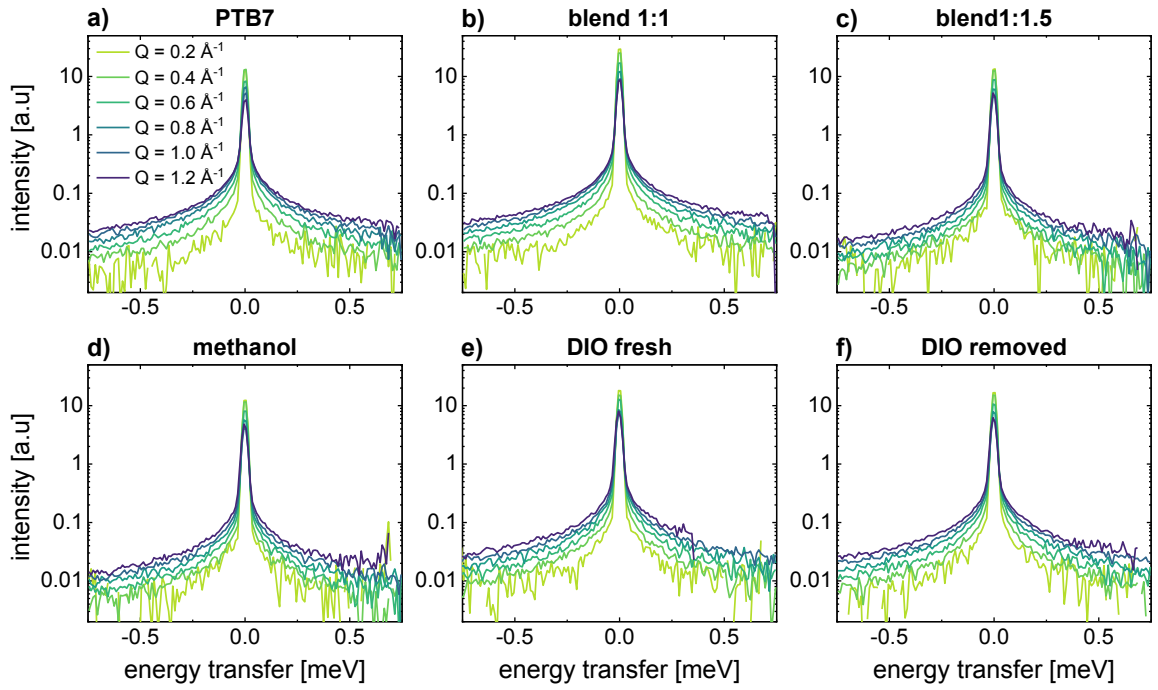

Figure 66: Dynamic structure factor $S(\vec{Q}, \omega)$ for all samples at a temperature of 400 K. The binning interval in $\vec{Q}$-space is 0.1 Å^{-1} and the central value is given in the legend.

The spectra in Figure 66are not normalized to their respective intensity, which makes a comparison rather difficult. Thus, Figure 67 shows a direct comparison between $S(\vec{Q}, \omega)$ spectra of all samples normalized to the intensity of the elastic line at the two different temperatures 300 K and 400 K.

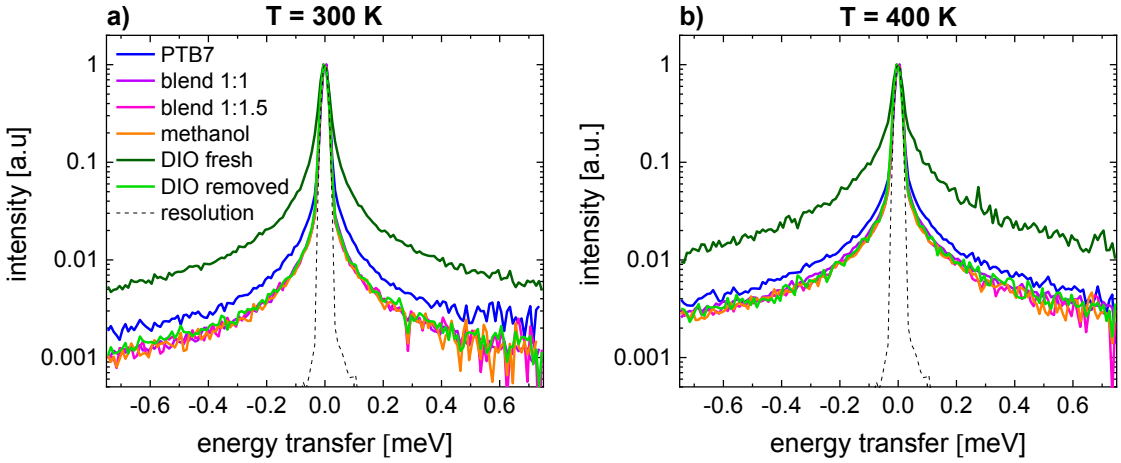

Figure 67: Dynamic structure factor normalized to $S(\vec{Q}, \omega=0)$ measured at 300 K (a) and 400 K (b). All spectra are binned in the momentum transfer range between 1.0 Å^{-1} and 1.1 Å^{-1}. A measurement of the 1:1.5 blend at 10 K is plotted as resolution function in dashed. Graphics reproduced from [27] with permission from ACS publishing.

It is evident that the general scattering intensity is higher at 400 K for all samples compared to 300 K. This applies particularly for the relative quasielastic intensity, as all spectra are normalized to the elastic intensity. For both temperatures, the fresh DIO sample shows by far the highest quasielastic intensity. This is a sign for comparably high diffusive mobility of hydrogen-rich parts inside the sample. It is followed by the PTB7 homopolymer sample, which also shows significantly stronger quasielastic broadening. A higher diffusion coefficient of pure PTB7 compared to a blend with PCBM has been shown in the previous chapter and in [26]. All other curves are very similar and basically indistinguishable within the data fluctuation.

The normalized S($\vec{Q}$, ω) spectra as shown in Figure 67 were used to determine values for mean square displacements (MSDs) of localized hydrogen dislocations as introduced in Chapter 2.2.6.

QENS: I($\vec{Q}$, t) spectra

For the determination of diffusion coefficients from the QENS data, the route over the intermediate scattering function was chosen, as already described in the previous chapter. The Fourier transform of all S($\vec{Q}$, ω) spectra from frequency to time domain and normalization by the respective low temperature measurement yields I($\vec{Q}$, t) spectra. The intermediate scattering functions of all samples are shown in Figure 68 for different momentum transfers from 0.2 Å^{-1} up to 1.2 Å^{-1}. The x-axis describing the timescale of the respective motion is given on a linear scale, thus the exponential decay is well visible. As discussed before, the gradually stronger decrease of I($\vec{Q}$, t) with increasing momentum transfer for pure PTB7 (Figure 68) indicates rather free diffusional dynamics. When blended equally with PCBM (1:1 wt.), this diffusion gets spatially obstructed, which is suggested by I($\vec{Q}$, t) at 1.2 Å^{-1} moving closer to I($\vec{Q}$, t) at 1.0 Å^{-1}, as visible in Figure 68b. By adding even more PCBM (resulting in a 1:1.5 wt. blend), the intermediate scattering functions at 1.0 Å^{-1} and 1.2 Å^{-1} are almost superimposed and do not show any significant differences (Figure 68c, d, f). The general decay of the 1:1.5 blends is also reduced compared to the 1:1 blend by approximately 8 %.

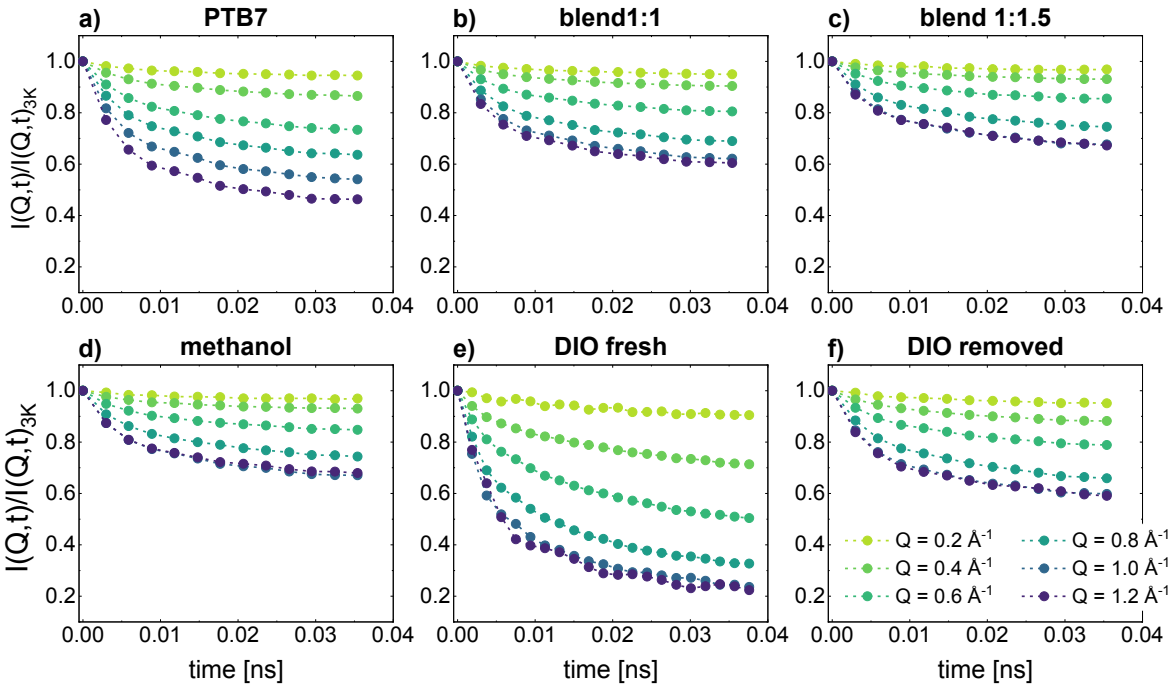

Figure 68: Intermediate scattering function I($\vec{Q}$, t) for all samples at 400 K. For each sample different $\vec{Q}$-values are shown. The shown $\vec{Q}$-values are the average value of the respective binning window (width: 0.1 Å^{-1}). All spectra are normalized to a low temperature measurement of the respective sample. Figure adapted from [27].

As expected from the comparison of the dynamic structure factor in Figure 67, the fresh DIO sample shows by far the strongest decay of the intermediate scattering function at all $\vec{Q}$-values, visible in Figure 68e. At a momentum transfer of 1.2 Å^{-1}, I($\vec{Q}$, t) already becomes very noisy and is characterized by comparably large fluctuation. This is a sign for the strong displacements of the studied hydrogen atoms, which limits the $\vec{Q}$-range that is still representative.

Analysis: diffusion coefficients and MSD

For the calculation of an effective relaxation time τ, a stretched exponential fit was applied to the I($\vec{Q}$, t) spectra in the same was as in the previous chapter.

Due to the apparently higher spatial obstruction of the observed diffusive motions in the samples compared to the previous chapter, most likely caused by a higher PCBM content, the applied stretching coefficient β is reduced from 0.66 to 0.5.

Resulting effective relaxation times are plotted in Figure 69 exemplarily for the temperatures 300 K and 400 K. Because identical scales are chosen, the comparison between Figure 69a and Figure 69b shows that the relaxation times are lower by almost one order of magnitude for the higher temperature. This is expected as thermal motions are faster at higher temperatures and thus occur on shorter timescales. A comparison of the different samples shows that the simple 1:1.5 (PTB7:PCBM wt.) blend and the methanol treated sample show the highest relaxation times, followed by the DIO removed sample, the 1:1 blend and pure PTB7. From a first guess, this might also be the order of ascending diffusive mobility of the shown samples.

The obstructing effect of the presence of PCBM in the blend films is visible at both temperatures in the high-Q region ($\vec{Q}$ > 1.0 Å^{-1}) where the relaxation times of PTB7 drop further but the blend samples seem to reach kind of a plateau.

The fresh DIO sample is not shown in Figure 69 because the obtained relaxation times are in a completely different range and would make a comparison of the other samples among themselves difficult.

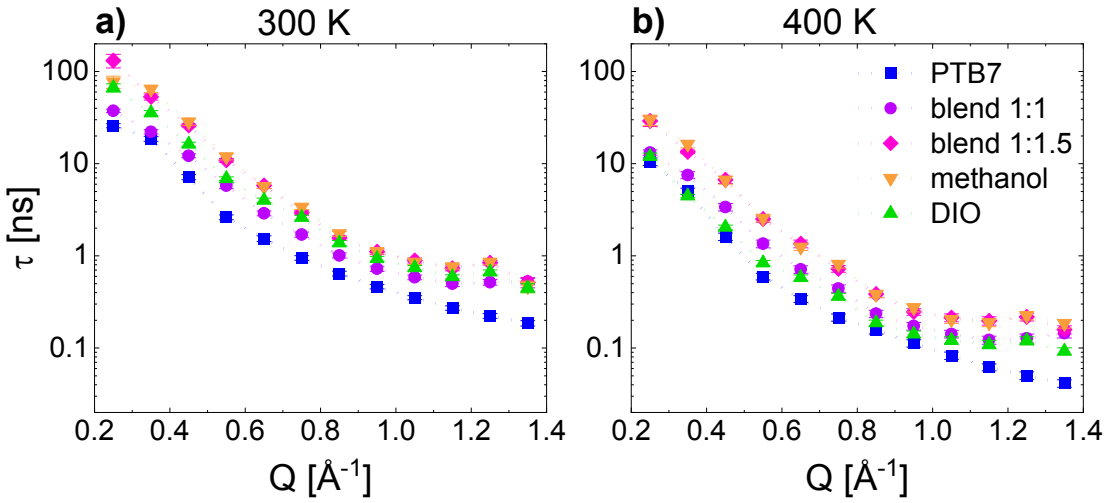

Figure 69: Calculated relaxation times of all samples at temperatures of 300 K (a) and 400 K (b) over a $\vec{Q}$-range from 0.2 Å^{-1} up to 1.4 Å^{-1}. the dotted lines are a guide to the eye only.

From the $\vec{Q}$-dependence of the β-corrected average relaxation times $\langle\tau\rangle$ an effective diffusion coefficient D_{eff} is calculated for every sample for the measurements at 300 K, 350 K and 400 K according to the spatially obstructed Chudley-Elliott model as already used in the previous chapter with Equation (71).[184]

The $\vec{Q}$-range that is chosen for the analysis of $\langle\tau\rangle$ for the evaluation of the diffusivity has significant influence on the resulting diffusion coefficients. Thus, the results are not absolute and uniform but representative for the chosen parameters such as $\vec{Q}$-range. The fits of $\langle\tau\rangle$ vs Q^2 for Figure 70 were performed in the $\vec{Q}$-range between 0.15 Å^{-1} and 0.85 Å^{-1}, since this range provided solid fits for all samples at all temperatures.

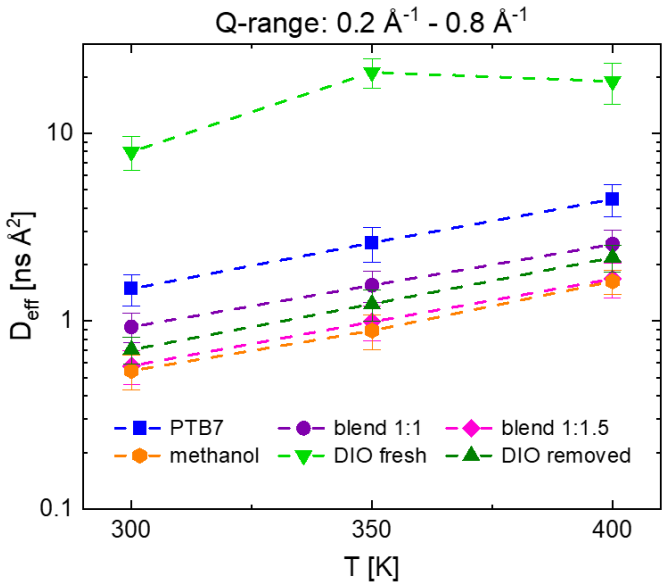

Figure 70: Effective diffusion coefficients according to the spatially obstructed jump diffusion model (Equation (71)). Results from fits in the $\vec{Q}$-range between 0.15 Å^{-1} and 0.85 Å^{-1}. The dashed lines are guides to the eye, only. Reproduced from [27] with permission from ACS publishing.

The $\vec{Q}$-range that is chosen for the analysis critically influences the obtained results, especially in terms of absolute values of D_{eff} since different ranges in $\vec{Q}$-space yield information about different spatial regimes of motions. For consistency of D_{eff} and the comparability among all samples, the rather narrow $\vec{Q}$-range mentioned above was used for the analysis.

The fresh DIO sample, which has undergone the regular heat treatment but not the special one of the DIO removed sample, plotted in light green shows an entirely different behavior compared to all other samples. First of all, the calculated effective diffusion coefficients are far above all other samples, including pure PTB7. This was not expected because the diffusional motions of the polymer side chains are suggested to be obstructed upon blending with PCBM (the fresh DIO sample is a 1:1.5 wt. blend) by all results so far. Further, the behavior D_{eff} of the fresh DIO sample over temperature

gives rise to questions. The significant increase from 300 K to 350 K is still expected, but for the measurements at 400 K the calculated effective diffusion coefficients are decreased compared to the 350 K measurement, irrespective of the chosen $\vec{Q}$-range, which seems rather counterintuitive. A detailed discussion about the effects that lead to this outlier-behavior of the fresh DIO sample is given in a following section (Chapter 6.6).

All samples with "regular" diffusive properties show a linear temperature dependence of D_{eff} in the linear-logarithmic plot in Figure 70a. This implies Arrhenius-type thermally activated diffusive modes. The respective slope in the D_{eff} vs T^{-1} Arrhenius plots is identical for all samples within the error range and the common activation energy of the studied process is calculated to be in the order of 10-11 kJ mol^{-1}. The slight difference to the activation energies reported in Chapter 5.5 for principally the same samples measured with the same instrumental settings can be explained with the narrower $\vec{Q}$-window that was used for the present analysis. This directs the focus to diffusive motions on the respective energy scale and cuts parts of the long-ranged diffusion. This leads to the apparent increase of the activation energy.

A comparison of the calculated effective diffusion coefficients shows that pure PTB7 has the highest values, followed by the 1:1 (wt. PTB7:PCBM) blend and the DIO removed sample. Then follow the simple 1:1.5 blend and the sample that was treated with methanol after drop casting, both yielding identical values for D_{eff} within the errors. These relations hold for every measured temperature due to the Arrhenius behavior of the calculated diffusion coefficient with temperature.

S($\vec{Q}$,ω) evaluation: mean square displacement

Beyond the effective diffusion coefficients, also mean square displacements (MSDs) were calculated for the present samples (not including the fresh DIO sample). Same as in Chapter 5.4 the decay of the elastic intensity of S($\vec{Q}$, ω) is analyzed over $\vec{Q}$ by Equation (85) as shown in Chapter 5.4.

The resulting MSD values as a measure for the vibrational amplitude of PTB7 are shown in Figure 71. It can be assumed that the obtained MSD is also representative for the more rigid polymer backbone as its motions are more characterized by vibrations than by diffusion, compared to the side chains.

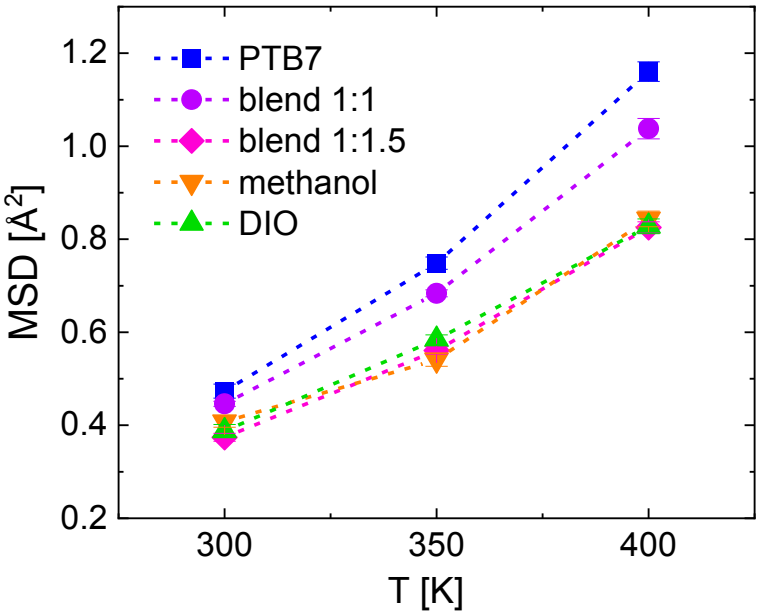

Figure 71: Effective mean square displacement for all samples (excluding the fresh DIO sample) calculated for the three temperatures 300 K, 350 K and 400 K. Dashed lines are guides to the eye, only. Figure adapted from [27].

The qualitative analysis of the apparent MSD gives a similar picture as the effective diffusion coefficient. The PTB7 homopolymer shows the highest vibrational amplitudes. Blending with PCBM reduces the effective MSD. This reduction becomes more distinct with increasing PCBM ratio. The 1:1.5 (PTB7:PCBM wt.) blends (including neat DIO & methanol treated samples) show identical values within their error margin.

Based on the calculated molecular dynamic characteristics the following sections discuss the initial questions about the influence of the PTB7:PCBM blend ratio (Chapter 6.3), of a methanol post-treatment of the drop casted blend film (Chapter 6.4) and of the use of DIO as solvent additive (Chapter 6.5) on PTB7 dynamics.

6.3 Discussion: Influence of PTB7:PCBM blend ratio

The results from Chapter 5 and [26] suggest a distinct obstruction of the PTB7 side chain motions when blended with PCBM. In this study, the influence of an additional blend ratio is investigated in order to learn, if an increased PCBM loading further

reduces diffusive and vibrational dynamics. This is not the case for the investigated structural and optical properties as described earlier in this chapter, which appear to be very similar for various blend ratios from 1.5:1 up to 1:2 (PTB7:PCBM wt.). For the QENS study, the weight ratio of 1:1.5 was chosen because it represents the ideal composition in terms of photovoltaic performances.[78], [241], [242] Figure 72 shows both, vibrational and diffusional aspects in absolute and normalized representations. As pure PTB7 is used as the reference for the unobstructed motions of the polymer side-chains, the data are normalized to the results for pure PTB7 in Figure 72b and Figure 72d.

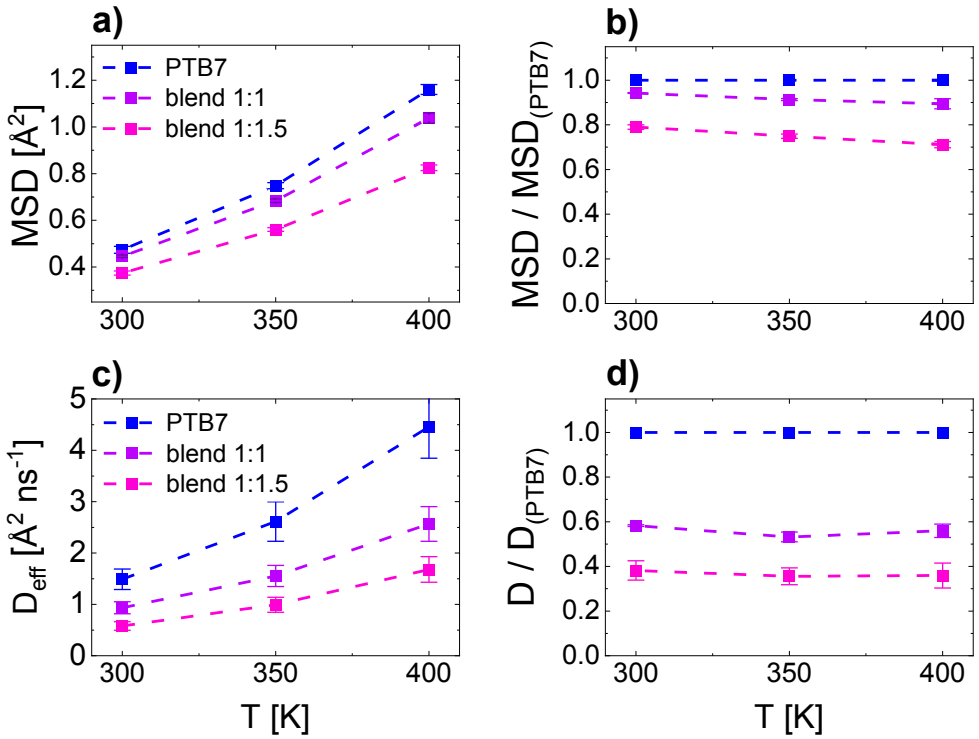

Figure 72: a) Apparent MSD for pure PTB7 and the PTB7:PCBM blends; b) the respective relative MSDs, normalized to pure PTB7; c) effective diffusion coefficients for pure PTB7 and the blends; d) relative diffusion coefficients, normalized to pure PTB7. Dashed lines are guides to the eye, only. Reproduced from [27] with permission from ACS publishing.

The calculated MSDs are a measure for random displacements of the polymer backbone that can not be identified as diffusion with the used instrumental settings. Values for the calculated MSDs as function of temperature are plotted in Figure 72a for pure PTB7 and two different blend ratios. As expected, for all samples the MSD increases strongly with increasing temperature. Figure 72b shows a decrease of the normalized MSDs (normalized by the MSD value of PTB7 at the respective

temperature) with increasing temperature for the two blend samples. For the 1:1 blend, the MSD drops from 94 % at 300 K to 90 % at 400 K compared to neat PTB7. The relative MSD of the 1:1.5 blend drops from 80 % at 300 K down to 71 % at 400 K. This shows an increasingly obstructing effect of the presence of PCBM on vibrational motions in the film with increasing temperatures.

For the diffusive motions this effect is not found as the normalized diffusion coefficients of the blends are not changing significantly within the studied temperature range between 300 K and 400 K (see Figure 72d).

Another difference can be found in the degree of obstruction of the motions. Here, blending has a significantly larger effect on the effective diffusion coefficients compared to the apparent MSDs. While the reduction of the MSD in in the range of 5-10 % for the 1:1 blend and 20-30 % for the 1:1.5 blend, it is around 45 % for D_{eff} in the 1:1 blend and 65 % in the 1:1.5 blend, respectively.

It is evident that blending with PTB7 gradually decreases (i.e. higher PCBM content leads to a stronger decrease) the vibrational as well as diffusional dynamics of the BTB7 side chains. Albeit, diffusive motions are much stronger affected by the presence of PCBM.

Figure 73 shows the extracted relaxation time (a), the calculated effective diffusion coefficients (b) and the mean square displacements as a function of PCBM content for temperatures of 300 K and 400 K.

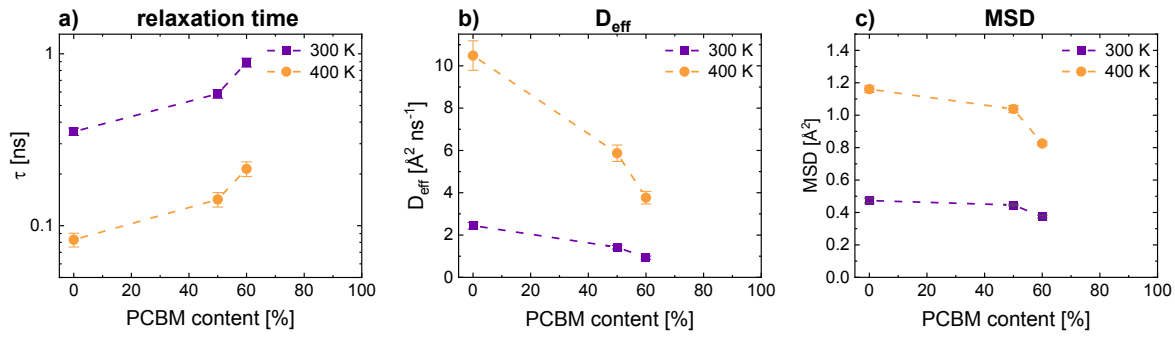

Figure 73: Relaxation time τ (a), effective diffusion coefficient D_{eff} (b) and mean square displacement (c) in dependence of the PCBM content in the PTB7:PCBM blend film. Dashed lines are guides to the eye, only.

It is obvious that neither relaxation time, nor effective diffusion coefficient or mean spare displacement follow a linear relation with PCBM content. Rather, an exponential

like behavior can be inferred from the data in Figure 73. Thus, the polymer side chains get more sensitive to the obstructing effect of PCBM in the blend at higher PCBM ratios. This effect is more pronounced for the diffusion coefficient than for the MSD considering the entire range of blend ratios. If the PCBM content exceeds 50 %, the observed downward kink is significantly stronger for the vibrational amplitude (Figure 73c). This indicates that 50 % to 60 % PCBM loading might be a critical value, where strong obstruction of the respective motions sets in. For diffusional motions, this value seems to be below 50 % PCBM content as the negative slopes of the dashed lines in Figure 73b is already substantial in this region.

For a more sophisticated analysis of the concentration series, more data from additional blend ratios would be necessary.

6.4 Influence of a methanol post-treatment

An alcohol treatment of the casted bulk heterojunction active layer in organic solar cells is applied frequently because in has proved to increase the resulting PCEs significantly.[243], [252] The selective solubility of the alcohols can influence the critical solvent behavior and removal during film formation, potentially yielding a more favorable interpenetrated network of electron donor and acceptor material characterized by decreased domain sizes.[212] In this section the possible influence of a methanol post-treatment of a PTB7:PCBM 1:1.5 (wt.) blend film on the polymer side chain dynamics is studied.

The relaxation time τ, which is directly calculated from the stretched exponential fit to the intermediate scattering function I($\vec{Q}$, t), is presumably the most sensitive parameter to changes in the dynamic behavior o the samples. Thus, τ is used as comparison parameter for the influence of the methanol post-treatment. Figure 74 thus shows τ of the two samples in the whole $\vec{Q}$-range from 0.2 Å^{-1} up to 1.3 Å^{-1} for all three studied temperatures (300, 350 & 400 K).

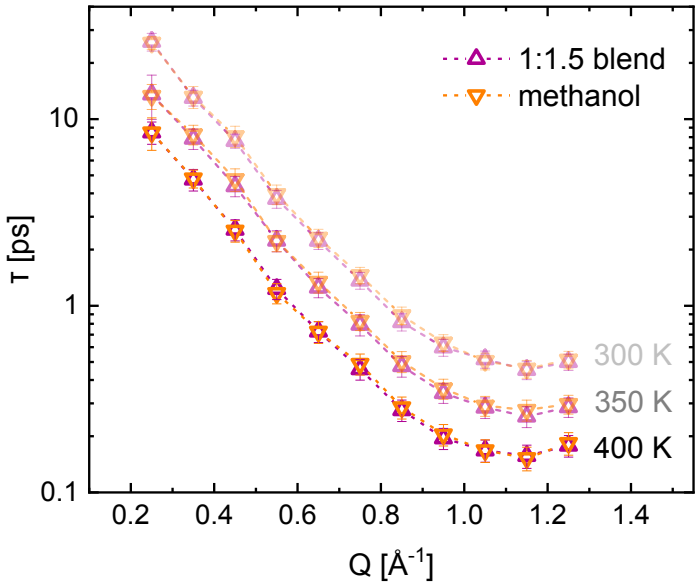

Figure 74: Calculated relaxation times for the 1:1.5 (PTB7:PCBM wt.) blends produced without (purple) and with (orange) a methanol treatment after the casting process. Different temperatures are plotted in different shadings of the respective color. Dashed lines are guides to the eye, only. Reproduced from [27] with permission from ACS publishing.

At all temperatures the calculated relaxation times are very much identical. No hint for a influence of the methanol post-treatment on the dynamic behavior of the PTB7 side chain in the polymer:fullerene blend film can be found. Also the error bars plotted in Figure 74 are almost perfectly superimposed and thus do not indicate any possible difference between the two samples.

Consequently, also quantities like diffusion coefficients and MSDs of the methanol sample, which are derived from the relaxation times, show no significant differences from the simple 1:1.5 (PTB7:PCBM wt.) blend sample. This is also visible in Figure 70 and Figure 71.

Based on these results, the reported PCE improvements achieved by a methanol treatment can most probably be assigned to the modification of the blend film morphology as no influence on the polymer dynamics of the final PTB7:PCBM is detected.

6.5 Influence of DIO as solvent additive

After the investigation of the influence of the PTB7:PCBM blend ratio and a methanol post-treatment of the blend film on polymer side chain dynamics, the analysis of the influence of the use of 1,8-diiodooctane (DIO) as solvent additive in the film production will be the third topic in the present chapter. Most organic solar cells in recent studies are produced with solvent additives because they are a good tool to engineer the resulting blend microstructure. The basic principle is the relatively freely choosable solubility and boiling points of solvent additives. Among all solvent additives, DIO is one of the most frequently used and best understood ones, also very successfully applied for the present polymer:fullerene material system of PTB7:PCBM.[244], [245], [246]

Figure 66 to Figure 71 already show QENS data and results for PTB7:PCBM films produced with DIO as solvent additive. In some cases, it is differentiated between the samples “DIO fresh” and “DIO removed”. The explanation for this will be given in the following section.

The results from the first QENS measurement of a sample produced with DIO and the regular drying procedure were rather surprising as they showed extremely intense quasielastic scattering (compare Figure 67) and diffusion coefficients that exceed the other samples by around one order of magnitude (compare Figure 70). The reason for this significantly different behavior compared to the other samples (produced in the same way, thus expected to behave similarly) was not obvious until a change in the scattering behavior of the DIO sample was observed when heated to 350 K or higher in vacuum of the TOFTOF sample environment. Figure 75 shows an excerpt of the TOFTOF log file from the measurement of the “as prepared” DIO sample. Specific run number, sample name and measurement title are given in the first three columns, followed by the respective measurement time in seconds and the used neutron wavelength (WL). The usual protocol of an initial cooling to 10 K to obtain the resolution function followed by heating to 300 K, 350 K and 400 K and 6 hours counting time at each temperature was applied. The actual temperature at the sample position and the respective variation can be found in the columns T_{min}, T_{ave} and T_{max}. A measure for the incoming neutron flux is the monitor rate (R_{mon}), whereas the actual count rate of the detectors (scattered neutrons, only) is shown in the last column (R_{det}).

Run	Sample	Title	Time	WL	Tmin	Tave	Tmax	Rmon	Rdet
79593	blend_1:1.5_DIO	blend_1:1.5_DIO,base	3600	8.000AA	10.00	10.00	10.00	15.77	339.20
79594	blend_1:1.5_DIO	blend_1:1.5_DIO,base	3600	8.000AA	10.00	10.00	10.00	15.78	337.11
79595	blend_1:1.5_DIO	blend_1:1.5_DIO,base	3600	8.000AA	10.00	10.00	10.00	15.81	338.00
79596	blend_1:1.5_DIO	blend_1:1.5_DIO,base	3600	8.000AA	10.00	10.00	10.00	15.77	337.16
79597	blend_1:1.5_DIO	blend_1:1.5_DIO,base	3600	8.000AA	10.00	10.00	10.00	15.69	337.07
79598	blend_1:1.5_DIO	blend_1:1.5_DIO,300K	3600	8.000AA	300.03	300.68	302.23	15.80	466.45
79599	blend_1:1.5_DIO	blend_1:1.5_DIO,300K	3600	8.000AA	300.00	300.01	300.04	15.86	463.74
79600	blend_1:1.5_DIO	blend_1:1.5_DIO,300K	3600	8.000AA	300.00	300.00	300.01	15.75	461.31
79601	blend_1:1.5_DIO	blend_1:1.5_DIO,300K	3600	8.000AA	300.00	300.00	300.01	15.85	462.25
79602	blend_1:1.5_DIO	blend_1:1.5_DIO,300K	3600	8.000AA	300.00	300.00	300.01	15.79	460.74
79603	blend_1:1.5_DIO	blend_1:1.5_DIO,300K	3600	8.000AA	300.00	300.00	300.01	15.70	459.83
79604	blend_1:1.5_DIO	blend_1:1.5_DIO,heating,300,350	1800	8.000AA	299.75	341.85	355.03	15.86	474.03
79605	blend_1:1.5_DIO	blend_1:1.5_DIO,350K	3600	8.000AA	350.00	350.03	350.35	15.79	470.18
79606	blend_1:1.5_DIO	blend_1:1.5_DIO,350K	3600	8.000AA	349.95	349.99	350.01	15.88	453.77
79607	blend_1:1.5_DIO	blend_1:1.5_DIO,350K	3600	8.000AA	350.00	350.00	350.01	15.76	412.77
79608	blend_1:1.5_DIO	blend_1:1.5_DIO,350K	3600	8.000AA	350.00	350.00	350.01	15.66	367.94
79609	blend_1:1.5_DIO	blend_1:1.5_DIO,350K	3600	8.000AA	350.00	350.00	350.01	15.86	333.26
79610	blend_1:1.5_DIO	blend_1:1.5_DIO,350K	3600	8.000AA	350.00	350.00	350.01	15.71	307.25

Figure 75: Excerpt from the TOFTOF log data from the first measurements of a PTB7:PCBM (1:1.5 wt.) film produced with DIO to determine the scattering statistics.

Since the incident neutron flux, indicated by the monitor count rate (second last column, R_{mon}) is rather constant and the direct beam is not measured by the detectors, the detector count rate (R_{det}) is a direct measure of the rate of scattered neutrons (into the covered solid angle element), i.e. neutrons that have interacted with the sample. This detector count rate is plotted for the respective 6-hour measurements at 10 K (blue), 300 K (orange) and 350 K (red) in Figure 76.

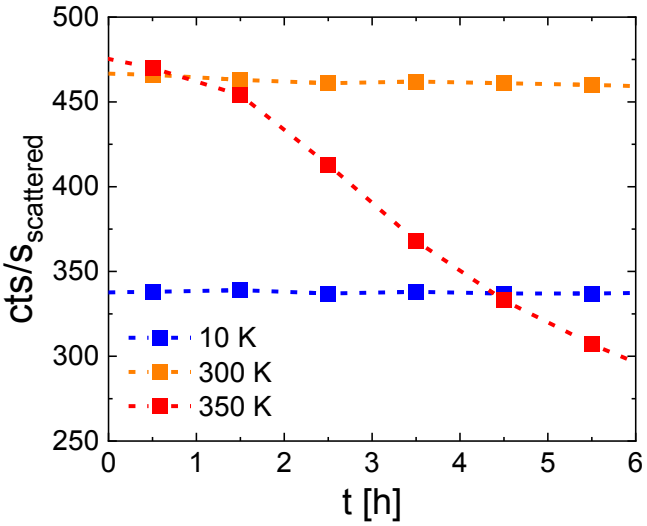

Figure 76: Evolution of the count rate of scattered neutrons for the DIO-sample as produced at 10 K (blue), 300 K (orange) and 350 K (red). Data represents the number of neutrons that are detected by the active TOFTOF detectors per second.

At 10 K, the scattering rate of the sample does not change over the course of the measurement. At 300 K, the scattering rate is increased by approximately 35 % compared to the low temperature measurement, which is expected due to the increased thermal motion of the molecules and thus increased cross sections. Also at

300 K the scattering intensity stays constant over the 6 hours of the experiment. The situation changes when the sample is heated further to 350 K. Initially a further slight increase of the scattering rate, compared to 300 K, can be inferred, but during the measurement it decreases significantly.

This indicates a change of the DIO sample itself that was not found for any other sample in this study. Since the only change is the addition of DIO in the production process, it is the only alteration in the sample and a first increased quasielastic intensity and then a reduction of scattering intensity at elevated temperature are the apparent consequences. The hypothesis arose, that the DIO was not removed completely by the standard drying procedure. The leftover DIO accounts for the excess scattering in the first place. Reaching certain conditions of temperature and pressure leads to a mobilization of the DIO molecules, which then can leave the film and promote full drying. Measured QENS data and the calculated relaxation times, diffusion coefficients, etc. are thus a combination of the PTB7:PCBM film and the leftover DIO molecules.

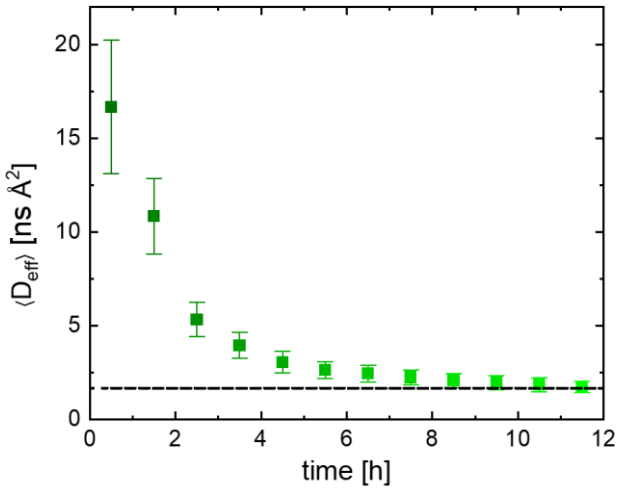

Figure 77: Evolution of the apparent effective diffusion coefficient of the DIO-sample as produced at 400 K in vacuum. Data points represent average effective diffusion coefficients calculated from data that was binned in 60-minute steps. The dashed line represents the effective diffusion coefficient of the regular PTB7:PCBM (1:1.5 wt.) film. Reproduced from [27] with permission from ACS publishing

To follow this compound diffusion coefficient during the loss of DIO from the film, a further, “fresh” DIO sample was prepared and after the acquisition of the resolution function heated to 400 K in vacuum conditions and measured for 12 hours at constant conditions. The calculated average effective diffusion coefficients for each hour of the

experiment are plotted in Figure 77 together with the effective diffusion coefficient of a neat PTB7:PCBM (1:1.5 wt.) sample (dashed line) as a reference.

It is clearly visible that the apparent diffusion coefficient, which is a compound from PTB7 side chain dynamics and DIO diffusion inside the film, decreases over time and converges towards D_{eff} of the solvent additive free polymer:fullerene film. At 400 K in vacuum, it takes more than 10 hours to obtain a film with the expected diffusional behavior.

To analyze the correlation between DIO evaporation and the development of the apparent diffusion coefficient of the film, in the following section the amount of DIO that is left in the film and decay constants of both, DIO loss and reduction of D_{eff} are quantified.

In order to estimate the amount of DIO that is left in the film after the regular drying procedure, the respective scattering intensities of the PTB7:PCBM film and the DIO molecules therein are used. Figure 78 shows the calculated scattering intensity of a hypothetic PTB7:PCBM (1:1.5 wt.) film with various DIO content, normalized to the calculated scattering intensity of a respective DIO-free film. 100 % of theoretical DIO content equals the entire amount of DIO used in the synthesis. If all DIO would be left in the dried, solid film, the scattering intensity would thus be around 5 times the one of the regular film produced without DIO. During the drying procedure, DIO evaporates from the film and the theoretical scattering intensity moves from top left towards bottom right along the dashed line in Figure 78. Comparison of the scattering intensities of as-produced DIO and normal blend samples showed that the rate of scattered neutrons is approximately 2 times higher for the former, meaning that the drying process was stopped at this point. According to Figure 78, this corresponds to 25 % of the initially used DIO left over in the film as the QENS experiment starts. The green shaded area in Figure 78 describes just that range, which is represented by the QENS data, e.g. in Figure 77.

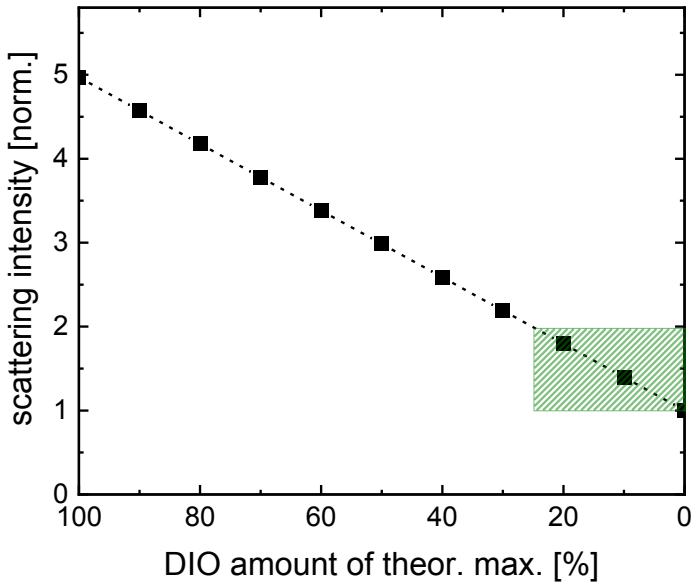

Figure 78: Calculated excess scattering intensity from the DIO used in the production of the PTB7:PCBM blend films, normalized to the scattering intensity of a DIO-free PTB7:PCBM (1:1.5 wt.) film. 100 % corresponds to the total DIO used and the green shaded area to the amount of DIO that was not removed by the regular drying procedure. Reproduced from [27] with permission from ACS publishing

Figure 79 shows a zoom into the shaded area of Figure 78 where the scattering intensity is not calculated but measured at the DIO sample at 400 K over 12 hours (analogous to Figure 77) and normalized to unity by the DIO-free sample. The excess scattering of DIO, which in average results in a factor of 2 for the first hour of the experiment, decreases fast and reaches values that are comparable with the neat PTB7:PCBM film within 6 to 8 hours. Because neither polymer, nor fullerene molecules can escape the film once formed, it can be assumed that the excess scattering (values exceeding 1 in Figure 79) is directly proportional to the number of DIO molecules that are inside the film. Thus, the decay function for the DIO content during the QENS measurement of the fresh DIO sample at 400 K is determined by a fit of the normalized scattering intensity as shown in Figure 79.

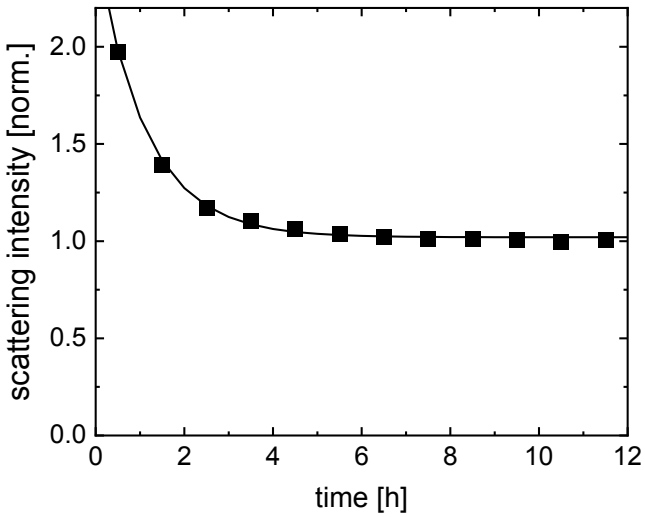

Figure 79: Evolution of the measured scattering intensity of the DIO sample as produced at 400 K. The intensity is normalized to the scattering intensity of the DIO-free PTB7:PCBM (1:1.5 wt.) film. The solid line represents a single exponential fit to the data. Reproduced from [27] with permission from ACS publishing

Figure 80 shows the according normalized average effective diffusion coefficients for the respective 12-hour QENS measurement of the DIO sample at 400 K. The plotted diffusion coefficients are also normalized to the sample produced without DIO and their decay function is indicated as solid black line.

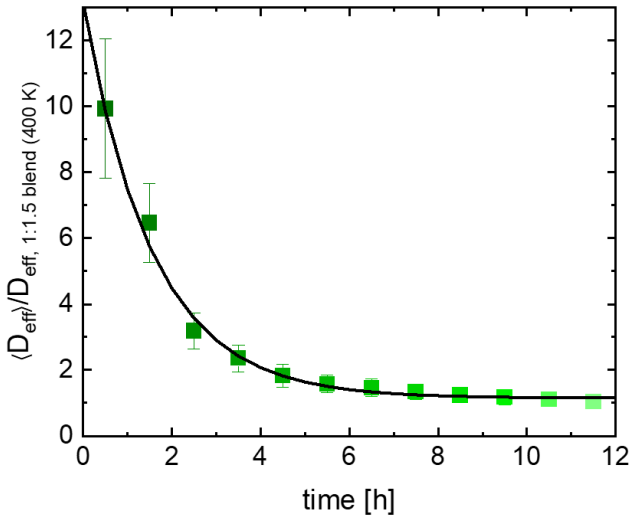

Figure 80: Evolution of the relative effective diffusion coefficient of the DIO sample at 400 K as produced. The apparent average effective diffusion coefficient is normalized the calculated diffusion coefficient of the regular PTB7:PCBM (1:1.5 wt.) sample at 400 K. The solid line represents a single exponential fit to the data. Reproduced from [27] with permission from ACS publishing

For a rough estimation of the diffusion coefficient of DIO in the PTB7:PCBM film, the respective first data points from Figure 79 and Figure 80 are used. For this time period the neutron scattering rate of DIO and the film itself is approximately the same, whereas the apparent diffusion coefficient is increased by a factor of ten compared to a DIO free film. To cause a tenfold increase of D_{eff} with the same amount of scattered neutron, D_{eff} of DIO must be in the range of 20 times higher than D_{eff} of the neat film. At 400 K, this would imply an effective diffusion coefficient of approximately 30 $Å^2ns^{-1}$ to 35 $Å^2ns^{-1}$ for the motion of DIO in a PTB7:PCBM blend film on the timescale that is observable in the present QENS study.

In Figure 81, the previous diagrams are combined for better visual comparability. The relation between calculated and measured scattering rates is indicated in a) and b). In addition, the decay functions for both, the DIO content and the apparent diffusion coefficient are given in b) and c). The derived decay constants are −0.89 ± 0.03 for the DIO content and −0.64 ± 0.05 for the reduction of the diffusion coefficient.

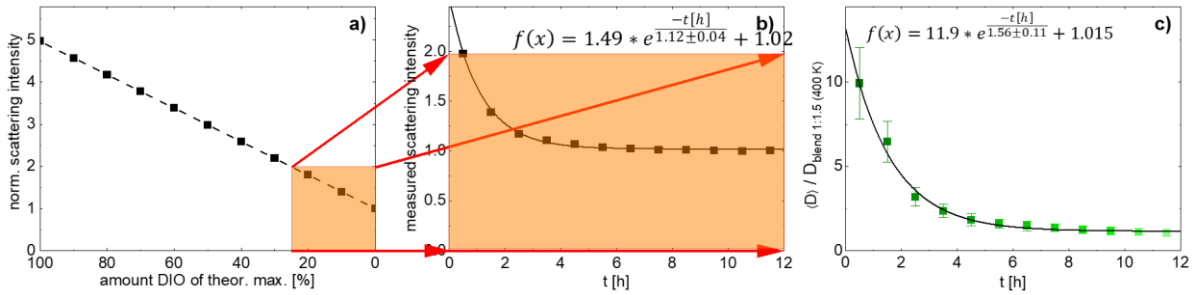

Figure 81: Confluence of Figures 83 – 85, including the equations of the decay functions for the reduction of DIO-content (b) and the effective diffusion coefficient (c). Reproduced from [27] with permission from ACS publishing.

The difference in the decay constants indicates that the residual DIO leaves the PTB7:PCBM much faster than the apparent combined diffusion coefficient decreases, even though the increased diffusion coefficient was caused by the DIO and reflects the DIO dynamics to a large fraction.

A possible explanation for the present results is that the film structure is rather unstable and undergoes significant reorientations, also when the DIO is already gone from the film. This additional mobility could be beneficial for the resulting blend microstructure as it might further promote the microphase separation beyond the selective solubility of DIO and lead to purer domains.

6.6 Summary

In this chapter, QENS was applied to investigate polymer side chain dynamics in PTB7:PCBM bulk heterojunction films in the temperature range from 300 K to 400 K. New insights into the blending behavior of the system as well as into the influence of a methanol post-treatment of the film and the use of 1,8-diiodooctane (DIO) as a solvent additive in the solution based film fabrication were obtained.

The QENS investigation of PTB7:PCBM blend films of varying mixing ratios between polymer and fullerene shows a distinct reduction of the polymer side chain mobility with increasing fullerene content. This is found for both, vibrational and diffusional dynamics. Nonetheless, on the probed timescale, the vibrational amplitude is significantly less affected than the calculated effective diffusion coefficients. This might be explained by the intrinsically smaller range of the vibrational, compared to the diffusional motions. As described in the previous chapter, spatial hindrance of the PTB7 side chain motions, induced by the presence of PCBM domains, could be the main explanation for their reduced mobility. This would convincingly explain the larger impact on the longe-ranged diffusion and the smaller impact on the short-ranged vibrations.

The methanol treatment of a freshly cast PTB7:PCBM that has been reported to increase power conversion efficiencies (PCEs) of resulting solar cell devices by a reduction of the relevant small inner film structure sizes[212] has not lead to an observable effect on the PTB7 side chain dynamics. The calculated relaxation times and diffusion coefficients were indifferentiable at all investigated temperatures. The effect of the methanol treatment seems to be of pure morphological nature and not influencing the relaxation dynamics of the PTB7:PCBM film.

The last topic of this chapter is the investigation of the influence of the use of DIO as solvent additive in the solution based production of PTB7:PCBM bulk heterojunction (BHJ) films. It is found that the regular drying procedure was not sufficient to remove the DIO molecules completely from the film. This is reflected by extremely increased apparent diffusion coefficients from the QENS measurement, which are a compound of the diffusion coefficient of the PTB7 side chains and the DIO molecules. When certain temperature and pressure conditions are fulfilled, complete DIO removal from the film is possible. This process was studied *in situ* with QENS and the kinetics of evolution of DIO content and the apparent diffusion coefficient are compared. Since

the DIO content decreases significantly faster than the apparent diffusion coefficient is reduced, the conclusion arises that DIO leaves a more mobile PTB7:PCBM BHJ structure which undergoes reorientations also after the solvent additive has evaporated. This increased mobility can be beneficial for the healing of structural defects and the creation of purer polymer and fullerene domains in the blend film. This can be considered as a further positive effect of the application of solvent additive in addition to its selective solubility behavior.

If the drying of PTB7:PCBM films with DIO that are used for devices is incomplete, this offers additional pathways for alteration of chemical and physical structure and thus degradation of the device. It is still to be investigated, if the changes that are studied in this chapter at elevated temperatures under low pressure conditions can occur on slower timescale at operating conditions.

A direct effect of the polymer side chain dynamics as determined with QENS in the present chapter on solar cell performance is not trivial since conflicting processes are involved. While high molecular mobility fosters charge carrier mobility and short circuit current, slow molecular dynamics might be favored in terms of charge recombination and open circuit voltage.[218], [224], [225] This is similar in the formation of the desired microstructure, where high mobility might be beneficial.[222], [223] Once the ideal (metastable) structure is achieved, it might be desired to freeze this structure, thus suppress diffusion, which can facilitate undesired structural degradation over the lifetime of the respective devices.

7 Stability of PTB7:PCBM active layers

The polymer side chain dynamics in a PTB7:PCBM bulk heterojunction were extensively studied with QENS in the previous chapters. An *in situ* QENS study showed the behavior and the influence of the solvent additive DIO during its evaporation out of the film. The following chapter intends to further investigate the influence of solvent additives and different drying procedures on physical and chemical stability of PTB7:PCBM blend films under operating conditions of solar cells. Based on the findings of the previous chapter, two drying temperatures are chosen. With the low temperature of 70 °C or 60 °C, respectively, it is presumed that solvent additive molecules are not removed completely from the film, whereas the high drying temperature of 150 °C should provide fully dried films. As a reference, also films without solvent additive are produced for comparison. For this purpose, UV-vis absorption spectroscopy, Fourier-transform-infrared (FTIR) spectroscopy and Raman spectroscopy were applied *in situ* during illumination of the active layer films, as used for organic solar cells. This chapter is based on the article "*In-situ* study of degradation in PTB7:PCBM films prepared with the binary solvent additive DPE:DIO" (Schwaiger et al. Journal of Polymer Science, 2023, DOI: 10.1002/pol.20230072) [28], where the main findings and most relevant data are published.

7.1 Introduction

The QENS studies in the previous chapters have shown that a regular drying procedure of the active layer in polymer:fullerene bulk heterojunction organic solar cells (OSCs) might not be sufficient to remove all solvent (-additive) molecules from the film, especially if high boiling point solvents are used for the optimization of the microstructure. For the immense progress that was made in the field of organic photovoltaics in recent years,[253], [254], [255] though, the application of solvent additives is essential. By their selective solubility and controllable boiling points, the structure formation of the bulk heterojunctions, which are essential for the working

principle of organic solar cells, can be influenced in a way to improve the resulting devices.[217], [245], [249], [250], [256], [257], [258] For the system PTB7:PCBM that is the scope of this thesis, the use of a binary solvent additive of 1,8-diiodooctane (DIO) and diphenyl ether (DPE) has been reported to improve the achieved power conversion efficiencies (PCEs) significantly. The addition of 3 vol % DIO and 2 vol % DPE to the coating solution increased the PCE from 7 % up to 9.25 %.[216] Such an increase is a major step towards the profitable large scale application of any OSC system. Nonetheless, this method also brings along some challenges. The used solvent additives yield boiling points of around 168 °C (DPE) and 259 °C (DPE), which are clearly higher than the boiling point of the bulk solvent chlorobenzene (132 °C). If the drying procedure is too short or happens at too low temperature, molecules of the solvent additives might stay in the film, which can have consequences for the resulting solar cells. For example, the film structure remains mobile and undergoes alterations. Several additional degradation pathways can be activated when the solvents are not removed completely before encapsulation of the devices.[27], [252], [257], [259], [260], [261]

In this chapter, the stability of drop casted PTB7:PCBM (1:1.5 wt.) films produced with DIO:DPE (3 vol % : 2 vol %) binary solvent additives, dried at different temperatures, under illumination at ambient atmospheric conditions is investigated. Two drying temperatures are chosen: 150 °C for a complete removal of all solvent(s) (additives) and 60 °C (70 °C for UV-vis), which is suspected to not completely remove the solvent additive molecules from the film. A reference sample is produced without the use of solvent additives for each experiment. All samples were dried for 10 minutes at their respective temperature. Further details in the fabrication of the samples can be found in Chapter 3. For the investigation of electronic transitions, ultraviolet-visible (UV-vis) spectroscopy is used. The vibrational spectroscopy methods Fourier-transform-infrared (FTIR) and Raman spectroscopy are applied to gain information about the chemical bond structure of the samples. For the UV-vis and FTIR spectroscopy, the samples are illuminated with high power LED modules, whereas the degradation was induced by the excitation laser itself during Raman spectroscopy.

The influence of photodegradation in active layers in the similar system PTB7-Th:PCBM has been connected to both, morphological and chemical alterations of the conjugated network.[262] This leads to a dramatic decrease in photovoltaic performance, thus it must be of major concern to develop materials, that can prevent e.g. the loss of optical or characteristic IR absorbance. The application of FTIR and

Raman spectroscopy shows the process of photooxidation and thus degradation of the conjugated system.[263], [264], [265]

7.2 Calculation of illumination intensity

Since photoinduced oxidation is the main degradation mechanism of the system PTB7:PCBM when exposed to illumination under ambient atmospheric conditions, it is vital to know about the incident illumination intensity. For UV-vis and FTIR absorption spectroscopy, the degradation was induced with MinoStar high power LED modules (Signal Construct GmbH, Germany). Figure 82 shows the normalized spectra of the used blue (a), red (b) and white (c) modules as specified by the manufacturer. Further characteristics of the light sources are given in Table 12. The blue and the red LEDs show a relatively sharp intensity peak caused by certain transitions at around 475 nm and 630 nm, respectively. The white LED shows a broad spectral intensity distribution containing more than one diffuse peak, resulting in the colorless appearance of the produced light.

	blue LED	red LED	white LED
voltage	3.4 V	3.5 V	2.5 V
current	700 mA	700 mA	700 mA
power	2.37 W	2.42 W	1.74 W
viewing angle	15°	45°	45°
luminous flux	36 lm	104 lm	63 lm
peak emission wavelength	475 nm	630 nm	-

Table 12: Characteristics of the used MinoStar high power LED modules according to the manufacturer Signal Construct GmbH.

From the LED luminous flux and opening angle of the diodes, reference working distances for the illumination of the sample films were calculated to ensure constant illumination intensity, irrespective form the choice of LED color. The distances are 30 mm for the blue, 23 mm for the red and 14 mm for the white LED module for an incident intensity of approximately 36 lm/cm^2.

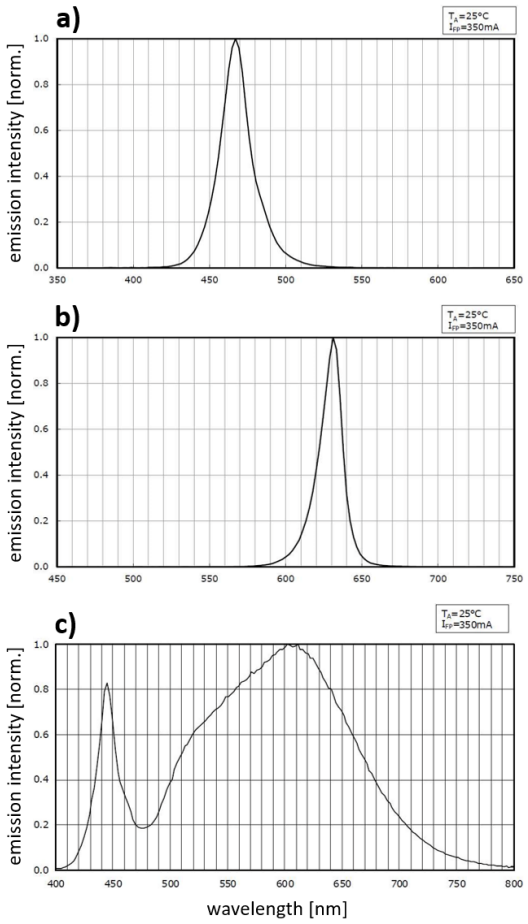

Figure 82: Relative emission intensity of the used LED light sources. Blue (a), red (b) and white (c) MinoStar power LED modules are shown. The intensity is normalized to the respective peak intensity. Graphics are provided from the manufacturer Signal-Construct GmbH (Germany) and modified with permission.

The laser that is used for both, excitation of the sample spot for the measurement of Raman scattering and simultaneously bringing about the photodegradation, yields a wavelength of 785 nm at continuous 100 mW. Since the laser beam is divergent, an universal determination of the illumination intensity per unit area is not possible. Assuming an average spot diameter at the sample of 2 mm, the incident energy would be in the order of 6 W/cm^2. This is roughly one order of magnitude higher compared to the LED illumination in the UV-vis and FTIR experiments, assuming an approximate overall efficiency of ~30 % (diode + geometrical losses). The timescale of the *in situ* Raman degradation study is thus not directly comparable with the timescale of degradation under LED illumination.

7.3 UV-vis characterization under LED-illumination

For the functioning of (organic) solar cells, one of the key mechanisms is the absorption of photons in the active layer as this leads to the creation of excitons, which can be split in order to achieve charge separation. This absorption happens by activating certain electronic transitions in the molecules, provided mainly by the conjugated network of PTB7 in the present case of a PTB7:PCBM blend layer. PCBM has relatively low absorption power in the spectral range of the available solar radiation (compare Figure 48 in Chapter 5.2). Thus, the optical absorbance of the active layer is a good indicator for the state of the conjugated network and the availability of a solar cell to absorb light, even though many more properties and processes have to be provided.

Figure 83 shows the absorbance spectra in the relevant spectral range between 400 nm and 800 nm of thin PTB7:PCBM (1:1.5 wt.) films. The spectra in Figure 83a are plotted as measured, whereas they are normalized to the peak at ~685 nm in Figure 83b. Red spectra show data from films produced without solvent additives and blue spectra represent samples that were produced with DIO:DPE binary solvent additive. In the further analysis of UV-vis data in this chapter, mainly normalized UV-vis spectra are shown since the relative changes are of interest. They were normalized to the highest wavelength peak at ~685 nm as shown in Figure 83.

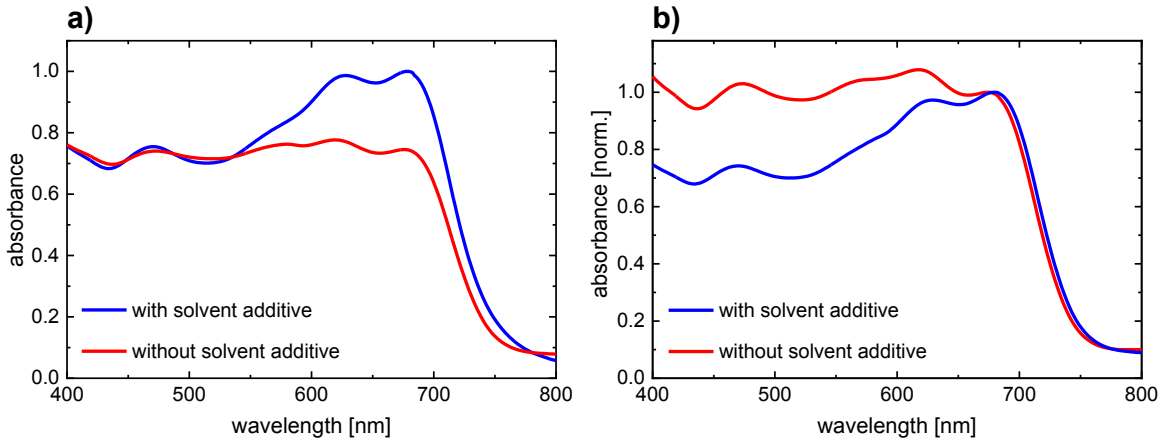

Figure 83: UV-vis absorbance spectra of PTB7:PCBM thin films drop cast from CB-solution with (blue) and without (red) DIO:DPE binary solvent additive. a) shows absorbance data as measured, whereas the curves in b) are normalized to the peak at ~685 nm. The shown samples were dried at 150 °C. Adapted from [28] with permission from Wiley Publishing.

The direct comparison of normalized and not normalized spectra in Figure 83 may be helpful to understand that the use of the binary solvent additive rather increases the characteristic absorbance peaks at ~630 nm and ~685 nm than decreases the lower wavelength absorbance as could be the first impression from the normalized representation. This increase in absorbance by the use of solvent additives can be considered as beneficial for the application in solar cells as it increases the theoretical photon absorption rate at a certain film thickness. Both, DIO and DPE do not show any absorbance in the range between 500 nm and 800 nm, thus the increase of absorbance in this region can be attributed to an improved microstructure of the PTB7:PCBM bulk heterojunction upon the use of DIO:DPE as solvent additive. The different drying procedures had no influence on the initial UV-vis absorbance profiles, as visible in Figure 87. Thus, only samples dried at 150 °C are shown in Figure 83.

The present study intends to investigate the behavior of PTB7:PCBM film at ambient atmosphere under illumination. In order to rule out that the respective films degrade in these conditions irrespective of illumination, a reference set of samples that was stored in the dark between the measurements was tested with UV-vis spectroscopy. The only direct irradiation on these films occurred during the measurements themselves.

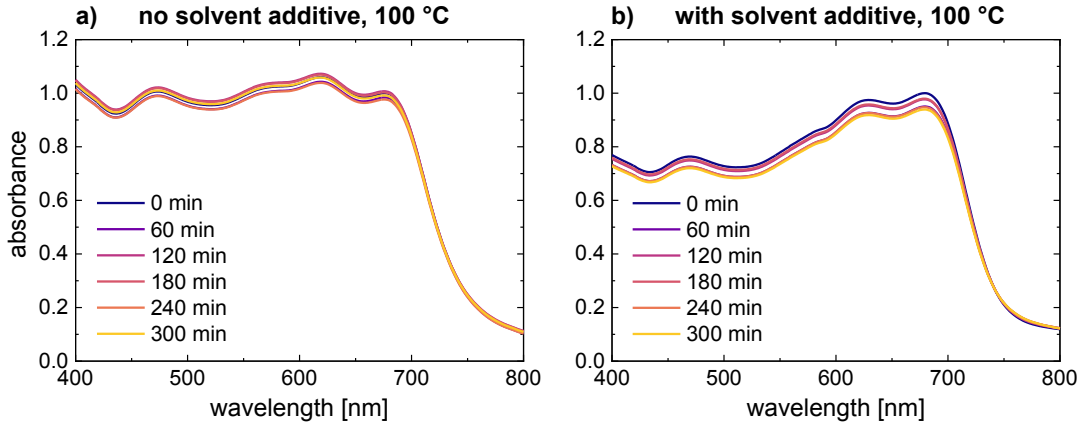

Figure 84: Evolution of the UV-vis absorbance of PTB7:PCBM (1:1.5 wt.) films dried at 100 °C, stored at ambient atmosphere in the dark. The sample shown in a) was produced without and the sample in b) with DIO:DPE as binary solvent additive. Adapted from [28] (supporting information) with permission from Wiley Publishing.

Figure 84 exemplarily shows the development of the optical absorbance of freshly casted PTB7:PCBM (1:1.5 wt.) films up to a storage time at ambient (indoor)

atmosphere of 300 minutes. Thus, to observe significant degradation without illumination, the waiting time would have to be much longer than the timespan that was needed for all individual degradation experiments from removal of the samples out of the glovebox until acquiring the final spectra (also for FTIR and Raman experiments). Figure 84a shows spectra of a sample produced without solvent additive, whereas DIO:DPE was used as binary solvent additive for the sample shown in Figure 84b. Over all measurements presented in Figure 84 neither the shape of the spectrum, nor the absolute values show any significant changes. Slight variations of the intensity may be caused by not perfectly accurate sample placement in the spectrometer for every measurement, as they had to be removed for storage and reinstalled for measurement. These slight deviations, though, do not describe a trend and the final measurement taken more than 4 days after the first aligns almost in the center of the slight scatter (not sown in Figure 84). Similar results for the stability in the dark were obtained for the film produced with binary solvent additives, irrespective of the drying temperature.

Thus, possible changes of the film in the following illumination experiments are considered to be induced by the irradiation. Without illumination, no significant changes of the absorbance spectra occur.

As described above, three different LED modules were available for illumination of the sample films, blue, red and white. The relevant optical absorption region of the PTB7:PCBM films used in this study begins at ~750 nm with the first electronic transition located at 685 nm (1.81 eV) and continues towards smaller wavelengths. The used color LEDs have their spectral peaks at different positions within the PTB7:PCBM absorption spectrum (475 nm for the blue and 630 nm for the red) and don´t overlap, whereas the white LED covers a broader wavelength range, better comparable to the solar spectrum. The samples were individually measured in the UV-vis spectrometer and repeatedly taken out for illumination with the respective LED and then placed back into the spectrometer. A detailed description and images of the experimental setup can be found in Chapter 4. Figure 85 compares the evolution of UV-vis spectra for illumination with the three different LEDs in order to understand, if the wavelength of the incident radiation has an influence on the way the absorbance spectra are affected.

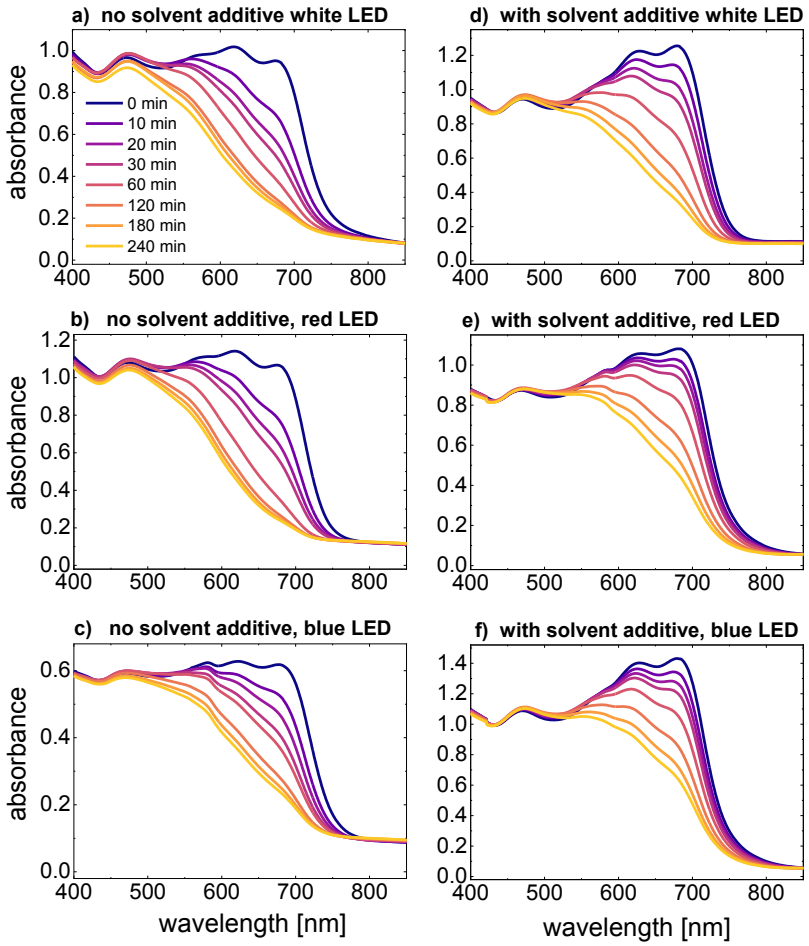

Figure 85: Comparison of the degradation effect on the optical absorption spectra, caused by differently colored LEDs: white (a & d); red (b & e); blue (c & f). The spectra in a) to c) show PTB7:PCBM films produced without solvent additive, d) to f) show spectra from samples produced with the addition of DIO:DPE. All samples were dried at 150°C and spectra are not normalized. Adapted from [28] (supporting information) with permission from Wiley Publishing.

Figure 85a-c show the data as measured for a PTB7:PCBM (1:1.5 wt.) blend film produced without any solvent additive for the white (a), the red (b) and the blue (c) LED. The equivalent data is plotted in Figure 85 d - f for samples that were produced with DIO:DPE as binary solvent additive. Over the investigated timescale of 4 hours of illumination, all samples show a distinct loss of absorbance for illumination with all LEDs, particularly in the range between 520 nm and 800 nm, where the intrinsic absorption edge is located.

To identify possible wavelength dependencies of the photobleaching, the absorbance spectra were integrated in two different spectral ranges, one around the blue irradiation LED from 430 nm to 530 nm and one around the red irradiation LED

from 580 nm to 680 nm. The normalized integrated absorbance in the different characteristic ranges for the simple PTB7:PCBM blend films is compared in Figure 86. In the blue wavelength region between 430 nm and 530 nm (Figure 86a), the films are rather stable as the absorbance decreases by less than 10 % within 6 hours of illumination at ambient atmosphere. An influence of the LED color in this region is not observed. For the wavelength range between 580 nm and 680 nm (Figure 86b) the situation is different. The films lose a significant portion of their absorbance in this wavelength interval. Irradiation with the blue LED seems to cause the photodegradation of the film at a lower rate than the red and the white LED. The difference in the bleaching rates between blue and the other LEDs is in the range of 25 % to 30 %. Between red and white LEDs, a slight difference in the form of a higher bleaching susceptibility for the red LED could be inferable, even though on a low significance level.

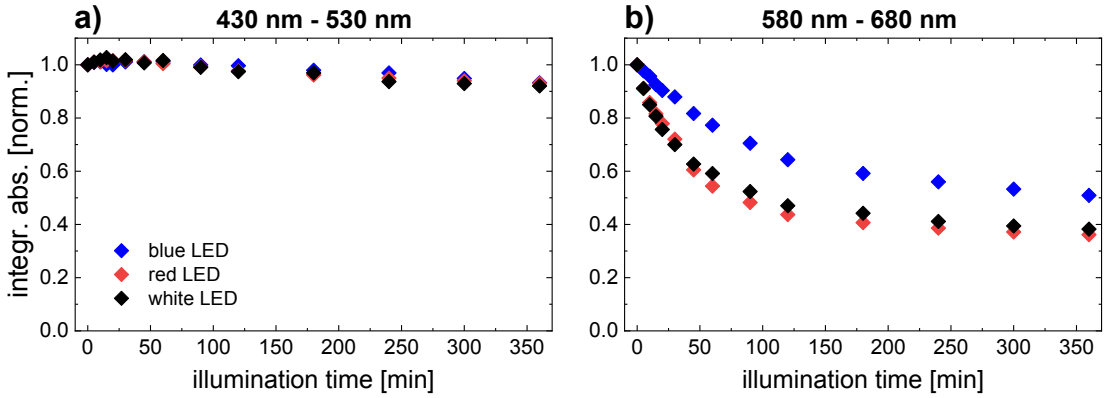

Figure 86: Integrated optical absorbance of a simple PTB7:PCBM blend film in the wavelength ranges 430 nm to 530 nm (a) and 580 to 680 nm (b). Values are normalized to the absorbance at t = 0 min. Blue symbols represent degradation caused by the blue LED, red symbols stand for the red LED and black symbols for the white LED. Adapted from [28] with permission from Wiley Publishing.

As a result, it has been found that illumination color has no influence on the loss of absorbance in the low wavelength region. In the higher wavelength region, a higher fraction of red light accelerates the photobleaching. Since the bleaching patterns are qualitatively very similar for all LED colors, the studied degradation seems to be more dependent on the irradiation intensity than on the wavelength (as long as it stays in the tested range), the occurring processes are identical and induced by all LEDs, even though partly faster for the red one.

Due to these findings, in the following part of this chapter all LED degradation experiments are performed with the blue LED, also because it offers experimental advantages due to the largest working distance of 30 mm.

After the comparison of light sources of different color, in the following part the influence of the use of the binary solvent additive DIO:DPE in the production of PTB7:PCBM (1:1.5 wt.) blend films and different drying procedures applied to them is investigated. Figure 87 shows the degradation studied *in situ* with UV-vis spectroscopy for four different samples. Always two are produced without (a, c) and with (b, d) solvent additive and dried at 150 °C (a, b) and 70 °C (c, d). Spectra from samples produced with DIO:DPE can be easily identified by the pronounced absorption peaks at ~630 nm and ~685 nm. As expected, all samples show a decrease in absorbance in the wavelength range between 500 nm and 800 nm, indicative for photooxidation of the conjugated polymer chain.[241]

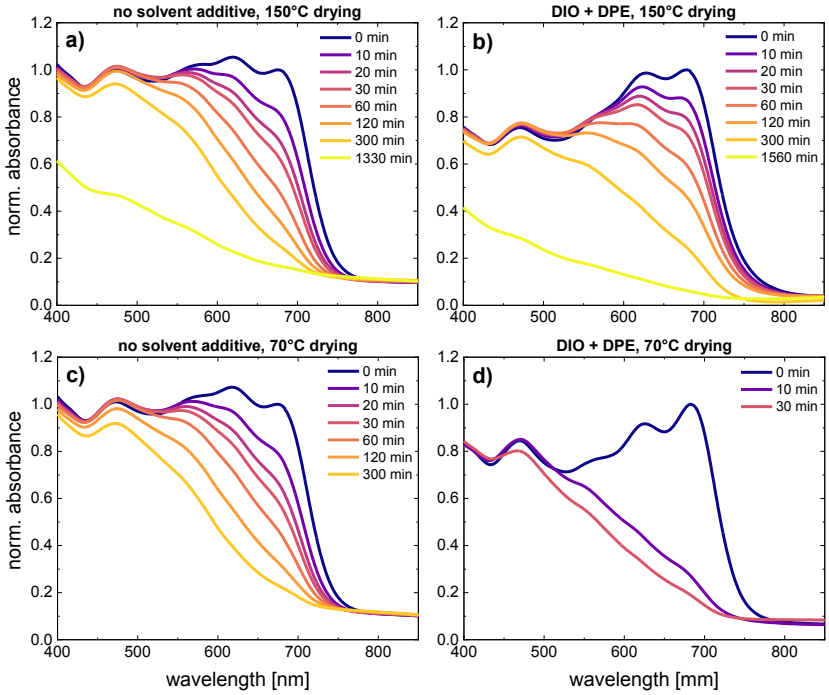

Figure 87: In situ UV-vis absorbance spectra under illumination for PTB7:PCBM thin films produced with (b, d) and without (a, c) solvent additive at high (a, b) and low temperature (c, d) for the film drying. Each data set is normalized to the initial (0 min) spectrum´s peak at around 680 nm. Adapted from [28] with permission from Wiley Publishing.

For the samples produced without solvent additives, no difference in the bleaching behavior can be identified within the first 300 minutes of illumination. After this, most of the characteristic PTB7 absorbance is lost already. Thus, for the further analysis

only the sample dried at 150 °C will be compared with the samples produced with solvent additives. Among them, a drastic difference is visible. The sample prepared with DIO and DPE dried at 150 °C (Figure 87b) shows a gradual degradation behavior, comparable to the samples produced without solvent additive. Its equivalent, dried at 70 °C (Figure 87d) loses its characteristic absorbance almost completely after only 10 minutes of LED illumination. The state of the DIO:DPE sample dried at 70 °C after these first 10 minutes of irradiation is comparable to all others after the entire 300 minutes of the experiment, whereafter only slight and slow changes are detectable. For the samples dried at 150 °C, after the initial 300 minutes of illumination a long term illumination was performed for another 1030 minutes for the simple PTB7:PCBM blend and 1260 minutes for the solvent additive sample, respectively. The long-term light degraded spectra are shown in yellow in Figure 87a and b. While the low wavelength tail of the absorbance was relatively unaffected by the photobleaching within the first two hours, a global reduction of the absorbance starts to occur after this initial phase. This is already indicated by a slight drop of the spectra, acquired after 300 minutes, but much stronger by the samples that were illuminated for approximately one day.

To quantify the loss of absorbance of the different samples, the normalized UV-vis spectra were fitted with sets of Gaussian functions of equal width and distance to each other. Both, width and distance were determined with the two distinct peaks at ~685 nm and ~630 nm. Each fitted Gauss peak stands exemplarily for one observable electronic transition where its area is proportional to the probability of the transition. [159], [266], [267] For example the Gauss peak located at the lowest energy represents the 0-0 transition, the next one the 0-1 transition and so on. Details about the fitting procedure and an example can be found in Chapter 2.2.2.

Figure 88 shows the results for the respective 0-0 and 0-1 transitions. Higher order transitions were fitted to not impair the reliability of the first two (because the peaks do overlap), but not analyzed further since they become increasingly indistinct due to the high structural and electronic disorder of the polymer:fullerene bulk heterojunctions.

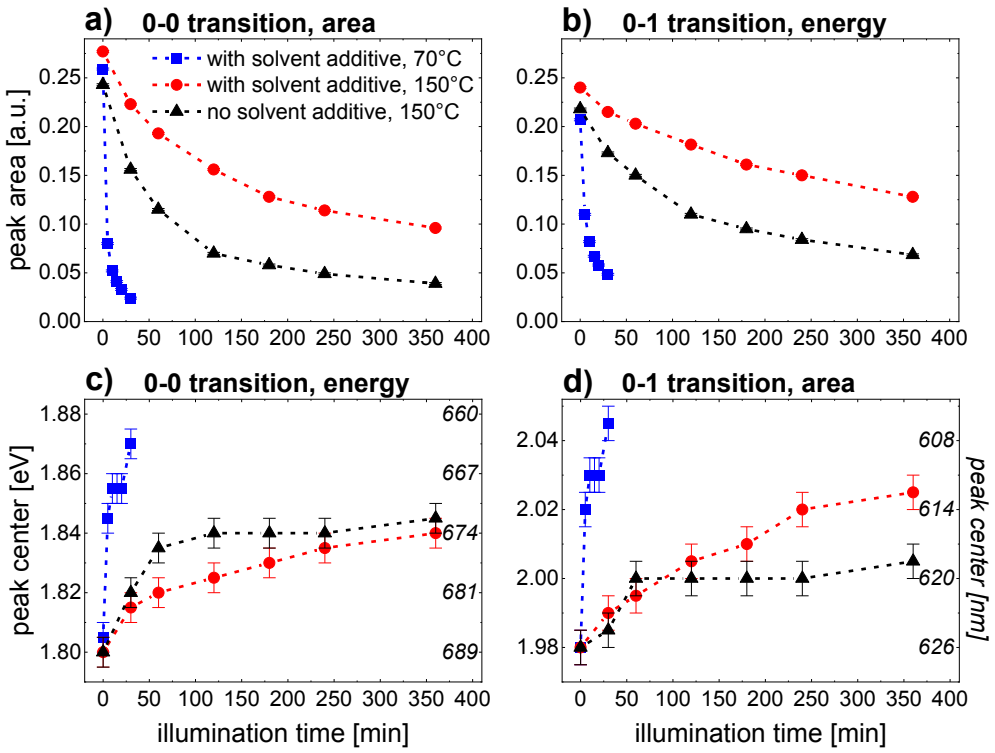

Figure 88: Results from UV-vis spectroscopy. UV-vis absorbance spectra are fitted with Gaussian functions to determine the optical transitions of PTB7. a) and b) show the resulting area for the 0-0 and 0-1 transition, respectively, over illumination time. c) and d) show the corresponding position of the transitions in terms of energy. The dashed lines are guides to the eye only. Adapted from [28] with permission from Wiley Publishing.

In Figure 88a and Figure 88b, the peak integrals of the 0-0 and the 0-1 transition, respectively, are plotted as a function of irradiation time. The probability of both transitions decreases monotonously for all samples, which is expected from the continuous loss of absorbance in these spectral regions, visible in Figure 87. The transition probabilities of the sample produced with solvent additives dried at 70 °C (blue squares) decreases very fast and drops below 10 % within 20 min for the 0-0 transition and below 20 % within 30 min for the 0-1 transition. A comparison of the two samples that were dried at 150 °C shows that the sample produced with solvent additives (red circles) is significantly more stable than the simple PTB7:PCBM blend (black triangles). Corrected for the slightly different initial peak areas, the latter loses the respective peak areas approximately twice as fast as the former. An explanation for this effect could be that the structure modification, which is responsible for the different absorbance spectrum, achieved by the use of DIO:DPE, comes along also with increased stability against light induced oxidation. In general, the 0-0 transition is more susceptible to the initial photodegradation. This is supported by the data shown

in Figure 87 that implies a particularly strong loss of absorbance in the high wavelength range upon illumination in ambient atmosphere.

Characteristic transition energies, according to the centers of the respective Gaussian functions, are shown in Figure 88c and d. They tendentially shift towards higher energies with proceeding film degradation. For the samples dried at 150 °C, both peaks are shifted by 0.03 eV to 0.04 eV within 360 minutes of illumination. The difference among the two samples is not as distinct here as it was for the peak areas. The sample produced with DIO:DPE dried at 70 °C, though, again shows exceptional behavior. Both transitions are shifted by ~0.07 eV towards higher energies and thus around twice as much as observed for the other two samples. Not only the magnitude but also the timescale on which the peak shift occurs in the DIO:DPE, 70 °C sample is on another scale as it around ten times faster than the discussed changes in the other two samples.

The results from UV-vis spectroscopy clearly show that solvent additive molecules, potentially left over in the PTB7:PCBM blend film can have dramatic influence on the stability of the conjugated network of the polymer and its susceptibility to photooxidation. The properties of the initial samples as cast are still very similar for all samples, but all studied features like characteristic absorption as well as the transition-probability and -energy are subjected to much stronger changes if the solvent additive sample is dried at lower temperature. A sufficient drying of the sample produced with solvent additives, on the other hand, can lead to an improvement of the stability compared to a simple PTB7:CBM blend (produced without solvent additive). This improvement of stability comes along together with the well-known increase of characteristic PTB7 absorbance.

7.4 *In situ* FTIR spectroscopy under LED-illumination

After the investigation of the optical properties with UV-visible spectroscopy, Fourier-transform-infrared (FTIR) spectroscopy is used to study the chemical bond situation of the samples. The samples were continuously illuminated by the blue LED light source and the acquisition of IR absorption spectra was triggered automatically by a customized script in the desired time intervals. A generic spectrum of the neat

PTB7:PCBM (1:1.5 wt.) blend is shown in Figure 89 with the relevant peaks from Table 13 indicated for a better comprehensibility of the spectra shown in the following.

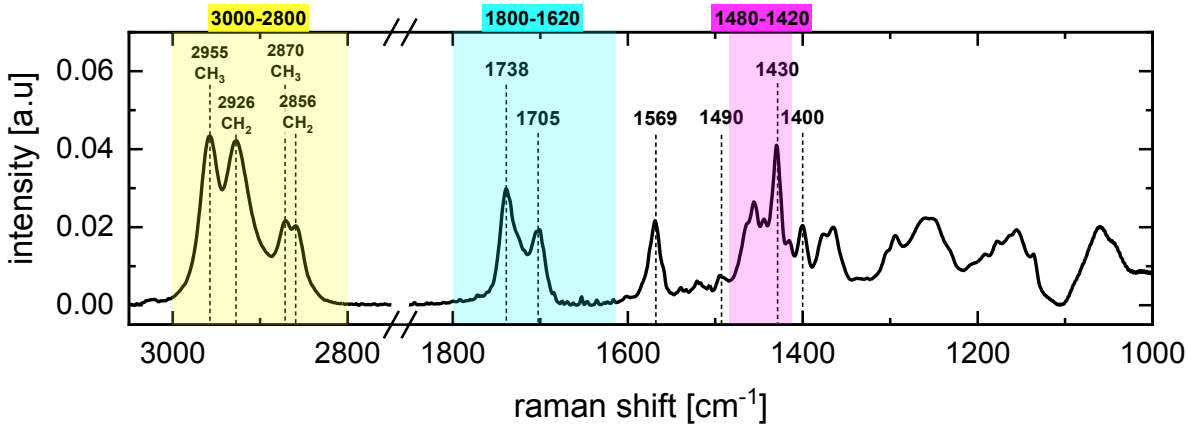

Figure 89: Generic FTIR spectrum of a PTB7:PCBM (1:1.5 wt.) blend film in the wavenumber regions 3050 cm^{-1} to 2750 cm^{-1} and 1850 cm^{-1} to 1000 cm^{-1}. Relevant peaks are marked with dashed lines and their position is given in cm^{-1} according to Table 13. Characteristic broad bands including multiple or less distinct peaks are shaded in different colors.

The obtained initial and final (after 1200 min of illumination) spectra from the *in situ* FTIR spectroscopy of all three samples are shown in Figure 90 and contain information about both, CH_2/CH_3 groups and the conjugated network of PTB7. Figure 90 shows spectra of all three PTB7:PCBM (1:1.5 wt.) blend film samples, one produced with DIO:DPE (3 vol % : 2 vol %) as binary solvent additive dried at 60 °C (Figure 90a), the equivalent dried at 150 °C (Figure 90) and one produced without solvent additive also dried at 150 °C (Figure 90c). The blue spectra represent fresh samples as cast, whereas the red spectra represent the respective samples after 1200 minutes of illumination at ambient atmosphere.

In the general appearance of the IR absorbance spectra, all samples show the same peaks at their characteristic positions. Upon illumination in the presence of atmospheric oxygen, all spectra undergo significant changes that are caused by an alteration of the respective bond environment.

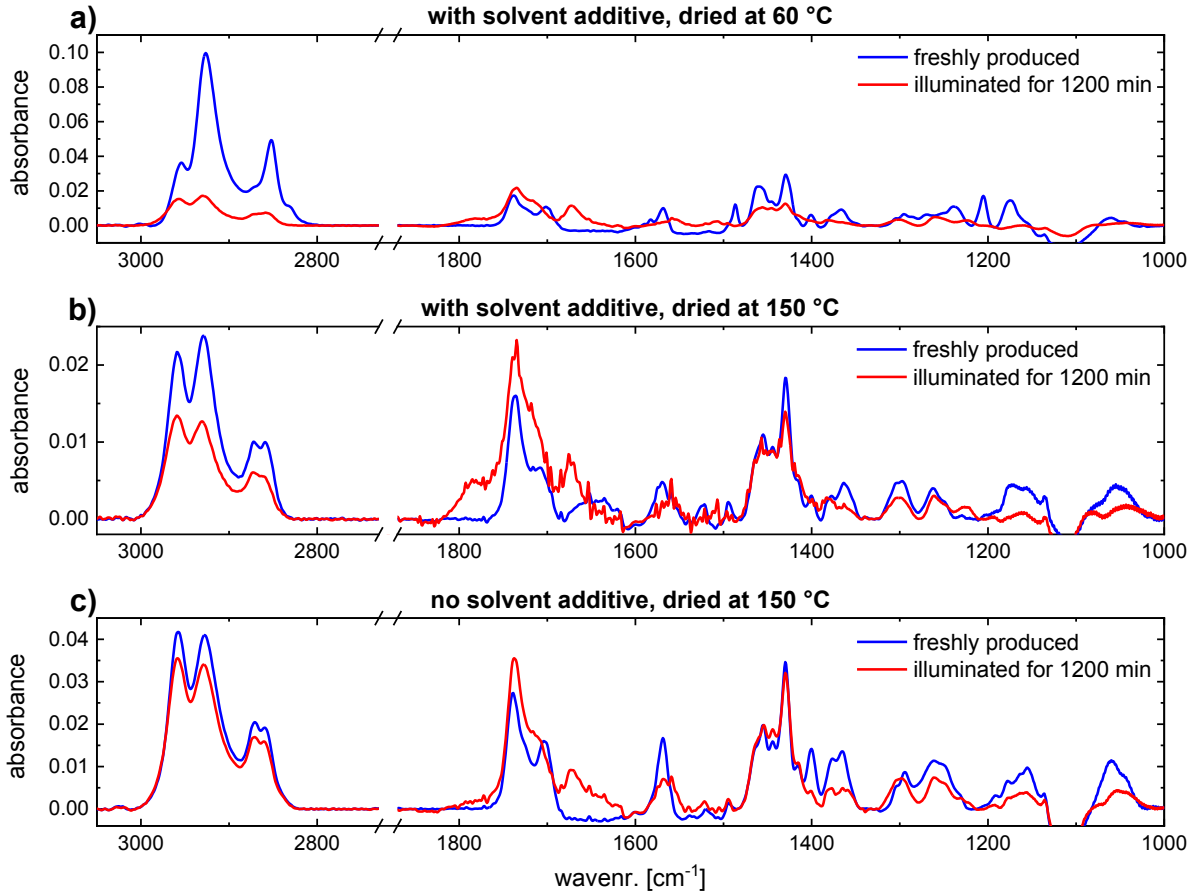

Figure 90: FTIR absorbance spectra of PTB7:PCBM thin film samples produced without (c) and with (a, b) solvent additive, both, dried at 150 °C (b, c) and 60° C (a), around the relevant ranges from 3000 cm^{-1} to 2800 cm^{-1} and 1800 cm^{-1} to 1000 cm^{-1}, respectively. Blue curves are recorded with freshly prepared samples, whereas red curves show measurements of light and oxygen degraded samples. Adapted from [28] with permission from Wiley Publishing.

Multiple characteristic peaks are evident in the studied wavenumber ranges between 3000 cm^{-1} and 2800 cm^{-1} and between 1800 cm^{-1} and 1000 cm^{-1}. Table 13 gives the assignment of the most prominent peaks according to literature.[22], [259], [262], [268] At a first glance, the former wavenumber range (3000 cm^{-1} to 2800 cm^{-1}) represents the CH_2 and CH_3 side group signature of the sample and the latter (1800 cm^{-1} to 1000 cm^{-1}) the state of the conjugated systems of both, the polymer PTB7 and the fullerene PCBM. The absorbance peaks for CH_2 and CH_3 stretching modes of alkyl side chains show a slight decrease upon illumination for the film that is produced without solvent additive. This decrease is more pronounced in the solvent additive sample, dried at 150 °C, and even much more in the solvent additive sample,

dried at low temperature (60°C). Peaks in the region between 1800 cm^{-1} and 1600 cm^{-1} are assigned to C=O stretching modes. Their emergence during the illumination is a clear indication for photooxidation.[259], [269] The freshly fabricated films feature two distinct peaks at 1738 cm^{-1} and 1705 cm^{-1}, respectively for C=O stretching modes of ester side chains, which are present in both, PTB7 and PCBM. These peaks are sharper for the additive-free sample. The thieothiophene (TT)-related peak at 1705 cm^{-1} is also observable for all samples. This and the neighboring peak at 1738 cm^{-1} seem to not increase or decrease during illumination but it seems that they get superimposed by adjacent broader peaks. Comparing the samples that were dried at 150 °C, this effect is more pronounced in the sample that is produced with solvent additives. The general increase of absorbance in this region can be caused by the uptake of oxygen and the formation of new C=O bonds as one effect of the light induced degradation process.[259], [269] The peak that is found at 1569 cm^{-1} is attributed to C=C stretching modes in the thiophene rings of the thienothiophene segments.

peak position	assigned bond vibration
3000 – 2800 cm^{-1}	CH_2/CH_3 stretch in alkyl side chains
1800 – 1620 cm^{-1}	newly created C=O stretch
1738, 1705 cm^{-1}	C=O stretch in ester groups of PCBM & TT side chain
1569 cm^{-1}	C=C stretch in TT-thiophene rings
1490 cm^{-1}	C=C stretch in BDT-thiophene rings (weak)
1480 - 1420 cm^{-1}	CH_2/CH_3 bend, C=C stretch
1430 cm^{-1}	C=C stretch in PCBM benzene rings (const.)
1400 cm^{-1}	C-F stretch (TT)

Table 13: Peak positions of the most prominent IR absorption features with the assigned types of vibrations that are expected from the sample according to literature.[259], [262], [268], [269]

At lower wavenumbers, there are broad absorption bands between 1480 cm^{-1} and 1420 cm^{-1} attributed to C-H bending modes. A characteristic peak at 1430 cm^{-1} reflects the stretching vibration in the benzene rings of PCBM. At 1400 cm^{-1} a sharp peak is present in the spectra of the pristine films. It almost vanishes upon illumination. This peak is assigned to the C-F stretching mode. This bond is present only once per PTB7 monomer, whereas most C=C and C-H bonds are more abundant. Even though the peaks are stationary at the characteristic energy, their relative ratios are varying

strongly between the samples, which indicates an influence of the used solvent additives and the applied drying procedure on the formation of the chemical structure of the PTB7:PCBM bulk heterojunction film.

Figure 91 shows a zoom into the relevant wavenumber regions, where the peaks are located that are analyzed by Lorentzian fits. In addition, the temporal evolution of the respective peaks is visualized by the presence of multiple spectra that were acquired during 1200 minutes of illumination.

Figure 91a, c and e show the peaks that are representative predominantly for the alkyl side chains in the three samples. It is obvious that the initial shape of the spectra as well as the development with illumination time is very similar for both samples dried at 150 °C (Figure 91c & e). The slight decrease of the absorbance of around 15 % seems to be uniform for all peaks in this region. Figure 91 yields a different picture for the sample that was produced with binary solvent additive and dried at 60 °C. Already in the freshly produced films, the respective higher wavenumber peaks of the observed double peaks at ~2957 cm^{-1} and ~2869 cm^{-1} are strongly suppressed. This might be a hint that possibly leftover molecules of the solvent additives somehow obstruct the CH_3 stretching vibrations at the end positions of the alkyl side chains.[259] The decrease of absorbance upon illumination, especially in the first 240 minutes, is much more pronounced in comparison to the other two samples. The relative decrease of IR absorbance that is observed in the 150 °C dried samples over the whole course of the experiment is reached after only ~45 minutes of illumination in the DIO:DPE sample dried at 60 °C. After the entire 1200 minutes of illumination, the absorbance loss exceeds 80 % in this region. Even though the scales differ slightly between the samples, an effect of sample thickness is not expected for the present experiment, since the 60 °C dried solvent additive sample shows the highest initial IR absorbance and nonetheless the fastest response to the illumination at ambient conditions.

The right column of Figure 91 (b, d & f) shows the wavenumber region that contains the peaks that are representative for the conjugated network of the polymer and fullerene. For some peaks like the C=C stretching peaks at 1569 cm^{-1} (TT) and 1490 cm^{-1} (BDT), a differentiation between the thienothiophene (TT) and the benzodithiophene (BDT) building blocks is feasible. The peaks of particular interest due to their high significance in this region are the TT C=C stretch peak at 1569 cm^{-1} and the C-F stretch peak at 1400 cm^{-1}, but also the PCBM-related band from 1480 cm^{-1} to 1420 cm^{-1} and the BDT C=C stretch at 1490 cm^{-1} are located in the shown region. The polymer absorbance peaks at 1400 cm^{-1}, 1490 cm^{-1} and 1569 cm^{-1} are lost almost

completely and immediately in the solvent additive sample dried at 60 °C (Figure 91b). The band between 1480 cm^{-1} and 1420 cm^{-1} loses the intensity significantly slower, more gradually and after 1200 minutes of illumination still ~50 % are remaining. Thus, the chemical stability of PCBM seems to be less affected by the presence of residual DIO or DPE molecules in the PTB7:PCBM blend film. If the film is dried at 150 °C (Figure 91d & f), this PCBM band appears to be very stable. In these samples (dried at 150 °C), the peak at 1490 cm^{-1} is not that distinct, which suggests an influence of the presence of DPE or DIO on the formation of the chemical structure. The prominent TT C=C stretching peak at 1569 cm^{-1} and the C-F stretching peak at 1400 cm^{-1} show a gradual decrease over the 1200 minutes of illumination, resulting in an absorbance reduction of around 50 % at the end of the experiment.

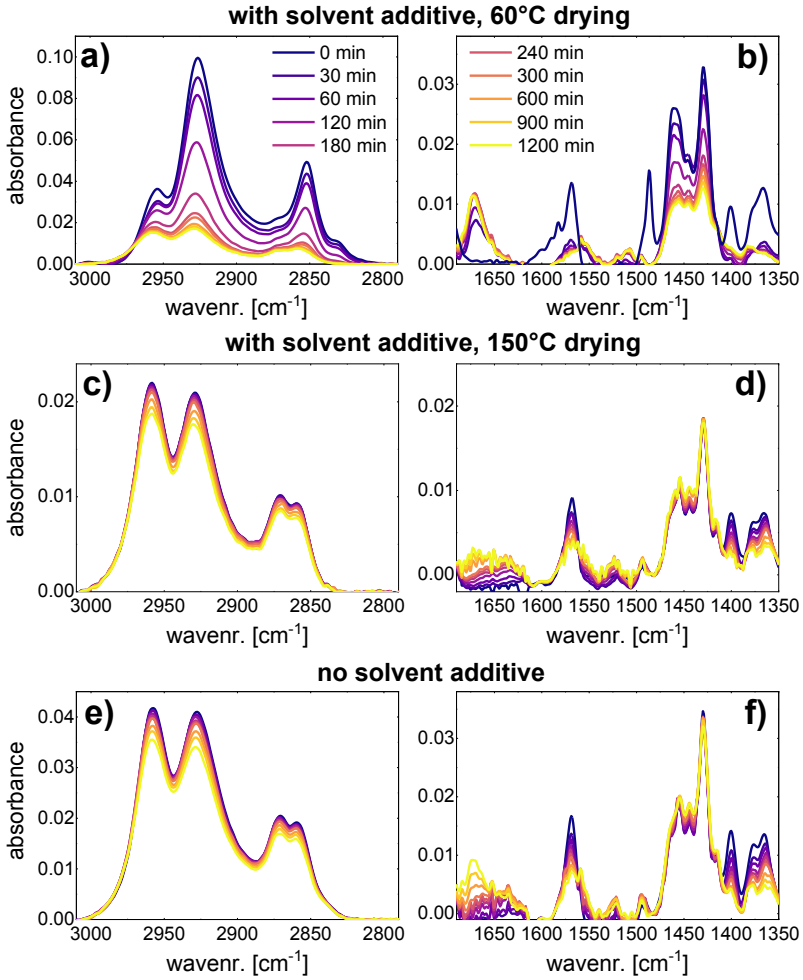

Figure 91: In situ FTIR absorbance spectra of PTB7:PCBM blend films under LED illumination in the wavenumber ranges 3000 cm^{-1} to 2800 cm^{-1} (a, c e) and 1690 cm^{-1} to 1350 cm^{-1} (b, d, f). From top to bottom, the different samples with solvent additive dried at 60°C (a, b), with solvent additive dried at 150°C (c, d) and without solvent additive (e, f) are displayed. Adapted from [28] with permission from Wiley Publishing.

At wavenumbers higher than 1600 cm^{-1}, the FTIR intensity increases upon illumination in ambient atmosphere. These absorbance bands are assigned to C=O bonds that are formed during photooxidation of the PTB7:PCBM blend film. The creation of the new C=O bonds come with the breakage of existing bonds of the conjugated network, which is the key structural feature for the application of the studied material system as active layer in organic solar cells. Thus, the observed chemical changes are supposed to directly impair the desired material properties.

For a quantitative comparison of the development of e.g. peak positions and intensities, isolated parts of the spectra were fitted with Lorentzian functions. This is illustrated for the example of the methyl(ene) region of the fresh PTB7:PCBM sample produced without solvent additives in Figure 92. Every evident peak is fitted with one Lorentzian function, which is considered representative for the respective assigned bond vibration mode (according to Table 13). Where necessary, an underground correction was performed to isolate the peak of interest from the influence of neighboring features or compensate a negative baseline.

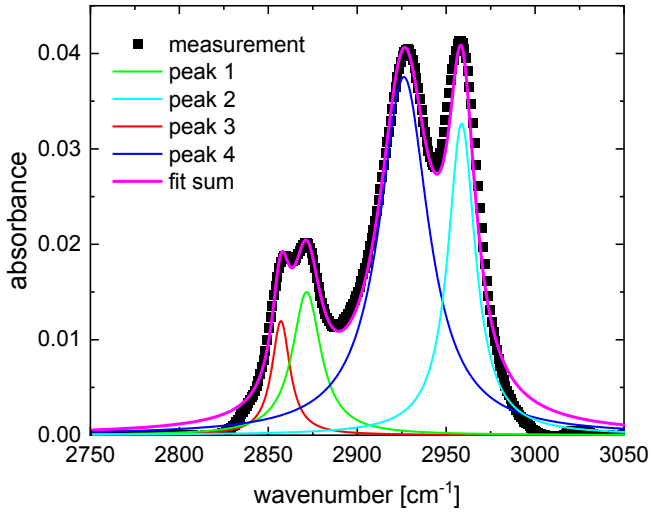

Figure 92: Exemplary fit of a region of the FTIR spectrum of a PTB7:PCBM film sample. Differently to the data shown in other figures, the energy scale on the x-axis is plotted from low to high wavenumbers. Adapted from [28] (supporting information) with permission from Wiley Publishing.

The resulting peak integrals from the Lorentzian fits of the respective parts of the FTIR spectra are plotted in Figure 93. The alkyl peaks are shown in red/orange, the C=C stretching mode of the thienothiophene unit in cyan and the C-F stretch, also located in the TT unit, in blue. Figure 93a confirms the very fast loss of intensity of the peaks at 1400 cm^{-1} and 1569 cm^{-1} for the solvent additive sample dried at 60 °C. Already after 20 minutes, they have decreased by more than 90 % indicating a very

rapid photoinduced degradation. The intensity of peaks related to the alkyl side chains also decrease significantly to approximately 20 % of the initial values, even though much slower than the TT associated features. Thereby, CH_3 peaks (as far as identifiable) decrease faster by a factor of around two compared to CH_2 peaks. This shows that the end positions of the side chains are not only below-average occupied by CH_3 groups after production with solvent additives and dried at 60 °C, but also stronger affected by the photodegradation.

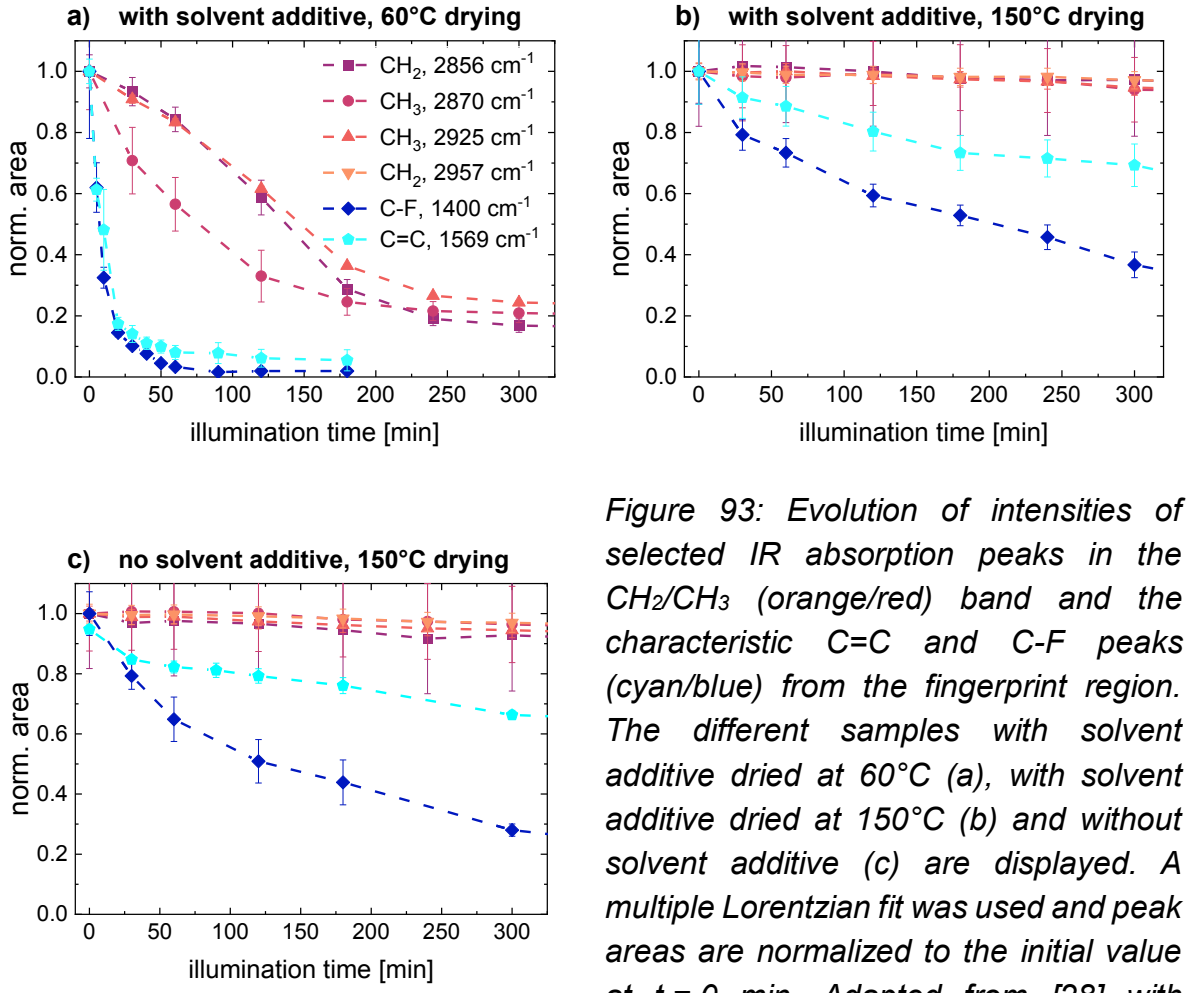

Figure 93: Evolution of intensities of selected IR absorption peaks in the CH_2/CH_3 (orange/red) band and the characteristic C=C and C-F peaks (cyan/blue) from the fingerprint region. The different samples with solvent additive dried at 60°C (a), with solvent additive dried at 150°C (b) and without solvent additive (c) are displayed. A multiple Lorentzian fit was used and peak areas are normalized to the initial value at t = 0 min. Adapted from [28] with permission from Wiley Publishing.

When comparing the two samples dried at 150 °C, it becomes evident that the relative development of the IR absorption peaks behaves rather similar for the sample produced with (Figure 93b) and without (Figure 93c) DIO:DPE as binary solvent additive. Their alkyl chain associated peaks are almost constant in intensity, which implies that the photoxidation that is evident from the rising intensity >1600 cm^{-1} (see Figure 90 and Figure 91) due to the creation of C=O bonds occurs predominantly at the conjugated backbone of the polymer.[263], [264], [265] The peaks, which are

representative for this part of the polymer at 1400 cm^{-1} and 1569 cm^{-1} decrease continuously during the first 300 minutes of illumination. The C-F absorption band decreases to approximately 30 % after 300 minutes and thus more than twice as fast as the C=C band, which reaches approximately 65 % - 70 % after this period. This indicates that the C-F bond is more susceptible for the photoinduced oxidation compared to the C=C bonds.

Complementary to the results from UV-vis spectroscopy, FTIR confirms that an incomplete drying of PTB7:PCBM blend films produced with DIO:DPE leads to an unstable bulk heterojunction structure that is significantly more prone to light induced degradation. FTIR helps to identify the locations in the chemical structure that are affected by photooxidation. For all samples, the conjugated network of the polymer, which is essential for the use of PTB7:PCBM bulk heterojunctions in organic solar cells, is much more affected than the alkyl side chains. This confirms the findings of previous reports.[22], [268], [270] Here, the C-F bond seems to be even more instable compared to the C=C bonds in the aromatic structures. When solvent additive molecules are left in the film, the observed degradation is accelerated dramatically. In this case also an oxidation of the alkyl side chains (which are relatively stable in the other samples) is observed. This might be due to the very fast complete oxidation of other parts of the molecules.

7.5 *In situ* Raman spectroscopy under Laser-illumination

In addition to UV-vis and FTIR, also Raman spectroscopy is used to study the response of PTB7:PCBM blend films to light and oxygen. Raman spectroscopy is a powerful method to investigate vibrations in conjugated systems such as polymers and follow possible changes of the bonding structure on molecular level induced by e.g. photo-oxidation. In the studies with UV-vis and *in situ* FTIR spectroscopy presented before, a high power LED module was used to illuminate the samples and cause the degradation of PTB7:PCBM blend films, but also lasers can be used to induce the photooxidation in the samples.[22], [271] For the *in situ* Raman spectroscopy experiment that is presented in this chapter, the light of the Raman laser (785 nm) is used as cause for the degradation of the PTB7:PCBM films. Complementary to FTIR, the laser mediated *in situ* Raman spectroscopy is primarily sensitive to the

development of C-C and C=C bonds of the PTB7 conjugated system. Raman spectroscopy has been successfully used before to follow changes in polymer bond structures.[272], [273], [274] The timescale on which the degradation occurs is expected to be shorter because the laser yields a significantly higher power per unit area than the LED. Since the used laser acts as both, cause for the degradation and probe for the Raman measurement, it can be assumed, that the degradation at the probed spot progresses linearly as long as the experimental geometry remains unchanged, which was the case as the experiment. The measurements were performed for one sample after the other. The modular Horiba Raman system, designed for the application in the TOFTOF neutron spectrometer as described in Chapter 4.5 is used for the Raman measurements that are presented in this chapter. The measurements were performed in the sample chamber of TOFTOF.

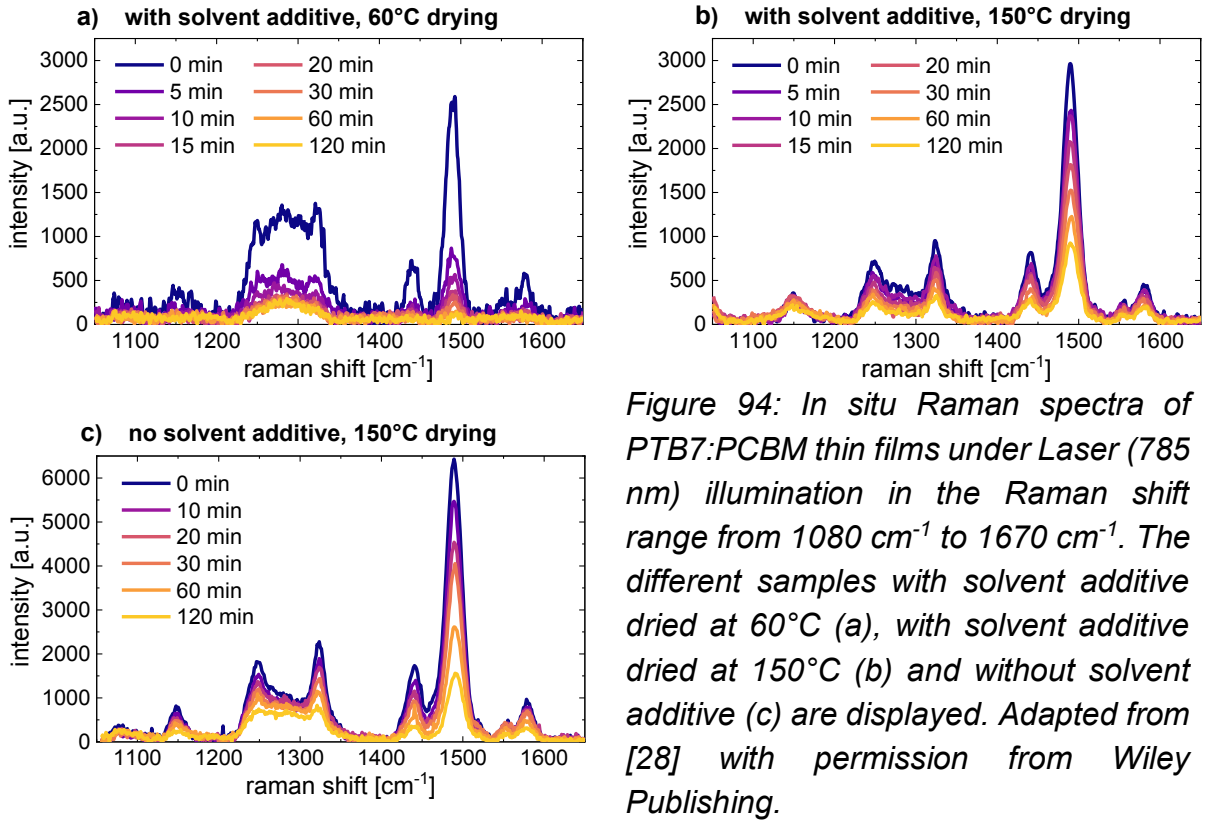

Figure 94: In situ Raman spectra of PTB7:PCBM thin films under Laser (785 nm) illumination in the Raman shift range from 1080 cm^{-1} to 1670 cm^{-1}. The different samples with solvent additive dried at 60°C (a), with solvent additive dried at 150°C (b) and without solvent additive (c) are displayed. Adapted from [28] with permission from Wiley Publishing.

Figure 94 shows the Raman spectra of the three samples, which were already analyzed by UV-vis and FTIR spectroscopy in the previous sections, in the relevant Raman shift range between 1050 cm^{-1} and 1650 cm^{-1}. The spectra were recorded *in situ* under continuous laser illumination for 120 minutes. Figure 94a comprises the spectra of a PTB7:PCBM (1:1.5 wt.) film produced with DIO:DPE (3 vol % : 2 vol %)

as binary solvent additive dried at 60 °C, Figure 94b the spectra of the sample produced with DIO and DPE dried at 150 °C and Figure 94c the spectra of the sample, produced without any solvent additive also dried at 150 °C.

Except the peak at 1250 cm^{-1} that represents C-H vibrations, all distinct Raman peaks in the studied range are representative for the conjugated network of the polymer PTB7 and the fullerene PCBM. The assignment of the individual peaks according to literature is given in Table 14.[22], [271], [275] The peak at 1325 cm^{-1} represents the stretching vibration of C-C single bonds. The characteristic Raman features between 1400 cm^{-1} and 1600 cm^{-1} contain information about stretching vibrations of C=C double bonds that are found in the materials´ conjugated networks. According to Table 14 the peak at 1440 cm^{-1} stands for the TT-thiophene rings and the BDT-backbone, the peak at 1490 cm^{-1} for the BDT in general and the peaks at 1550 cm^{-1} and 1580 cm^{-1} for the non-fluorinated and fluorinated TT-entities. The spectra from the low temperature dried solvent additive sample in Figure 94a is clearly noisier compared to the other spectra. An effect from the film surface morphology might account for this but no significant differences in the film topography have been found with profilometry. In particular the two samples produced with solvent additives (60 °C and 150 °C dried) appear very similar, thus effects from e.g. surface roughness are unlikely.

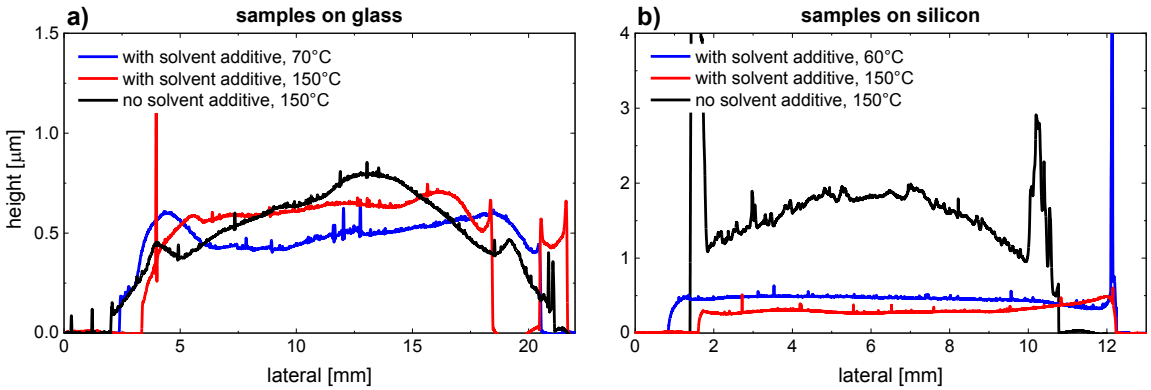

Figure 95: Film profiles of the different samples on glass (a) as used for UV-vis absorption spectroscopy and silicon (b) as used for XRD, FTIR and Raman spectroscopy.

This is evident from Figure 95, which shows the profiles of exemplary films on both, glass (Figure 95a) and silicon as used for FTIR and Raman (Figure 95b). Film thicknesses of around 0.5 µm are found except for the sample prepared without solvent additive, which is thicker when prepared in silicon. All samples appear to be relatively

homogeneous and flat, especially the samples that are produced with DIO:DPE coated on silicon that are of relevance here.

Raman peak position	assigned bond vibration
1250 cm^{-1}	C-H asymmetric bend
1325 cm^{-1}	C-C stretch
1440 cm^{-1}	C=C stretch in TT-thiophene rings & BDT backbone
1490 cm^{-1}	C=C stretch in BDT backbone & side chains
1550 cm^{-1}	C=C stretch in non-fluorinated TT-thiophene rings
1580 cm^{-1}	C=C stretch in fluorinated TT-thiophene rings

Table 14: Positions of the relevant Raman peaks in the range between 1200 cm^{-1} and 1600 cm^{-1} with the assigned types of bond vibration according to literature.[22], [271], [275]

From Figure 94 it is evident that upon laser illumination in ambient atmosphere, the characteristic Raman features loose intensity. This is an indication for the photooxidation of the PTB7:PCBM bulk heterojunction, which that damages the conjugated network of the polymer and thus impairs its usability as active material in organic solar cells. In analogy to the previous results, obtained by UV-vis and FTIR spectroscopy, the solvent additive sample that was dried at only 60 °C loses its Raman peaks significantly faster compared to the other two samples. For a quantitative comparison of the development of the Raman features of the three samples, all spectra were fitted with Lorentzian functions as depicted in Figure 96 after the removal of the background. Every Raman peak is described by one Lorentzian. In the range between 1220 cm^{-1} and 1350 cm^{-1} a third broader Lorentzian at around 1280 cm^{-1} is needed in addition to the two peaks described in Table 14 to describe the data. This additional Lorentzian is not identified as a particular bond vibration as it is likely to be a superposition of several modes in this Raman shift region, which likely originate from solvent(additive) bond vibrations as the feature is much more pronounced in the insufficiently dried sample (see Figure 94a). This peak seems to be relatively stable upon laser illumination and it decays relatively slow compared to the peaks at higher Raman shifts. It is even the last remaining peak in the low temperature dried solvent additive sample. The very low significant peaks at 1390 cm^{-1} and 1550 cm^{-1}, visible in Figure 96, were not fitted with their own Lorentzian because this influenced the results for the more significant peaks. Especially if these smaller peaks completely disappear

during the experiment, the fit function would have to be adapted, which would significantly influence the results of the peaks that are of actual interest.

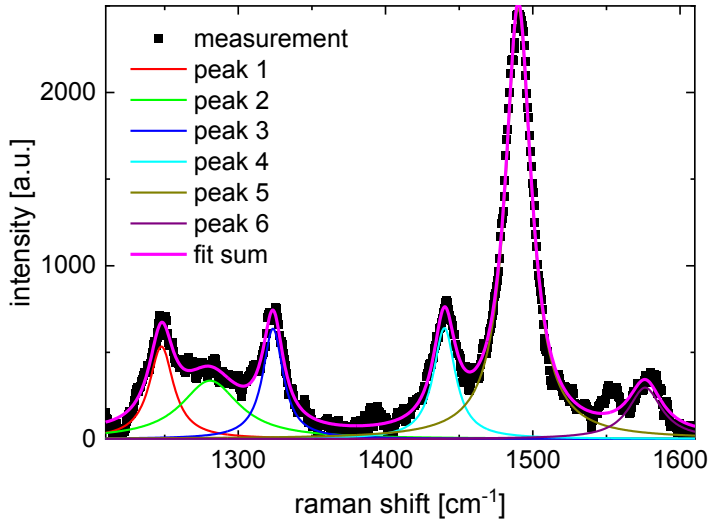

Figure 96: Exemplary fit for the region from 1210 cm^{-1} to 1610 cm^{-1} of the Raman spectrum of an undegraded PTB7:PCBM film sample produced with DIO and DPE as solvent additives.

Results from the Lorentz fits of the *in situ* Raman spectra are presented in Figure 97, which shows the development of the peak integrals over the first 60 minutes of laser illumination normalized to the respective initial value. As sample and experimental geometry were unchanged during the laser induced *in situ* Raman degradation experiment of each sample, the peak integral can be seen as a measure of the abundance of the respective bond in the probed area. In the sample that was prepared with solvent additives and dried at 60 °C, all Raman peaks lose their intensity very fast. After only 10 minutes of laser illumination the peak integrals reach values between 10 % and 30 % of the initial. After this very fast initial decrease, the peaks continue to shrink and especially the ones representative for the conjugated network, located at 1440 cm^{-1}, 1490 cm^{-1} and 1580 cm^{-1}, become practically unrecognizable within the significance of the fit.

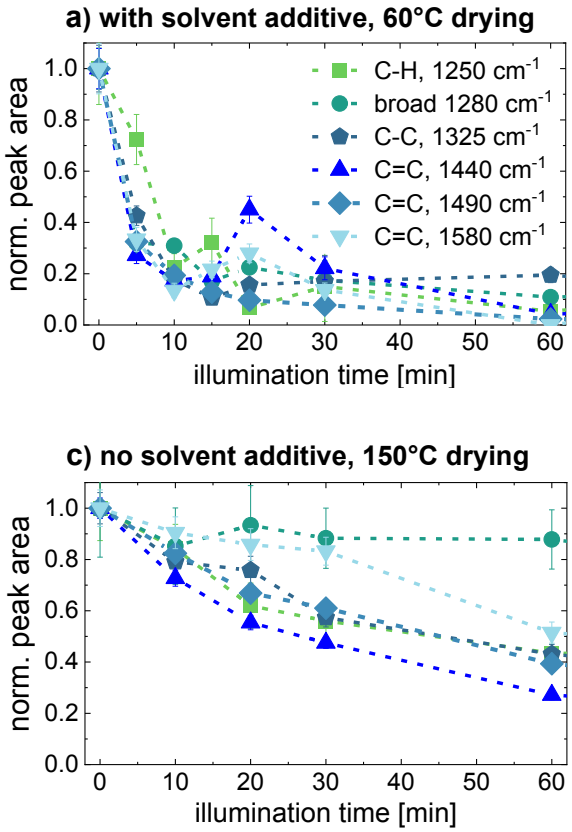

Figure 97: Development of intensities of selected Raman peaks. The different samples with solvent additive dried at 60°C (a), with solvent additive dried at 150°C (b) and without solvent additive (c) are displayed. A multiple Lorentzian fit is used and peak areas are normalized to their initial value at t = 0 min. Dashed lines are guides to the eye. Adapted from [28] with permission from Wiley Publishing.

Both samples that were dried at 150 °C produced with (Figure 97b) and without (Figure 97c) solvent additives show improved stability of their Raman features. After 10 minutes of laser irradiation, the relevant peaks still retain between 60 % and 90 % of their initial area, whereas 60 minutes of laser irradiation lead to a decrease down to between 30 % and 50 %. Over prolonged laser induced degradation, the peak at 1580 cm^{-1} seems to be the most stable, which indicates that the thienothiophene units of PTB7 might be less affected by the photooxidation than the benzodithiophene units. The very prominent peaks at 1440 cm^{-1} and 1490 cm^{-1}, which predominantly represent the benzodithiophene segments, decrease significantly faster than the 1580 cm^{-1} peak in the initial phase in both 150 °C dried samples. For longer laser-induced degradation, they behave differently, though. For the samples produced with solvent additives, the degradation rates of all peaks parallelize after 30 - 60 minutes. In contrast, for the sample produced without solvent additives, the differences that develop in the initial phase persist over the studied timescale for the sample. It should be noted, that the broad peak at 1280 cm^{-1} is almost stable in the pure PTB7:PCBM sample, whereas it decreases similar to the other peaks in both samples that were produced with DIO and DPE as solvent additives. This could support the assumption that this Raman feature might be induced by solvent effects.

To study the composition of the Raman spectra and the relative ratios of the individual peaks among each other, Figure 98 shows the fractions of the respective peak integral from the total fitted area, irrespective of its absolute value. The relative evolution of the Raman peaks is followed for the entire 120 minutes of the *in situ* laser induced degradation experiment.

The most prominent feature in the present Raman spectra, the BTD-associated peak at 1490 cm^{-1}, is shown in red in Figure 98. Its relative intensity compared to the total Raman intensity decreases in all three samples upon the laser irradiation. The PTB7:PCBM (1:1.5 wt.) film produced with DIO:DPE (3 vol % : 2 vol %) as binary solvent additive dried at 60 °C is represented by Figure 98a and shows clearly the strongest decay of this peak as it accounts for more than 30 % of the total fitted intensity in the beginning and reaches less than 5 % after 120 minutes of laser illumination. The solvent additive sample dried at 150 °C (Figure 98b) and the sample produced without solvent additives (Figure 98c) show a weaker decay of the 1490 cm^{-1} peak, which starts to occur after around 30 minutes. While the former (with solvent additives) shows good stability of the peak, only losing around 20 % of the initial relative intensity, the latter (without solvent additives) loses around 30 %. This indicates a stabilization of the conjugated system, if the PTB7:PCBM film is produced with binary solvent additive and dried properly. The negative effects on degradation behavior from insufficient drying seem to exceed the effect of not using solvent additives, for the present sample preparation conditions.

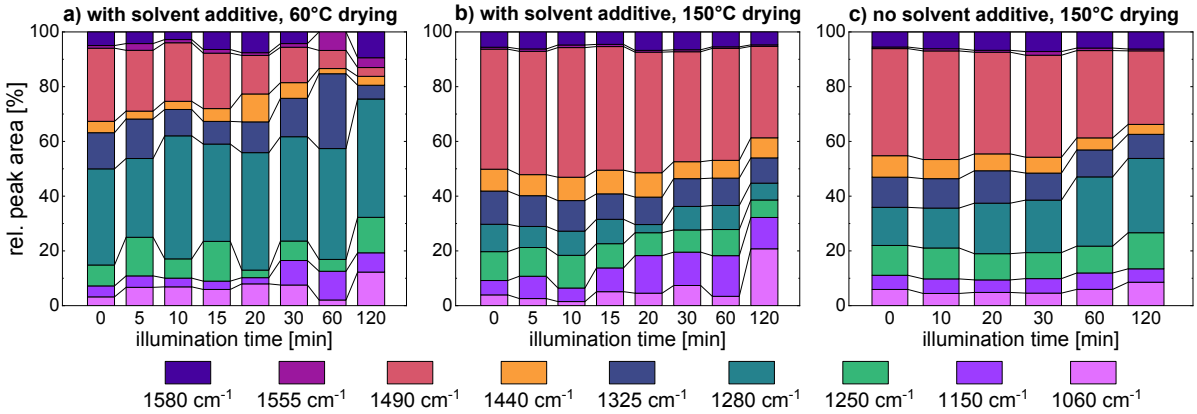

Figure 98: Development of the relative Raman peak intensities of PTB7:PCBM thin films during laser (785 nm) illumination. From left to right the different samples with solvent additive dried at 60°C (a), with solvent additive dried at 150°C (b) and without solvent additive (c) are displayed. A multiple Lorentzian fit is used and peak areas are normalized to 100 %, irrespective of the absolute intensities for each measurement. Adapted from [28] with permission from Wiley Publishing.

While the peaks of the conjugated network shown in the top part of Figure 98 (orange, red, dark violet) generally decrease over illumination time, the peaks of simple C-C and C-H bonds at lower wavenumbers, shown at the bottom (violet, green) tend to increase in their relative intensity. This suggests that photooxidation reduces the degree of conjugation in the PTB7:PCBM bulk heterojunction and increases the relative fraction of singly bonded carbon chains and C-H groups. It occurs that the distribution of colors is rather similar for the first column (initial state) of Figure 98a (sample with solvent additive dried at 60 °C) and the last column (final, degraded state) of Figure 98c (sample without solvent additive). This implies that already the structure formation of the conjugated network is incomplete in the sample with residual solvent additive molecules as its initial state is comparable to the 120 minutes laser-degraded state of a properly dried sample.

As mentioned before, the peak at 1490 cm^{-1} is a good measure for the state of the conjugated network in the studied PTB7:PCBM bulk heterojunction films and in addition it is fitable with good reliability. Beyond a decrease of intensity, a shift of this Raman peak towards larger wavenumbers has been interpreted as an measure for the degradation of the PTB7 conjugated system.[271] The respective peak positions for the three samples as a function of illumination time are shown in Figure 99.

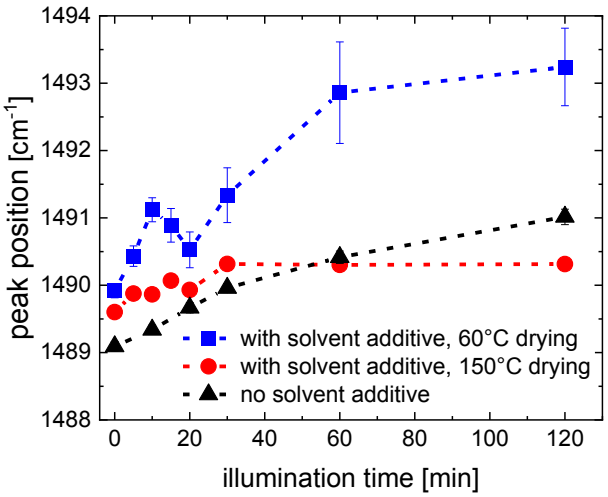

Figure 99: Evolution of peak position of the most prominent PTB7 Raman peak at around 1490 cm^{-1} during laser (785 nm) illumination. Respective peak positions are displayed for the different samples with solvent additive dried at 60°C (blue), with solvent additive dried at 150°C (red) and without solvent additive (black). The peak is fitted with a single Lorentzian function. Adapted from [28] with permission from Wiley Publishing.

The solvent additive sample dried at 60 °C (blue) shows a distinct peak shift of more than 3 cm^{-1} towards higher wavenumbers after 20 minutes of laser illumination. In the first 20 minutes, the shift of the peak is not following a clear trend, which indicates a short delay of the BDT degradation.

The samples that were dried at 150 °C show a more gradual upshift of the position of the 1490 cm^{-1} Raman peak. The dimension of this shift is in the range of 1 cm^{-1} and 2 cm^{-1} and thus significantly smaller compared to the low temperature dried solvent additive sample. Comparing the peak shifts of the films dried at 150 °C, the sample produced with solvent additive (red) seems to be more stable against the laser induced degradation of the PTB7 conjugated network compared to the neat sample (black). This is in accordance with results shown earlier in this chapter.

In summary, the *in situ* Raman degradation study using the Raman laser as cause for the photooxidation of PTB7:PCBM blend films confirms the findings from UV-vis and FTIR spectroscopy. The presence of leftover solvent additives in the PTB:7PCBM bulk heterojunction structure leads to extremely high degradation susceptibility. If dried properly, the use of solvent additives can not only have positive effects on solar cell performance, but possibly also on the stability of the active layer at ambient atmosphere. This underlines the importance of the appropriate drying procedure when solvent additives are used.

7.6 Summary

In the present chapter, a detailed study of the degradation behavior of PTB7:PCBM blend films under illumination at ambient atmosphere is presented. The focus is on the influence of the use of DIO and DPE as binary solvent additive during the solution-based film fabrication and different drying temperatures. UV-vis spectroscopy is used to study the optical absorption properties and electronic transitions, FTIR spectroscopy for the investigation of the chemical bonding and Raman spectroscopy to probe the general state of the conjugated network. While for UV-vis and *in situ* FTIR spectroscopy a high-power LED module is used for the large-area illumination of the samples, the Raman laser itself was used for this purpose in the *in situ* Raman experiment. All methods coincide in their result that all PTB7:PCBM samples undergo severe degradation under the applied conditions. The sample that was produced with solvent additives and dried at 60 °C shows by far the fastest and most pronounced

degradation in all studied aspects. This is attributed to solvent additive molecules that can be removed from the film at a higher drying temperature of 150 °C but are left over after drying at 60 °C (70 °C in the UV-vis study). They are assumed to prevent the formation of a stable blend microstructure and provide pathways for material transport. Thus, e.g. oxygen or other reactive species can easily penetrate into the film and, together with the incident photons providing the required energy, alter the chemical bonds and physical structure and properties of the materials. These effects might be fostered by the high mobility of solvent additive molecules inside the “solid” film that was shown in Chapter 6.5. The C-F bond in the thienothiophene unit of PTB7 was found to be one of the first and most vulnerable attack points for the photooxidation followed by the conjugated rings along the polymer backbone. As an intact conjugated system is essential for the function of the studied material as active layer in organic solar cells, the photodegradation has to be avoided in devices. The detrimental influence of leftover solvent molecules and photooxidation of the active layer on the long term stability of OPV devices has been shown frequently.[252], [259], [260], [276], [277], [278]

The present findings underline the importance of an adequate drying of the active layer material before the application in solar cells. It should be noted that the drying procedure can be finely tuned and its effect may decrease/increase gradually with the applied temperature, duration or vacuum. Thus, the present findings may be of relevance for the development of the next generation of organic solar cell materials.

8 Conclusion and Outlook

The objective of the present thesis is the extension of the knowledge base for PTB7:PCBM blend films. If blended in a suitable ratio and with an adequate procedure, the two materials arrange in a bulk heterojunction (BHJ) structure. This represents an important model system for low band gap polymer:fullerene organic solar cells. Thus, the results are of considerable interest for a large audience from this and related fields of organic electronics. Structural and characteristic photovoltaic properties were well studied before, but no measurements of dynamics are available for PTB7:PCBM films and only very few for related systems. Therefore, the first reported quasielastic neutron scattering (QENS) study in the material system PTB7:PCBM was realized and the results were evaluated with regard to internal dynamics of the polymer PTB7 within the blend. Beyond this, the influence of an alcohol treatment of the casted film and the use of solvent additives in the solution-based production process of the films on PTB7 dynamics were studied, also with QENS.

Based on the results of the QENS experiments, the degradation behavior of PTB7:PCBM BHJ films was investigated. In this study, the chemical and physical stability of the films were tracked with UV-vis, FTIR and Raman spectroscopy. Samples with and without solvent additives dried at high and low temperature were produced and exposed to ambient atmosphere and light irradiation to investigate a potentially unfavorable influence of residual solvent additive molecules in the BHJ structure.

For the first QENS study in the material system PTB7:PCBM the cold neutron time-of-flight chopper spectrometer TOFTOF (MLZ, Garching) was chosen due to its high specific neutron flux and appropriate energy resolution of ~20 µeV at a neutron wavelength of 8 Å. Energy transfer spectra S($\vec{Q}$, ω) were measured in the momentum transfer range from 0.2 Å^{-1} to 1.6 Å^{-1} and Fourier transformed to I($\vec{Q}$, t) spectra. This transformation was assessed to be beneficial since a solid fit of S($\vec{Q}$, ω) was not possible due to the inhomogeneity of motions in the studied system. A stretched exponential decay fit of I($\vec{Q}$, t) helps to account for this continuous spread of relaxation times and is commonly applied for polymer sample systems. By fits to the decay of the elastic component of S($\vec{Q}$, ω) and the decay of I($\vec{Q}$, t), values for mean square

displacements (MSDs) and effective diffusion coefficients (D_{eff}), respectively, were obtained. While the MSD can be seen as a measure for vibrational displacements of the whole molecule, including the backbone, D_{eff} describes the diffusive reorientations of the hydrogen-rich PTB7 side chains.

Both, diffusion coefficients and mean square displacements were determined as a function of temperature for pure PTB7 and blends with PCBM in weight ratios of 1:1 and 1:1.5 (PTB7:PCBM). Pure PCBM did not show any detectable diffusive dynamics within the studied energy/timescale window. One of the key findings presented in this thesis is the dynamic frustration of the PTB7 side chain motions in the presence of PCBM in a blend. This frustration is more pronounced if the PCBM content of the blend is increased. A logical explanation for this effect would be a spatial hindrance of the PTB7 side chain motions by embedded PCBM domains. For D_{eff}, this hindrance seems to be independent from temperature, whereas the degree of hindrance increases with temperature for the MSD.

The frequently applied alcohol treatment of the PTB7:PCBM blend film, which has proven to significantly increase power conversion efficiencies of resulting organic solar cells by a reduction of inner domain sizes, has no influence on molecular dynamics. The extracted relaxation times were unchanged upon the methanol treatment at all studied temperatures over the whole momentum transfer range.

The investigation of the influence of the use of solvent additives on molecular dynamics in an PTB7:PCBM bulk heterojunction structure yielded new insights. A regular drying procedure, as also applied before for e.g. OSC devices, was not sufficient to remove the high boiling point solvent additive DIO completely from the film. For the residual DIO molecules a high diffusivity, compared to the present PTB7 polymer side chain motions, was measured with QENS. At elevated temperatures in vacuum conditions, the leftover solvent additive can be extracted from the film, the measured apparent effective diffusion coefficient decreases and converges towards the value that was found for a neat film. Nonetheless, the film that develops when DIO is used as solvent additive, shows increased diffusivity of the PTB7 side chains, which is a sign for intense reorientations within the structure. For resulting devices, this means that the formed metastable microstructures might be modified easily and need special stabilization measures to ensure reasonable long-termusability.

Beyond the QENS analysis of molecular dynamics, the physical and chemical stability of PTB7:PCBM bulk heterojunction blend films under illumination in the

presence of oxygen were studied with XRD, UV-vis, FTIR and Raman spectroscopy. Samples with solvent additive were prepared with different drying temperatures to yield both, samples presumably with residual solvent additive molecules as well as fully dried. A reference sample produced without solvent additive was studied for comparison. The optical absorbance in the wavelength regime that is relevant for the application in organic solar cells is dramatically reduced upon illumination in ambient atmosphere. FTIR and Raman spectroscopy come to the coinciding result that the conjugated network degrades by the brakeage of C=C bonds under the combined influence of light and oxygen. Furthermore, an uptake of oxygen into the film by the formation of C=O bonds was detected. If the PTB7:PCBM blend films are dried properly, these unfavorable effects, namely photobleaching and photooxidation, occur on comparable time- and intensity scales, irrespective if solvent additives are used or not. This picture changes if the drying temperature is reduced and solvent additive molecules are expected to remain in the film. In this case, the destruction of the conjugated system and the bleaching of the sample happens much faster and to a much larger extent. It was also demonstrated, that UV-irradiation is not needed for photooxidation as stated frequently, but regular LED light sources without UV contribution do also trigger this process in the present study. These results underline the great importance of an adequate drying procedure of PTB7:PCBM active layers for a reasonable long-term operation of respective PV modules, especially if solvent additives are used in the fabrication process. It can be assumed that this importance also holds for other applications and material systems.

Summarizing, the findings of the present thesis cover the molecular dynamics and the degradation behavior of the material system PTB7:PCBM. The results extend the knowledge base in this important model system for low band gap polymer organic solar cells. The critical role of a suitable film drying for device stability is shown. Since the degradation mechanisms might be fundamentally different in other material systems, they must be fully understood to be prevented. A detailed investigation similar to the present one is needed for all novel compounds of interest. This is well represented in the latest research, which also targets its focus towards real world applicability and long-term usability of third-generation solar cells in terms of photo-, air-, thermal- as well as mechanical stability and not only on achieving new performance records with potentially very fragile materials or structures. Other actual topics like green fabrication processes for OSCs or the transition from lab- to industrial scale are important steps towards the economic breakthrough of the emerging solar cell technologies. This has

the potential to promote a shift towards a sustainable production of green energy to serve the rapidly increasing world demand.

Annex: Laser Pump – Neutron Probe Setup

In the framework of the present PhD thesis, a laser pump – neutron probe setup was developed and constructed. It is designed as a novel sample environment at the cold neutron time-of-flight chopper spectrometer TOFTOF (FRM II, Garching). Goal of the new setup is to illuminate the sample with pulsed monochromatic light of adjustable wavelength and intensity during the quasielastic neutron scattering experiment. This capability would be a unique feature among neutron spectrometers at present state. Samples that are intended to be investigated with the setup are e.g. photosensitive proteins, which undergo a structural change in the form of a photocycle upon absorption of a photon. Proofs of the concept at other neutron spectrometers have been performed by Pieper et al. for the system of bacteriorhodopsin (BR) and its purple membrane.[279], [280], [281], [282] Other in-operando neutron studies using light as stimulus have been attempted in the 1990s already (groups of R.E. Lechner and M.C. Bellissent-Funel, unpublished), but experimental parameters were lacking elaborateness in terms of sufficient light excitation of the sample or the matching of the QENS time window and the dynamics time scale. A chemical stabilization of intermediate photocycle state has been performed successfully,[283] but an excitation with light is essential to probe protein dynamics under physiological conditions.

Further conceivable application systems for the new laser pump – neutron probe setup at TOFTOF are the light sensitive functions of photosystem II,[284] the pigment protein c-phycocyanin of cyanobacteria [285] or the photosynthetic system of rhodopsuedomonas viridis.[286]

Due to spatial restrictions in the TOFTOF sample chamber, the excitation laser has to be placed outside and the light has to be guided to the sample position by an optical system. Figure 100 shows the schematic layout of the system.

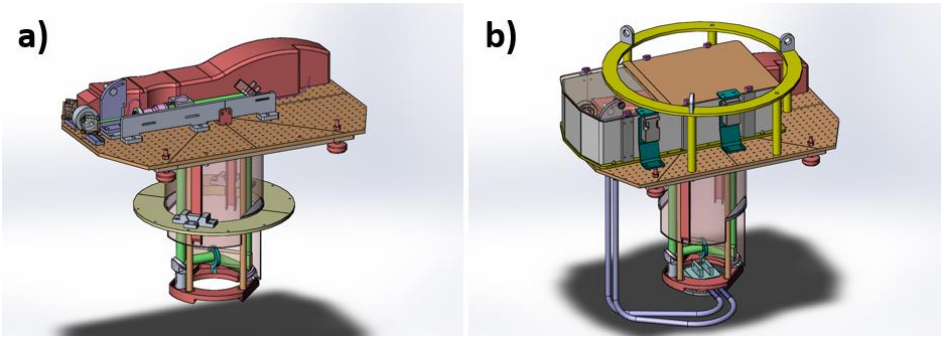

Figure 100: Schematic layout of the laser pump – neutron probe setup for TOFTOF. a) shows the laser module in red and the optical system with the beam path indicated in green. b) shows the implemented safety precautions. An eloxed aluminum cage with interlocks on top of the base plate and a respective tube around the light paths under the base plate. 3D model images produced by Herbert Meier (former instrument technician at TOFTOF).

A matte black eloxed optical plate is used as the base of the setup. The laser module (red in Figure 100) is mounted on the plate and the beam (green in Figure 100) with initial diameter of 6 mm is redirected by 180 ° by two mirrors, between which a laser monitor can be placed to measure the pulse energy. Then the beam is expanded by a factor of 5, i.e. to a diameter of 30 mm and spited in a beam splitter cube. One beam is directed directly downwards by the cube and the other beam continues to travel horizontally to a mirror that also directs it downwards (partly hidden by the mounting plate in Figure 100). Once they reach the approximate height of the sample position (slightly below), the two vertical beams hit mirrors that are aligned to direct them onto the sample from both sides. One of the mirrors has to be placed slightly below the sample height to not interfere with the neutron beam. The intended sample cell consists of an aluminum frame and two quartz windows to allow illumination from both sides. The sample thickness between the quartz windows is 0.6 mm but can be varied by simple modifications of the cell. Figure 101 shows detail images of the actual setup (laser off). The black shielding and the grounding cable are visible in Figure 101a. Figure 101b shows the optical system on top of the base plate with opened safety shielding. Figure 101c and d show the dismantled mirror system below the base plate, which direct the vertical beams towards the sample position. The approximate sample position of TOFTOF when the system is installed in the TOFTOF sample chamber is indicated as yellow symbol.

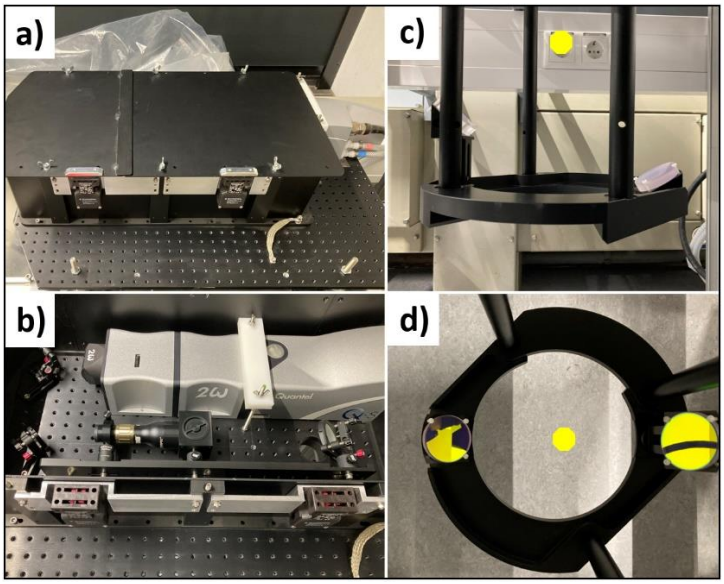

Figure 101: Photographs of the laser pump – neutron probe setup. a) closed shielding around the optical system above the base plate, b) a view on the laser and the optical system above the base plate, c) and d) the mirror system under the baseplate with the approximate intended sample position indicated with a yellow polygon

As source for the laser light a Q-smart 450 Nd-YAG laser module was purchased from the company Quantel (France) together with an attenuation module that allows for stepless reduction of the laser intensity and harmonic modules to convert the initial 1032 nm laser into the desired wavelength. Characteristic properties of the Laser are listed in Table 15.

Pulse frequency	10 Hz (20 Hz)
Pulse energy	220 mJ (200 mJ)
Pulse duration	5 ns
Pointing stability	< 40 µrad
Beam divergence	< 0.5 mrad
Jitter	± 0.5 ns
Beam diameter	6.5 mm
Polarization	> 90 % (> 80 %) vertical

Table 15: Characteristics of the Quantel Q-smart 450 Laser module as used for the laser pump – neutron probe setup. Values are given for the operation with one harmonic generator, i.e. with 532 nm according to the manufacturer´s datasheet.

Since the used high-power pulsed laser is classified as class 4 laser, special safety regulations apply for its use in the neutron guide hall of FRMII, where TOFTOF is located. As visible in Figure 101a, the entire beam path on top of the base plate is enclosed in a black eloxed aluminum housing. The lower part of the optical system that is inserted into the TOFTOF sample chamber is also covered by a respective aluminum tube to prevent the uncontrolled escape of intense laser radiation (not visible in Figure 101). For complete optical sealing of the laser pump system installed at the TOFTOF neutron spectrometer, the window of the sample chamber was covered with a foil that absorbs potentially leaking light at the intended wavelength of 532 nm, that can be changed if other laser wavelengths are used.

Optical parts like mirrors, beam expander and splitter and the appropriate mounting material was purchased from Edmund Optics (Great Britain). The safety shielding was developed by the instrument technicians of TOFTOF in cooperation with the FRMII radiation protection authorities and manufactured in the internal workshops of FRMII ant TUM Physics.

The choice of the laser was also influenced by the necessity of a Q-switch and the possibility for external triggering by the TOFTOF chopper signal. This is required since the studied processes occur on microsecond timescale and the neutron probe pulses of TOFTOF and the laser pump pulses of the setup need to be exactly coordinated in time in order to obtain meaningful results and resolve the molecular dynamics as a function of the time after laser excitation of the sample. Therefore, also the TOFTOF detector electronics had to be changed from the continuous recording mode to a time resolved event mode, synchronized with the laser pulses. This task was performed mainly by the instrument control group of FRMII in cooperation with the TOFTOF instrument scientists.

Even though all components of the laser pump – neutron probe setup were taken in operation and tested successfully, a final implementation into the TOFTOF neutron spectrometer and in-operando QENS measurement of light induced processes is still pending at the present state. As soon as FRMII comes back to regular operation respective experimental beamtime will be scheduled.

Bibliography

[1] *2022 Energy Statistics Pocketbook*; Statistics papers / Department of Economic and Social Affairs Series E No. 5; United Nations Publications, 2022.

[2] Solomon, S.; Qin, D.; Manning, M.; Averyt, K.; Marquis, M. *Climate Change 2007 - The Physical Science Basis: Working Group I Contribution to the Fourth Assessment Report of the IPCC* 4; Cambridge university press, 2007.

[3] Ritchie, Hannah, Roser, Max, Rosado, Pablo. CO_2 and Greenhouse Gas Emissions. https://ourworldindata.org/co2-and-greenhouse-gas-emissions (accessed on 2023/08/08).

[4] Burger, B. Öffentliche Nettostromerzeugung in Deutschland im Jahr 2022. *Fraunhofer ISE* **2023**.

[5] Wirth, H. Aktuelle Fakten zur Photovoltaik in Deutschland. *Fraunhofer ISE* **2023**.

[6] Vigil-Galán, O.; Courel, M.; Andrade-Arvizu, J. A.; Sánchez, Y.; Espíndola-Rodríguez, M.; Saucedo, E.; Seuret-Jiménez, D.; Titsworth, M. Route Towards Low Cost-High Efficiency Second Generation Solar Cells: Current Status and Perspectives. *J Mater Sci: Mater Electron* **2015,** *26* (8), 5562–5573.

[7] Kant, N.; Singh, P. Review of Next Generation Photovoltaic Solar Cell Technology and Comparative Materialistic Development. *Materials Today: Proceedings* **2022,** *56*, 3460–3470.

[8] Zdyb, A. *Third Generation Solar Cells;* Taylor & Francis, 2023.

[9] Espinosa, N.; Garcia-Valverde, R.; Urbina, A.; Krebs, F. C. A Life Cycle Analysis of Polymer Solar Cell Modules Prepared using Roll-To-Roll Methods under Ambient Conditions. *Solar Energy Materials and Solar Cells* **2011,** *95* (5), 1293–1302.

[10] Lungenschmied, C.; Dennler, G.; Neugebauer, H.; Sariciftci, S. N.; Glatthaar, M.; Meyer, T.; Meyer, A. Flexible, Long-Lived, Large-Area, Organic Solar Cells. *Solar Energy Materials and Solar Cells* **2007,** *91* (5), 379–384.

[11] Kaltenbrunner, M.; White, M. S.; Głowacki, E. D.; Sekitani, T.; Someya, T.; Sariciftci, N. S.; Bauer, S. Ultrathin and Lightweight Organic Solar Cells with High Flexibility. *Nature communications* **2012,** *3* (1), 770.

[12] Koeppe, R.; Hoeglinger, D.; Troshin, P. A.; Lyubovskaya, R. N.; Razumov, V. F.; Sariciftci, N. S. Organic Solar Cells with Semitransparent Metal Back Contacts for Power Window Applications. *ChemSusChem: Chemistry & Sustainability Energy & Materials* **2009,** *2* (4), 309–313.

[13] Chen, C.-C.; Dou, L.; Gao, J.; Chang, W.-H.; Li, G.; Yang, Y. High-Performance Semi-Transparent Polymer Solar Cells Possessing Tandem Structures. *Energy Environ. Sci.* **2013,** *6* (9), 2714–2720.

[14] Gangwar, P.; Kumar, N. M.; Singh, A. K.; Jayakumar, A.; Mathew, M. Solar Photovoltaic Tree and its End-Of-Life Management using Thermal and Chemical Treatments for Material Recovery. *Case Studies in Thermal Engineering* **2019,** *14*, 100474.

[15] Krebs, F. C. Polymer Solar Cell Modules Prepared using Roll-To-Roll Methods: Knife-Over-Edge Coating, Slot-Die Coating and Screen Printing. *Solar Energy Materials and Solar Cells* **2009,** *93* (4), 465–475.

[16] Søndergaard, R.; Hösel, M.; Angmo, D.; Larsen-Olsen, T. T.; Krebs, F. C. Roll-To-Roll Fabrication of Polymer Solar Cells. *Materials Today* **2012,** *15* (1-2), 36–49.

[17] Graetzel, M.; Janssen, R. A. J.; Mitzi, D. B.; Sargent, E. H. Materials Interface Engineering for Solution-Processed Photovoltaics. *Nature* **2012,** *488* (7411), 304–312.

[18] Noh, J. H.; Im, S. H.; Heo, J. H.; Mandal, T. N.; Seok, S. I. Chemical Management for Colorful, Efficient, and Stable Inorganic-Organic Hybrid Nanostructured Solar Cells. *Nano letters* **2013,** *13* (4), 1764–1769.

[19] Magadley, E.; Kabha, R.; Dakka, M.; Teitel, M.; Friman-Peretz, M.; Kacira, M.; Waller, R.; Yehia, I. Organic Photovoltaic Modules Integrated Inside and Outside a Polytunnel Roof. *Renewable Energy* **2022,** *182*, 163–171.

[20] Riede, M.; Spoltore, D.; Leo, K. Organic Solar Cells—The Path to Commercial Success. *Advanced Energy Materials* **2021,** *11* (1), 2002653.

[21] Manceau, M.; Rivaton, A.; Gardette, J.-L.; Guillerez, S.; Lemaître, N. The Mechanism of Photo- and Thermooxidation of Poly(3-hexylthiophene) (P3HT) Reconsidered. *Polymer Degradation and Stability* **2009,** *94* (6), 898–907.

[22] Kim, S.; Rashid, M. A. M.; Ko, T.; Ahn, K.; Shin, Y.; Nah, S.; Kim, M. H.; Kim, B.; Kwak, K.; Cho, M. New Insights into the Photodegradation Mechanism of the PTB7-Th Film: Photooxidation of π-Conjugated Backbone upon Sunlight Illumination. *J. Phys. Chem. C* **2020,** *124* (5), 2762–2770.

[23] Bertho, S.; Janssen, G.; Cleij, T. J.; Conings, B.; Moons, W.; Gadisa, A.; D'Haen, J.; Goovaerts, E.; Lutsen, L.; Manca, J.; others. Effect of Temperature on the Morphological and Photovoltaic Stability of Bulk Heterojunction Polymer: Fullerene Solar Cells. *Solar Energy Materials and Solar Cells* **2008,** *92* (7), 753–760.

[24] Conings, B.; Bertho, S.; Vandewal, K.; Senes, A.; D'Haen, J.; Manca, J.; Janssen, R. A. J. Modeling the Temperature Induced Degradation Kinetics of the Short Circuit Current in Organic Bulk Heterojunction Solar Cells. *Appl. Phys. Lett.* **2010,** *96* (16), 81.

[25] Dennler, G.; Lungenschmied, C.; Neugebauer, H.; Sariciftci, N. S.; Labouret, A. Flexible, Conjugated Polymer-Fullerene-Based Bulk-Heterojunction Solar Cells: Basics, Encapsulation, and Integration. *J. Mater. Res.* **2005,** *20* (12), 3224–3233.

[26] Schwaiger, D.; Lohstroh, W.; Müller-Buschbaum, P. Investigation of Molecular Dynamics of a PTB7:PCBM Polymer Blend with Quasi-Elastic Neutron Scattering. *ACS Appl. Polym. Mater.* **2020**.

[27] Schwaiger, D. M.; Lohstroh, W.; Müller-Buschbaum, P. The Influence of the Blend Ratio, Solvent Additive, and Post-Production Treatment on the Polymer Dynamics in PTB7:PCBM Blend Films. *Macromolecules* **2021,** *54* (13), 6534–6542.

[28] Schwaiger, D. M.; Lohstroh, W.; Wolf, M.; Garvey, C. J.; Müller-Buschbaum, P. In-Situ Study of Degradation in PTB7 : PCBM Films Prepared with the Binary Solvent Additive DPE : DIO. *J. Polym. Sci.* **2023,** *61* (15), 1660–1674.

[29] Chiang, C. K.; Fincher Jr, C. R.; Park, Y. W.; Heeger, A. J.; Shirakawa, H.; Louis, E. J.; Gau, S. C.; MacDiarmid, A. G. Electrical Conductivity in Doped Polyacetylene. *Physical review letters* **1977,** *39* (17), 1098.

[30] Shirakawa, H.; Louis, E. J.; MacDiarmid, A. G.; Chiang, C. K.; Heeger, A. J. Synthesis of Electrically Conducting Organic Polymers: Halogen Derivatives of Polyacetylene, (CH)x. *Journal of the Chemical Society, Chemical Communications* **1977,** No. 16, 578–580.

[31] AKAMATU, H.; Inkuchi, H.; MATSUNAGA, Y. Electrical Conductivity of the Perylene-Bromine Complex. *Nature* **1954,** *173* (4395), 168–169.

[32] K, N.; Rout, C. S. Conducting Polymers: a Comprehensive Review on Recent Advances in Synthesis, Properties and Applications. *RSC advances* **2021,** *11* (10), 5659–5697.

[33] Pope, M.; Swenberg, C. E. Electronic Processes in Organic Crystals and Polymers. *Oxford Univ. Press* **1999**.

[34] Geoghegan, M.; Hadziioannou, G. *Polymer Electronics* 22; OUP Oxford, 2013.

[35] Su, W. P.; Schrieffer, J. R.; Heeger, A. J. Solitons in Polyacetylene.

[36] Atala, M.; Aidelsburger, M.; Barreiro, J. T.; Abanin, D.; Kitagawa, T.; Demler, E.; Bloch, I. Direct Measurement of the Zak Phase in Topological Bloch Bands. *Nature Phys* **2013,** *9* (12), 795–800.

[37] Rudolph, A. Electron Transfer at Electrodes and in Solution: Comparison of Theory and Experiment. *Electrochimica Acta* **1968,** *13* (5), 995–1004.

[38] Miller, A.; Abrahams, E. Impurity Conduction at Low Concentrations. *Physical Review* **1960,** *120* (3), 745.

[39] Bässler, H. Charge Transport in Disordered Organic Photoconductors a Monte Carlo Simulation Study. *phys. stat. sol. (b)* **1993,** *175* (1), 15–56.

[40] Stephen, M.; Genevičius, K.; Juška, G.; Arlauskas, K.; Hiorns, R. C. Charge Transport and its Characterization using Photo-CELIV in Bulk Heterojunction Solar Cells. *Polym. Int.* **2017,** *66* (1), 13–25.

[41] Smith, W. Effect of Light on Selenium during the Passage of an Electric Current. *Nature* **1873,** *7*, 303.

[42] Hertz, H. Ueber einen Einfluss des Ultravioletten Lichtes auf die Electrische Entladung. *Ann. Phys.* **1887,** No. 267, 983–1000.

[43] Hallwachs, W. Ueber den Einfluss des Lichtes auf Electrostatisch geladene Körper. *Ann. Phys.* **1888,** *269* (2), 301–312.

[44] Planck, M. Ueber das Gesetz der Energieverteilung im Normalspectrum. *Ann. Phys.* **1901,** *4* (3), 553–564.

[45] Millikan, R. A. A Direct Photoelectric Determination of Planck's h. *Phys. Rev.* **1916,** No. 7, 355–388.

[46] Tang, C. W. Two-layer Organic Photovoltaic Cell. *Appl. Phys. Lett.* **1986,** *48* (2), 183–185.

[47] Chamberlain, G. A. Organic Solar Cells: A Review. *Solar Cells* **1983,** No. 8, 47–83.

[48] Frenkel, J. On the Transformation of Light into Heat in Solids. I. *Phys. Rev.* **1931,** No. 37, 17–44.

[49] Davydov, A. S. The Theory of Molecular Excitations. *Sov.Phys.* **1964,** No. 82, 393–448.

[50] Zhu, T.; Wan, Y.; Huang, L. Direct Imaging of Frenkel Exciton Transport by Ultrafast Microscopy. *Accounts of chemical research* **2017,** *50* (7), 1725–1733.

[51] Hertel, D.; Bässler, H. Photoconduction in Amorphous Organic Solids. *ChemPhysChem* **2008,** *9* (5), 666–688.

[52] Condon, E. U. The Franck-Condon Pprinciple and Related Topics. *American journal of physics* **1947,** *15* (5), 365–374.

[53] Spano, F. C. Absorption and Emission in Oligo-Phenylene Vinylene Nanoaggregates: The Role of Disorder and Structural Defects. *The Journal of chemical physics* **2002,** *116* (13), 5877–5891.

[54] Spano, F. C. Modeling Disorder in Polymer Aggregates: The Optical Spectroscopy of Regioregular Poly(3-hexylthiophene) Thin Films. *The Journal of chemical physics* **2005,** *122* (23), 234701.

[55] Spano, F. C. Emission from Aggregates of Oligo-Phenylene Vinylenes: A Recipe for Superradiant H-Aggregates. *Chemical Physics Letters* **2000,** *331* (1), 7–13.

[56] Spano, F. C.; Silva, C. H- and J-Aggregate Behavior in Polymeric Semiconductors. *Annu. Rev. Phys. Chem.* **2014,** *65* (1), 477–500.

[57] University Science Books, Ed. *Principles of Molecular Photochemistry*. *An Introduction*, 3rd ed.; University Science Books, 2009.

[58] Menke, S. M.; Holmes, R. J. Exciton diffusion in organic photovoltaic cells. *Energy Environ. Sci.* **2014,** *7* (2), 499–512.

[59] Sajjad, M. T.; Ruseckas, A.; Samuel, I. D. Enhancing Exciton Diffusion Length Provides New Opportunities for Organic Photovoltaics. *Matter* **2020,** *3* (2), 341–354.

[60] Förster, T. Experimentelle und theoretische Untersuchung des zwischenmolekularen Übergangs von Elektronenanregungsenergie. *Zeitschrift für Naturforschung A* **1949,** *4* (5), 321–327.

[61] Feron, K.; Belcher, W. J.; Fell, C. J.; Dastoor, P. C. Organic Solar Cells: Understanding the Role of Förster Resonance Energy Transfer. *International journal of molecular sciences* **2012,** *13* (12), 17019–17047.

[62] Jang, Y. J.; Kawaguchi, D.; Yamaguchi, S.; Lee, S.; Lim, J. W.; Kim, H.; Tanaka, K.; Kim, D. H. Enhancing the Organic Solar Cell Efficiency by Combining Plasmonic and Förster Resonance Energy Transfer (FRET) Effects. *Journal of Power Sources* **2019,** *438*, 227031.

[63] Gautam, B. R.; Younts, R.; Carpenter, J.; Ade, H.; Gundogdu, K. The Role of FRET in Non-Fullerene Organic Solar Cells: Implications for Molecular Design. *The journal of physical chemistry. A* **2018,** *122* (15), 3764–3771.

[64] Blom, P. W. M.; Mihailetchi, V. D.; Koster, L. J. A.; Markov, D. E. Device Physics of Polymer:Fullerene Bulk Heterojunction Solar Cells. *Adv. Mater.* **2007,** *19* (12), 1551–1566.

[65] Hood, S. N.; Kassal, I. Entropy and Disorder Enable Charge Separation in Organic Solar Cells. *The journal of physical chemistry letters* **2016,** *7* (22), 4495–4500.

[66] Carsten, B.; Szarko, J. M.; Lu, L.; Son, H. J.; He, F.; Botros, Y. Y.; Chen, L. X.; Yu, L. Mediating Solar Cell Performance by Controlling the Internal Dipole Change in Organic Photovoltaic Polymers. *Macromolecules* **2012,** *45* (16), 6390–6395.

[67] Wang, X.; Wang, W.; Yang, C.; Han, D.; Fan, H.; Zhang, J. Thermal Transport in Organic Semiconductors. *J. Appl. Phys* **2021,** *130* (17), 170902.

[68] Strobl, G. *The Physics of Polymers*. *Concepts for Understanding Their Structures and Behavior*, 3rd Edition; Springer, 2007.

[69] Deibel, C.; Dyakonov, V. Polymer–Fullerene Bulk Heterojunction Solar Cells. *Rep. Prog. Phys.* **2010,** *73* (9), 96401.

[70] Tong, Y.; Xiao, Z.; Du, X. e. a. Progress of the Key Materials for Organic Solar Cells. *Sci. China Chem* **2020,** No. 63, 758–765.

[71] Yu, G.; Gao, J.; Hummelen, J. C.; Wudl, F.; Heeger, A. J. Polymer Photovoltaic Cells: Enhanced Efficiencies via a Network of Internal Donor-Acceptor Heterojunctions. *Science* **1995,** *270* (5243), 1789–1791.

[72] Li, G.; Shrotriya, V.; Huang, J.; Yao, Y.; Moriarty, T.; Emery, K.; Yang, Y. High-efficiency solution processable polymer photovoltaic cells by self-organization of polymer blends. *Nature Mater* **2005,** *4* (11), 864–868.

[73] Shaheen, S. E.; Brabec, C. J.; Sariciftci, N. S.; Padinger, F.; Fromherz, T.; Hummelen, J. C. 2.5% Efficient Organic Plastic Solar Cells. *Appl. Phys. Lett.* **2001,** *78* (6), 841–843.

[74] Schilinsky, P.; Waldauf, C.; Brabec, C. J. Recombination and Loss Analysis in Polythiophene Based Bulk Heterojunction Photodetectors. *Appl. Phys. Lett.* **2002,** *81* (20), 3885–3887.

[75] Lu, L.; Yu, L. Understanding Low Bandgap Polymer PTB7 and Optimizing Polymer Solar Cells Based on it. *Adv. Mater.* **2014,** *26* (26), 4413–4430.

[76] Bartesaghi, D.; Ye, G.; Chiechi, R. C.; Koster, L. J. A. Compatibility of PTB7 and [70]PCBM as a Key Factor for the Stability of PTB7:[70]PCBM Solar Cells. *Adv. Energy Mater.* **2016,** *6* (13), 1502338.

[77] Liang, Y.; Xu, Z.; Xia, J.; Tsai, S.-T.; Wu, Y.; Li, G.; Ray, C.; Yu, L. For the Bright Future-Bulk Heterojunction Polymer Solar Cells with Power Conversion Efficiency of 7.4%. *Advanced materials (Deerfield Beach, Fla.)* **2010,** *22* (20), E135-8.

[78] He, Z.; Zhong, C.; Su, S.; Xu, M.; Wu, H.; Cao, Y. Enhanced Power-Conversion Efficiency in Polymer Solar Cells using an Inverted Device Structure. *Nature Photon* **2012,** *6* (9), 591–595.

[79] Huo, L.; Zhang, S.; Guo, X.; Xu, F.; Li, Y.; Hou, J. Replacing Alkoxy Groups with Alkylthienyl Groups: a Feasible Approach to improve the Properties of Photovoltaic Polymers. *Angewandte Chemie (International ed. in English)* **2011,** *50* (41), 9697–9702.

[80] Zhang, G.; Zhao, J.; Chow, P. C. Y.; Jiang, K.; Zhang, J.; Zhu, Z.; Zhang, J.; Huang, F.; Yan, H. Nonfullerene Acceptor Molecules for Bulk Heterojunction Organic Solar Cells. *Chemical reviews* **2018,** *118* (7), 3447–3507.

[81] Lin, Y.; Wang, J.; Zhang, Z.-G.; Bai, H.; Li, Y.; Zhu, D.; Zhan, X. An Electron Acceptor Challenging Fullerenes for Efficient Polymer Solar Cells. *Advanced materials (Deerfield Beach, Fla.)* **2015,** *27* (7), 1170–1174.

[82] Zhao, J.; Li, Y.; Yang, G.; Jiang, K.; Lin, H.; Ade, H.; Ma, W.; Yan, H. Efficient Organic Solar Cells Processed From Hydrocarbon Solvents. *Nat Energy* **2016,** *1* (2).

[83] Yuan, J.; Zhang, Y.; Zhou, L.; Zhang, G.; Yip, H.-L.; Lau, T.-K.; Lu, X.; Zhu, C.; Peng, H.; Johnson, P. A.; Leclerc, M.; Cao, Y.; Ulanski, J.; Li, Y.; Zou, Y. Single-Junction Organic Solar Cell with over 15% Efficiency Using Fused-Ring Acceptor with Electron-Deficient Core. *Joule* **2019,** *3* (4), 1140–1151.

[84] Sharma, R.; Lee, H.; Gupta, V.; Kim, H.; Kumar, M.; Sharma, C.; Chand, S.; Yoo, S.; Gupta, D. Photo-Physics of PTB7, PCBM and ICBA based Ternary Solar Cells. *Org. Electron.* **2016,** *34*, 111–117.

[85] Meng, L.; Zhang, Y.; Wan, X.; Li, C.; Zhang, X.; Wang, Y.; Ke, X.; Xiao, Z.; Ding, L.; Xia, R.; Yip, H.-L.; Cao, Y.; Chen, Y. Organic and Solution-Processed Tandem Solar Cells with 17.3% Efficiency. *Science (New York, N.Y.)* **2018,** *361* (6407), 1094–1098.

[86] Bi, P.; Zhang, S.; Chen, Z.; Xu, Y.; Cui, Y.; Zhang, T.; Ren, J.; Qin, J.; Hong, L.; Hao, X.; Hou, J. Reduced Non-Radiative Charge Recombination enables Organic Photovoltaic Cell Approaching 19% Efficiency. *Joule* **2021,** *5* (9), 2408–2419.

[87] Cui, Y.; Yao, H.; Hong, L.; Zhang, T.; Tang, Y.; Lin, B.; Xian, K.; Gao, B.; An, C.; Bi, P.; Ma, W.; Hou, J. Organic Photovoltaic Cell with 17% Efficiency and Superior Processability. *National science review* **2020,** *7* (7), 1239–1246.

[88] Cui, Y.; Xu, Y.; Yao, H.; Bi, P.; Hong, L.; Zhang, J.; Zu, Y.; Zhang, T.; Qin, J.; Ren, J.; Chen, Z.; He, C.; Hao, X.; Wei, Z.; Hou, J. Single-Junction Organic Photovoltaic Cell with 19% Efficiency. *Adv. Mater.* **2021,** *33* (41), e2102420.

[89] Sun, R.; Wu, Y.; Yang, X.; Gao, Y.; Chen, Z.; Li, K.; Qiao, J.; Wang, T.; Guo, J.; Liu, C.; Hao, X.; Zhu, H.; Min, J. Single-Junction Organic Solar Cells with 19.17% Efficiency Enabled by Introducing One Asymmetric Guest Acceptor. *Advanced materials (Deerfield Beach, Fla.)* **2022,** *34* (26), e2110147.

[90] Zhang, G.; Xie, C.; You, P.; Li, S. *Introduction to Organic Electronic Devices*, 1st ed. 2022; Springer eBook Collection; Springer Nature Singapore; Imprint Springer: Singapore, 2022.

[91] Servaites, J. D.; Ratner, M. A.; Marks, T. J. Organic Solar Cells: A New Look at Traditional Models. *Energy Environ. Sci.* **2011,** *4* (11), 4410.

[92] Ma, H.; Yip, H.-L.; Huang, F.; Jen, A. K.-Y. Interface Engineering for Organic Electronics. *Adv. Funct. Mater.* **2010,** *20* (9), 1371–1388.

[93] Li, S.; Cao, Y.-L.; Li, W.-H.; Bo, Z.-S. A Brief Review of Hole Transporting Materials Commonly Used in Perovskite Solar Cells. *Rare Met.* **2021,** *40* (10), 2712–2729.

[94] Xu, H.; Yuan, F.; Zhou, D.; Liao, X.; Chen, L.; Chen, Y. Hole Transport Layers for Organic Solar Cells: Recent Progress and Prospects. *J. Mater. Chem. A* **2020,** *8* (23), 11478–11492.

[95] Steim, R.; Kogler, F. R.; Brabec, C. J. Interface Materials for Organic Solar Cells. *J. Mater. Chem.* **2010,** *20* (13), 2499.

[96] Shrotriya, V.; Li, G.; Yao, Y.; Chu, C.-W.; Yang, Y. Transition Metal Oxides as the Buffer Layer for Polymer Photovoltaic Cells. *Appl. Phys. Lett.* **2006,** *88* (7), 73508.

[97] Jin Young Kim, Kwanghee Lee, Nelson E. Coates, Daniel Moses, Thuc-Quyen Nguyen, Mark Dante and Alan J. Heeger. Efficient Tandem Polymer Solar Cells Fabricated by All-Solution Processing. *Science* **2007,** *317* (5835), 222–225.

[98] Xu, B.; Gopalan, S.-A.; Gopalan, A.-I.; Muthuchamy, N.; Lee, K.-P.; Lee, J.-S.; Jiang, Y.; Lee, S.-W.; Kim, S.-W.; Kim, J.-S.; Jeong, H.-M.; Kwon, J.-B.; Bae, J.-H.; Kang, S.-W. Functional Solid Additive Modified PEDOT:PSS as an Anode Buffer Layer for Enhanced Photovoltaic Performance and Stability in Polymer Solar Cells. *Scientific reports* **2017,** *7*, 45079.

[99] Xing, W.; Chen, Y.; Wu, X.; Xu, X.; Ye, P.; Zhu, T.; Guo, Q.; Yang, L.; Li, W.; Huang, H. PEDOT:PSS-Assisted Exfoliation and Functionalization of 2D Nanosheets for High-Performance Organic Solar Cells. *Adv. Funct. Mater.* **2017,** *27* (32), 1701622.

[100] Smith, C. T. G.; Rhodes, R. W.; Beliatis, M. J.; Imalka Jayawardena, K. D. G.; Rozanski, L. J.; Mills, C. A.; P. Silva, S. R. Graphene Oxide Hole Transport Layers for Large Area, High Efficiency Organic Solar Cells. *Appl. Phys. Lett.* **2014,** *105* (7), 73304.

[101] Zhang, F.; Ceder, M.; Inganäs, O. Enhancing the Photovoltage of Polymer Solar Cells by Using a Modified Cathode. *Adv. Mater.* **2007,** *19* (14), 1835–1838.

[102] Ji, T.; Tan, L.; Hu, X.; Dai, Y.; Chen, Y. A Comprehensive Study of Sulfonated Carbon Materials as Conductive Composites for Polymer Solar Cells. *Physical chemistry chemical physics : PCCP* **2015,** *17* (6), 4137–4145.

[103] Gu, X.; Cui, W.; Wu, Z.; Zeng. Z.; Lee, S.-T.; Zhang, H.; Sun, B. A Solution-Processed Hole Extraction Layer Made from Ultrathin MoS 2 Nanosheets for Efficient Organic Solar Cells. *Adv. Energy Mater.* **2014,** *4* (2), 1262-1268.

[104] Braun, S.; Salaneck, W. R.; Fahlman, M. Energy-Level Alignment at Organic/Metal and Organic/Organic Interfaces. *Adv. Mater.* **2009,** *21* (14-15), 1450–1472.

[105] Hoppe, H.; Sariciftci, N. S. Organic Solar Cells: An Overview. *J. Mater. Res.* **2004,** *19* (7), 1924–1945.

[106] Keru, G.; Ndungu, P. G.; Nyamori, V. O. A Review on Carbon Nanotube/Polymer Composites for Organic Solar Cells. *Int. J. Energy Res.* **2014,** *38* (13), 1635–1653.

[107] Cataldo, S.; Salice, P.; Menna, E.; Pignataro, B. Carbon Nanotubes and Organic Solar Cells. *Energy Environ. Sci.* **2012,** *5* (3), 5919–5940.

[108] Rowell, M. W.; Topinka, M. A.; McGehee, M. D.; Prall, H.-J.; Dennler, G.; Sariciftci, N. S.; Hu, L.; Gruner, G. Organic Solar Cells with Carbon Nanotube Network Electrodes. *Appl. Phys. Lett.* **2006,** *88* (23), 233506.

[109] Steven K. Hau; Hin-Lap Yip; Kirsty Leong; Alex K.-Y. Jen. Spraycoating of Silver Nanoparticle Electrodes for Inverted Polymer Solar Cells. *Organic Electronics [Online]* **2009,** *10* (4), 719–723. https://www.sciencedirect.com/science/article/pii/S1566119909000482.

[110] Koo, D.; Jung, S.; Seo, J.; Jeong, G.; Choi, Y.; Lee, J.; Lee, S. M.; Cho, Y.; Jeong, M.; Lee, J.; Oh, J.; Yang, C.; Park, H. Flexible Organic Solar Cells Over 15% Efficiency with Polyimide-Integrated Graphene Electrodes. *Joule* **2020,** *4* (5), 1021–1034.

[111] Tang, H.; Feng, H.; Wang, H.; Wan, X.; Liang, J.; Chen, Y. Highly Conducting MXene-Silver Nanowire Transparent Electrodes for Flexible Organic Solar Cells. *ACS applied materials & interfaces* **2019,** *11* (28), 25330–25337.

[112] J. Wu, H. A. Becerril, Z. Bao, Z. Liu, Y. Chen, P. Peumans. Organic Solar Cells with Solution-Processed Graphene Transparent Electrodes. *Appl. Phys. Lett.* **2008,** No. 92, 263302.

[113] Yu, G.; Heeger, A. J. Charge Separation and Photovoltaic Conversion in Polymer Composites with Internal Donor/Acceptor Heterojunctions. *Journal of Applied Physics* **1995,** *78* (7), 4510–4515.

[114] Halls, J. J. M.; Walsh, C. A.; Greenham, N. C.; Marseglia, E. A.; Friend, R. H.; Moratti, S. C.; Holmes, A. B. Efficient Photodiodes from Interpenetrating Polymer Networks. *Nature* **1995,** *376* (6540), 498–500.

[115] Ruderer, M. A.; Müller-Buschbaum, P. Morphology of Polymer-based Bulk Heterojunction Films for Organic Photovoltaics. *Soft Matter* **2011,** *7* (12), 5482.

[116] Zeng, W.; Chong, K. S. L.; Low, H. Y.; Williams, E. L.; Tam, T. L.; Sellinger, A. The Use of Nanoimprint Lithography to Improve Efficiencies of Bilayer Organic Solar Cells Based on P3HT and a Small Molecule Acceptor. *Thin Solid Films* **2009,** *517* (24), 6833–6836.

[117] Park, J. Y.; Hendricks, N. R.; Carter, K. R. Solvent-Assisted Soft Nanoimprint Lithography for Structured Bilayer Heterojunction Organic Solar Cells. *Langmuir : the ACS journal of surfaces and colloids* **2011,** *27* (17), 11251–11258.

[118] Ye, L.; Hu, H.; Ghasemi, M.; Wang, T.; Collins, B. A.; Kim, J.-H.; Jiang, K.; Carpenter, J. H.; Li, H.; Li, Z.; McAfee, T.; Zhao, J.; Chen, X.; Lai, J. L. Y.; Ma, T.; Bredas, J.-L.; Yan, H.; Ade, H. Quantitative Relations Between Interaction Parameter, Miscibility and Function in Organic Solar Cells. *Nature materials* **2018,** *17* (3), 253–260.

[119] Madogni, V. I.; Kounouhéwa, B.; Akpo, A.; Agbomahéna, M.; Hounkpatin, S. A.; Awanou, C. N. Comparison of degradation mechanisms in organic photovoltaic devices upon exposure to a temperate and a subequatorial climate. *Chemical Physics Letters* **2015,** *640*, 201–214.

[120] Nam, S.; Seo, J.; Woo, S.; Kim, W. H.; Kim, H.; Bradley, D. D. C.; Kim, Y. Inverted Polymer Fullerene Solar Cells Exceeding 10% Efficiency with Poly(2-ethyl-2-oxazoline) Nanodots on Electron-Collecting Buffer Layers. *Nature communications* **2015,** *6*, 8929.

[121] Holliday, S.; Li, Y.; Luscombe, C. K. Recent Advances in High Performance Donor-Acceptor Polymers for Organic Photovoltaics. *Progress in polymer science* **2017,** *70*, 34–51.

[122] Dong, S.; Jia, T.; Zhang, K.; Jing, J.; Huang, F. Single-Component Non-halogen Solvent-Processed High-Performance Organic Solar Cell Module with Efficiency over 14%. *Joule* **2020,** *4* (9), 2004–2016.

[123] Jeong, S.; Park, B.; Hong, S.; Kim, S.; Kim, J.; Kwon, S.; Lee, J.-H.; Lee, M. S.; Park, J. C.; Kang, H.; Lee, K. Large-Area Nonfullerene Organic Solar Cell Modules Fabricated by a Temperature-Independent Printing Method. *ACS applied materials & interfaces* **2020,** *12* (37), 41877–41885.

[124] Proctor, C. M.; Kuik, M.; Nguyen, T.-Q. Charge Carrier Recombination in Organic Solar Cells. *Progress in polymer science* **2013,** *38* (12), 1941–1960.

[125] Shockley, W.; Queisser, H. J. Detailed Balance Limit of Efficiency of p-n Junction Solar Cells. *Journal of Applied Physics* **1961,** *32* (3), 510–519.

[126] Rühle, S. Tabulated Values of the Shockley–Queisser Limit for Single Junction Solar Cells. *Solar Energy* **2016,** *130*, 139–147.

[127] Ji, Y.; Xu, L.; Hao, X.; Gao, K. Energy Loss in Organic Solar Cells: Mechanisms, Strategies, and Prospects. *Sol. RRL* **2020,** *4* (7), 2000130.

[128] Huang, H., Huang, J., Eds. *Organic and Hybrid Solar Cells*, 1st ed. 2014; Springer International Publishing; Imprint: Springer: Cham, 2014.

[129] Stranks, S. D.; Burlakov, V. M.; Leijtens, T.; Ball, J. M.; Goriely, A.; Snaith, H. J. Recombination Kinetics in Organic-Inorganic Perovskites: Excitons, Free Charge, and Subgap States. *Physical Review Applied* **2014,** *2* (3), 34007.

[130] Langevin, P. Sur la loi de recombinationdes ions. *Ann. Chim. Phys.* **1903,** No. 28, 433–530.

[131] Wetzelaer, G.-J. A. H.; van der Kaap, N. J.; Koster, L. J. A.; Blom, P. W. M. Quantifying Bimolecular Recombination in Organic Solar Cells in Steady State. *Adv. Energy Mater.* **2013,** *3* (9), 1130–1134.

[132] Shockley, W.; Read, W. T., JR. Statistics of the Recombinations of Holes and Electrons. *Phys. Rev.* **1952,** No. 87, 835–842.

[133] Hall, R. N. Electron-Hole Recombination in Germanium. *Phys. Rev.* **1952,** No. 87, 387–397.

[134] Klimov, V. I.; Mikhailovsky, A. A.; Xu, S.; Malko, A.; Hollingsworth, J. A.; Leatherdale, C. A.; Eisler, H.; Bawendi, M. G. Optical Gain and Stimulated Emission in Nanocrystal Quantum Dots. *Science (New York, N.Y.)* **2000,** *290* (5490), 314–317.

[135] Wang, M.; Xie, F.; Du, J.; Tang, Q.; Zheng, S.; Miao, Q.; Chen, J.; Zhao, N.; Xu, J. B. Degradation Mechanism of Organic Solar Cells with Aluminum Cathode. *Solar Energy Materials and Solar Cells* **2011,** *95* (12), 3303–3310.

[136] Vitoratos, E.; Sakkopoulos, S.; Paliatsas, N.; Emmanouil, K.; Choulis, S. A. Conductivity Degradation Study of PEDOT: PSS Films under Heat Treatment in Helium and Atmospheric Air. *OJOPM* **2012,** *02* (01), 7–11.

[137] Huang, J.; Miller, P. F.; Mello, J. C. de; Mello, A. J. de; Bradley, D. Influence of Thermal Treatment on the Conductivity and Morphology of PEDOT/PSS Films. *Synthetic Metals* **2003,** *139* (3), 569–572.

[138] Norrman, K.; Madsen, M. V.; Gevorgyan, S. A.; Krebs, F. C. Degradation Patterns in Water and Oxygen of an Inverted Polymer Solar Cell. *Journal of the American Chemical Society* **2010,** *132* (47), 16883–16892.

[139] Rivaton, A.; Tournebize, A.; Gaume, J.; Bussière, P.-O.; Gardette, J.-L.; Therias, S. Photostability of Organic Materials used in Polymer Solar Cells. *Polym. Int.* **2014,** *63* (8), 1335–1345.

[140] Hermenau, M.; Riede, M.; Leo, K.; Gevorgyan, S. A.; Krebs, F. C.; Norrman, K. Water and Oxygen Induced Degradation of Small Molecule Organic Solar Cells. *Solar Energy Materials and Solar Cells* **2011,** *95* (5), 1268–1277.

[141] Seemann, A.; Sauermann, T.; Lungenschmied, C.; Armbruster, O.; Bauer, S.; Egelhaaf, H.-J.; Hauch, J. Reversible and Irreversible Degradation of Organic Solar Cell Performance by Oxygen. *Solar Energy* **2011,** *85* (6), 1238–1249.

[142] Rao, A. M.; Zhou, P.; Wang, K.; Hager, G. T.; Holden, J. M.; Wang, Y.; Lee, W. T.; Bi, X. X.; Eklund, P. C.; Cornett, D. S.; Duncan, M. A.; Amster, J. Photoinduced Polymerization of Solid C60 Films. *Science* **1993,** No. 259, 955–957.

[143] Ostwald, W. Studien über die Bildung und Umwandlung fester Körper. *Zeitschrift für Physikalische Chemie* **1897,** No. 22, 289–330.

[144] Schuller, S.; Schilinsky, P.; Hauch, J.; Brabec, C. J. Determination of the Degradation Constant of Bulk Heterojunction Solar Cells by Accelerated Lifetime Measurements. *Appl. Phys. A* **2004,** *79* (1), 37–40.

[145] Ray, B.; Nair, P. R.; Alam, M. A. Annealing Dependent Performance of Organic Bulk-Heterojunction Solar Cells: A Theoretical Perspective. *Solar Energy Materials and Solar Cells* **2011,** *95* (12), 3287–3294.

[146] Bruner, C.; Dauskardt, R. Role of Molecular Weight on the Mechanical Device Properties of Organic Polymer Solar Cells. *Macromolecules* **2014,** *47* (3), 1117–1121.

[147] Yan, C.; Barlow, S.; Wang, Z.; Yan, H.; Jen, A. K.-Y.; Marder, S. R.; Zhan, X. Non-Fullerene Acceptors for Organic Solar Cells. *Nat Rev Mater* **2018,** *3* (3).

[148] Baran, D.; Ashraf, R. S.; Hanifi, D. A.; Abdelsamie, M.; Gasparini, N.; Röhr, J. A.; Holliday, S.; Wadsworth, A.; Lockett, S.; Neophytou, M.; Emmott, C. J. M.; Nelson, J.; Brabec, C. J.; Amassian, A.; Salleo, A.; Kirchartz, T.; Durrant, J. R.; McCulloch, I. Reducing the Efficiency-Stability-Cost Gap of Organic Photovoltaics with Highly Efficient and Stable Small Molecule Acceptor Ternary Solar Cells. *Nature materials* **2017,** *16* (3), 363–369.

[149] Griffini, G.; Douglas, J. D.; Piliego, C.; Holcombe, T. W.; Turri, S.; Fréchet, J. M. J.; Mynar, J. L. Long-Term Thermal Stability of High-Efficiency Polymer Solar Cells Based on Photocrosslinkable Donor-Acceptor Conjugated Polymers. *Advanced materials (Deerfield Beach, Fla.)* **2011,** *23* (14), 1660–1664.

[150] Li, F.; Yager, K. G.; Dawson, N. M.; Yang, J.; Malloy, K. J.; Qin, Y. Complementary Hydrogen Bonding and Block Copolymer Self-Assembly in Cooperation toward Stable Solar Cells with Tunable Morphologies. *Macromolecules* **2013,** *46* (22), 9021–9031.

[151] Snaith, B.; Edmondst, M. J.; Probert, S. D. Use of a Profilometer for Surface Mapping. *Precision Engineering [Online]* **1981,** *3* (2), 87–90. https://www.sciencedirect.com/science/article/pii/0141635981900416.

[152] Teague, E. C.; Scire, F. E.; Baker, S. M.; Jensen, S. W. Three-Dimensional Stylus Profilometry. *Wear* **1982,** *83* (1), 1–12.

[153] Beer, A. Bestimmung der Absorption des Rothen Lichts in Farbigen Flussigkeiten. *Ann. Physik* **1852,** *162*, 78–88.

[154] Mayerhöfer, T. G.; Mutschke, H.; Popp, J. Employing Theories Far Beyond Their Limits - The Case of the (Boguer-) Beer-Lambert Law. *ChemPhysChem* **2016,** *17* (13), 1948–1955.

[155] Tauc, J.; Grigorovici, R.; Vancu, A. Optical Properties and Electronic Structure of Amorphous Germanium. *phys. stat. sol. (b)* **1966,** *15* (2), 627–637.

[156] Franck, J.; Dymond, E. G. Elementary processes of photochemical reactions. *Trans. Faraday Soc.* **1926,** *21* (February), 536–542.

[157] Condon, E. U. Nuclear motions associated with electron transitions in diatomic molecules. *Physical Review* **1928,** *32* (6), 858.

[158] Fantz, U.; Wünderlich, D. Franck-Condon Factors, Transition Probabilities, and Radiative Lifetimes for Hydrogen Molecules and Their Isotopomeres. *Atomic Data and Nuclear Data Tables* **2006,** *92* (6), 853–973.

[159] Hoffmann, S. T.; Bässler, H.; Köhler, A. What Determines Inhomogeneous Broadening of Electronic Transitions in Conjugated Polymers? *J. Phys. Chem. B* **2010,** *114* (51), 17037–17048.

[160] Fujiwara, H. *Spectroscopic Ellipsometry: Principles and Applications;* John Wiley & Sons, 2007.

[161] Brentano, J. Focussing Method of Crystal Powder Analysis by X-Rays. *Proceedings of the Physical Society of London* **1924,** *37* (1), 184.

[162] Stokes, A. R.; Wilson, A. J. C. A method of calculating the integral breadths of Debye-Scherrer lines. In *Mathematical Proceedings of the Cambridge Philosophical Society*, 1942; pp 313–322.

[163] Dudenko, D.; Kiersnowski, A.; Shu, J.; Pisula, W.; Sebastiani, D.; Spiess, H. W.; Hansen, M. R. A Strategy for Revealing the Packing in Semicrystalline \Pi-Conjugated Polymers: Crystal Structure of Bulk Poly-3-Hexyl-Thiophene (P3HT). *Angewandte Chemie* **2012,** *124* (44), 11230–11234.

[164] Yamamoto, T.; Arai, M.; Kokubo, H.; Sasaki, S. Copolymers of Thiophene and Thiazole. Regioregulation in Synthesis, Stacking Structure, and Optical Properties. *Macromolecules* **2003,** *36* (21), 7986–7993.

[165] Somoza, M. Graphical depiction of the Morse potential with a harmonic potential for comparison. https://commons.wikimedia.org/wiki/File:Morse-potential.png (accessed on 2023/08/08).

[166] Siesler, H. W., Ed. *Polymer Science: A Comprehensive Reference*. *Polymer Characterization, Vibrational Spectroscopy*, 2nd ed.; Elsevier, 2012.

[167] McCreery, R. L. *Raman spectroscopy for Chemical Analysis;* John Wiley & Sons, 2005.

[168] Schulte, A.; Guo, Y. Laser Raman Spectroscopy. *Handbook of Applied Solid State Spectroscopy*; Springer, 2006; pp 661–688.

[169] Broglie, L. de. The Wave Nature of the Electron. *Nobel lecture* **1929,** No. 12, 244–256.

[170] Brückel, T., Heger, G., Richter, D., Roth, G., Zorn, R., Eds. *Neutron scattering. Lectures of the JCNS laboratory course held at Forschungszentrum Jülich and the research reactor FRM II of TU Munich*; Schriften des Forschungszentrums Jülich Reihe Schlüsseltechnologien 15; Forschungszentrum Jülich: Jülich, 2010.

[171] Lefmann, K. Lecture Notes Neutron Scattering: Theory, Instrumentation and Simulation. https://e-learning.pan-training.eu/wiki/index.php/The_neutron_cross_sections (accessed on 2023/08/08).

[172] Furrer, A.; Mesot, J. F.; Straessle, T. *Neutron Scattering In Condensed Matter Physics*; Series On Neutron Techniques And Applications; World Scientific Publishing Company, 2009.

[173] Sears, V. F. Neutron Scattering Lengths and Cross Sections. *Neutron News* **1992,** *3* (3), 26–37.

[174] Berrod, Q.; Lagrené, K.; Ollivier, J.; Zanotti, J.-M. Inelastic and Quasi-Elastic Neutron Scattering.: Application to Soft-Matter. *EPJ Web of Conferences* **2018,** *188*, 5001.

[175] van Hove, L. Correlations in Space and Time and Born Approximation Scattering in Systems of Interacting Particles. *Phys. Rev.* **1954,** No. 95, 249–262.

[176] Dahlborg, U.; Gudowski, W.; Davidovic, M. Van Hove Correlation Functions From Coherent Neutron Inelastic Scattering. *J. Phys.: Condens. Matter.* **1989,** *1* (35), 6173–6179.

[177] Folland, G. B., Ed. *Fourier Analysis and Its Applications*, 2nd ed.; Am. Math. Soc., 2009.

[178] Embs, J. P.; Juranyi, F.; Hempelmann, R. Introduction to Quasielastic Neutron Scattering. *Zeitschrift für Physikalische Chemie* **2010,** *224* (1-2), 5–32.

[179] Lechner, R. E.; Heidemann, A. Rotational Motion in Plastic Adamantine. The Elastic Structure Factor. *Commun. Phys.* **1976,** No. 1, 213–221.

[180] Dianoux, A. J.; Volino, F.; Hervet, H. Incoherent Scattering Law for Neutron Quasi-Elastic Scattering in Liquid Crystals. *Molecular Physics* **1975,** *30* (4), 1181–1194.

[181] Beniere, F., Catlow, C., Eds. *Mass Transport in Solids;* NATO ASI, 1981.

[182] Bée, M. Localized and Long-Range Diffusion in Condensed Matter: State of the Art of QENS Studies and Future Prospects. *Chemical Physics* **2003,** *292* (2-3), 121–141.

[183] Bée, M. J. *Quasielastic Neutron Scattering*. *Principles and applications in solid state chemistry, biology and materials science;* Hilger: Bristol, 1988.

[184] Chudley, C. T.; Elliott, R. J. Neutron Scattering from a Liquid on a Jump Diffusion Model. *Proc. Phys. Soc.* **1961,** *77* (2), 353–361.

[185] Hall, P. L.; Ross, D. K. Incoherent Neutron Scattering Functions for Random Jump Diffusion in Bounded and Infinite Media. *Mol. Phys.* **1981,** *42* (3), 673–682.

[186] Singwi, K. S.; Sjölander, A. Diffusive Motions in Water and Cold Neutron Scattering. *Phys. Rev. [Online]* **1960,** *119* (3), 863–871. https://link.aps.org/doi/10.1103/PhysRev.119.863.

[187] Springer, T. *Quasielastic neutron scattering for the investigation of diffusive motions in solids and liquids*; Springer tracts in modern physics 64; Springer: Berlin, 1972.

[188] Hempelmann, R. *Quasielastic Neutron Scattering and Solid State Diffusion;* Oxford University Press, 2000.

[189] Kohlrausch, R. Ueber das Dellmann'sche Elektrometer. *Ann. Phys. Chem.* **1847,** *148* (11), 353–405.

[190] Kohlrausch, R. Theorie des elektrischen Rückstandes in der Leidener Flasche. *Ann. Phys. Chem.* **1854,** *167* (2), 179–214.

[191] Williams, G.; Watts, D. C. Non-symmetrical dielectric relaxation behaviour arising from a simple empirical decay function. *Trans. Faraday Soc.* **1970,** *66*, 80.

[192] Mukhopadhyay, R.; Alegría, A.; Colmenero, J.; Frick, B. Methyl Group Dynamics in Poly(vinyl acetate): A Neutron Scattering Study. *Macromolecules* **1998,** *31* (12), 3985–3993.

[193] Varley F. Sears. Neutron Scattering Lengths and Cross Sections. *Neutron News* **1992,** *3* (3), 26–37.

[194] NIST Center for Neutron Research. Neutron Scattering Lengths and Cross Sections. https://ncnr.nist.gov/resources/n-lengths/ (accessed on 2023/08/08).

[195] Hippert, F., Geissler, E., Hodeau, J. L., Lelievre-Berna, E., Regnard, J.-R., Eds. *Neutron and X-ray Spectroscopy;* Springer, 2006.

[196] Liang, L., Rinaldi, R., Schober, H., Eds. *Neutron Applications in Earth, Energy and Environmental Sciences;* Springer US: Boston, MA, 2009.

[197] Heidemann, A., Frick, B. Web Site for Neutron Backscattering Spectroscopy. https://www.ill.eu/other_sites/BS-review/index.htm (accessed on 2023/08/08).

[198] Gardner, J. S.; Ehlers, G.; Faraone, A.; Garc\'\ia Sakai, V. High-Resolution Neutron Spectroscopy using Backscattering and Neutron Spin-Echo spectrometers in soft and hard condensed matter. *Nature Reviews Physics* **2020,** *2* (2), 103–116.

[199] Mezei, F. Neutron Spin Echo: A New Concept in Polarized Thermal Neutron Techniques. *Z. Physik* **1972,** *255* (2), 146–160.

[200] Mezei, F., Pappas, C., Gutberlet, T., Eds. *Neutron Spin Echo Spectroscopy*. *Bacics, Trends and Applications*; Lecture Notes in Physics; Springer, 1980.

[201] Golub, R.; Gähler, R. A Neutron Resonance Spin Echo Spectrometer for Quasi-Elastic and Inelastic Scattering. *physics letters A* **1987,** *123* (1), 43–48.

[202] Gähler, R.; Golub, R. A High Resolution Neutron Spectrometer for Quasielastic Scattering on the Basis of Spin-Echo and Magnetic Resonance. *Zeitschrift für Physik B Condensed Matter* **1987,** *65* (3), 269–273.

[203] Pike, E. R.; Sabatier, P. C. *Scattering, Two-Volume Set Scattering and Inverse Scattering in Pure and Applied Science;* Elsevier, 2001.

[204] Richter, D.; Monkenbusch, M.; Arbe, A.; Colmenero, J. Neutron spin echo in polymer systems. *Neutron Spin Echo in Polymer Systems* **2005**, 1–221.

[205] Unruh, T.; Neuhaus, J.; Petry, W. The High-Resolution Time-of-Flight Spectrometer TOFTOF. *Nuclear Instruments and Methods in Physics Research Section A: Accelerators, Spectrometers, Detectors and Associated Equipment* **2007,** *580* (3), 1414–1422.

[206] Lohstroh, W.; Evenson, Z. TOFTOF: Cold Neutron Time-of-Flight Spectrometer. *JLSRF* **2015,** *1*.

[207] TOFTOF. https://mlz-garching.de/toftof/de (accessed on 2023/08/08).

[208] Lechner, R. E. Tof-Tof Spectrometers at Pulsed Neutrons Sources and at Steady-State Reactors. In *Proc. Workshop on Neutron Scattering for SNQ, Maria Laach*, 1954; pp 202–223.

[209] Paternò, Giuseppe Maria, Warren, Anna J., Aj, Warren, Spencer, Jacob, Evans, Gwyndaf, Garcia Sakai, V., Sakai, Victoria Garcia, Blumberger, Jochen, Cacialli, Franco. *Micro-Focused X-Ray Diffraction Characterization Of High-Quality [6,6]-Phenyl-C61-Butyric Acid Methyl Ester Single Crystals Without Solvent Impurities;* Zenodo, 2013.

[210] Caddeo, C.; Filippetti, A.; Bosin, A.; Videlot-Ackermann, C.; Ackermann, J.; Mattoni, A. Theoretical Insight on PTB7: PC71BM, PTB7-Th: PC71BM and Si-PCPDTBT: PC71BM Interactions Governing Blend Nanoscale Morphology For Efficient Solar Cells. *Nano Energy* **2021,** *82*, 105708.

[211] Goswami, A. *Thin Film Fundamentals;* New age international, 1996.

[212] Guo, S.; Cao, B.; Wang, W.; Moulin, J.-F.; Müller-Buschbaum, P. Effect of alcohol treatment on the performance of PTB7:PC71BM bulk heterojunction solar cells. *ACS applied materials & interfaces* **2015,** *7* (8), 4641–4649.

[213] Guilbert, A. A. Y.; Zbiri, M.; Jenart, M. V. C.; Nielsen, C. B.; Nelson, J. New Insights into the Molecular Dynamics of P3HT:PCBM Bulk Heterojunction: A Time-of-Flight Quasi-Elastic Neutron Scattering Study. *The journal of physical chemistry letters* **2016,** *7* (12), 2252–2257.

[214] Paternó, G.; Cacialli, F.; García-Sakai, V. Structural and dynamical characterization of P3HT/PCBM blends. *Chemical Physics* **2013,** *427*, 142–146.

[215] Etampawala, T.; Ratnaweera, D.; Morgan, B.; Diallo, S.; Mamontov, E.; Dadmun, M. Monitoring the dynamics of miscible P3HT:PCBM blends: A quasi elastic neutron scattering study of organic photovoltaic active layers. *Polymer* **2015,** *61*, 155–162.

[216] Zheng, Y.; Wang, G.; Di Huang; Kong, J.; Goh, T.; Huang, W.; Yu, J.; Taylor, A. D. Binary Solvent Additives Treatment Boosts the Efficiency of PTB7:PCBM Polymer Solar Cells to Over 9.5%. *Sol. RRL* **2018,** *2* (4), 1700144.

[217] Guo, S.; Herzig, E. M.; Naumann, A.; Tainter, G.; Perlich, J.; Müller-Buschbaum, P. Influence of Solvent and Solvent Additive on the Morphology of PTB7 Films Probed via X-ray scattering. *J. Phys. Chem. B* **2014,** *118* (1), 344–350.

[218] Ebenhoch, B.; Thomson, S. A.; Genevičius, K.; Juška, G.; Samuel, I. D. Charge carrier mobility of the organic photovoltaic materials PTB7 and PC71BM and its influence on device performance. *Organic Electronics* **2015,** *22*, 62–68.

[219] Foster, S.; Deledalle, F.; Mitani, A.; Kimura, T.; Kim, K.-B.; Okachi, T.; Kirchartz, T.; Oguma, J.; Miyake, K.; Durrant, J. R.; Doi, S.; Nelson, J. Electron Collection as a Limit to Polymer:PCBM Solar Cell Efficiency: Effect of Blend Microstructure on Carrier Mobility and Device Performance in PTB7:PCBM. *Adv. Energy Mater.* **2014,** *4* (14), 1400311.

[220] Liu, F.; Zhao, W.; Tumbleston, J. R.; Wang, C.; Gu, Y.; Wang, D.; Briseno, A. L.; Ade, H.; Russell, T. P. Understanding the Morphology of PTB7:PCBM Blends in Organic Photovoltaics. *Adv. Energy Mater.* **2014,** *4* (5), 1301377.

[221] Ciammaruchi, L.; Brunetti, F.; Visoly-Fisher, I. Solvent effects on the morphology and stability of PTB7:PCBM based solar cells. *Solar Energy* **2016,** *137*, 490–499.

[222] Obrzut, J.; Page, K. A. Electrical conductivity and relaxation in poly(3-hexylthiophene). *Phys. Rev. B* **2009,** *80* (19), 859.

[223] Pankaj, S.; Hempel, E.; Beiner, M. Side-Chain Dynamics and Crystallization in a Series of Regiorandom Poly(3-alkylthiophenes). *Macromolecules* **2009,** *42* (3), 716–724.

[224] Pivrikas, A.; Sariciftci, N. S.; Juška, G.; Österbacka, R. A review of charge transport and recombination in polymer/fullerene organic solar cells. *Prog. Photovolt: Res. Appl.* **2007,** *15* (8), 677–696.

[225] Foertig, A.; Kniepert, J.; Gluecker, M.; Brenner, T.; Dyakonov, V.; Neher, D.; Deibel, C. Nongeminate and Geminate Recombination in PTB7:PCBM Solar Cells. *Adv. Funct. Mater.* **2014,** *24* (9), 1306–1311.

[226] Mens, R.; Chambon, S.; Bertho, S.; Reggers, G.; Ruttens, B.; D'Haen, J.; Manca, J.; Carleer, R.; Vanderzande, D.; Adriaensens, P. Description of the Nanostructured Morphology of 6,6-phenyl-C61 -Butyric Acid Methyl Ester (PCBM) by XRD, DSC and Solid-State NMR. *Magnetic resonance in chemistry : MRC* **2011,** *49* (5), 242–247.

[227] Zhong, Y.; Suzuki, K.; Inoue, D.; Hashizume, D.; Izawa, S.; Hashimoto, K.; Koganezawa, T.; Tajima, K. Interface-Induced Crystallization and Nanostructure Formation of [6,6]-Phenyl-C 61 -Butyric Acid Methyl Ester (PCBM) in Polymer Blend Films and its Application in Photovoltaics. *J. Mater. Chem. A* **2016,** *4* (9), 3335–3341.

[228] Casalegno, M.; Zanardi, S.; Frigerio, F.; Po, R.; Carbonera, C.; Marra, G.; Nicolini, T.; Raos, G.; Meille, S. V. Solvent-Free Phenyl-C61-Butyric Acid Methyl Ester (PCBM) from Clathrates: Insights for Organic Photovoltaics from Crystal Structures and Molecular Dynamics. *Chemical communications* **2013,** *49* (40), 4525–4527.

[229] Supasai, T.; Amornkitbamrung, V.; Thanachayanont, C.; Tang, I.-M.; Sutthibutpong, T.; Rujisamphan, N. Visualizing Nanoscale Phase Morphology for Understanding Photovoltaic Performance of PTB7: PC71BM Solar Cell. *Applied Surface Science* **2017,** *422*, 509–517.

[230] Thambidurai, M.; Kim, J. Y.; Song, J.; Ko, Y.; Song, H.; Kang, C.; Muthukumarasamy, N.; Velauthapillai, D.; Lee, C. High Performance Inverted Organic Solar Cells with Solution Processed Ga-Doped ZnO as an Interfacial Electron Transport Layer. *J. Mater. Chem. C* **2013,** *1* (48), 8161.

[231] Bencheikh, F.; Duché, D.; Ruiz, C. M.; Simon, J.-J.; Escoubas, L. Study of Optical Properties and Molecular Aggregation of Conjugated Low Band Gap Copolymers: PTB7 and PTB7-Th. *J. Phys. Chem. C* **2015,** *119* (43), 24643–24648.

[232] Mantid (2013): Manipulation and Analysis Toolkit for Instrument Data.; Mantid Project. http://dx.doi.org/10.5286/SOFTWARE/MANTID (accessed on 2023/08/08).

[233] Arnold, O.; Bilheux, J. C.; Borreguero, J. M.; Buts, A.; Campbell, S. I.; Chapon, L.; Doucet, M.; Draper, N.; Ferraz Leal, R.; Gigg, M. A.; Lynch, V. E.; Markvardsen, A.; Mikkelson, D. J.; Mikkelson, R. L.; Miller, R.; Palmen, K.; Parker, P.; Passos, G.; Perring, T. G.; Peterson, P. F.; Ren, S.; Reuter, M. A.; Savici, A. T.; Taylor, J. W.; Taylor, R. J.; Tolchenov, R.; Zhou, W.; Zikovsky, J. Mantid—Data analysis and visualization package for neutron scattering and μ SR experiments. *Nuclear Instruments and*

Methods in Physics Research Section A: Accelerators, Spectrometers, Detectors and Associated Equipment **2014,** *764*, 156–166.

[234] Paalman, H. H.; Pings, C. J. Numerical Evaluation of X-ray Absorption Factors for Cylindrical Samples and Annular Sample Cells. *Journal of Applied Physics* **1962,** *33* (8), 2635–2639.

[235] Sears, V. F. Slow-Neutron Multiple Scattering. *Advances in Physics* **1975,** *24* (1), 1–45.

[236] Colmenero, J.; Arbe, A. Recent Progress on Polymer Dynamics by Neutron Scattering: From Simple Polymers to Complex Materials. *J. Polym. Sci. B Polym. Phys.* **2013,** *51* (2), 87–113.

[237] Colmenero, J.; Arbe, A. Segmental Dynamics in Miscible Polymer Blends: Recent Results and Open Questions. *Soft Matter* **2007,** *3* (12), 1474–1485.

[238] Hoffmann, S.; Willner, L.; Richter, D.; Arbe, A.; Colmenero, J.; Farago, B. Origin of Dynamic Heterogeneities in Miscible Polymer Blends: A Quasielastic Neutron Scattering Study. *Physical review letters* **2000,** *85* (4), 772–775.

[239] Pérez-Aparicio, R.; Alvarez, F.; Arbe, A.; Willner, L.; Richter, D.; Falus, P.; Colmenero, J. Chain Dynamics of Unentangled Poly(ethylene- alt -propylene) Melts by Means of Neutron Scattering and Fully Atomistic Molecular Dynamics Simulations. *Macromolecules* **2011,** *44* (8), 3129–3139.

[240] Swenson, J.; Jansson, H.; Howells, W. S.; Longeville, S. Dynamics of water in a molecular sieve by quasielastic neutron scattering. *The Journal of chemical physics* **2005,** *122* (8), 84505.

[241] Liu, C.; Yi, C.; Wang, K.; Yang, Y.; Bhatta, R. S.; Tsige, M.; Xiao, S.; Gong, X. Single-Junction Polymer Solar Cells with Over 10% Efficiency by a Novel Two-Dimensional Donor-Acceptor Conjugated Copolymer. *ACS applied materials & interfaces* **2015,** *7* (8), 4928–4935.

[242] Song, L.; Wang, W.; Barabino, E.; Yang, D.; Körstgens, V.; Zhang, P.; Roth, S. V.; Müller-Buschbaum, P. Composition-Morphology Correlation in PTB7-Th/PC71BM Blend Films for Organic Solar Cells. *ACS applied materials & interfaces* **2019,** *11* (3), 3125–3135.

[243] Liu, X.; Wen, W.; Bazan, G. C. Post-Deposition Treatment of an Arylated-Carbazole Conjugated Polymer for Solar Cell Fabrication. *Adv. Mater.* **2012,** *24* (33), 4505–4510.

[244] Peet, J.; Kim, J. Y.; Coates, N. E.; Ma, W. L.; Moses, D.; Heeger, A. J.; Bazan, G. C. Efficiency Enhancement in Low-Bandgap Polymer Solar Cells by Processing with Alkane Dithiols. *Nat. Mater.* **2007,** *6* (7), 497–500.

[245] Lee, J. K.; Ma, W. L.; Brabec, C. J.; Yuen, J.; Moon, J. S.; Kim, J. Y.; Lee, K.; Bazan, G. C.; Heeger, A. J. Processing Additives for Improved Efficiency from Bulk Heterojunction Solar Cells. *Journal of the American Chemical Society* **2008,** *130* (11), 3619–3623.

[246] Lou, S. J.; Szarko, J. M.; Xu, T.; Yu, L.; Marks, T. J.; Chen, L. X. Effects of Additives on the Morphology of Solution Phase Aggregates Formed by Active Layer Components of High-Efficiency Organic Solar Cells. *J. Am. Chem. Soc.* **2011,** *133* (51), 20661–20663.

[247] Etzold, F.; Howard, I. A.; Forler, N.; Cho, D. M.; Meister, M.; Mangold, H.; Shu, J.; Hansen, M. R.; Müllen, K.; Laquai, F. The Effect of Solvent Additives on Morphology and Excited-State Dynamics in PCPDTBT:PCBM Photovoltaic Blends. *J. Am. Chem. Soc.* **2012,** *134* (25), 10569–10583.

[248] Yu, J.; Zheng, Y.; Huang, J. Towards High Performance Organic Photovoltaic Cells: A Review of Recent Development in Organic Photovoltaics. *Polymers* **2014,** *6* (9), 2473–2509.

[249] Ito, M.; Palanisamy, K.; Kumar, A.; Murugesan, V. S.; Shin, P.-K.; Tsuda, N.; Yamada, J.; Ochiai, S. Characterization of the Organic Thin Film Solar Cells with Active Layers of PTB7/PC 71 BM Prepared by Using Solvent Mixtures with Different Additives. *Int. J. Photoenergy* **2014,** *2014* (126), 1–8.

[250] Dkhil, S. B.; Pfannmöller, M.; Saba, M. I.; Gaceur, M.; Heidari, H.; Videlot-Ackermann, C.; Margeat, O.; Guerrero, A.; Bisquert, J.; Garcia-Belmonte, G.; Mattoni, A.; Bals, S.; Ackermann, J. Toward High-Temperature Stability of PTB7-Based Bulk Heterojunction Solar Cells: Impact of Fullerene Size and Solvent Additive. *Adv. Energy Mater.* **2017,** *7* (4), 1601486.

[251] Liao, H.-C.; Ho, C.-C.; Chang, C.-Y.; Jao, M.-H.; Darling, S. B.; Su, W.-F. Additives for Morphology Control in High-Efficiency Organic Solar Cells. *Mater. Today* **2013,** *16* (9), 326–336.

[252] Ye, L.; Jing, Y.; Guo, X.; Sun, H.; Zhang, S.; Zhang, M.; Huo, L.; Hou, J. Remove the Residual Additives toward Enhanced Efficiency with Higher Reproducibility in Polymer Solar Cells. *J. Phys. Chem. C* **2013,** *117* (29), 14920–14928.

[253] Wang, X.; Sun, Q.; Gao, J.; Wang, J.; Xu, C.; Ma, X.; Zhang, F. Recent Progress of Organic Photovoltaics with Efficiency over 17%. *Energies* **2021,** *14* (14), 4200.

[254] van der Staaij, F. M.; van Keulen, I. M.; Hauff, E. von. Organic Photovoltaics: Where Are We Headed? *Sol. RRL* **2021,** *5* (8), 2100167.

[255] Giannouli, M. Current Status of Emerging PV Technologies: A Comparative Study of Dye-Sensitized, Organic, and Perovskite Solar Cells. *Int. J. Photoenergy* **2021,** *2021*, 1–19.

[256] Kniepert, J.; Lange, I.; Heidbrink, J.; Kurpiers, J.; Brenner, T. J. K.; Koster, L. J. A.; Neher, D. Effect of Solvent Additive on Generation, Recombination, and Extraction in PTB7:PCBM Solar Cells: A Conclusive Experimental and Numerical Simulation Study. *J. Phys. Chem. C* **2015,** *119* (15), 8310–8320.

[257] Kim, W.; Kim, J. K.; Kim, E.; Ahn, T. K.; Wang, D. H.; Park, J. H. Conflicted Effects of a Solvent Additive on PTB7:PC 71 BM Bulk Heterojunction Solar Cells. *J. Phys. Chem. C* **2015,** *119* (11), 5954–5961.

[258] Manley, E. F.; Strzalka, J.; Fauvell, T. J.; Jackson, N. E.; Leonardi, M. J.; Eastham, N. D.; Marks, T. J.; Chen, L. X. In Situ GIWAXS Analysis of Solvent and Additive Effects on PTB7 Thin Film Microstructure Evolution during Spin Coating. *Adv. Mater.* **2017,** *29* (43).

[259] Tremolet de Villers, B. J.; O'Hara, K. A.; Ostrowski, D. P.; Biddle, P. H.; Shaheen, S. E.; Chabinyc, M. L.; Olson, D. C.; Kopidakis, N. Removal of Residual Diiodooctane Improves Photostability of High-Performance Organic Solar Cell Polymers. *Chem. Mater.* **2016,** *28* (3), 876–884.

[260] Tournebize, A.; Rivaton, A.; Peisert, H.; Chassé, T. The Crucial Role of Confined Residual Additives on the Photostability of P3HT:PCBM Active Layers. *J. Phys. Chem. C* **2015,** *119* (17), 9142–9148.

[261] Waters, H.; Bristow, N.; Moudam, O.; Chang, S.-W.; Su, C.-J.; Wu, W.-R.; Jeng, U.-S.; Horie, M.; Kettle, J. Effect of Processing Additive 1,8-octanedithiol on the Lifetime of PCPDTBT based Organic Photovoltaics. *Org. Electron.* **2014,** *15* (10), 2433–2438.

[262] Löhrer, F. C.; Senfter, C.; Schaffer, C. J.; Schlipf, J.; Moseguí González, D.; Zhang, P.; Roth, S. V.; Müller-Buschbaum, P. Light-Induced and Oxygen-Mediated Degradation Processes in Photoactive Layers Based on PTB7-Th. *Adv. Photo. Res.* **2020,** *1* (1), 2000047.

[263] Reese, M. O.; Morfa, A. J.; White, M. S.; Kopidakis, N.; Shaheen, S. E.; Rumbles, G.; Ginley, D. S. Pathways for the Degradation of Organic Photovoltaic P3HT:PCBM Based Devices. *Sol. Energy Mater. Sol. Cells* **2008,** *92* (7), 746–752.

[264] Griffini, G.; Turri, S.; Levi, M. Degradation and Stabilization of poly(3-hexylthiophene) Thin Films for Photovoltaic Applications. *Polym. Bull.* **2011,** *66* (2), 211–222.

[265] Alem, S.; Wakim, S.; Lu, J.; Robertson, G.; Ding, J.; Tao, Y. Degradation Mechanism of Benzodithiophene-Based Conjugated Polymers When Exposed to Light in Air. *ACS Appl. Mater. Interfaces* **2012,** *4* (6), 2993–2998.

[266] Wienhold, K. S.; Chen, W.; Yin, S.; Guo, R.; Schwartzkopf, M.; Roth, S. V.; Müller-Buschbaum, P. Following in Operando the Structure Evolution-Induced Degradation in Printed Organic Solar Cells with Nonfullerene Small Molecule Acceptor. *Sol. RRL* **2020,** *4* (9), 2000251.

[267] Wienhold, K. S.; Körstgens, V.; Grott, S.; Jiang, X.; Schwartzkopf, M.; Roth, S. V.; Müller-Buschbaum, P. In Situ Printing: Insights into the Morphology Formation and Optical Property Evolution of Slot-Die-Coated Active Layers Containing Low Bandgap Polymer Donor and Nonfullerene Small Molecule Acceptor. *Sol. RRL* **2020,** *4* (7), 2000086.

[268] Shah, S.; Biswas, R.; Koschny, T.; Dalal, V. Unusual Infrared Absorption Increases in Photo-Degraded Organic Films. *Nanoscale* **2017,** *9* (25), 8665–8673.

[269] Perthué, A.; Gorisse, T.; Santos Silva, H.; Bégué, D.; Rivaton, A.; Wantz, G. Influence of Traces of Oxidized Polymer on the Performances of Bulk Heterojunction Solar Cells. *Mater. Chem. Front.* **2019,** *3* (8), 1632–1641.

[270] Darlatt, E.; Muhsin, B.; Roesch, R.; Lupulescu, C.; Roth, F.; Kolbe, M.; Gottwald, A.; Hoppe, H.; Richter, M. Irradiation-Induced Degradation of PTB7 Investigated by Valence Band and S 2p photoelectron spectroscopy. *Nanotechnology* **2016,** *27* (32), 324005.

[271] Razzell-Hollis, J.; Wade, J.; Tsoi, W. C.; Soon, Y.; Durrant, J.; Kim, J.-S. Photochemical Stability of High Efficiency PTB7:PC 70 BM Solar Cell Blends. *J. Mater. Chem. A* **2014,** *2* (47), 20189–20195.

[272] Tsoi, W. C.; James, D. T.; Kim, J. S.; Nicholson, P. G.; Murphy, C. E.; Bradley, D. D. C.; Nelson, J.; Kim, J.-S. The Nature of In-Plane Skeleton Raman Modes of P3HT and their Correlation to the Degree of Molecular Order in P3HT:PCBM Blend Thin Films. *J. Am. Chem. Soc.* **2011,** *133* (25), 9834–9843.

[273] Tsoi, W. C.; Zhang, W.; Razzell Hollis, J.; Suh, M.; Heeney, M.; McCulloch, I.; Kim, J.-S. In-Situ Monitoring of Molecular Vibrations of Two Organic Semiconductors in Photovoltaic Blends and their Impact on Thin Film Morphology. *Appl. Phys. Lett.* **2013,** *102* (17), 173302.

[274] Razzell-Hollis, J.; Tsoi, W. C.; Kim, J.-S. Directly Probing the Molecular Order of Conjugated Polymer in OPV Blends Induced by Different Film Thicknesses, Substrates and Additives. *J. Mater. Chem. C* **2013,** *1* (39), 6235.

[275] Lesoine, M. D.; Bobbitt, J. M.; Carr, J. A.; Elshobaki, M.; Chaudhary, S.; Smith, E. A. Quantitative Comparison of Organic Photovoltaic Bulk Heterojunction Photostability Under Laser Illumination. *J. Phys. Chem. C* **2014,** *118* (51), 30229–30237.

[276] Barreiro-Argüelles, D.; Ramos-Ortiz, G.; Maldonado, J.-L.; Pérez-Gutiérrez, E.; Romero-Borja, D.; Meneses-Nava, M.-A.; Nolasco, J. C. Stability Study in Organic Solar Cells Based on PTB7: PC71BM and the Scaling Effect of the Active Layer. *Solar Energy* **2018,** *163*, 510–518.

[277] Yang, D.; Löhrer, F. C.; Körstgens, V.; Schreiber, A.; Bernstorff, S.; Buriak, J. M.; Müller-Buschbaum, P. In-Operando Study of the Effects of Solvent Additives on the Stability of Organic Solar Cells Based on PTB7-Th:PC 71 BM. *ACS Energy Lett.* **2019,** *4* (2), 464–470.

[278] Duan, L.; Yi, H.; Zhang, Y.; Haque, F.; Xu, C.; Uddin, A. Comparative Study of Light- and Thermal-Induced Degradation for Both Fullerene and Non-Fullerene-Based Organic Solar Cells. *Sustainable Energy Fuels* **2019,** *3* (3), 723–735.

[279] Fitter, J.; Lechner, R. E.; Büldt, G.; Dencher, N. A. Internal Molecular Motions of Bacteriorhodopsin: Hydration-Induced Flexibility Studied by Quasielastic Incoherent Neutron Scattering using Oriented Purple Membranes. *Proc. Natl. Acad. Sci USA* **1996,** No. 93, 7600–7605.

[280] Pieper, J.; Buchsteiner, A.; Dencher, N. A.; Lechner, R. E.; Hauß, T. Transient Protein Softening During the Working Cycle of a Molecular Machine. *Physical review letters* **2008,** *100* (22), 228103.

[281] Pieper, J.; Buchsteiner, A.; Dencher, N. A.; Lechner, R. E.; Hauss, T. Light-induced Modulation of Protein Dynamics During the Photocycle of Bacteriorhodopsin. *Photochemistry and photobiology* **2009,** *85* (2), 590–597.

[282] Burankova, T.; Hauß, T.; Ollivier, J.; Lechner, R. E.; Dencher, N. A.; Pieper, J. Data Analysis for Time-Resolved QENS Experiments in Biophysics. *arXiv preprint arXiv:1710.10442* **2017**.

[283] Fitter, J.; Verclas, S. A.; Lechner, R. E.; Büldt, G.; Ernst, O. P.; Hofmann, K. P.; Dencher, N. A. Bacteriorhodopsin and Rhodopsin Studied by Incoherent Neutron Scattering: Dynamical Properties of Ground States and Light Activated Intermediates. *Phys. B* **1999,** *266* (1-2), 35–40.

[284] Pieper, J.; Hauss, T.; Buchsteiner, A.; Baczyński, K.; Adamiak, K.; Lechner, R. E.; Renger, G. Temperature-and Hydration-Dependent Protein Dynamics in Photosystem II of Green Plants Studied by Quasielastic Neutron Scattering. *Biochemistry* **2007,** *46* (40), 11398–11409.

[285] Combet, S.; Pieper, J.; Coneggo, F.; Ambroise, J.-P.; Bellissent-Funel, M.-C.; Zanotti, J.-M. Coupling of Laser Excitation and Inelastic Neutron Scattering: Attempt to Probe the Dynamics of Light-Induced C-Phycocyanin Dynamics. *European Biophysics Journal* **2008,** *37*, 693–700.

[286] Furrer, A.; Stoeckli, A. Inelastic Neutron Scattering Study of Light-Induced Dynamics of a Photosynthetic Membrane System. *Physical Review E* **2010,** *81* (1), 11901.

List of publications

Publications related to this dissertation

- D. Schwaiger, W. Lohstroh, P. Müller-Buschbaum, „Investigation of Molecular Dynamics of a PTB7:PCBM Polymer Blend with Quasi-Elastic Neutron Scattering", *ACS Appl. Polym. Mater., 2 (9), 3797-3804, 2020*

- D.M. Schwaiger, W. Lohstroh, P. Müller-Buschbaum, „The Influence of the Blend Ratio, Solvent Additive, and Post-production Treatment on the Polymer Dynamics in PTB7:PCBM Blend Films", *Macromolecules, 54 (13), 6534-6542, 2021*

- D.M. Schwaiger, W. Lohstroh, M. Wolf, C.J. Garvey, P. Müller-Buschbaum, „In-situ study of degradation in PTB7:PCBM films prepared with the binary solvent additive DPE:DIO", *Polym. Sci., 61 (15), 1660-1670, 2023*

Further publications

- X. Zhang, L.P. Kreuzer, D.M. Schwaiger, M. Lu, Z. Mao, R. Cubitt, P. Müller-Buschbaum, Q. Zhong, „Abnormal fast dehydration and rehydration of light- and thermo-dual-responsive copolymer films triggered by UV radiation", *Soft Matter, 17, 2603-2613, 2021*

- P. Zhang, X. Zhang, L.P. Kreuzer, D.M. Schwaiger, M. Lu, R. Cubitt, Q. Zhong, P. Müller-Buschbaum, „Kinetics of UV Radiation-Induced Fast Collapse and Recovery in Thermally Cycled and Rehydrated Light- and Thermo- Double-Responsive Copolymer Films Probed by *In Situ* Neutron Reflectivity", *Langmuir, 39 (30), 10464-10474, 2023*

Scientific reports

- D. Schwaiger, W. Lohstroh, J. Pieper, P. Müller-Buschbaum, „Laser-Neutron pump-probe experiment at the neutron time-of-flight spectrometer TOFTOF“, *Lehrstuhl für Funktionelle Materialien, Annual Report, 2018, 110-111.*

- D. Schwaiger, W. Lohstroh, P. Müller-Buschbaum, „Investigation of molecular dynamics of a PTB7:PCBM polymer blend with quasielastic neutron scattering“, *Lehrstuhl für Funktionelle Materialien, Annual Report, 2019, 44-45.*

- D.M. Schwaiger, W. Lohstroh, P. Müller-Buschbaum, „Dynamics in polymer-fullerene blends for photovoltaic applications”, *Lehrstuhl für Funktionelle Materialien, Annual Report, 2020, 62-63.*

- MLZ Press Release „Windows that generate electricity“, 2021-02-25; „Fensterscheiben, die Strom erzeugen“, 2021-03-15.

- D.M. Schwaiger, W. Lohstroh, P. Müller-Buschbaum, „Influence of solvent additives on molecular dynamics in polymer-fullerene blends“, *Lehrstuhl für Funktionelle Materialien, Annual Report, 2021, 54-55.*

- D.M. Schwaiger, P. Müller-Buschbaum, „Chemical and physical stability of PTB7:PCBM bulk heterojunction films for photovoltaic applications“, *Lehrstuhl für Funktionelle Materialien, Annual Report, 2022, 72-73.*

- MLZ Press Release “Ohne Zusatzstoffe: Wie organische Solarzellen effizienter warden“ August 2023; „Without additives: How organic solar cells become more efficient” August 2023

Talks

- D.M. Schwaiger, “Laser-neutron pump-probe experiment at the neutron time-of-flightspectrometer TOFTOF”, *Seminar: Struktur und Dynamik*

kondensierter Materie, Chair for Functional Materials, Physics-Department, TU München, Garching, Germany, January 2019.

- D.M. Schwaiger, "Dynamics in polymer-fullerene blends for photovoltaic applications", *Seminar: Struktur und Dynamik kondensierter Materie, Chair for Functional Materials, Physics-Department, TU München, Garching, Germany, January 2020.*

- D.M. Schwaiger, "Dynamics in polymer-fullerene blends for photovoltaic applications", *Seminar: Struktur und Dynamik kondensierter Materie, Chair for Functional Materials, Physics-Department, TU München, Garching Germany, December 2020.*

- D.M. Schwaiger, W. Lohstroh, P. Müller-Buschbaum, "Dynamics in polymer-fullerene blends for photovoltaic applications and the influence of performance enhancing measures", *Virtuelle 84. Jahrestagung der DPG und DPG-Tagung der SKM, online, Germany, September 2021.*

- D.M. Schwaiger, "Dynamics in polymer-fullerene blends and the influence of DIO as solvent additive studied with quasielastic neutron scattering", *Seminar: Struktur und Dynamik kondensierter Materie, Chair for Functional Materials, Physics-Department, TU München, Garching, Germany, November 2021.*

- D.M. Schwaiger, W. Lohstroh, P. Müller-Buschbaum, "Dynamics in polymer-fullerene blends for photovoltaic applications and the influence of performance enhancing measures", *QENS/WINS 2022,* San Sebastian*, Spain, May 2022.*

- D.M. Schwaiger, W. Lohstroh, P. Müller-Buschbaum, "Dynamics in Polymer-Fullerene Blends for Photovoltaic Applications studied with Quasielastic Neutron Scattering**",** *DPG-Tagung der Sektion Kondensierte Materie (SKM), Regensburg, Germany, September 2022.*

- D.M. Schwaiger, "Quasielastic neutron scattering in polymer-fullerene blends", *5th MLZ internal biannual science meeting, Grainau, Germany, June 2023*

Conference poster presentations

- D. Schwaiger, W. Lohstroh, P. Müller-Buschbaum, “Laser-neutron pump-probe experiment at the neutron time-of-flight spectrometer TOFTOF”, *German Conference for Research with Synchrotron Radiation, Neutrons and Ion Beams at Large-Scale Facilities, Garching, 2018.*

- D. Schwaiger, M. Golub, I. Seuffert, A. Zouni, W. Lohstroh, P. Müller-Buschbaum, J. Pieper, „Protein dynamics of a thermophile photosystem”, *DPG-Tagung der Sektion Kondensierte Materie (SKM), Regensburg, Germany, April 2019.*

- D. Schwaiger, W. Lohstroh, P. Müller-Buschbaum, „Studying the dynamics of PTB7:PCBM organic photovoltaic active layers”, *9th Colloquium of the Munich School of Engineering*, *Garching, Germany, August 2019.*

- D.M. Schwaiger, W. Lohstroh, P. Müller-Buschbaum, „Dynamics in polymer-fullerene blends for photovoltaic applications”, *ACS Spring 2021, online, USA, April 2021*

- D.M. Schwaiger, W. Lohstroh, P. Müller-Buschbaum, „Studying the dynamics of PTB7:PCBM blend films with quasielastic neutron scattering”, *QENS/WINS 2021, online, Spain, May 2021.*

- D.M. Schwaiger, W. Lohstroh, P. Müller-Buschbaum, „ Dynamics in polymer-fullerene blends for photovoltaic applications”, *11th Colloquium of the Munich School of Engineering*, *Garching, Germany, July 2021.*

- D.M. Schwaiger, W. Lohstroh, P. Müller-Buschbaum, „Dynamics in polymer-fullerene blends and the influence of DIO as solvent additive studied with quasielastic neutron scattering”, *European Conference on Neutron Scattering 2023, Garching, Germany, March 2023*

Acknowledgements

During my time as a PhD candidate at the Chair of Functional Materials, I had the privilege to meet and work with many people with various backgrounds and to develop in a professional environment as an independent researcher. I was able to develop not only my scientific but also my personal skills, which will be valuable assets for all aspects of my future life. This would not have been possible without the help and support of many persons, which I want to thank at the end of this thesis and I will never forget about.

First, I want to thank my supervisor Prof. Peter Müller-Buschbaum for the unique opportunity to perform my PhD at his Chair of Functional Materials at the Technical University Munich. This offered the precious experiences of working at large scale synchrotron and neutron facilities as well as numerous visits at national and international conferences, summer schools, collaborators, etc. Further I would like to thank Peter for the trust he put in me as his student and co-worker and his guidance and constructive advice whenever I needed it.

Definitely one of the most important persons for me in my time as PhD student and for the completion of this thesis was Dr. Wiebke Lohstroh, who officially was my mentor during this time, but in fact was committed far beyond this bald title. I want to express my deepest thank for your constant support in all aspects of my PhD. I enjoyed all our valuable discussions and highly appreciated your reviews of my work. Both were a great source of knowledge and inspiration for me. Especially your introduction into the execution and evaluation of quasielastic neutron scattering experiments were a great privilege to receive and far from being a matter of course. You contributed significantly to this thesis and it would not have been possible without you.

In the Chair of Functional Materials, or shorter E13, I have to thank many colleagues, most of them turned into real friends. In close symbiosis with the chair E59, thoroughly lead by Prof. Christine Papadakis, these chairs have provided an excellent research environment. At this point, I thank Christine for her very helpful comments and fruitful discussions at many occasions. Julian Heger joined the chair on the exact same day as I did and was the best companion during our time as PhD students you can imagine. Thanks Julian for being always available and your commitment for the

chair and all of your colleagues. There are many more colleagues that I want to thank for the good working atmosphere at the chairs as well as for making group activities super fun and also spending our free time together: Fabian Apfelbeck, Dr. Lorenz Bießmann, Dr. Wei Cao, Dr. Wei Chen, Christopher Everett, Dr. Marc Gensch, Sebastian Grott, Dr. Renjun Guo, Constantin Harder, Dr. Nuri Hohn, Tobias Hölderle, Linus Huber, Dr. Xinyu Jiang, Dr. Florian Jung, Dr. Jia-Jhen Kang, Dr. Chia-Hsin Ko, Dr. Volker Körstgens, Dr. Lucas Kreuzer, Morgan Le Du, Dr. Nian Li, Yanan Li, Dr. Franziska Löhrer, Dr. Bart-Jan Niebuur, Anna-Lena Öchsle, Dominik Petz, Thien An Pham, Ivana Pivarnikova, Dr. Shambhavi Pratap, Lennard Reb, Julija Reitenbach, Manuel Reus, Dr. Nitin Saxena, Simon Schaper, Lukas Spanier, Kun Sun, Sou Tu, Kun Wang, Peixi Wang, Christian Weindl, Tobias Widmann, Dr. Dan Yang and Dr. Senlin Xia. These are a lot of names, but all of them have contributed to my development during the PhD and helped me with personal discussions and their responsibilities for laboratories or instruments for the chair. Thus, the order is alphabetical and nothing else. Thank you all!

A special thank goes to my office neighbors, with whom I always worked together very well, who often were the first recipients for my questions and problems and who certainly had a mayor contribution to the good working atmosphere for me. Thank you for everything Roy Schaffrinna, Ting Tiang as well as the already mentioned Wei, Christian and Peixi.

Productive work at the chair would not be possible without many people in the background. Thus, I would like to thank our secretaries Marion Waletzki and Carola Kappauf for their constant administrative support when it came to things like ordering materials, planning and invoicing travels, planning group events and much more. Reinhold Funer was always available in the workshop and helped to plan and manufacture pieces of equipment, without which, many experiments would not have been possible. Terry Weinmann operated the electronic workshop where we could get the necessary electronic equipment on a daily basis. This possibility was particularly appreciated by me in my function as network administrator and IT responsible for the chair over several years. For providing the IT services, just mentioned, in my first year at the chair and for the seamless handover of knowledge and responsibilities, I want to thank Dieter Müller.

For my work as E13 network administrator, the support from Dr. Josef Homolka and especially from Mareike Stoller-Häfele was essential. Thank you for your patient instructions and explanations, always open doors and your willingness to help

whenever I ran out of talent. I really enjoyed the extension of some of our meetings to update each other about our latest bike travels or new bikes and parts of equipment.

The key part of this thesis is the performance and evaluation of QENS experiments at the TOFTOF instrument. Thus, I would like to thank the TOFTOF team around the instrument scientists Dr. Marcell Wolf and Dr. Christopher Garvey as well as the technicians Herbert Meier and Adrian Stephan for their support in planning, performing and evaluating the measurements. Further I have to thank the entire organization of the Heinz Meier-Leibnitz Zentrum for the possibility of getting neutron beamtime and performing these very unique experiments.

Some further members of MLZ deserve special thank for constructive discussions and good cooperation, namely Neslihan Aslan, Dr. Sebastian Busch, Dr. Johanna Jochum and Dr. Apostolos Vagias as well as the administrative helpers Dr. Diana Fleischer and Dr. Christoph Kreileder.

For the warm welcome during my stay in Tartu (Estonia), and a good introduction into the field of protein research, I want to thank Prof. Jörg Pieper and Dr. Maksym Golub.

I want to thank all of my coauthors for the good collaboration in preparing manuscripts, valuable input and thorough reading of drafts. This allowed good quality presentations of our research results in the form of articles, talks, posters and other reports. This research would not have been possible without the financial support from BMBF (Bundesministerium für Bildung und Forschung).

After all, my biggest gratitude belongs to my family and friends because I can always trust in your unconditional support, no matter if I deserve it or not. Without you, nothing of this would have been possible. You are my safe haven and my source of strength, so I want to deeply thank my parents Sonja and Martin Schwaiger, my siblings Alina, Patrick and Tim Schwaiger as well as my closest friends Aaron, Alex, Jules and Mario for existing and everything they do for me.

Ultimately, I want to gratefully express my highest appreciation for my precious Tanja Priller, who always endures my highs and lows and decided to be with me despite all of my shortcomings. You are the person that always supports me the most, that motivates me to go the next step, that I look forward to spend my life with together and the one that I love.